DEPARTMENT OF PHYSICS, UNIVERSITY OF JYVÄSKYLÄ
RESEARCH REPORT No. 7/2012

STUDY OF THE NEUTRAL PION AND DIRECT PHOTON PRODUCTION IN AU+AU COLLISIONS AT $\sqrt{s_{NN}}$ = 39 - 200 GeV

BY
NORBERT NOVITZKY

Academic Dissertation
for the Degree of
Doctor of Philosophy

To be presented, by permission of the Faculty of Mathematics and Science of the University of Jyväskylä, for public examination in Auditorium FYS-1 of the University of Jyväskylä on September 19, 2013 at 12 o'clock noon

Jyväskylä, Finland
July 2013

ISBN 978-951-39-5289-1 (e-book)

Author

Norbert Novitzky
University of Jyväskylä
Helsinki Institute of Physics
Finland

Supervisors

Dr. Jan Rak
University of Jyväskylä
Helsinki Institute of Physics
Finland

Dr. Gabor David
Brookhaven National Laboratory
USA

Reviewers

Prof. Saskia Mioduszewski
Texas A&M University
USA

Dr. Martin Spousta
Charles University in Prague
Czech Republic

Opponent

Dr. David d'Enterria
CERN, European Organization
for Nuclear Research
Switzerland

This thesis is dedicated to the memory of my father,
Dr. Béla Novitzky, who encouraged me to pursue physics.

Acknowledgements

I would like to express my great gratitude to my supervisors, Dr. Jan Rak and Dr. Gabor David, who supervised me in my research. I would like to thank them for providing me this golden opportunity to join into this interesting field of physics. My results could not have been achieved without their guidance and encouragement. I would like to thank for the financial support from the Helsinki Institute of Physics.

Special thanks to our ALICE Jyväskylä Group, namely to Dr. DongJo Kim, Dr. Filip Křížek and Dr. Sami Räsänen, for providing a wonderful atmosphere in the group, as well as for the many useful help and discussions about my work. I would like to thank Dr. Wladek Trzaska in helping me in my hardware work at the beginning of my studies. Also thanks to my fellow students who were working next to me: Mr. Jiří Král, Mr. Beomsu Chang, Mr. Jussi Viinikainen, Mr. Esko Pohjoisaho.

I would like to thank my fellow PHENIX collaborators for all their help in my data analysis. I have to acknowledge the help provied from the Pi0/Photon Topical Group, namely Dr. Takao Sakaguchi, Mr. József Imrek, Dr. Ondřej Chvála, Dr. Baldo Sahlmueller, Dr. Martin Purschke and Dr. Robert Pak. Special thanks to Dr. Michael J. Tannenbaum, for his very useful advices in my data analysis, and also countless discussions about physics. My gratitude goes also to Dr. Stephan Bathe and all the detector experts participating in the 2010 run, and such providing excellent data for my analysis. Furthermore, I am thankful to Dr. Chris Pinkenburg and Dr. Joseph Seele in helping me to debug and to run my analysis codes. I would like to thank the past and present spokespersons of PHENIX, Prof. Barbara Jacak, Prof. Jamie Nagle and Dr. David Morrison, for providing an excellent management of the collaboration. My gratitude goes also to the Hard/Photon a PLHF Physics Working Groups for their many comments to improve my data analysis.

I would like also express my thanks to Prof. Ivan Vitev, Prof. Jan Nemcik, Prof. Boris Kopeliovich and Dr. Thorsten Renk for providing me theoretical calculations to the data presented in the thesis. Furthermore, I would like to thank the theoretical physicists related to heavy ion physics at University of Jyväskylä for their help and fruitful discussions about the heavy ion field, namely to Prof. Kari Eskola, Dr. Thorsten Renk, Dr. Harri Niemi, Dr. Tuomas Lappi, Dr. Hannu Holopainen, Dr. Redamy Perez-Ramos, Dr. Hannu Paukkunen, Mr. Risto Paatelainen, Mr. Ilkka Helenius, Mr. Heikki Mäntysaari.

Last, but not least, I would like to thank to my parents and my family for their continued encouragement and moral support to accomplish this work.

Contents

Chapter 1

Introduction

Quantum Chromodynamics (QCD) is the non-Abelian Quantum Field Theory of strong interactions. The study of non-perturbative aspects in QCD is one of the main goals of Ultra-Relativistic Heavy Ion (URHI) physics. In URHI collisions the deconfined medium called Quark Gluon Plasma (QGP) [1] is created and thus, URHI experiments provide a unique opportunity to study the QCD phase transition.

One of the most striking manifestations of the QGP in URHI collisions is the observation of high-p_T hadron suppression as compared to p+p collisions, known as jet quenching [2, 3, 4, 5]. The large suppression (factor of $\sim$5) of final state hadrons was first observed at Relativistic Heavy Ion Collider (RHIC) in Au+Au collisions at c.m. energy $\sqrt{s_{NN}}$ = 130 [6, 7] and 200 GeV [8], and later also at the Large Hadron Collider in Pb+Pb $\sqrt{s_{NN}}$=2.76 TeV [9, 10]. Such a large suppression of hadrons was not observed in the lower c.m. energy experiments at SPS/CERN in Pb+Pb collisions at $\sqrt{s_{NN}}$ = 17.3 GeV, although, a hint for suppression was seen in the high-p_T π^0 yield studied by WA98 experiment [11]. It is natural to expect that the threshold collision energy, when the suppression becomes dominant over other nuclear effects, should be related to the threshold energy for the QGP formation. RHIC started the low-energy program in 2010 to investigate the QGP properties. The main objective of this thesis focuses on the study of the neutral pion and eta production in the Au+Au "low-energy" collisions at $\sqrt{s_{NN}}$=39 and 62.4 GeV and this work was published in [12].

Another important probe of the medium is the direct photon production [13, 14, 15]. Due to their small electromagnetic coupling, as compared to QCD, photons leave the medium without further interaction and thus they provide an important probe of the initial stages of URHI collisions. Direct photon production in Au+Au collisions at $\sqrt{s_{NN}}$=62.4 GeV data is also part of this work.

This thesis is organized as follows: In the first chapter I present a short introduction to the QCD and URHI physics. In addition, a short overview of direct photon production in heavy ion collisions is presented. I will discuss some of the experimental results which triggered an increasing interest in the study of the threshold phenomena.

The following chapter III describes the PHENIX detector apparatus with the focus on EMCal, the main detector used for this analysis. The EMCal detector consists of two types: (i) a shashlik type lead-scintillator and (ii) Cherenkov type lead-glass. The details on the clusterization method, energy reconstruction and the neutral meson and direct photon identification are discussed.

Chapter IV presents the summary of data and centrality selection in Au+Au collisions at $\sqrt{s_{NN}}$ = 39 and 62.4 GeV. The identification of the dead, hot and warm channels in EMCal is explained here. The section closes with the description of the Monte-Carlo simulations used for the efficiency and the acceptance corrections.

In Chapter V the neutral meson data analysis is presented. The neutral mesons, specifically π^0 and η particles, were reconstructed via the 2-photon invariant mass method. In order to study the suppression of final state hadrons in heavy ion collisions, the knowledge of the p+p reference is needed at same collision energy. Thus, I also describe the procedure used to obtain the π^0 reference data of p+p collisions at $\sqrt{s}$ = 39 and 62.4 GeV.

The following chapter VI summarizes the direct photon analysis in Au+Au collisions at $\sqrt{s_{NN}}$=62.4 GeV using the subtraction method. The main idea of the subtraction method is to use the knowledge of the measured π^0 spectrum which can be used to determine the decay photon background. The preliminary results are presented in this chapter.

In the last chapter VII, I summarize the main results, the nuclear modification factor extracted from the $\sqrt{s_{NN}}$ = 39 and 62.4 GeV data is compared to three different theoretical models: (i) an analytical calculation in the GLV energy loss framework [16], (ii) a Monte Carlo energy loss model [17] in a realistic hydrodynamics and (iii) a new dipole approach in color transparency model [18].

1.1 Foundation of QCD

There are four known fundamental forces which are believed to govern this universe: gravitational, electromagnetic, weak and strong interaction. The Quantum Field Theory (QFT) was developed to describe the electromagnetic interaction almost at the same time as the discovery of the Dirac equation in 1930's [19]. It turned out to be a natural tool to describe the dynamics of elementary particle physics. One of the early successes of QFT was the successful description of the neutron β-decay by Fermi [20].

However, soon the theory faced severe difficulties due to infinities popping out in the calculations. These infinity problems were solved by introducing the renomalization method. After Feynman developed the path integral formulation, which turned out to be a useful and intuitive way of performing perturbation theory, the QFT description of electromagnetic and weak interactions became rather successful.

Similar attempt of using the QFT framework to describe the strong interaction was first proposed by Yukawa [21], who formulated the field theory by introducing the pion and nucleon fields. The early success of this theory was due to the discovery of the $\pi^{\pm}$ particles in the predicted mass region. However, the further experimental discovery of strange baryons and mesons shattered the basis of this approach. The newly discovered particles appeared to be as fundamental as the nucleons or pions, there was no evidence of their constituents.

In 1960's, Gell-Mann [22] and Ne'eman [23] realized that particles sharing the same quantum numbers (spin, parity) follow the symmetry of the group SU(3) which is based on 3 elementary generators, up, down, strange, or u, d, s, with spin $1/2$ and fractional electrical charge, which Gell-Mann called quarks [24] and Zweig called aces [25]. Now we know that it is the symmetry of hadrons and it is arising from the relatively small masses of up, down and strange (u, d, s) quarks compared to scale of the strong interaction (~ 1 GeV).

The interactions between quarks were not yet understood. In the light of the experimental results at hadron-hadron colliders, Blankenbecler, Brodsky and Gunion developed the Constituent Interchange Model (CIM) [26]. The basic idea of CIM was that the strong interaction is mediated by the quarks. The model proposed a scaling law of single-particle inclusive scattering at 90° and large transverse momentum. However, the model was proved to be wrong by experimental results (see more in Sec. 1.1.2). In order to understand the interaction mechanism between quarks, one important step was made in the development of the colored QFT by re-introduction of the non-Abelian gauge theory [27]. Nowadays, the Abelian QED and non-Abelian QCD are part of the Standard Model (SM) of electroweak and strong interactions.

1.1.1 Discovery of proton structure

This section gives a short overview of the experimental facts leading to discovery of the parton model and how these facts led to the establishment of QCD as the gauge field theory of the strong interactions. The discovery of the proton constituents, partons, has quite similar history as the discovery of atomic nuclei, in the famous Rutherford experiment [28] so I will first recall some historical facts related to the electron-proton scattering.

Rutherford experiment

Rutherford studied the α and β particles penetration through a thin sheet of mica [29]. From the observation of the unexpectedly large scattering angles of α as compared to the β particle, Rutherford concluded that single scattering in case of α-particles would always dominate multiple Coulomb scattering as it is in the case of β rays. This observation was later interpreted as a scattering on "point-like" constituents of the atom, nowadays known as the atomic nuclei.

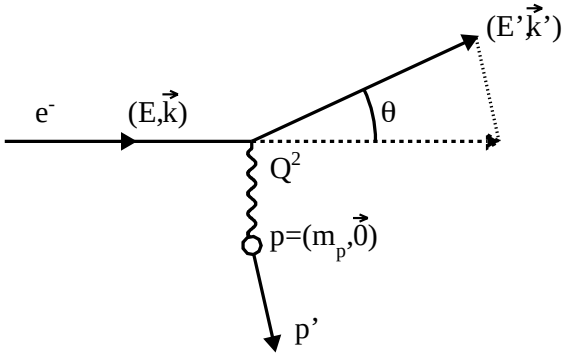

Figure 1.1: Schematic view of the electron elastic scattering on a heavy target (with mass m_p). When the target is infinitely heavy ($m_p \to \infty$) then the target does not recoil, $p^{'} \equiv p$.

A schematic view of the elastic scattering of an electron on a heavy target of mass m_p is shown in Fig. 1.1. The electron of four-momentum k scatters $k = (E, \vec{k}) \to k' = (E', \vec{k'})$ by exchanging a virtual photon $q = (\nu, \vec{q})$ and in the approximation of infinitely heavy target ($m_p \to \infty$), the target does not recoil $p' \equiv p$. Rutherford derived the following differential cross section known as the "Rutherford formula" [30]:

$$\left(\frac{d\sigma}{d\Omega}\right)_{\text{Rutherford}} = \frac{\alpha^2}{4E^2 \sin^4\left(\frac{\theta}{2}\right)}, \tag{1.1}$$

where $\alpha \approx 1/137$ is the electromagnetic coupling constant and θ is the scattering angle. Eq. (1.1) holds only for the non-relativistic limit of the electron ($E \ll m_e$) and only depends on the electric charges of the particles. Increasing the energy of the electron and entering the relativistic regime, the electron current becomes spin-dependent. If a target stays still heavy and point-like the differential cross section is written as (Mott formula):

$$\left(\frac{d\sigma}{d\Omega}\right)_{\text{Mott}} = \frac{\alpha^2 \cos^2\left(\frac{\theta}{2}\right)}{4E^2 \sin^4\left(\frac{\theta}{2}\right)}, \tag{1.2}$$

where the $\cos^2(\theta/2)$ arose as a consequence of the helicity conservation when the initial and final state electron wave functions overlap.

Elastic electron - proton scattering

When we consider the target to be a proton with finite mass m_p, it will recoil in the collision. The differential cross section of two spin-$\frac{1}{2}$ point like particles is given by

$$\left(\frac{d\sigma}{d\Omega}\right)_{\text{Dirac}} = \left(\frac{d\sigma}{d\Omega}\right)_{\text{Rutherford}} \frac{E^{'}}{E}\left(\cos^2\left(\frac{\theta}{2}\right) - \frac{q^2}{2m_p^2}\sin^2\left(\frac{\theta}{2}\right)\right), \tag{1.3}$$

where the fraction E'/E is due to proton recoil and the new term $\propto \sin^2(\theta/2)$ corresponds to the magnetic term due to the spin-spin interaction. Note that in the heavy target limit $E^{'} = E$ and $m_p \to \infty$ we obtain the Mott formula (Eq. (1.2)).

In 1953-1956 Hofstadter and collaborators at Stanford's Hansen Experimental Physics Lab (HEPL) studied the elastic electron-proton scattering [31]. They used a high precision moveable single arm spectrometer, in which the angle and energy of the scattered electrons were measured by a single arm spectrometer (PID by Čerenkov counters). They observed the differential cross section deviates from that in Eq. (1.3). This observation led to the revolutionary conclusion that the proton is not a point-like object but it must be instead compound of more elementary constituents.

In this case, the proton can be described as a charge density within the radius r and the total charge of $\int d^3\vec{r}\rho(\vec{r}) = 1$. The differential cross section of the elastic electron scattering is:

$$\frac{d\sigma}{d\Omega} = \left(\frac{d\sigma}{d\Omega}\right)_{\text{point-like}} |F(\vec{q}^2)|^2, \tag{1.4}$$

where the "form factor", $F(\vec{q}) = \int d^3\vec{r}\rho(\vec{r})e^{i\vec{q}\vec{r}}$, is the Fourier transform of the spatial charge distribution of the target particle. The finite size of the scattering centre introduces a phase difference between plane waves "scattered from different points in space". If the wavelength is large compared to the target then $F(\vec{q}^2) = 1$. An inclusion of the proton form factor led to the differential cross section form known as Rosenbluth

formula [32]):

$$\left(\frac{d\sigma}{d\Omega}\right)_{\text{Rosenbluth}} = \left(\frac{d\sigma}{d\Omega}\right)_{\text{Mott}} \frac{E'}{E}\left[\left(\frac{G_E^2 + (Q^2/4m_p^2)G_M^2}{1+(Q^2/4m_p^2)}\right) + \frac{Q^2}{4m_p^2} 2G_M^2 \tan^2\left(\frac{\theta}{2}\right)\right], \tag{1.5}$$

where $Q^2/4m_p^2 = -q^2/4m_p^2$ is Lorentz invariant, G_E and G_M are the *electric* and *magnetic* form factors of the proton, respectively. The form factors were introduced as pure empirical factors with the boundary conditions of $G_E^{(n \text{ or } p)}(0) = 0 \text{ or } 1$ and $G_M^{(n \text{ or } p)} = -1.91 \text{ or } 2.79$ (due to their magnetic moment) where n and p represent neutrons and protons, respectively. The experimental measurements of a 188 MeV electron beam showed that there are three regions according to Q^2: (i) $Q^2 < 0.02$ GeV^2 the electric form factor dominates, (ii) $0.02 < Q^2 < 3$ GeV^2 both form factors are measurable, (iii) $Q^2 > 3$ GeV^2 the magnetic form factor dominates [33].

Inelastic and deep-inelastic electron-proton scattering

As Q^2 increases, the elastic form factors become small and the probability of the inelastic scattering (schematically shown in Fig. 1.2) increases. While in elastic scatterings only the electron and proton are present in the final state, in the inelastic scattering the proton absorbs the virtual photon and breaks up mostly into the resonances. Such inelastic scatterings were studied at DESY [34] and at SLAC [35]. At even higher Q^2 the scattering becomes deep inelastic, and instead of the resonances a hadronic shower appears in the final state.

The schematic view of the kinematics of inelastic scattering is shown in Fig. 1.2. In the high energy deep inelastic scattering (DIS) experiments one measures the variables of the incoming and outgoing electron: E, E', θ. The kinematical variables with the proton target at rest $\vec{p} = 0$:

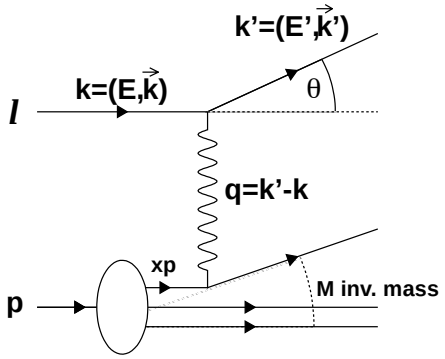

Figure 1.2: The schematic view of the electron-proton (deep) inelastic scattering.

$$
\begin{aligned}
Q^2 &= (\vec{k} - \vec{k'})^2 - (E - E')^2, \quad Q^2 = -q^2, \\
\nu &= E - E', \\
M^2 &= [(E - E') + E_p]^2 - \left[(\vec{k} - \vec{k'} + \vec{p'})\right]^2 = -Q^2 + m_p^2 + 2m_p\nu,
\end{aligned}
$$

where Q^2 is the momentum transfer, ν is the recoil energy and M represents the invariant mass of the final state hadrons. In the elastic case, $M = m_p$ and the space and time components of the virtual photon is related with the proton mass $Q^2 = 2m_p\nu = 2m_p(E - E') = 2EE'(1 - \cos\theta)$. However in the inelastic case, the M varies continuously and the measured variables are E', θ and the incoming electron energy E. Analogous to form factors in the elastic cross section in Eq. (1.5), in the inelastic case we can introduce the W_1 and W_2 "structure functions" and the double differential cross section in the laboratory frame is:

$$
\frac{\mathrm{d}^2\sigma}{\mathrm{d}\Omega \mathrm{d}E'} = \frac{\alpha^2}{4E^2 \sin^4(\theta/2)} \cdot \left[W_2(Q^2, \nu)\cos^2(\theta/2) + 2W_1(Q^2, \nu)\sin^2(\theta/2)\right],
$$

where $Q^2 = 4EE'\sin^2\theta/2$, $\nu = qp/m_p$, p is the four-momentum of target nucleon. At higher energy exchange, the elastic cross section is decreasing rapidly, while the inelastic cross section is changing slowly as a function of Q^2 (experimental data from SLAC are shown in Fig. 1.3).

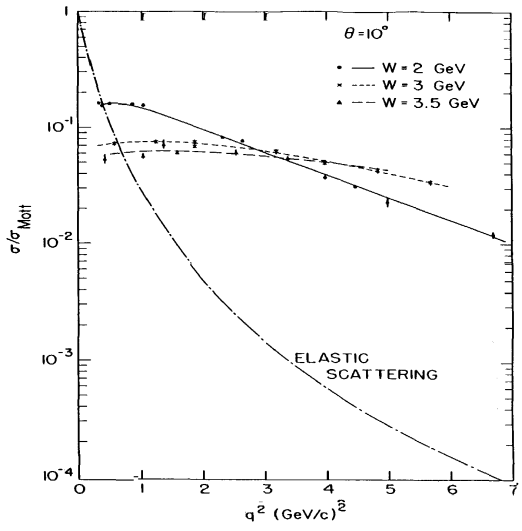

Figure 1.3: The experimental cross section [35] of electron-proton scattering as a function of Q^2 compared to the Mott cross section at fixed angle ($\theta = 10^\circ$). The inelastic cross section depends weakly on Q^2.

The W_1 and W_2 structure functions cannot be interpreted as the Fourier transforms of the charge and magnetic moment distribution. Instead, the structure functions describe the momentum distribution of the quarks within the proton. In the high energy limit, the structure functions become independent of Q and ν and depend only on the ratio $x = Q^2/2m_p\nu$ [33, 36]:

$$\begin{aligned} \lim_{Q^2\to\infty,\ \nu/Q^2 fixed} \nu W_2(Q^2,\nu) &= m_p F_2(x), \\ \lim_{Q^2\to\infty,\ \nu/Q^2 fixed} W_1(Q^2,\nu) &= F_1(x) \end{aligned}$$

where x (often denoted as x_B) refers to the Bjorken-variable and it expresses the momentum fraction of the proton carried by the proton constituent. The experimental results at SLAC [37] with a high energy electron beam indicated that the cross section remains quasi-constant as the function of ν/Q^2 (right panel of Fig. 1.4 [38]). At fixed x, the structure functions are almost independent of Q^2 indicating the scattering on the "point-like" constituents of the proton.

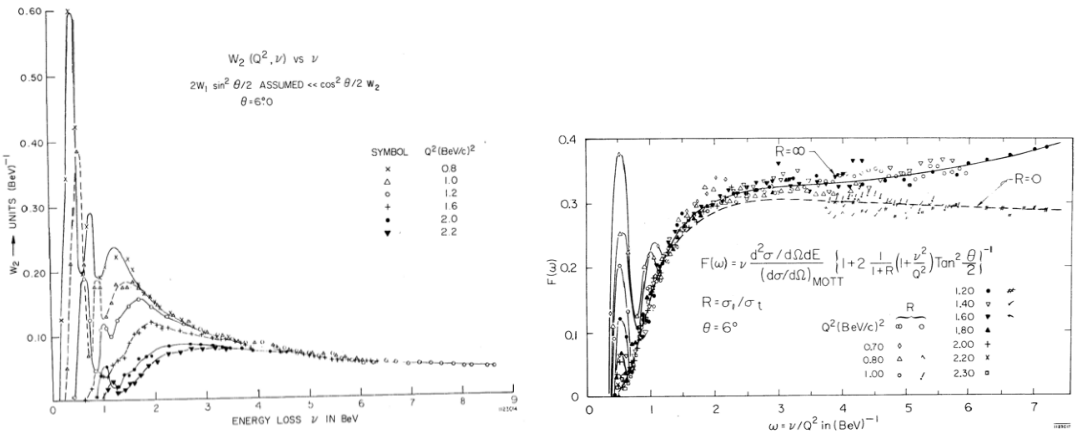

Figure 1.4: Left panel shows the structure function $W_2(Q^2,\nu)$ from SLAC data [38] dependence as a function of the energy loss ν, assuming that W_1 to vanish. Right panel shows the Bjorken scaling when the structure function $F(\omega) = \nu W_2(Q^2,\nu)$ becomes dependent only on $\omega = 2m_p/x = \nu/Q^2$ [38]. Note that in Bjorken limit the structure function is expressed as $F_2(x) = m_p F(1/2m_p\omega)$.

The results from the SLAC experiments led Feynman to suggest a *"parton picture"* of the deep inelastic scattering [39]. This intuitive model described the deep inelastic scattering and could be used to describe other processes as well. If we further assume that the constituents are spin-1/2 particles, i.e. quarks, it can be shown that the structure functions obey the Callan-Gross relation [40]:

$$F_2(x,Q^2) = 2xF_1(x,Q^2) = x\sum_q e_q^2 q(x), \tag{1.6}$$

where the measured structure functions relate to the underlying parton momentum distributions. The structure function $F_2(x)$ then describes the momentum fraction x ($0 < x < 1$) distribution of parton constituents inside the proton.

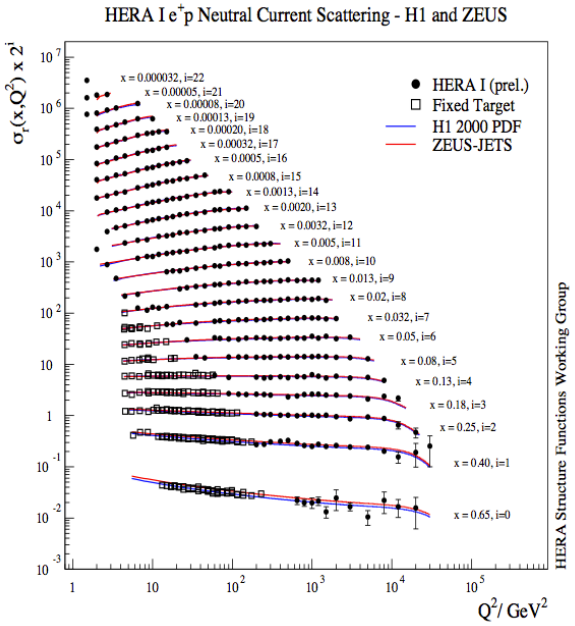

Figure 1.5: Deep inelastic neutral current e^+p scattering cross section data from combined measurements by H1 and ZEUS collaborations at HERA [41]. The curves represent next-to-leading QCD fits separately on each data set.

Recent measurement of cross section $\sigma_r(x, Q^2)$ were measured at HERA experiments (H1 and ZEUS) in e^+p and e^-p deep inelastic scattering [41]. Fig. 1.5 shows the measured data of the neutral current cross section which is proportional to the structure function, $\sigma_r(x, Q^2) \sim F_2(x)$. At low-$x$ and high-x the structure functions are not independent of Q^2. This phenomenon is know as "scaling violation". It is a consequence of the soft QCD radiation which becomes more prominent at high-Q^2 (parton showering). This process "splits" off more and more soft partons from the high-x one as Q^2 increases. Consequently the $F_2(Q^2)$ increases with Q^2 in the low-x region. Simultaneously this mechanism depletes the large-x partons (momentum conservation) leading to the decreasing trend of $F_2(Q^2)$ at large-x values.

1.1.2 Origin of the high-p_T physics

In the early studies of cosmic rays and p+p collisions at low energies G. Cocconi proposed an empirical formula to describe the pion cross section at different angles [42]:

$$\frac{\mathrm{d}\sigma}{\mathrm{d}\Omega} \sim e^{-p\sin\theta/b} = e^{-p_T/b}, \tag{1.7}$$

where the p is the momentum of the created particle, θ is the angle with respect to beam and b is the fit parameter, typically $b \sim 1/6$ GeV/c. The formula successfully described the angular distributions of inelastic proton-proton scattering at incident momenta in the range from 7 to 12 GeV/c at Proton Synchrotron [43].

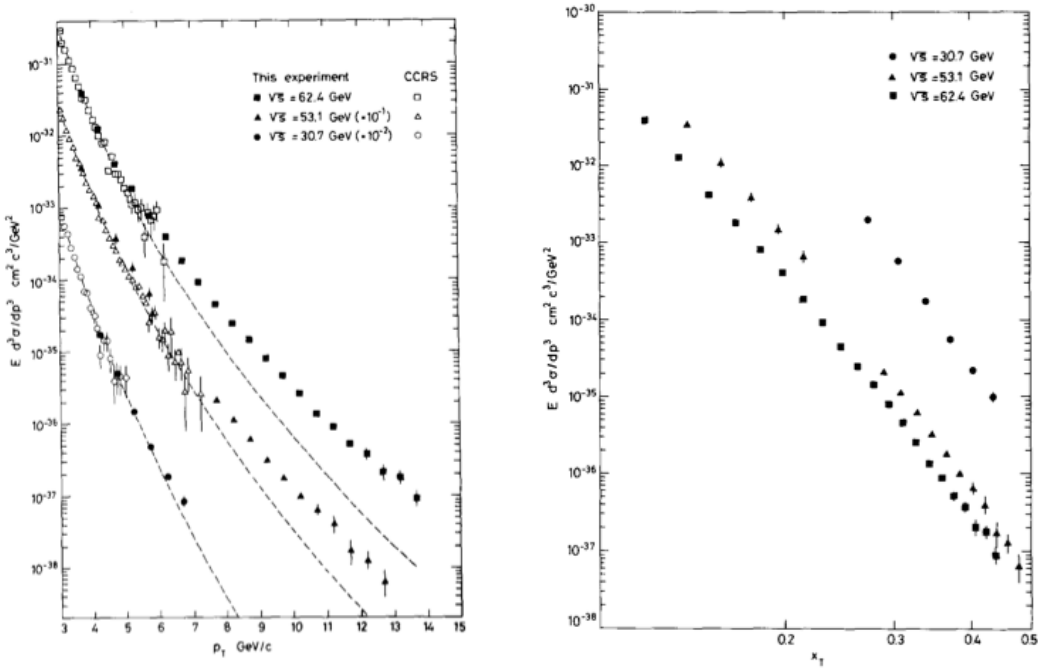

Figure 1.6: Left: Invariant cross sections [44, 45] for reactions p+p $\to \pi^0$ + X as a function of p_T at $\sqrt{s} = 62.4$ GeV, 53.1 GeV (scaled by 1/10) and 30.6 GeV (scaled by 1/100). Right: Invariant cross-sections as a function of $x_T = 2p_T/\sqrt{s}$ at same energies.

Later the CCOR experiment at Intersecting Storage Ring (ISR) observed an excess at high-p_T neutral pion production in p+p collisions at $\sqrt{s} = 30 - 62.4$ GeV [44, 45]. The high-p_T tail follows the power law functions rather than the Cocconi formula (see left panel in 1.7).

Breaking of the e^{-6p_T} law in the high-p_T and the absence of the intrinsic scale in the theory (in the parton model with point-like couplings among the partons) led Berman, Bjorken and Kogut [46] to the conclusion that the inclusive particle cross section, generally of the form $F(p_T, \sqrt{s}, \vartheta)$ should scale as $p_T^{-4}G(x_\mathrm{T}, \vartheta)$ where $x_\mathrm{T} \equiv 2p_T/\sqrt{s}$, ϑ stands for the polar angle and $G(x_\mathrm{T}, \vartheta)$ is a universal dimensionless function. However, measured p_T-distributions were found to be significantly steeper than the power law function with the exponent $n = 4$. In fact, a typical value of n at the ISR c.m. energy

range is approximately $n \sim 8$. This observation inspired a new general scaling law for the invariant cross section at different collision energies [47]

$$E\frac{d^3\sigma}{dp^3} = \frac{1}{p_T^{n_{\rm eff}}} F\left(x_T\right), \tag{1.8}$$

where the exponent $n_{\rm eff} = 2(n_{\rm active} - 2)$ and $n_{\rm active}$ is the number of elementary fields participating in the subprocess. For quark–quark scattering ($n_{\rm active} = 4$) one obtains the p_T^{-4} dependency. Perhaps more importantly, they predicted $n_{\rm eff} = 8$ ($n_{\rm active} = 6$) for the case of quark–meson scattering by the exchange of a quark. In this Constituent Interchange Model (CIM), single vector–gluon exchange contributes insignificantly to wide-angle hadronic collisions [48]. Further experimental results from Fermilab [49] also observed scaling behavior of $n \sim 8$ and the CIM model became one of the most interesting candidates to describe the strong interactions.

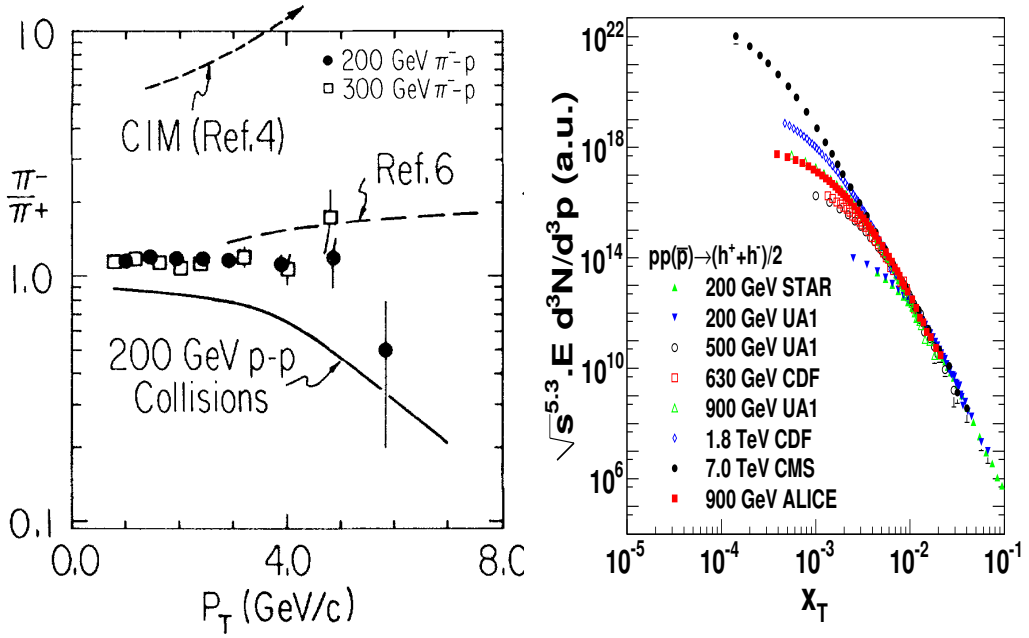

Figure 1.7: Left: The ratio of π^-/π^+ produced by 200 and 300 GeV in π^-+p collisions [50]. The solid line represents the corresponding ratio in p+p collisions and the upper dashed line with an arrow is the prediction from the CIM model [51]. Right: Compilation of x_T distributions scaled by a factor $n_{\rm eff} = 5.3$ as in Eq. (1.9).

However, in the CIM model where the quark–meson scattering is dominated by a quark exchange the π^- should dominate π^+ production in $\pi^- + p$ collisions at large p_T. Data from Fermilab experiment at beam energies 200 and 300 GeV [50] observed a

constant $\pi^-/\pi^+ \sim 1$ ratio whereas the CIM model predicted at least a factor of 5 with steeply rising π^-/π^+ ratio.

In the modern QCD language the scaling violation ($n_{\rm eff} > 4$) is mainly due to the QCD running coupling, evolution of parton distributions functions, soft QCD radiation and the higher-twist phenomena [52].

Equation (1.8) can be rewritten as

$$E\frac{d^3\sigma}{dp^3} = \frac{1}{\sqrt{s}^{n_{\rm eff}(x_T,\sqrt{s})}} G(x_T), \tag{1.9}$$

where $n_{\rm eff}(x_T, \sqrt{s})$ is generally a function of x_T and $\sqrt{s}$. By comparing the measured cross sections at two different c.m. energies, $\sqrt{s_1}$ and $\sqrt{s_2}$, one can extract $n_{\rm eff}(x_T)$ as

$$n_{\rm eff}(x_T) = \frac{\log\left(\sigma(x_T, \sqrt{s_1})/\sigma(x_T, \sqrt{s_2})\right)}{\log\left(\sqrt{s_2}/\sqrt{s_1}\right)}. \tag{1.10}$$

The x_T scaling of the charge hadrons in p+p and p+$\bar{\rm p}$ collisions in wide energy range $\sqrt{s} = 200$ GeV $-$ 7.0 TeV is shown in the right panel of Fig. 1.7. It is also expected that the effect of the "violating" phenomena should vanish at some sufficiently large c.m. energies and $n_{\rm eff}(x_T, \sqrt{s} \to \infty) \to 4$ (see later Fig. 1.29 and Sec. 6.1.1).

1.1.3 Colors, flavors and the birth of QCD

From the experimental results discussed above it was clear that the proton consists of point-like constituents nowadays known as quarks. However, it was not yet clear how the interaction between quarks is mediated. The CIM model which assumed that the interaction is mediated by quarks, successfully described the inclusive high-p_T spectra but it faced severe difficulties when this model was confronted with π^-/π^+ data.

Another important fact came from the discovery of the Δ^{++} baryon found in 1951 [53], which led to the discovery of a new quantum number - nowadays known as "color". In the context of the quark model the flavor and spin content of the Δ^{++} baryon is

$$|\Delta^{++}\rangle = |u_\uparrow u_\uparrow u_\uparrow\rangle$$

clearly a highly symmetric configuration. However, since the Δ^{++} is a fermion and it contains three identical quarks ($u_\uparrow$), it must have an overall antisymmetric wave function, in order to satisfy the Pauli exclusion principle. In 1965, fourteen years after its discovery, the mystery of $|\Delta^{++}\rangle$ baryon was solved by introduction of a new quantum number, "color", associated with the group SU(3) by Nambu, Han and Greenberg [54, 55]. The Δ^{++} wave function can now be made antisymmetric by arranging its three quarks antisymmetrically in this new degree of freedom,

$$|\Delta^{++}\rangle = \frac{1}{\sqrt{6}}\ \varepsilon^{ijk}\ |u_{i\uparrow} u_{j\uparrow} u_{k\uparrow}\rangle.$$

Another direct experimental test of the number of colors was first provided by the measurement of the $\pi^0 \to \gamma\gamma$ decay width. According to the quark model the flavor state of the π^0 in terms of quark states is given by

$$\left|\pi^0\right\rangle = \frac{1}{\sqrt{2}}\left(\left|u\bar{u}\right\rangle - \left|d\bar{d}\right\rangle\right) \tag{1.11}$$

Fig. 1.8 shows the leading order Feynman diagrams for the π^0 decay into two photons with the branching ratio of 98.8% due to quark antiquark annihilation.

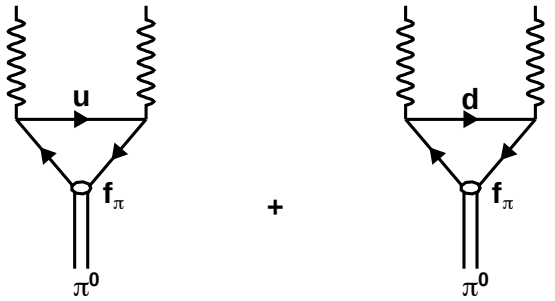

Figure 1.8: The Feynman diagrams of the π^0 decay into two photons. The blob means the decay constant f_π.

In order to calculate the differential cross section of the process, one has to calculate decay amplitudes. The matrix elements of the π^0 decays are expanded in form factors (constituents are u and d quarks) which are proportional to

$$M \propto N_C \frac{1}{\sqrt{2}}\left[(2/3)^2 - (-1/3)^2\right] e^2, \tag{1.12}$$

where N_C is the number of colors, and $2/3$ and $-1/3$ are the electric charges of u and d quarks. More precisely, the matrix element is given by

$$M = \frac{e^2}{2\pi^2}\frac{N_C}{3\sqrt{2}f_\pi}, \tag{1.13}$$

where f_π is the pion decay constant. The pion decay constant was measured in the leptonic decay of charged pions $\pi^\pm \to \mu^\pm\nu_\mu$ (see Fig. 1.9) and was found to be $f_\pi = 130.7 \pm 0.1 \pm 0.36$ MeV [56]. The decay rate (width) of neutral pions is then

$$\Gamma(\pi^0 \to \gamma\gamma) = \frac{\alpha^2}{2\pi}\frac{N_C^2}{3^2}\frac{m_\pi^3}{f_\pi^2} = 7.75 \text{ eV} \quad (\text{for } N_C = 3) \tag{1.14}$$

and the measured value [57]

$$\Gamma(\pi^0 \to \gamma\gamma)_{\text{meas}} = (7.86 \pm 0.54) \text{ eV}, \tag{1.15}$$

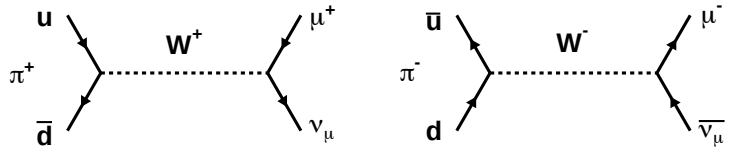

Figure 1.9: The Feynman diagrams of the $\pi^{\pm}$ decays into muon and neutrino.

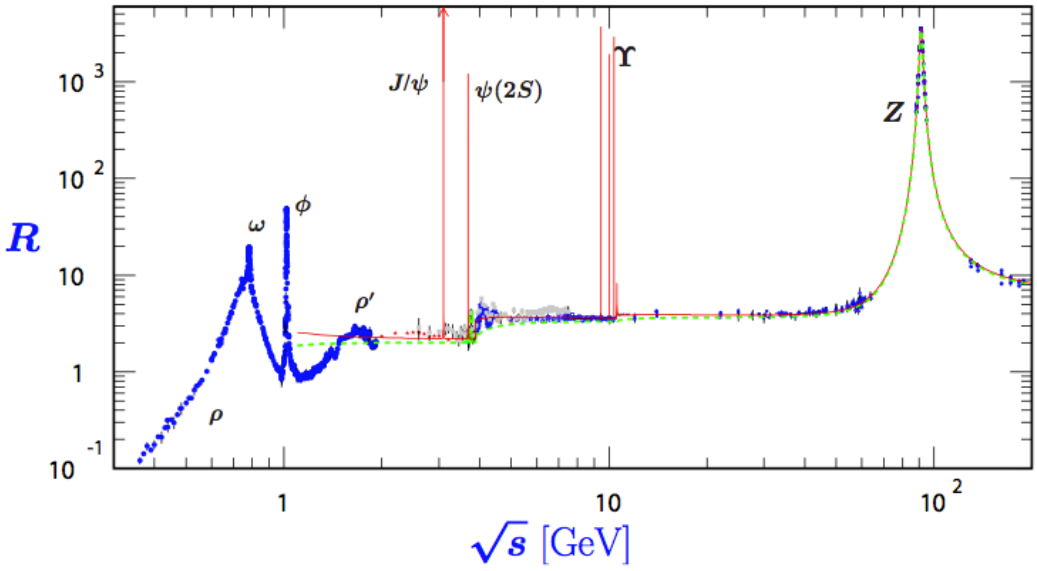

Figure 1.10: World data on the ratio $R(s) = \sigma(e^+e^- \to hadrons, s)/\sigma(e^+e^- \to \mu^+\mu^-, s)$. The $\sigma(e^+e^- \to hadrons, s)$ is the experimental cross section corrected for initial state radiation and electron-positron vertex loops, $\sigma(e^+e^- \to \mu^+\mu^-, s) = 4\pi\alpha^2(s)/3s$.

The experimental result clearly supports the existence of three color states, $N_C = 3$.

An experimental evidence for another quantum number, "flavor", was found in $e^+e^- \to q\bar{q}$ annihilation process. In the quark model the total annihilation cross section for hadron production is given by the square of the quark charges Q_f multiplied with the number of colors N_C of each individual quark flavor (f)

$$\sigma(e^+e^- \to hadrons) = \frac{4\pi\alpha^2}{3s} N_C \sum_f Q_f^2, \tag{1.16}$$

where $\alpha \simeq e^2/137$ is the fine structure constant and the c.m. energy is $\sqrt{s}$. Dividing by the cross section for the $\mu^+\mu^-$ production cross section $\sigma(e^+e^- \to \mu^+\mu^-) = 4\pi\alpha^2/3s$,

one obtains the famous Drell-ratio R, defined as

$$R = \frac{\sigma(e^+e^- \to hadrons)}{\sigma(e^+e^- \to \mu^+\mu^-)} = N_C \sum_f Q_f^2, \tag{1.17}$$

which has the numerical value 2 (for $f = u, d, s$) and increases to value 10/3 (for $f = u, d, s, c$) and 11/3 (for $f = u, d, s, c, b$) when the collision energy reaches the threshold for heavy quark production $e^+e^- \to c\bar{c}$ and $e^+e^- \to b\bar{b}$ processes, respectively. The experimental data are summarized in Fig. 1.10 where various resonances are clearly visible. There are evident steps in the $\sqrt{s}$ dependency of R indicating the threshold energy for production of quark flavors according to Eq. (1.17). The last threshold at $\sqrt{s} \sim 350$ GeV of $t\bar{t}$ production was not reached by any e^+e^- collider operated so far.

In the mid-1970's quantum chromodynamics (QCD) was generally accepted as the "candidate" theory of the strong interactions. The interaction is mediated by the gauge quanta, gluons, however, until late 1970ties there were no evidences for the gluon existence. In 1978 the PLUTO collaboration at DORIS collider [58], observed the decay $\Upsilon(1S) \to ggg$ and later PETRA [59, 60, 61, 62] observed the three jet event $e^+e^- \to q\bar{q}g \to 3$ jets.

Such events were predicted theoretically in QCD [63] also in which the quark pair produced in annihilation radiates a hard non-collinear gluon. The emitted gluon also transforms into hadron jet and they generate a characteristic pattern in the final states which proves the evidence of gluons. The quark and gluon jets become narrower with the increasing energy and the events show a characteristic Y-shape of the three separate jets. Since then QCD was finally accepted as a correct theory of the strong interactions.

QCD is the gauge quantum field theory of the color group SU(3). The Special Unitary Lie-group of 3×3 unitary matrices ($UU^\dagger = U^\dagger U = 1$) of determinant +1. Here, 3 represents the number of colors (red, green, blue) acting on its fundamental representation. Each quark can take three different color states in the fundamental representation, while a gluon can take up to 8 states in the so-called adjoint representation of $\mathrm{SU}(3)_c : \ 3 \otimes \bar{3} = 1 \oplus 8$. In QCD, these matrices can operate both on each other (gluon self-interactions) and on a set of complex 3-vectors (the fundamental representation), the latter of which represent quarks in color space. The Lagrangian of QCD is the sum of quark and gluon terms

$$\mathcal{L} = \mathcal{L}_{\mathrm{quark}} + \mathcal{L}_{\mathrm{gluon}} = \bar{\psi}_q^i \left[(i\gamma^\mu)(D_\mu)_{ij} - \delta_{ij} m_q \right] \psi_{qj} - \frac{1}{4} F^a_{\mu\nu} F^{a\mu\nu}$$

where the ψ_i are the quark fields, $F^a_{\mu\nu}$ is the gluon field strength tensor. The gauge covariant derivative and the gluon field tensor can be written in a form of covariant gluon field as

$$\begin{aligned} (D_\mu)_{ij} &= \delta_{ij}\partial_\mu - \frac{1}{2} i g \lambda^a_{ij} A_{a\mu}, \\ F^a_{\mu\nu} &= \partial_\mu A_{a\nu} - \partial_\nu A_{a\mu} + g f_{abc} A_{b\mu} A_{c\nu}, \end{aligned}$$

where g is the coupling constant, $(1/2)\lambda_{ij}^{\nu}$ and f_{abc} are the generators and structure constants of the SU(3) group.

1.1.4 Asymptotic freedom

One of the most striking features of QCD is that the generators $t^a = (1/2)\lambda_{ij}^a$ of SU(3) group do not commute $[t^a, t^b] = if^{abc}t^c$ or, in other words, gauge quanta, in contrast to QED, interact with each other. The theory with non-commuting generators is called non-Abelian theory. This has quite dramatic impact on the asymptotic behavior of QCD. At small distances and large momentum transferred the strong coupling constant, $\alpha_s = g^2(s)/4\pi$ vanishes. This phenomenon is known as asymptotic freedom and it has been verified experimentally [64]. In 2004 Gross, Politzer and Wilczek were awarded 2004 Nobel prize in physics [65, 66] for its discovery.

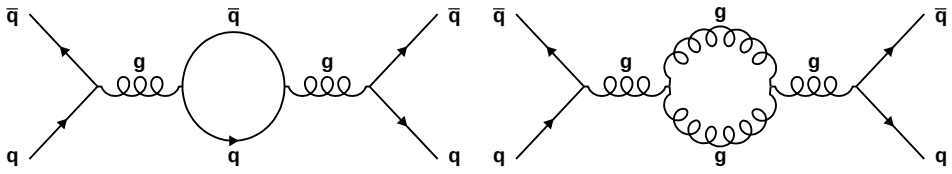

Figure 1.11: The quantum vacuum polarization which effectively changes the interaction strength. The left diagram refers to screening effect of $q\bar{q}$-pairs in the analogical way as e^+e^- fluctuations in QED. The right diagram arises from the non-Abelian interaction between gluons in QCD resulting in the anti-screening effect.

A simplified picture of the asymptotic freedom comes from the analogy with QED, where the e^+e^- dipoles are polarized by the bare charge causing the screening (similarly as in Fig. 1.11 left panel). The Coulomb force between two chargers q_1 and q_2 at distanced r in the medium with the dielectric constant $\varepsilon > 1$ is

$$F = \frac{1}{4\pi\varepsilon}\frac{q_1 q_2}{r^2} = \frac{q_{\text{eff}}^2}{4\pi r^2} = \frac{\alpha_{\text{em}}(r)}{r^2}.$$

This can be viewed as a force in the vacuum caused by an effective charge $q_{\text{eff}}/\sqrt{\varepsilon}$ or running coupling "constant" as a function of the distance r or momentum transfer $q \sim 1/r$. Thus the effect of the medium may be regarded as modifying the charges. The QCD vacuum is relativistically invariant which implies $\varepsilon\mu = 1/c^2$ (follows from the Maxwell equations) where μ is the magnetic permeability characterizing the magnetic resistance of material exposed to the external magnetic field. A medium where $\mu < 1$ and $\varepsilon > 1$ is called diamagnetic and the charge embedded in diamagnetic medium is screened. In the opposite case ($\mu > 1$ and $\varepsilon < 1$) the material is paramagnetic and the embedded charge will be anti-screened. The permeability of any material comes from

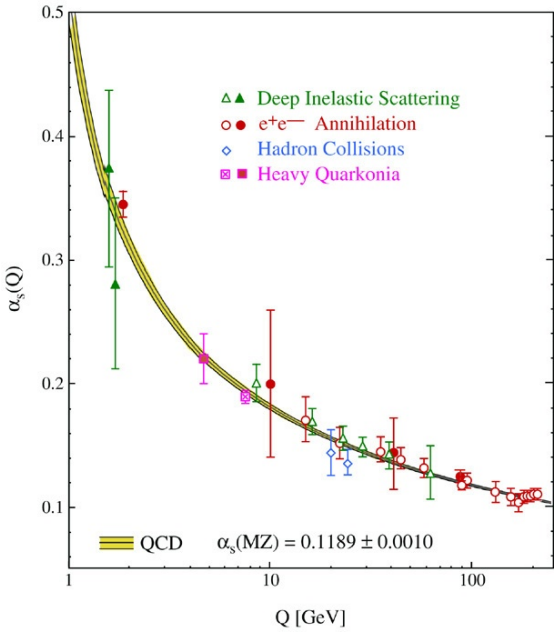

Figure 1.12: Experimental tests of the asymptotic freedom [67].

two microscopic phenomena: Pauli paramagnetism (spin magnetic moments) and Landau diamagnetism (orbital motion) [68]. It can be shown that in the case of QED [68] the Landau diamagnetic response of e^+e^- fluctuations is stronger, than the Pauli paramagnetism caused by $e^\pm$ spin and thus the QED charge is screened.

In the case of the QCD vacuum, the Landau orbital alignment of $q\bar{q}$ fluctuations are also stronger as in the $e^\pm$ fluctuations in QED. However, the non-Abelian nature of QCD gives rise to the gluon–gluon fluctuations and gluon is a particle spin-1 boson. The Pauli's spin magnetic alignment of gluon–gluon fluctuation is stronger than the $q\bar{q}$ orbital alignment and thus the QCD vacuum is causing anti-screening. The dependence of the effective strength of the QCD coupling constant on the momentum transfer Q can be determined by a differential equation

$$Q^2 \frac{\partial \alpha_s(Q^2)}{\partial Q^2} = \beta\left(\alpha_s(Q^2)\right) = -(\beta_0 \alpha_s^2 + \beta_1 \alpha_s^3 + \beta_2 \alpha_s^4 + \dots), \tag{1.18}$$

where the β-function expresses the Q^2 dependency of running coupling constant and β_n is the n$^{\text{th}}$-loop coefficient in α_s expansion. The zeroth coefficient $\beta_0 = (11 - \frac{2}{3} n_f)$ where n_f is the number of active quark flavor. The second term in β_0, $-\frac{2}{3} n_f$, comes from quark-antiquark pair effect in the first diagram in Fig. 1.11. It scales like the number of quark flavors and is negative (as it would be in QED). However, the first term, 11, has the opposite sign and comes from the non-linear gluon contribution shown in the second diagram in Fig. 1.11. This contribution is absent for QED. Thus the gluon self-coupling has an anti-screening effect.

The leading order solution of the equation Eq. (1.18) when the number of flavors is constant is

$$\alpha_s(Q^2) = \frac{1}{\beta_0 \ln\left(Q^2/\Lambda^2\right)}, \tag{1.19}$$

where the dimensional parameter $\Lambda = \mu^2/e^{1/\beta_0\alpha_s(\mu^2)}$ is introduced to include the higher order approximation. When the $Q^2 \to \Lambda^2$ then the coupling diverges $\alpha_s(Q^2) \to \infty$. The asymptotic freedom manifests itself through the minus sign in the Eq. (1.18). The calculation of the QCD coupling and the experimental data [67] are compared in Fig. 1.12. For the energy regime $Q^2 \sim 100$ GeV to TeV scales the $\alpha_s(Q^2) \sim 0.1$.

The discovery of QCD asymptotic freedom initiated the whole new field - Relativistic Heavy Ion physics as discussed in Sec. 1.5.1.

1.1.5 pQCD factorization

The term Hard Scattering (HS) is used in connection with the scattering of the two point-like constituents (partons) of colliding nucleons characterized by large momentum transfer Q^2 ($Q \gg \Lambda_{QCD}$). Fig. 1.13 shows the two incoming partons, quarks or gluons, usually exchange space-like virtual gluon and two outgoing highly virtual partons fragment into a pencil-like sprays of particles known as jets [69, 70].

The overall p+p hard-scattering cross section in the pQCD approximation is the sum over parton reactions $a+b \to c+d$ (e.g. $g+q \to g+q$) at parton-parton center-of-mass (c.m.) energy $\sqrt{\hat{s}}$,

$$\frac{d^3\sigma}{dx_1 dx_2 d\cos\theta^*} = \frac{1}{s}\sum_{ab} f_a(x_1) f_b(x_2) \frac{\pi\alpha_s^2(Q^2)}{2x_1x_2}\Sigma^{ab}(\cos\theta^*), \tag{1.20}$$

where $f_a(x_1)$, $f_b(x_2)$, are parton distribution functions (see later in this section and also in Sec. 1.1.1), the differential probabilities for partons a and b to carry momentum fractions x_1 and x_2 of their respective protons (e.g. $u(x_2)$), and where θ^* is the scattering angle in the parton-parton c.m. system. The parton-parton c.m. energy squared is $\hat{s} = x_1x_2s$, where $\sqrt{s}$ is the c.m. energy of the p+p collision. The parton-parton c.m. system moves with rapidity $y = (1/2)\ln(x_1/x_2)$ in the p+p c.m. system. In the leading order, the transverse momenta of partons, $\hat{p}_T$, are equal and opposite.

Equation 1.20 gives the p_T spectrum of outgoing parton c, where the pQCD matrix elements are summarized in Fig. 1.14. The matrix elements are expressed in form of $d\sigma^{ab\to cd}/d\hat{t}$ and the final state of the partons are described by their rapidities, y_i, resulted from the longitudinal boost. In order to translate the cross section Eq. (1.20) from $(x_1, x_2, \hat{t})$ variable set to the final parton observables $(y_c, y_b, \hat{p}_T)$, the Jacobian is needed

$$\frac{\partial(x_1, x_2, \hat{t}\,)}{\partial(y_c, y_b, \hat{p}_T)} = \frac{2\hat{p}_T\hat{s}}{s}, \tag{1.21}$$

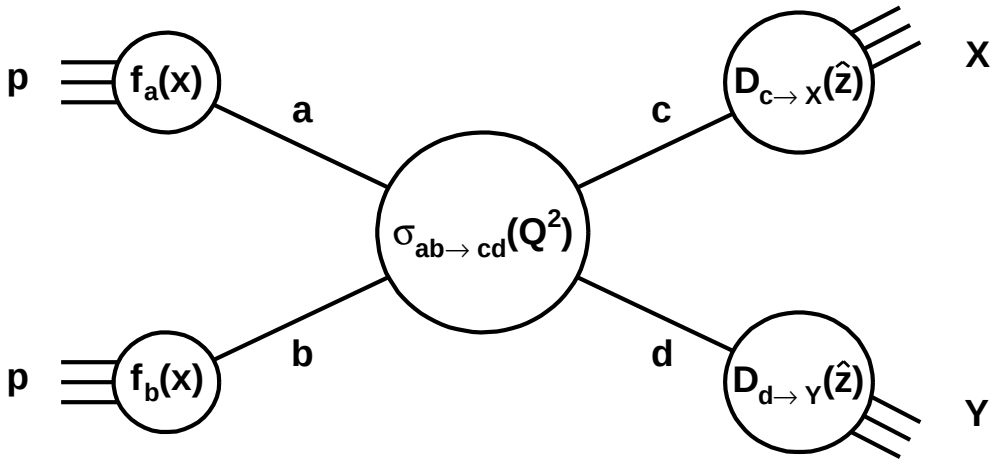

Figure 1.13: Schematic view of hard scattering process of p+p→ 2 jets.

where the Mandelstam variable $\hat{t}$ can be expressed with the scattering angle as $\hat{t} = (-1/2)\hat{s}(1 - \cos(\theta^*))$.

The emitted parton then fragments into hadrons, e.g. a π^0. The fragmentation function $D_c^{\pi^0}(z, \mu^2)$ is the probability for a π^0 to carry the fraction $z = p^{\pi^0}/p^c$ of the momentum of outgoing parton c. Equation 1.20 must be summed over all subprocesses leading to a π^0 in the final state. The parameter μ^2 is an unphysical "factorization" scale, where the collinear singularities are separated off, and the singularities are then absorbed into the structure and fragmentation functions [71, 72].

Parton Distribution Function

Parton Distribution Functions (PDFs) are essential to calculate scattering cross section. The distributions are extracted from comprehensive global analysis of hard scattering data from variety of fix-target and collider experiments in framework of pQCD. The measured proton structure function $F_2(x, Q^2)$ (see Fig. 1.5) corresponds to a sum of contributions from various quark flavors represented by unknown probability distributions $q_f(\xi)$ (parton sum rule), where $0 \leq \xi \leq 1$ is the fraction of the proton momentum carried by the parton. In the parton model, the $F_2(x, Q^2)$ can be then calculated as [73]

$$F_2(x, Q^2) = \sum_{\text{f=flavour}} \int_0^1 d\xi q_f(\xi) e_f^2 \delta(x - \xi) = x \sum_{\text{f=flavour}} e_f^2 q_f(x, Q^2), \tag{1.22}$$

where $q(\xi)d\xi$ represents the probability that a quark carries a momentum fraction between ξ and $\xi + d\xi$ $(0 \leq \xi \leq 1)$, the e_f represents the electric charge of the quarks.

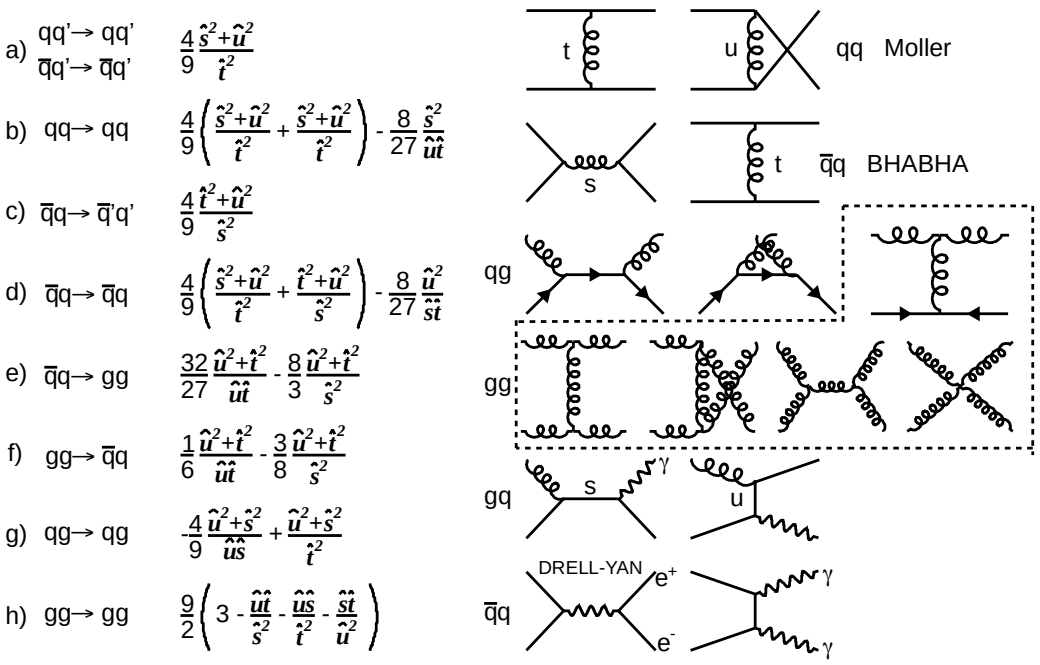

Figure 1.14: The basic pQCD processes and their quadratic matrix elements.

Eq. (1.22) is modified due to higher order corrections induced by the running coupling constant, α_s (see Eq. (1.19)). In order to calculate the higher order contributions, the "splitting functions" $P(x)$ are introduced, which characterize the probabilities of a parton splitting into two other partons (i.e. $q \to qg$, $g \to gq$). Then the proton structure function can be rewritten as

$$F_2(x,Q^2) = x\sum_{q,\bar{q}} e_q^2 \int_x^1 \frac{d\xi}{\xi} q(\xi,\mu^2)\left[\delta(1-\frac{x}{\xi}) + \frac{\alpha_S}{2\pi}\left(P\left(\frac{x}{\xi}\right)\ln\left(\frac{Q^2}{\mu^2}\right)\right) + \mathcal{O}(\alpha_S^2)\right]. \tag{1.23}$$

The second term in the above equation represents the first order correction in power of α_s which is, in fact, the origin of the Bjorken scaling violation discussed in Sec. 1.1.1. The "parton model" behavior of the theory is restored with the factorization theorem, which states that the long-distance (non-perturbative) and short-distance (perturbative) partonic interactions can be considered independently. The long distance, non-perturbative object in Eq. (1.23) is the parton density function $q(\xi,\mu^2)$. The perturbative short-distance object in Eq. (1.23) is the coefficient function, the expression between square brackets. The factorization assumption requires the introduction of a new scale, μ, to define the separation of these short- and long-distance effects. If we define $t = \mu^2$ and take the partial derivative of Eq. (1.23) we obtain:

$$t\frac{\partial}{\partial t}q(x,t) = \frac{\alpha_S(t)}{2\pi}\int_x^1 \frac{d\xi}{\xi}P_{qq}\left(\frac{x}{\xi},\alpha_S(t)\right)q(\xi,t), \tag{1.24}$$

where the $P_{qq}(z,\alpha_S) = P_{qq}^{(0)}(z) + (\alpha_S/2\pi)P_{qq}^{(1)}(z) + \ldots$ is the perturbative expansion in the running coupling. The Eq. (1.24) is also known as the Dokshitzer-Gribov-Lipatov-Altarelli-Parisi (DGLAP) evolution equation [74, 75, 76].

The nonperturbative parton distribution function $q(\xi,\mu^2)$ is parameterized and fitted using evolution equation (1.24) to the measured $F_2(x,Q^2)$ structure function (see Fig. 1.5). The resulting parameters from this global fits, CTEQ (or CT10) [77, 78], MSTW [79] and NNPDF2.0 [80], are then used to calculate $q_f(x,Q^2)$ in the cross section Eq. (1.20) (denoted here as $f_{a,b}(x)$) for various processes.

1.1.6 pQCD direct photon production

Prompt photons are created by initial hard scattering processes, leading-order (LO) pQCD photon contains two processes, namely annihilation and QCD Compton scattering:

$$q + \bar{q} \rightarrow g + \gamma, \tag{1.25}$$
$$q + g \rightarrow q + \gamma. \tag{1.26}$$

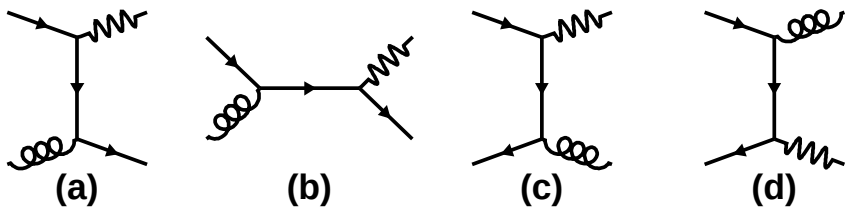

Figure 1.15: Leading order Feynman diagrams of direct photon production.

The differential cross section in p+p collision in the leading order can be written as (see also Eq. (1.20) and Eq. (1.21)) [81]:

$$\frac{d\sigma}{dy_1 dy_2 dp_T^2} = \frac{\pi\alpha_s\alpha_{\rm em}}{s^2}\sum_{a,b}\frac{f_{a/p}(x')f_{b/p}(x)}{x'x}H^U_{ab\to d\gamma}(\hat{s},\hat{t},\hat{u}), \tag{1.27}$$

where α_s and $\alpha_{\rm em}$ are the QCD and electromagnetic coupling constants, y_1, y_2 are the rapidities of the outgoing partons, $f_{a/p}$ is the parton distribution function, the momentum fractions are defined as

$$x' = \frac{p_{1T}}{\sqrt{s}}\left(e^{y_1} + e^{y_2}\right), \quad x = \frac{p_{1T}}{\sqrt{s}}\left(e^{-y_1} + e^{-y_2}\right). \tag{1.28}$$

The $H^U_{ab\to d\gamma}$ are the partonic cross sections as a function of the usual partonic Mandelstam variables ($\hat{s},\ \hat{t},\ \hat{u}$) are calculated from the Feynman diagrams in Fig. 1.15 and the matrixes are given by:

$$H^U_{qg\to\gamma q} = e_q^2 \frac{1}{N_C}\left[-\frac{\hat{s}}{\hat{t}} - \frac{\hat{t}}{\hat{s}}\right], \tag{1.29}$$

$$H^U_{gq\to\gamma q} = e_q^2 \frac{1}{N_C}\left[-\frac{\hat{s}}{\hat{u}} - \frac{\hat{u}}{\hat{s}}\right], \tag{1.30}$$

$$H^U_{q\bar{q}\to\gamma g} = e_q^2 \frac{N_C^2 - 1}{N_C}\left[\frac{\hat{t}}{\hat{u}} + \frac{\hat{u}}{\hat{t}}\right], \tag{1.31}$$

where e_q are the quark charges and $N_C = 3$ is the number of colors [82].

1.2 Heavy Ion Physics

Confinement and asymptotic freedom of quarks and gluons (see in Sec. 1.1.4) led to the idea that at high temperatures and/or high densities the quarks and gluons can propagate outside of the confinement of hadrons. Collins and Perry realized [83] that in the center of neutron stars, few microseconds after the Big Bang or during explosion of black holes, a "superdense" matter consisting of deconfined quarks is formed. The existence of the Quark Gluon Plasma (QGP) phase in the high-temperature and density QCD matter was first discussed by Shuryak in 1980 [1].

The experimental study of the heavy ion collisions started at fix-target experiments at Bevalac (LBNL, Berkeley) in 1984. Later, the heavy ion beams were explored at AGS (BNL, Brookhaven 1986-1994), SPS (CERN 1986-2000), RHIC (BNL 2000-present) and LHC (CERN (2009-present). The unequivocal evidence of the QGP formation was found at RHIC when the large high-p_T particle suppression was observed (see Sec. 1.5.1), although, some hints of QGP formation were seen already at lower energies.

1.2.1 QGP on Lattice

In the thermal equilibrium of massless non-interacting particles each bosonic degree of freedom contributes $\pi^2 T^4/30$ to energy density, where T refers to temperature. The fermionic degree of freedom contributes $7/8(\pi^2 T^4/30)$. The Stefan-Boltzmann limit of the energy density is

$$\varepsilon_{SB} = \left(\frac{7}{8} d_{\text{quark}} + d_{\text{gluon}}\right) \frac{\pi^2}{30} T^4, \tag{1.32}$$

where the d_{quark} and d_{gluon} are the quark and gluon numbers of degrees of freedom. After summing up for appropriate flavour, spin, quark/antiquark and color factors for quarks and gluons, the "Stefan-Boltzmann" limits of energy density are

$$\varepsilon_{\text{SB}} = \begin{cases} (2_f 2_s 2_q 3_c \frac{7}{8} + 2_s 8_c)\frac{\pi^2}{30} T^4 &= 37\frac{\pi^2}{30} T^4, \\ (3_f 2_s 2_q 3_c \frac{7}{8} + 2_s 8_c)\frac{\pi^2}{30} T^4 &= 47.5\frac{\pi^2}{30} T^4, \end{cases} \tag{1.33}$$

depending on assumption of 2 or 3 active flavours (horizontal arrows on right of Fig. 1.16).

In the non-perturbative regime of QCD around the critical temperature the lattice interpretation of QCD was developed. The numerical calculations of the lattice QCD was first developed by Wilson [84]. The study of the QCD phase transition on lattice [85] indicates that when the energy density of matter exceeds the critical energy density $\varepsilon_C \sim 1$ GeV/fm^3 and critical temperature $T_C \sim 170$ MeV, the matter becomes the deconfined medium of quarks and gluons. The Lattice QCD predicts [86] a phase transition from ordinary hadronic matter to QGP at temperature approximately $T_C \approx 170$ MeV $\approx 10^{12}$ K, shown in Fig. 1.16.

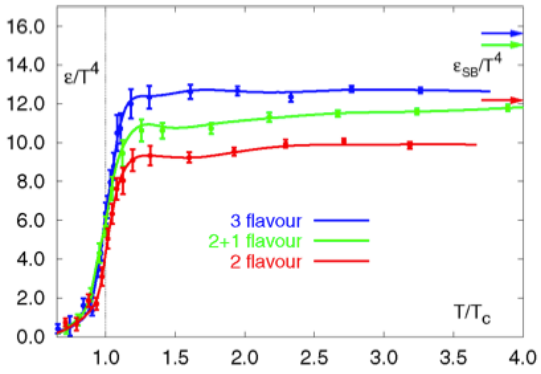

Figure 1.16: Lattice QCD calculations [86] to predict the energy density and temperature (ε/T^4 as a function of T/T_C) and the Stefan-Boltzmann limit (see Eq. (1.33)) indicated by arrows on the right.

The exact nature of this phase transition is not known. In a pure gauge theory containing only massless gluons the transition appears to be first order. However, inclusion of two light quarks (up and down) or three light quarks (adding the strange quark) and their masses can change the transition from first order to second order to a smooth crossover. These lattice QCD results are obtained at zero net baryon density ($\mu = 0$) [87]. Fig. 1.17 shows the schematic view of the QCD phase diagram. The given calculations were using non-zero values for light quark masses and infinite strange quark mass. For high baryon chemical potential ($\mu \gtrsim 400$ MeV) the transition between normal hadronic matter and QGP is a first order transition [88]. The dashed line in Fig. 1.17 becomes a smooth cross over and the critical point represents the end of the first order transition where the transition becomes second order.

Theoretical arguments [89] as well as experimental data suggest the nucleus-nucleus collisions at $\sqrt{s_{NN}} = 200$ GeV are at low baryon chemical potential. The recent low-energy scan program at RHIC collider (see later Sec. 1.5) is exploring the lower $\sqrt{s_{NN}}$ energies in order to map the QCD phase transition as a function of the net baryon density.

1.2.2 Goals of HI physics

The study of the strongly interacting matter and its phase transition is achieved by colliding heavy ions at large energies. Since the year 2000 the four experiments at RHIC were searching for the evidence of the QGP [90]:
"The early measurements have revealed compelling evidence for the existence of a new form of nuclear matter at extremely high density and temperature T – a medium in which the predictions of QCD can be tested, and new phenomena explored, under conditions where the relevant degrees of freedom, over nuclear volumes, are expected

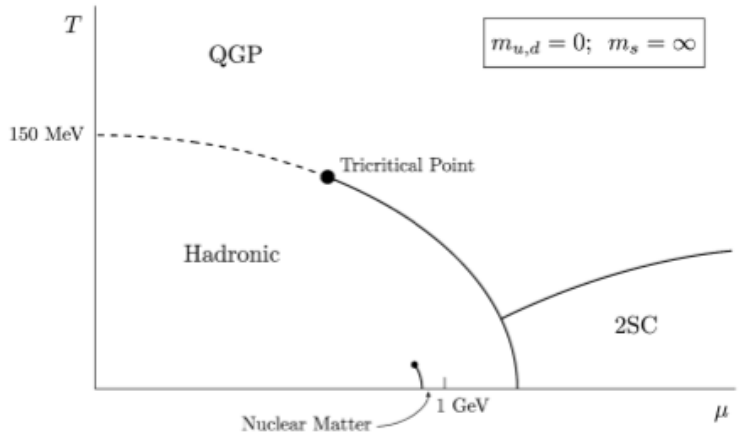

Figure 1.17: The schematic view of the QCD phase diagram. The normal nuclear matter is at located in the low temperatures ($T \ll T_C$) and baryon density about $\mu \approx 1$ GeV. The solid lines represent the first order transition, at tricritical point it is second order and the dashed line shows the smooth crossover region.

to be those of quarks and gluons, rather than of hadrons. This is the realm of the quark gluon plasma, the predicted state of matter whose existence and properties are now being explored by the RHIC experiments."
The recent experimental program at RHIC is aimed to study the features that would characterize the created QGP [91]:

- temperature, energy density, entropy,
- deconfinement, equation of state, thermalization leading to the QGP, time evolution of system parameters, collectivity,
- degrees of freedom in QGP phase,
- chiral symmetry restoration, quark recombination,
- opacity, transport properties, viscosity,
- critical behavior, existence of the critical point.

1.2.3 Colliding Heavy Ions

Geometry

In this section we introduce a simple descriptions of the geometry in ultra-relativistic heavy ion collisions. The two incoming nuclei (pancake-like due to Lorentz contraction)

are smashed together in order to created high enough energy density. The collision geometry of the two specific nuclei (Au in this case) is characterized by the impact parameter b which is the minimum distance between the centers of the nuclei. The central collisions are those with a small impact parameter ($b \sim 0$), while peripheral collisions are those with large impact parameter ($b \sim 2R_{\mathrm{Au}} = 12.6$ fm).

As the impact parameter rises, only parts of the nuclei are overlapping. The nucleons inside the nucleus can be roughly divided into two groups, participants and spectators. The schematic view of the geometry of the heavy ion collision is shown in Fig. 1.18 [92]. The geometry of the heavy ion collisions are estimated by the Glauber model discussed later in Sec. 3.1.2.

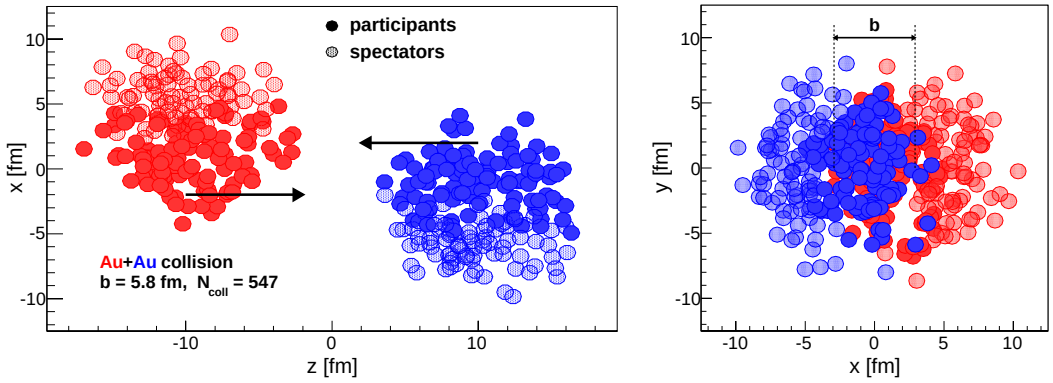

Figure 1.18: Distribution of nucleons in the two nuclei before the collision, for illustrative purposes the Lorentz contraction is not shown [92]. The impact parameter defines the minimum distance between the centers of nuclei. The region illustrate the overlap region of the two nuclei. The nucleons in the overlap region are called participants while the rest are the spectators. Nucleons are drawn with radius $r = \sqrt{\sigma_{\mathrm{inel}}^{NN}/\pi}/2$.

Energy Density

The simplest estimate of the energy density comes from the total energy of the colliding nuclei divided by the overlap volume in the instant of the full overlap. The energy density depends on the Lorentz frame, when a nucleus with energy density ρ_0 is boosted by Lorentz γ, from the rest frame it appears to have $\gamma^2\rho_0$ energy density. A meaningful energy density $\langle\varepsilon\rangle$ can be calculated in the rest frame of the system when the total momentum is zero.

One can calculate the energy density achieved at RHIC collision with colliding gold-gold nuclei at $\sqrt{s_{NN}} = 200$ GeV [91]. The gold nuclei are accelerated to the Lorentz $\gamma = 106$ and smashed to each other. In a case of a central collision, when the impact parameter $b = 0$ (in Fig. 1.18), the total energy density of the system is $\langle\varepsilon\rangle = 2\gamma^2\rho_0$ where $\rho_0 = 0.14$ GeV/fm^3 is the energy density of a the nucleus at rest. The total

energy density at the instant of the overlap is then $\langle\varepsilon\rangle = 3150$ GeV/fm^3. However, this energy density is not fully converted into the final-state particles.

A more realistic estimate was developed by Bjorken [93]. He assumed the relation between the energy density of the medium "formed" at a proper time τ_{form}. The volume of the medium is a disk of length $\Delta Z = \beta_{||}\tau_{\text{form}}$ times transverse area defined by an overlapping region of the two nuclei $A = \pi R^2$. The $\beta_{||}$ is the longitudinal velocity of the medium. The total energy stored in the volume is then carried away by the formed particles: $E_{\text{tot}} = \langle E\rangle \Delta N$ where $\langle E\rangle$ is the average energy of each particle and ΔN is the number of particles in the $dZ \times A$ cylinder. The spatial density of produced particles, dN/dz, is related to the measured particle momentum density, $dN/dp_{||}$. The number of particles in the thin disk is

$$\Delta N = \frac{dN}{d\beta_{||}}\Delta\beta_z = \frac{dN}{d\beta_{||}}\frac{dZ}{\tau_{\text{form}}} \approx \frac{dN}{dy}\frac{dZ}{\tau_{\text{form}}}, \tag{1.34}$$

where in the mid-rapidity $\beta_{||} \approx y \approx 0$. The average energy density of the medium is then equal to

$$\varepsilon_{BJ}(\tau_{\text{form}}) = \frac{E_{\text{tot}}}{V} = \frac{\langle E\rangle \Delta N}{V} = \frac{1}{\tau_{\text{form}} A}\langle E\rangle \frac{dN}{dy} = \frac{1}{\tau_{\text{form}}\pi R^2}\frac{dE_T}{dy}. \tag{1.35}$$

Historically, the Bjorken energy density (ε_{BJ}) was calculated using the measured final state dE_T/dy and a nominal value of formation time $\tau_{\text{form}} = 1$ fm/c. At lower collision energy, the Bjorken energy density is estimated as $\varepsilon_{BJ} \sim 1.5$ GeV/fm^3 at AGS in Au+Au collisions [94] ($\sqrt{s_{NN}} = 5$ GeV) and $\varepsilon_{BJ} \sim 2.9$ GeV/fm^3 at SPS in Pb+Pb collisions [95] ($\sqrt{s_{NN}} = 17.2$ GeV). In the most central (0-5%) Au+Au collisions at $\sqrt{s_{NN}} = 200$ GeV the measured value is $dE_T/dy = 600$ GeV [96] which results in $\varepsilon_{BJ} \sim 5$ GeV/fm^3. However, with use of arguments based on uncertainty relation $t \sim \hbar/\langle E\rangle$ it can be shown that the formation time could be as short as $\tau_{\text{form}} \sim 0.35$ fm/c. With this value of τ_{form} the energy density is $\varepsilon_{BJ} \sim 15$ GeV/fm^3.

Space-Time Evolution

The schematic Bjorken picture [93] of the space-time evolution of the heavy ion collision is shown in Fig. 1.19. In this picture the two heavy ions are propagating near the light cone, at the collision time $t = 0$ they excite the vacuum, leaving a medium consisting of partons. The created matter thermalize due to the multiple parton scatterings in time proper time, $\tau_0 = \sqrt{t^2 - z^2}$, represented by the hyperbola in Fig. 1.19. The estimated time for thermalization of the medium depends on different models and calculations. If the energy density of the thermalized medium exceeds the energy density of the phase transition (see above $\varepsilon > 1$ GeV/fm^3), the QGP is formed.

However, the formed QGP is a dynamical system, it starts to expand and cool down in the process. In this time period the tools of the hydrodynamics are applicable. Due

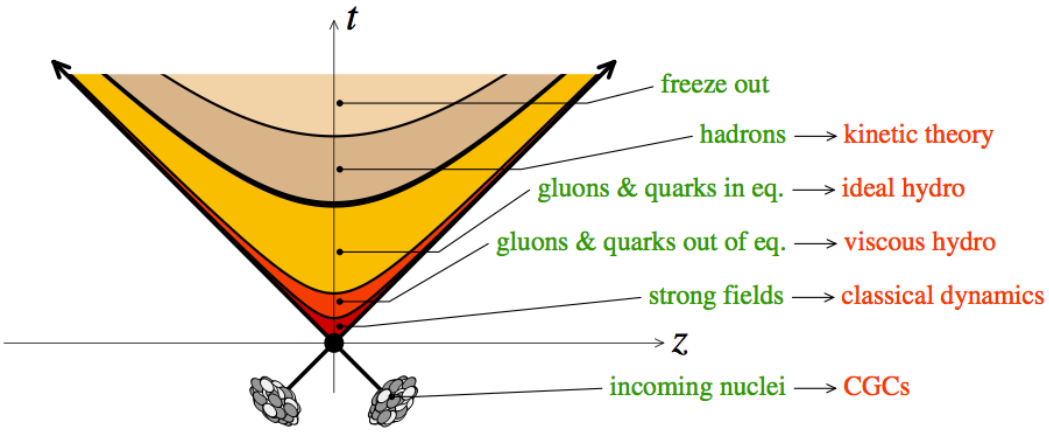

Figure 1.19: Schematic representation of the heavy ion collision [97] as the function of time t and longitudinal coordinates z. The various stages of the space-time evolution correspond to proper time, $\tau = \sqrt{t^2 - z^2}$ which is shown as hyperbolic curves separating the different stages.

to the pressure formed in the medium, it causes the expansion, and the formed QGP is cooled down until the final state hadrons are formed. The intermediate state is called the mixed phase when both QGP and hadron gas are present in the matter. The created hadrons interact with each other, forming the hadron gas. Further expansion causes the interaction between individual hadrons to fade. This transition is called "freeze-out" when the particles of the matter will not interact anymore.

1.3 Jet quenching

Hard probes in heavy ion collisions are used as tomographic tools to investigate the medium created during the collisions. The basic idea is that the hard processes are calculable in the pQCD framework in the vacuum (in p+p collisions). In the heavy ion collisions the rate of hard processes are increased due to the increased probability of binary nucleon-nucleon collisions. This probability is characterized as nuclear overlap function (T_{AA}) from the Glauber model framework. The parton propagates through the strongly interacting medium and loses its energy. Thus, the final state hadron production is suppressed in comparison to the T_{AA}-scaled p+p collisions at higher p_T, called "suppression" or "jet-quenching". In this section we described few common features of all energy-loss models. Later we discuss the experimental observables to study the jet-quenching phenomena. At last we list few of the known models and categorize them according to the energy loss processes.

Space-time distribution of hard scattering.

The hard processes are results from primary nucleon-nucleon collisions. Thus the distribution of the hard partons created in heavy ion collisions are following the spatial distribution of the nucleon distribution in both nuclei. The probability distribution ($P(\mathbf{r} =(x_0, y_0))$) of the hard verteces in nucleus-nucleus collision with impact parameter $\mathbf{b}$ is proportional to

$$P(\mathbf{r}) = \frac{T_A(\mathbf{r}_0 + \mathbf{b}/2)T_A(\mathbf{r}_0 - \mathbf{b}/2)}{T_{AA}(\mathbf{b})}, \tag{1.36}$$

where $\mathbf{r_0} = \sqrt{x_0^2 + y_0^2}$, and the nuclear thickness function is defined in terms of Woods–Saxon nuclear density ($\rho_A(\mathbf{r}, z)$) as

$$T_A(\mathbf{r}) = \int dz \rho_A(\mathbf{r}, z). \tag{1.37}$$

The spatial distribution of the hard vertices is relevant in correlation with the evolving hydrodynamical medium.

Basic (hydrodynamical) properties of the medium.

The hydrodynamical tools are used to describe the medium created in heavy ion collisions. The evolution of the medium from the initial state (after thermalization) until the final state, freeze-out, is described by different hydrodynamical models. The dynamical evolution of the medium may influence the energy loss of those partons propagating through it. The two main uncertainties of the energy loss mechanism may depend 1) on the choice of the initial time (τ_i) when the medium thermalizes, and 2) the freeze-out temperature (T_F) when the hydrodynamical medium stops interacting and it is converted to hadrons. However, the detailed study of the collective phenomena in different hydrodynamical models reveled small dependence on the τ_i and T_F parameters, of the order of $\mathcal{O}(15\%)$ [98]. Although, the different hydrodynamical evolutions results in large uncertainties in the jet-quenching observables, of the order of $\mathcal{O}(100\%)$.

Another important factor to consider in the energy loss mechanism is the smoothness of the medium. The nucleon spatial distribution fluctuates in every collision. This fluctuations cause fluctuation in the created medium, creating hotter and colder areas. The hot spots of the created medium coincide with the higher distribution of the hard verteces. The effect of the fluctuating medium on energy loss mechanism was found rather small [99], of the order of $\mathcal{O}(20\%)$ in most central collisions.

Transport coefficient.

The radiative energy loss mechanism introduces a transport coefficient $\langle \hat{q} \rangle$ which describes the average momentum transfer between the medium and parton [100]. The

exact definition of the transport coefficient depends on the formalism in which the theoretical description of the energy loss mechanism is described. The main theoretical models are introduced later in Sec. 1.3.2.

However, we discuss the embedding of the energy loss mechanism into the hydrodynamical medium. The effect of the choice of the model which describes the medium on the parton-medium interaction was studied in [101]. The transport coefficient of radiative energy loss is usually parametrized as [102, 103]

$$\hat{q}(\zeta) = K \cdot Q(\zeta) \left[\cosh(\rho(\zeta)) - \sinh\left(\rho(\zeta)\right) \cos\left(\alpha(\zeta)\right)\right], \tag{1.38}$$

where the $Q(\zeta)$ is the local density of scattering centers, $\rho(\zeta)$ is the local transverse flow rapidity of the medium and α is the angle between parton trajectory and flow direction. The K factor is an overall parameter to rescale the strength of the parton medium interaction to the given density of scattering centers.

Elastic and radiative energy loss

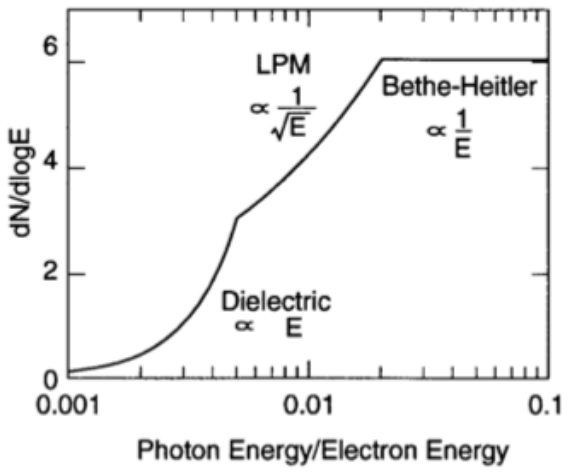

Figure 1.20: Schematic view of the expected bremsstrahlung spectrum in case of electron propagating through a material [104]. The three mechanism (see text) of bremsstrahlung emission are shown at their characteristic energy regimes and their energy dependency.

Many of the energy loss models exploit the analogy between the QCD interaction of parton propagating through the colored medium with the QED energy loss of electron propagating through the material. An electron propagating through the matter loses its energy by photon Bremsstrahlung radiation. In the simplest case, each individual scattering center results in a single emission of a photon. This is known as

Bethe-Heitler regime [105]. The energy spectrum of radiated photons dN/dE is, in this case, proportional to $1/E$. However, the Bremsstrahlung photon can be radiated only when the distance between the scattering centers is larger than the formation length. In the limit, when the scattering centers are closer than the formation length, the Bremsstrahlung process is suppressed. This phenomenon is known as Landau-Pomeranchuk-Migdal (LPM) [106, 107] suppression. The radiated spectrum is, in this regime, proportional to $1/\sqrt{E}$.

Yet lower energy photons are further suppressed by the destructive interference leading to the suppression of Bremsstrahlung photons of $E < \gamma\omega_p$, where ω_p is the plasma frequency of the radiator. This process is called "Dielectric Suppression". The photon energy distribution is, in this regime, proportional to photon energy. The photon energy dependency of the radiated spectrum is schematically shown in Fig. 1.20. Measured Bremsstrahlung photon spectrum of an electron in the carbon target [104] is shown in Fig. 1.21. The data are compared to the model where all three above mentioned mechanisms are included.

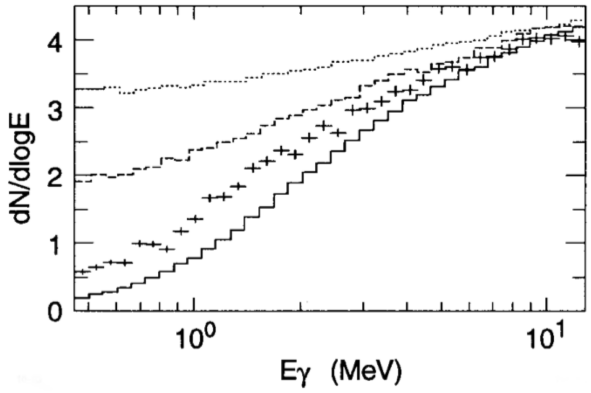

Figure 1.21: Bremsstrahlung spectrum of photons (crosses) for energy range 0.5 – 10 MeV on a 6% X_0 Carbon target [108]. Three Monte Carlo expectations are shown (see Fig. 1.20), the dotted line is Bethe-Heitler (t/X_0), dot-dashed in the middle is the LPM suppression only and solid line on the bottom is combined LPM and dielectric suppression.

The simplest energy loss process is elastic QCD scattering off the medium partons. The recoil energy of the scattered partons are absorbed by the thermal medium, thus the initial parton loses its energy. The mean energy loss of the parton propagating through the medium of density ρ and length L is:

$$\langle \Delta E \rangle_{\mathrm{el}} = \sigma \rho L \langle E \rangle_{\mathrm{1scatt}} \sim L, \tag{1.39}$$

where σ is the interaction cross section and $\langle E \rangle_{\mathrm{1scatt}}$ is the mean energy exchange of each individual scattering process. The assumption holds only if the mean energy

loss is independent of the total energy of the parton (E). The transport coefficient of elastic scattering, $\langle \hat{e} \rangle = \langle \Delta E \rangle_{\rm el} / L$, is defined as the mean energy loss per unit path length [109].

Another energy loss mechanism is due to medium-induced radiation. The basic radiation process is the elementary splitting processes $q \to q g_r$ and $g \to g g_r$ due to multiple scattering, where g_r is the radiated gluon. The transverse momentum of the emitted gluon k_T is limited by the phase space, $k_T < \chi\omega$ where $\chi = \sin(\theta)$ refers to the opening angle (θ) of the emitted gluon of total energy ω. The gluon will be emitted if it picks up sufficient transverse momentum for the decoherence from the parton, and the gluon will be emitted with a characteristic frequency $\omega = \hat{q}L/2$ [110]. The formation time of the radiation originates from the uncertainty relation $\tau \sim \omega/k_T^2$ or $\tau \sim E/Q^2$, where E is the total energy of the parton and $Q = \hat{q}\tau$ is the virtuality picked up by the medium. The transport coefficient $\hat{q}$ is refering to the rate of virtuality picked up by the medium dQ^2/dx. Assuming the parton is moving with the speed of light, $\tau = L$, where the L is the length of the medium,

$$\langle \Delta E \rangle_{\rm rad} \sim \omega \sim \hat{q} L^2 \sim T^3 L^2, \tag{1.40}$$

where $\hat{q} \sim T^3$ is the thermal medium parametrization. The difference of the power L^n in Eq. (1.39) and Eq. (1.40) is often argued the radiative dominates over the elastic energy loss. In case of strong coupling of the parton with its virtual gluon cloud the temperature and length dependence change compared to weak coupling $\omega \sim T^4 L^3$ [111].

1.3.1 Experimental Observables for Jet Quenching

In this section we introduce some experimental observables to study the energy loss mechanism in the heavy ion collisions. The low-p_T region of the spectra in collision is driven by collective phenomena, where the tools of hydrodynamics are applicable, while the high-p_T part is dominated by the pQCD processes. The transition between the two regions depends on the collision energy.

In the absence of any nuclear effects, the production rate in relativistic heavy-ion collisions in the pQCD regime, i.e., at sufficiently high p_T, would scale with the increased probability that a hard scattering occurs, due to the large number of nucleons. The nuclear modification factor is defined as

$$R_{AA}(p_T) = \frac{(1/N_{AA}^{evt}) d^2 N_{AA}^{\pi^0}/dp_T dy}{\langle T_{AA} \rangle \, d^2\sigma_{pp}^{\pi^0}/dp_T dy}, \tag{1.41}$$

where $\sigma_{pp}^{\pi^0}$ is the production cross section of π^0 in p+p collisions and $\langle T_{AA} \rangle = \langle N_{\rm coll} \rangle / \sigma_{pp}^{\rm inel}$ is the nuclear overlap function averaged over the range of impact parameters contributing to the given centrality class according to the Glauber model. In absence of any nuclear effects the $R_{AA} = 1$, in case when the jet quenching overwhelms other nuclear effects the $R_{AA} < 1$.

The azimuthal anisotropy of particle production can be characterized in terms of Fourier coefficients

$$\frac{dN}{d\phi} \propto 1 + \sum_{n=1} 2v_n(p_T)\cos\left(n[\phi - \psi_n]\right), \tag{1.42}$$

where $v_n = \langle\cos\left(n[\phi - \psi_n]\right)\rangle$ $(n = 1, 2, 3, \dots)$ and the ψ_n are the generalized participants planes at all orders for each event. In the low transverse momentum region ($p_T < 3$ GeV/c) the hadron dynamics is driven mainly by the collective hydrodynamical phenomena [112, 113], discussed in Sec. 1.5.1. However, the high-p_T region of $v_n(p_T)$ is driven by the hard scattering processes.

The hard scattering processes in the collisions of the two nuclei would be distributed according to the overlap function of the individual nucleus-nucleus collisions. The initial spatial distribution of the created medium will result in different pathlength which the parton will propagate through the QGP with respect to the participant plane. The nuclear modification factor as a function of $\Delta\phi = \phi - \psi_n$ is defined as

$$\begin{aligned} R_{AA}\left(\Delta\phi, p_T\right) &= \frac{(1/N_{AA}^{evt})d^2N^{AuAu}/d\Delta\phi dy}{\langle N_{coll}\rangle\,(1/N_{pp}^{evt})dN^{pp}/dy} \approx \frac{dN^{AuAu}/dy\,(1 + 2\cdot v_2\cos\left(2\Delta\phi\right))}{\langle N_{coll}\rangle\,dN^{pp}/dy} \\ &= R_{AA}^{incl}(p_T)\left(1 + 2\cdot v_2\cos\left(2\Delta\phi\right)\right). \end{aligned} \tag{1.43}$$

The yield of the p+p is independent of the reaction plane and the yield in the Au+Au is modulated by the second harmonics. We approximate the R_{AA} up to the second harmonics only. From Eq. (1.43) it follows that

$$\frac{R_{AA}\left(0, p_T\right) - R_{AA}\left(\pi/2, p_T\right)}{R_{AA}^{incl}(p_T)} \approx \frac{R_{AA}^{incl}(p_T)\left(1 + 2\cdot v_2 - (1 - 2\cdot v_2)\right)}{R_{AA}^{incl}(p_T)} = 4\cdot v_2 \tag{1.44}$$

At high-p_T, the pQCD processes are dominant, hence the v_n (or $R_{AA}(\Delta\phi, p_T)$) characterize the path length-dependence of the energy loss process.

The jet fragmentation can be modified due to the presence of the medium. In order to study the jet fragmentation function ($D(z)$, where $z = p_T^h/p_T^{part}$) modification due the medium, we use the two-particle correlations. The particle yield can be extracted from the correlation function. The background from the flow processes is correlated and need to be subtracted to get the particle yield associated only with the jet. The ratio of the jet yields in Au+Au and p+p collision $I_{AA} = Y^{Au+Au}/Y^{p+p}$ characterizes the jet fragmentation modification [114]. I_{AA} probes the interplay between the parton production spectrum, the relative importance of quark-quark, gluon-gluon and quark-gluon final states, and energy loss in the medium.

1.3.2 Theoretical models

There are several theoretical models attempting to describe the parton-medium interactions and understand the nature of the energy loss mechanism. In this section we provide a short overview of the models which exist and their basic properties. The great challenge of a successful theoretical model is to describe the real situation in nature, therefore they should aim to describe as many observables as possible simultaneously. The various theoretical approaches and/or models are summarized in Tab. 1.1.

	Energy Loss Implementation		
	Kinematics	Splitting Probabilities	Explicit
analytical energy loss	-	ASW [115], HT [5]	AMY [116], GLV [16]
analytical shower	-	HT resummed	-
Monte Carlo shower	YaJEM [17]	Q-Pythia [117]	JEWEL [118]
Monte Carlo hybrid	-	PYQUEN [119]	MARTINI [120]

Table 1.1: The classification of energy models based on the assumption of the models.

Opacity expansion models. In the Gyulassy-Levai-Vitev (GLV) formalism [16], the radiative energy loss is considered on few scattering centers, N_{scatt}. The radiated gluon is constructed by pQCD calculation as summing up the relevant scattering amplitudes in terms of the number of scatterings. The relation $\langle N_{scatt} \rangle = L/\lambda_{\text{m.f.p}}$, where $\lambda_{\text{m.f.p}}$ as the mean free path of the gluon, translates to opacity of the plasma, thus the formalism is known as the opacity expansion. Later, the formalism was extended to include massive quarks (DGLV [121]), and include the elastic energy loss, known as the WHDG model [122]. The GLV formalism is not the only approach for opacity expansion. The ASW mechanism was developed by Armesto, Salgado and Wiedermann (ASW) [115] which uses the non-abelian Furry approximation [4] on static color charges.

The modern elastic energy loss formalism were motivated mostly due to the heavy flavor results at RHIC. The heavy flavor suppression showed to be surprisingly high which could be explained by the underestimation of the elastic energy loss or collision energy loss. Mustafa and Thoma [123] started the investigation of the light parton elastic scattering in the longitudinal Bjorken expansion. The observation of suppression of electrons originating from the heavy quarks [124, 125] have suggested the importance to include the collisional energy loss into the radiative energy loss theoretical models.

AMY model. In contrast to previous approaches where they used static scattering centers, the Arnold, Moore and Yaffe (AMY) [116] model is based on leading order pQCD hard thermal loop (HTL) effective field theory where the scattering centers are dynamical. The model assumes the high temperature of the plasma causes the strong coupling constant can be treated as small, $g(T \gg T_C) \ll 1$. The parton propagating through the medium will lose the energy from soft scatterings ($\lambda_{\text{m.f.p}} \sim 1/g^2T$) and

hard scatterings ($q \sim T$ and $\lambda_{\text{m.f.p.}} \sim 1/g^4T$). Thus the energy loss is due to several soft scatterings or a single hard scattering.

HT approach The above models calculate the energy loss while the parton propagates through the medium, focusing on the pQCD part of Eq. (1.20). The higher twist (HT) approach by Wang and Guo implements the energy loss mechanism in the energy scale evolution of the fragmentation functions ($D^h_{q/g}(z, \mu^2)$) [5]. The analogy was taken from the forward photon-proton scattering amplitude which expansion is ordered by the difference of the dimension and spin. In QCD the result depends on both the diagonal and off-diagonal twist-four parton distributions in nuclei, demonstrates clearly the LPM interference features and predicts a unique nuclear modification of the quark fragmentation functions

Monte Carlo methods. A wide range of results in high-energy particle physics is described by the PYTHIA event generator [126]. It is then natural to use the PYTHIA event generator (or a phenomenologically similar event) in the Monte Carlo models of energy loss mechanism. The PYTHIA calculates the hard scattering process, the partonic shower is developed and then it uses the Lund string fragmentation formalism in producing final state hadrons. The two first MC models describing the energy loss mechanism are PYQUEN [119] and Q-Pythia [117]. PYQUEN model includes elastic (with the t-channel dominant) and radiational (using BDSM formalism [127]) energy loss. Q-Pythia is calculating the modified vaccum radiation spectrum from PYTHIA routine adding the medium radiation $dI^{\text{tot}} = dI^{\text{vac}} + dI^{\text{med}}$. The medium induced gluon radiation is treated by the BDMPS formalism. The MARTINI model [120] is an event generator for the hard and penetrating probes in high energy nucleus-nucleus collisions. Its main components are a time evolution model for the soft background, PYTHIA and the McGill-AMY parton evolution scheme including radiative as well as elastic processes. Two other MC models, JEWEL [118] and YaJEM [17, 128], are using similar shower calculation process and hadronization as in PYTHIA. The initial hard parton is increasing its virtuality by interacting with the medium what changes the shower that the parton generates.

1.4 Direct Photon Production in Heavy Ion Collisions

The photons present an excellent probe of the medium due to their small coupling to the medium. The created photons can leave the medium without further interaction [123, 13, 14, 15]. The mean-free-path of the photons is about $\lambda_{\text{mfp}} \approx 100$ fm, while the plasma is produced with a diameter of $d_{\text{QGP}} \approx 14$ fm. The time dependence of the individual photon sources in heavy-ion collisions is summarized in schematic view in Fig. 1.22 [129, 123].

The sources of direct photon production in p+p collisions are mainly originated from hard scattering (see in Sec. 1.1.6) and fragmentation of parton showers. In heavy ion

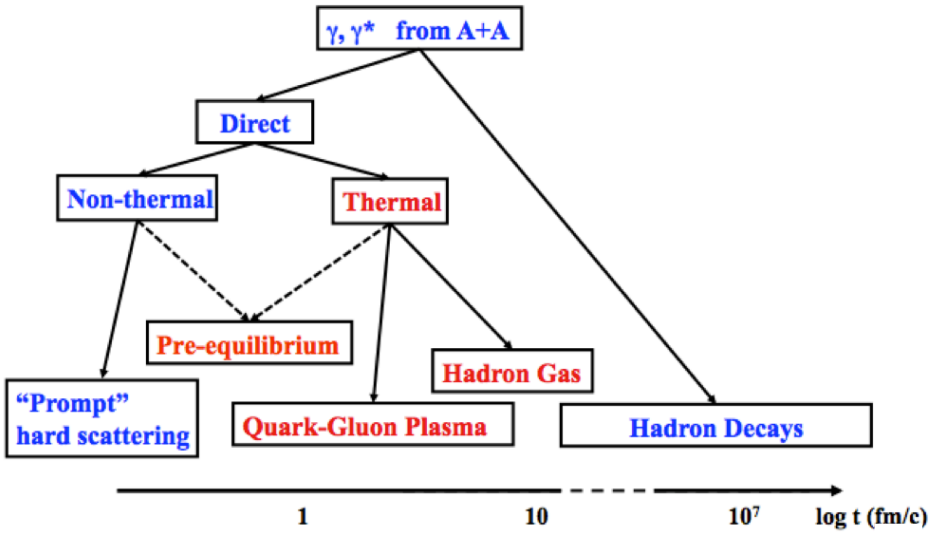

Figure 1.22: Schematic view of the production of photons in heavy ion collision.

collisions, the high-p_T part of the spectrum is dominated by the photons from the hard scattering processes. The hard scattered photons are, to the large extent, insensitive to the QGP evolution. Since the dominant production cross section of direct photon is calculable in pQCD frame and they are not modified by the medium, the measurement in this p_T region in heavy ion provides a valuable information about the initial yield from hard scattering. The comparison of photon yields in heavy ion to p+p collisions at high-p_T is also used to test the binary scaling behavior obtained from Glauber Model.

In the heavy ion collisions additional photons could be emitted from the produced hot and dense thermal medium. The thermal radiation dominates at the low-p_T region of the spectrum. However, the quark and gluons originating from hard scattering may interact with the medium and produce a mid- or high-p_T direct photon, called a "jet-photon" conversion [130]. In summary, the probability of jet-photon conversion is low [131], high-p_T direct photon production is dominated from hard scattered photon. Besides the direct photon production, large amount of photons are created from hadronic decays, mainly through the $\pi^0 \to 2\gamma$ and $\eta \to 2\gamma$ decays.

1.4.1 Thermal photons

Every thermal source emits thermal photon radiation. The electromagnetic radiation of highly excited hadronic state was already proposed in 1976 by Feinberg [132]. In QGP, the deconfined medium degrees of freedom are carried by gluons and quarks, the number of antiquarks and quarks is nearly equal, thus the $q_t\bar{q}_t \to g_t\gamma_t$ (where t refers to thermal) channel is enhanced. After the QGP cools down and hadron gas is formed which has appropriate degrees of freedom, then thermal photons can be emitted from

this medium. Thermal photons are emitted through the entire space-time evolution of the QGP and HG and carry important signatures of the temperature of the created medium.

There was a presumption that QGP produces a stronger photon radiation than a hadron gas at the same temperature. Because the quarks in QGP are massless, and they are able to interact strongly, it can be expected that there would be a lot of charges being scattered and so a large amount of electromagnetic radiation. However, it was turned out that hadron gas and QGP would produce very similar spectra of radiated photons at comparable temperatures, at the phase transition region ($\sim 150-200$ MeV). For example, following hadronic processes are included for the calculation:

$$\pi^{\pm} + \rho^0 \rightarrow \pi^{\pm} + \gamma, \tag{1.45}$$
$$\pi^{+} + \pi^{-} \rightarrow \rho^0 + \gamma, \tag{1.46}$$
$$\rho^0 \rightarrow \pi^{+} + \pi^{-} + \gamma, \tag{1.47}$$
$$\omega \rightarrow \pi^0 + \gamma. \tag{1.48}$$

The techniques to calculate the thermal photon yield both from QGP and HG phase were already invented in 1950s in the thermal field theory. In theoretical model calculations have included thermal photon yield from both phases.

1.5 Energy Scan Program

In 2010 the RHIC collider started a low energy program for Au+Au heavy ion collisions. The planned collision energy range of this program is in the interval of $\sqrt{s_{NN}} = 5$ - 200 GeV. The program provides an opportunity to study various signatures of the created matter, such as for example are jet-quenching, hydrodynamical flow. Furthermore, the beam energy scan serves to map a large part of the QCD phase diagram. In particular, the region of higher baryon chemical potential is predicted to be one of the more feature rich parts of the QCD phase diagram. At the center of the discussion is the possibility of the critical end point (CP) which could be located at finite density μ_B. Such a CP was not yet observed in experimental data. The earlier results provided at top RHIC energies are consistent with a smooth cross over phase transition [91]. The experimental observation of the CP or the first order transition would expand our current knowledge of the QCD phase diagram.

The main experimental focus during the energy scan program is to measure the observables which are sensitive to the different collision energies. The quark-number scaling of elliptic flow or parton energy loss can serve as powerful constraint for the available theoretical models. In the next section, we refer the experimental results which motivate the low-energy scan. We focus on the previous measurements relevant

for the analysis presented in this note. We summarize the experimental results at RHIC in Au+Au collisions at $\sqrt{s_{NN}} = 200$ GeV and at SPS in Pb+Pb collisions at $\sqrt{s_{NN}} =$ 17.3 GeV.

1.5.1 Previous Measurements

The measurement of fluctuation observables is expected to provide the most direct evidence that the system has approached the critical point. The multiplicity fluctuation is sensitive to the phase order transition. In a thermal system in the Grand Canonical Ensemble (GSE) [133] the isothermal compressibility ($k_T = -1/V(\delta V/\delta P)_T$ where V is the volume, T is the temperature, P is the pressure) relates to multiplicity fluctuations:

$$\left\langle (N - \langle N \rangle)^2 \right\rangle = \frac{k_B T \langle N \rangle^2}{V} k_T, \tag{1.49}$$

where N is the particle multiplicity and $\langle N \rangle = \mu_N$ is the mean multiplicity and k_B is the Boltzmann's constant. The multiplicity fluctuation measurements are presented in terms of the scaled variance $\omega_N = \left\langle (N - \langle N \rangle)^2 \right\rangle / \mu_N = (k_B T \mu_N / V) k_T$. Near the critical point, this divergence is described by a power law in the variable $\varepsilon = (T - T_C)/T_C$, where T_C is the critical temperature. Hence, the relationship between multiplicity fluctuations and the compressibility can be exploited to search for a clear signature of critical behavior by looking for the expected power law scaling of the compressibility:

$$k_T \approx \left(\frac{T - T_C}{T_C} \right)^{-\gamma} \approx \varepsilon^{-\gamma}, \tag{1.50}$$

where γ is the critical exponent for isothermal compressibility. If the QCD phase diagram contains a critical point, systems with a low value of baryo-chemical potential (μ_B) could pass through the cross-over region and undergo a continuous phase transition, see in Fig. 1.17. Simultaneous observation of an increase in fluctuations of $\langle p_T \rangle$ and multiplicity, along with observation of an increase in measurements of correlation lengths could identify the location of the critical point unambiguously.

Several other observables are studied during the RHIC beam-energy scan program. The identified particle ratios such as K/π or $p/\bar{p}$ are necessary in order to measure the location of the $\mu_B - T$ phase diagram (see in Fig. 1.17). In addition, the low-mass dielectrons may carry the information on chiral symmetry restoration. Such a measurement was never done between the collision energies of $\sqrt{s_{NN}} = 17.3$ - 200 GeV. In next subsections we focus on observables more relevant to the analysis presented in this report.

Elliptic Flow measurements

The many-body system, such as the QGP, may be described by hydrodynamics when the mean free path of the constituents are much smaller than the size of the

system. The initial spatial energy density distribution of the collision zone causes a different pressure gradient in different directions of the produced medium. Due to the finite size of the heavy ions the initial collision zone has an anisotropic (almond) shape for nonzero impact parameters. The pressure gradient consequently results in larger particle production in the reaction plane direction (in-plane) as compared to the perpendicular direction (out-plane). The azimuthal anisotropy ($v_n(p_T)$) of particle production in an event is defined in Eq. (1.42).

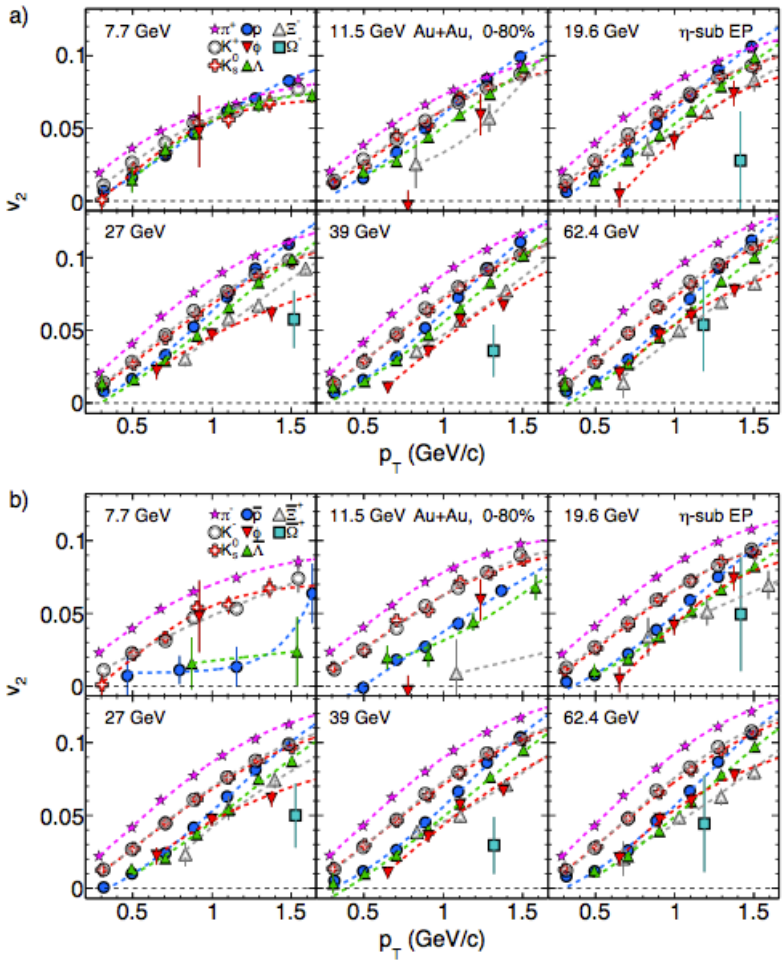

Figure 1.23: The elliptic flow ($v_2(p_T)$) in 0-80% centrality selection of Au+Au collisions for different paricles (a) in top panels and their anti-particles (b) in bottom panels [134]. The data points are fitted by function $f_{v_2}(n) = an/(1+\exp(-p_T/n-b)/c)-dn$, where n is the number of quarks and a, b, c, d are fitting parameters.

The observation of the critical point (CP) in the QCD phase diagram could be provided by the experimental extraction of the viscosity over the entropy density, η/s [135].

The $v_n(p_T)$ measurements provide a possibility to extraction of the η/s from the data [136, 137]. The initial estimates for the created matter at $\sqrt{s_{NN}} = 200$ GeV η/s were indicated as small number $\sim 1-4$ times the $1/4\pi$ the lower conjectured bound [138]. The recent hydrodynamical models which are successfully describing the measured $v_n(p_T, \text{cent})$ indicate also small value of $\eta/s \simeq 2/4\pi$ [139, 140]. However, the precision of all of these extractions has been hampered by significant theoretical uncertainty, especially those arising from poor constraints for the initial eccentricity and the relaxation time.

It is generally expected that the system will spend less time in the partonic phase as the beam energy is lowered. With decreasing beam energy, it is possible not to reach the QGP phase and the baryon chemical potential of the system at chemical freeze-out increases. If it still reaches the QGP phase, it is expected that the system crosses the first phase transition or the critical point, see in Fig. 1.17.

The first experimental data from flow measurements are shown in Fig. 1.23, where the wide range of identified particle $v_2(p_T)$ was already measured in the energy range $\sqrt{s_{NN}} = 7.7$ - 62.4 GeV [134]. For all of the particle species, v_2 increases with increasing energy at high transverse momenta, whereas v_2 at low-p_T values depend on the particle species. Significant difference between the particles and anti-particles were observed at low collision energies. The difference is larger at lower collision energies, while it is approximately constant from $\sqrt{s_{NN}} > 39$ GeV.

Jet quenching measurements

The suppression of high-p_T hadrons was first measured in Au+Au collisions at $\sqrt{s_{NN}} = 130$ GeV [6, 7] and later confirmed at $\sqrt{s_{NN}} = 200$ GeV [8]. The suppression was not observed in d+Au collisions at $\sqrt{s_{NN}} = 200$ GeV [141] which provides a convincing evidence that the suppression is mostly of the final state origin. In the d+Au collision a small enhancement was observed around $p_T \sim 3-4$ GeV/c which could be explained as Cronin enhancement [142], due to initial-state multiple scattering or anti-shadowing.

In 2005, the PHENIX experiment has measured π^0 yields in Cu+Cu collisions at three different c.m. energies: $\sqrt{s_{NN}} = 22.4$, 62.4 and 200 GeV, see in Fig. 1.24 [143]. The R_{AA} of π^0 in the most central collision (0-10%) shows strong suppression at c.m. energies $\sqrt{s_{NN}} = 200$ and 62.4 GeV and no pronounced suppression at $\sqrt{s_{NN}} = 22.4$ GeV. The nuclear modification factor shows an enhancement in the $3 < p_T < 5$ GeV/c region what may be the result of the Cronin enhancement. The corresponding p_T averaged ($2.5 < p_T < 3.5$ GeV/c) R_{AA} exhibits a strong centrality dependence in case of $\sqrt{s_{NN}} = 62.4$ and 200 GeV and no centrality dependence at $\sqrt{s_{NN}} = 22.4$ GeV. The data suggest that the suppression is no longer the dominant effect in Cu+Cu collisions at $\sqrt{s_{NN}} = 22.4$ GeV. The value of R_{AA} measured in the Cu+Cu and Au+Au collisions at $\sqrt{s_{NN}} = 200$ GeV are similar at the same number of participants (N_{part}).

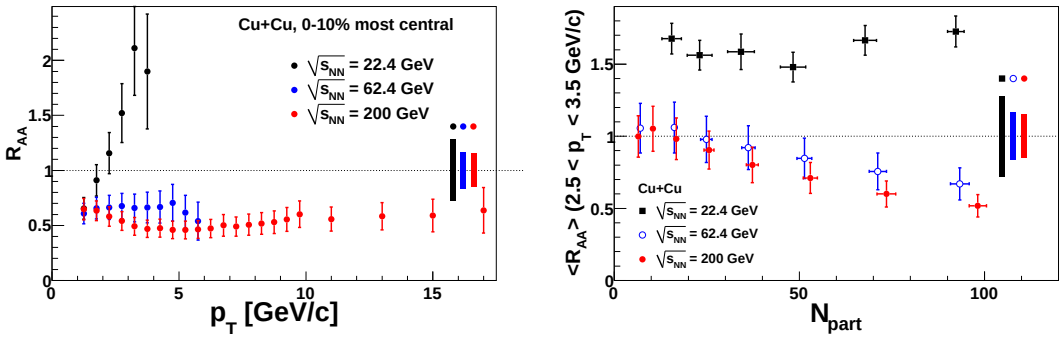

Figure 1.24: The nuclear modification factor (R_{AA}) of π^0 in Cu+Cu collisions at three collision energies $\sqrt{s_{NN}}$ = 22.4, 62.4 and 200 GeV [143]. The left panel shows the R_{AA} as a function of transverse momentum, p_T. The error bars on the points are the quadratic sum of the statistical and point-by-point uncorrelated and correlated systematic uncertainties. The boxes around unity indicate uncertainties of $\langle N_{\rm coll}\rangle$ and absolute normalization. The right panel shows the averaged R_{AA} in interval 2.5 < p_T < 3.5 GeV/c as a function of centrality. The boxes around unity represent the normalization and $\langle N_{\rm coll}\rangle$ uncertainties.

Another comparison is made with heavier nuclei, using Au+Au collision at RHIC and Pb+Pb collision at SPS. Fig. 1.25 shows the nuclear modification factor measured by the WA98 collaboration at $\sqrt{s_{NN}}$ = 17.3 GeV [11] and by the PHENIX collaboration at $\sqrt{s_{NN}}$ = 200 GeV [8]. In comparison of the measurement in central (0-10%) Au+Au collision at $\sqrt{s_{NN}}$ = 200 GeV, the R_{AA} in the central (0-13%) Pb+Pb collisions at $\sqrt{s_{NN}}$ = 17.3 GeV shows no suppression of particle yield. However, the p_T reach of the WA98 measurement is very limited, it may show only the characteristic of the Cronin enhancement. The ultra-central collisions (0-1%) presented in the same paper [11] shows suppression by a factor of $\sim$ 2, although the result could be due to the fluctuations in the centrality selection.

It is natural to ask where the suppression process starts to dominate the production of particles. The measurement in Cu+Cu collisions suggests the transition between the suppression ($R_{AA} < 1$) and enhancement ($R_{AA} > 1$) dominated region in this system is between collision energies $\sqrt{s_{NN}}$ = 22.4 and 62.4 GeV. The RHIC beam energy program is focusing to observe the transition in the Au+Au collision system in the collision energy region $\sqrt{s_{NN}}$ = 5 - 62.4 GeV.

Direct photon measurements

The observation of thermal photon radiation turned out to be extremely difficult to achieve by experiments. The first direct photon yield spectrum in heavy ion collisions

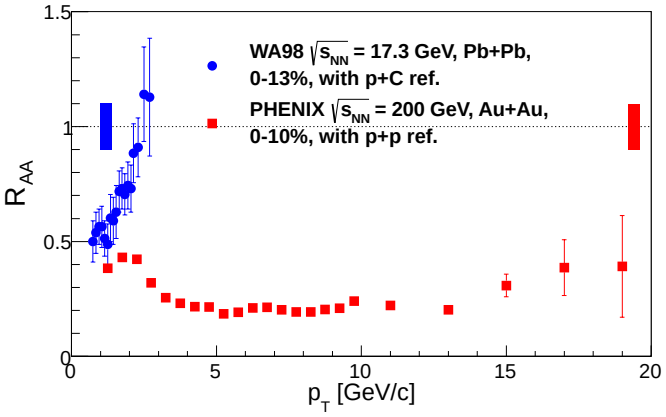

Figure 1.25: The nuclear modification factor ($R_{AA}(p_T)$) of π^0 in Pb+Pb collisions at SPS at $\sqrt{s_{NN}}$ = 17.3 GeV by WA98 collaboration [11] and in Au+Au collisions at RHIC at $\sqrt{s_{NN}}$ = 200 GeV [8]. As a reference, denominator in Eq. (1.41), the p+C collisions were used in WA98 case and a p+p collisions in PHENIX case. The error bars represent the quadratic sum of statistical and systematical uncertainties. The boxes around unity represent the systematic deviation from the $\langle N_{\rm coll}\rangle$, left for WA98 and right for PHENIX measurement.

was measured by WA98 collaboration [144] at $\sqrt{s_{NN}}$ = 17.3 GeV. Fig. 1.26 shows the direct photon spectrum measured at $\sqrt{s_{NN}}$ = 17.3 GeV can be interpreted as thermal radiation with initial temperature $T_{\rm init} \sim 250$ MeV.

The PHENIX experiment has measured the photon yield in Au+Au at $\sqrt{s_{NN}}$ = 200 GeV in the p_T region where the thermal radiation is expected ($p_T < 3$ GeV/c) and compared it to the spectrum obtained from the p+p, see in Fig. 1.27 [145]. The direct photon spectrum in p+p collision was fitted with a modified power-law fit. The minimum bias Au+Au collisions show larger photon yield in the low-p_T part when compared with the $T_{\rm AA}$ scaled up p+p cross section. The excess yield in the 1−4 GeV/c region in the most central Au+Au collisions (0-20%) is fitted by an exponential function with an inverse slope of $T = 221 \pm 19^{\rm stat} \pm 19^{\rm syst}$ MeV. If the direct photons in Au+Au collision are of thermal origin, the inverse slope T is related to the initial temperature ($T_{\rm init}$). In hydrodynamical models, the $T_{\rm init}$ is 1.5 to 3 times T due to space-time evolution [147, 148].

The low-p_T region is compared with several hydrodynamical models of thermal photon emissions [145]. The models assume the initial thermalization time around $\tau_0 \simeq 0.15 - 0.6$ fm/c and the initial temperature ranging $T_{\rm init} \simeq 300 - 600$ MeV. The initial time and the initial temperature of the medium are highly correlated in the hydrodynamical models [149]. The initial temperature of the medium clearly exceeds the predicted phase transition temperature from hadronic phase to QGP ($T_C \simeq 170$ MeV).

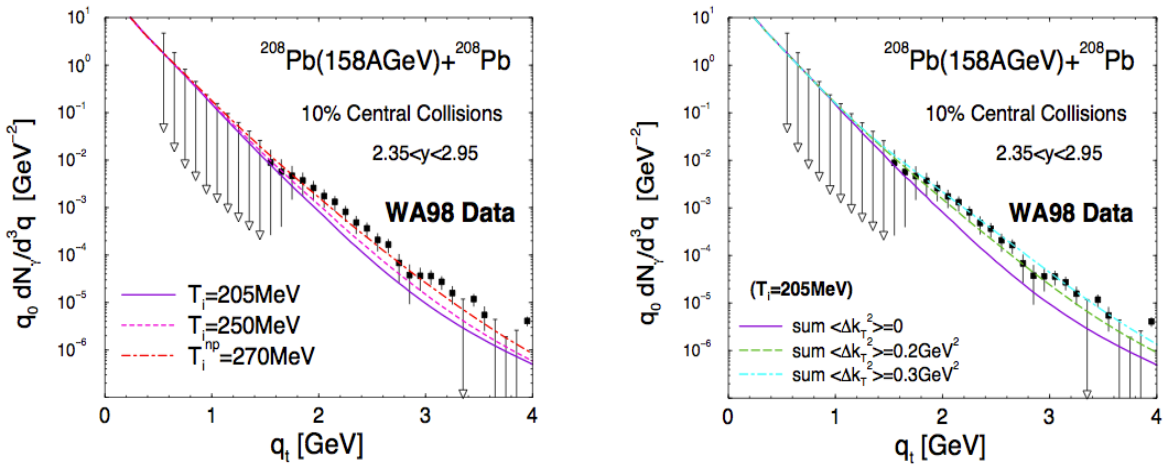

Figure 1.26: The direct photon spectrum observed in central (0-10%) Pb+Pb collisions at SPS fixed target collisions at $\sqrt{s_{NN}} = 17.3$ GeV [144]. The curves on the data points are the theoretical model calculations by Turbide et al. [131]. Left panel shows the direct photon rate can be approximately reproduced by thermal radiation from an initial state temperature $T_{\rm init} \sim 250$ MeV. Right panel shows the same spectrum with a photon yields from hard scattering combined with an initial parton transverse momentum Δk_T.

Another interesting probe of the medium is the azimuthal anisotropy of the thermal photons. The photon flow depends on the temperature of the medium and the dynamical flow of the medium. The expected azimuthal anisotropy of direct photons from hydrodynamical models is small [131, 150, 151], as the large fraction of the photons comes from the QGP phase from early times where the flow of the medium is not formed yet.

The new measurement of the direct photon azimuthal anisotropy, v_2 , has been done in Au+Au collisions in $1 < p_T < 13$ GeV/c at $\sqrt{s_{NN}} = 200$ GeV. The measurement was done with two independent methods: (i) using real photon combined with internal conversion of direct photon measurement [152] and (ii) the conversion of photons created ≈ 60 cm away from the interaction point [153]. The large elliptic flow of the direct photons was observed in heavy ion collisions, where both analyses agree within uncertainties in Fig 1.28.

The positive direct photon v_2 which is observed is comparable in the magnitude to the π^0 v_2 and consistent with early thermalization times and low viscosity of the medium. The magnitude of the direct photon v_2 is much larger than current theory models predict [151, 154]. The large thermal photon yield suggests the high initial temperatures of the plasma when the flow of the medium was not developed. On the other hand the large photon flow could be formed in later stage of the expansion

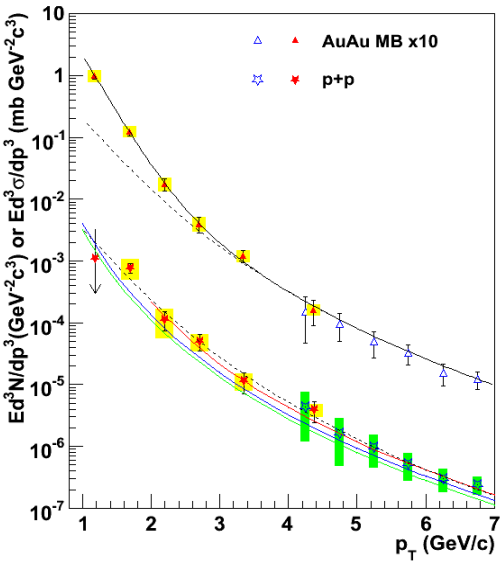

Figure 1.27: Direct photon invariant cross section in p+p collision and the invariant yield in Au+Au minimum bias collision at $\sqrt{s_{NN}} = 200$ GeV [145]. Filled points are from the dilepton analyses and the open points are from the calorimeter analysis. The three curves on the p+p data show the perturbative QCD calculations [13] and the dashed curve over Au+Au data is the power-law fit to the p+p data, scaled by $T_{\rm AA}$ from the Glauber Monte Carlo [146]. The solid curve going through the Au+Au data is the exponential plus the $T_{\rm AA}$ scaled up p+p fit.

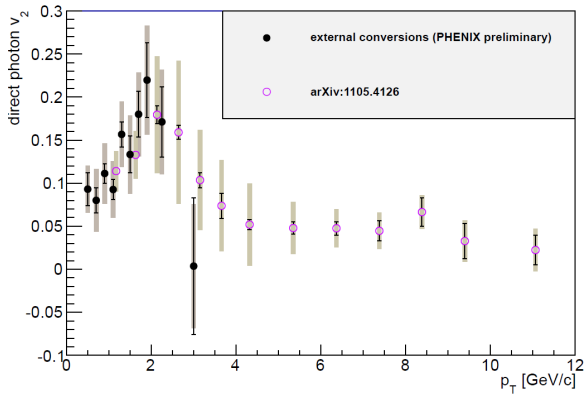

Figure 1.28: Direct photon azimuthal anisotropy (v_2) in Au+Au collisions at $\sqrt{s_{NN}} =$ 200 GeV. The measurement was done with two independent methods, electromagnetic calorimetry with internal conversion of photons and external conversion at ≈ 60 cm from the interaction point. The error bars represent the statistical uncertainty, while the bands give the systematic uncertainties.

when the temperature was lower. The large yield and azimuthal anisotropy results simultaneously are not explained by theoretical models [151, 154].

The production of direct photons [155] in p+p and p+$\bar{\text{p}}$ collisions at various $\sqrt{s}$ is described by the next-to-leading pQCD, and demonstrated by the x_T scaling with $n_{\text{eff}} = 4.5$ in left panel of Fig 1.29. Due to the scale breaking in QCD, the measured value of n_{eff} depends on the x_T value and the range of $\sqrt{s}$ used in the computation. It is assumed that the deviation from the expected single vector–gluon exchange, $n_{\text{eff}} - 4 = 0.5$, is caused by the scale breaking effects.

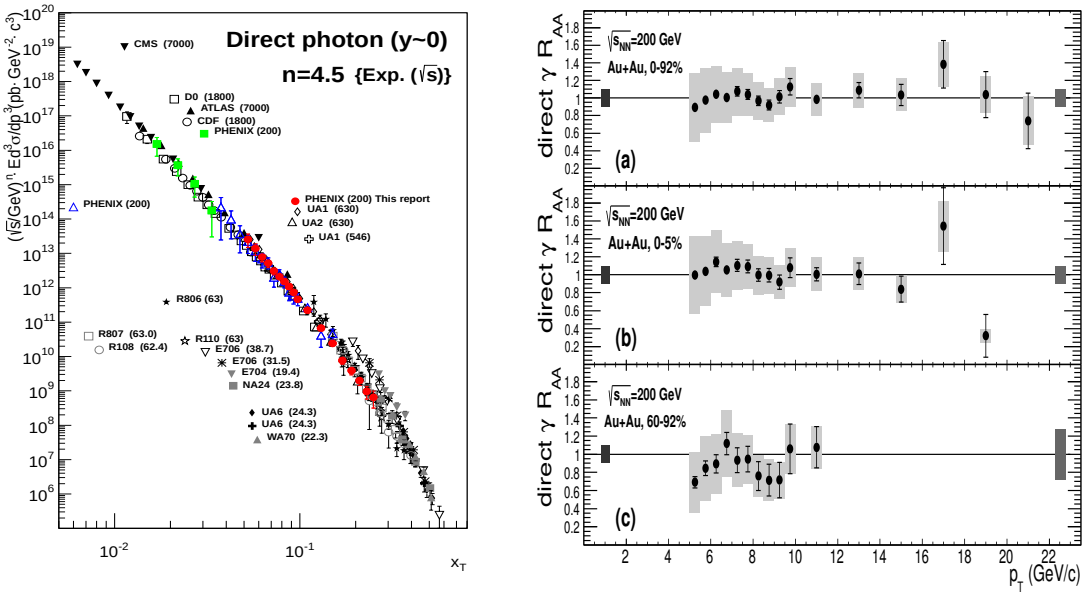

Figure 1.29: Left: Various direct photon cross section measurements in p+p and p+$\bar{\text{p}}$ collisions scaled by $\sqrt{s}^{4.5}$ as function of $x_T = 2p_T/\sqrt{s}$ [155]. The legend shows the experiment and the center of mass energy [GeV] in parenthesis. Right: The direct photon nuclear modification factor (R_{AA}) measured in Au+Au minimum bias, most central (0-5%) and peripheral collisions (60-92%) at $\sqrt{s_{NN}} = 200$ GeV.

The photon yield in minimum bias and two different centrality bins (most central, 0-10%, and most peripheral, 60-92%) of Au+Au collisions is compared to T_{AA} scaled up (see Eq. 1.41) p+p cross section in right panel of Fig 1.27 [156]. When comparing to p+p collisions, the direct photon production can be affected by the isospin effect, because the neutron content of the gold nuclei. The isospin effect is expected to be at most 10% at $p_T \sim 20$ GeV/c. The R_{AA} values are comparable with unity in each centrality class and for all $p_T > 4$ GeV/c. The azimuthal anisotropy of high-p_T direct photons ($5 < p_T < 13$ GeV/c) is consistent with zero within uncertainties, see Fig 1.28. The production of high-p_T photons is consistent with the scenario where they

are emitted from initial hard-scattering, and then traverse the medium without further interaction. It also implies that the fraction of fragmentation photons is small, the data are consistent with less than 10% contribution [155].

In Summary

In previous section I summarized the relevant measurements for this thesis in heavy ion collisions at top SPS and RHIC energies. In particular, the jet quenching shows dramatic change at the two different collision energies. This fact provides the main motivation for the study of the nuclear modification factor evolution as a function of the collision energy. The measurement of the neutral pion R_{AA} provides an excellent probe to study the medium modification. On other hand, the production of direct photons at high-p_T is not modified by the medium, which would provide a confirmation of the Glauber Model for the R_{AA}. The details of the analyses are explained in next sections.

Chapter 2

Experimental Setup

2.1 Relativistic Heavy Ion Collider

The RHIC collider [157] was the first heavy ion collider designed to accelerate Au ions to beam energy of 100 GeV per nucleon and protons at beam energy of 250 GeV. RHIC consists of two beam pipes (labeled "yellow" and "blue") at a total length of 3.8 km. The beam pipes cross at 6 interaction points. The RHIC is designed to accelerate up to 120 bunches of $N = 10^9$ Au ions in each pipes. The corresponding luminosity, when the angle between beams equals to zero, is calculated as

$$\mathcal{L} = \frac{b}{4\pi}\frac{N^2}{\sigma_x \sigma_y} f_{\text{rev}}, \tag{2.1}$$

where b and N are the number of bunches and particles per bunch, respectively, σ_x and σ_y are the cross sections of the bunches and $f_{\text{rev}} = 78$ kHz is the frequency of the particles. The designed luminosity of the bunches are $\mathcal{L} = 2 \times 10^{26}$ cm^{-2}s^{-1} for Au ions and $\mathcal{L} = 2 \times 10^{32}$ cm^{-2}s^{-1} for protons.

Heavy ions are produced at the source and transported through Tandem-Van-de-Graaff at energy of 200 AMeV. The ions enter the booster accelerator and the Alternating Gradient Synchrotron (AGS) where the Au ions are accelerated to 9 GeV per nucleon beam energy before entering the RHIC collider.

2.2 Pioneering High Energy Nuclear Interaction eXperiment

The PHENIX detector [158, 159] was designed to specialize on identification of photons, leptons and high-p_T hadrons. The sophisticated trigger system allows the PHENIX to focus on rare events. The final design of the detector emerged from multiple physics proposals and in its final form PHENIX consists of two major detector

systems as shown in Fig. 2.1, located in mid-rapidity $|\eta| < 0.35$ and forward pseudo-rapidity $1.8 < |\eta| < 2.2$, where $\eta = -\ln(\tan(\theta/2))$ and θ is the longitudinal scattering angle. The main sub-detectors, their acceptances and main purpose are summarized in Tab. 2.1. In this thesis, we focus on the central arm only, which consists of east and west arms as shown in Fig. 2.1, with limited ϕ acceptance ($2 \times 90°$).

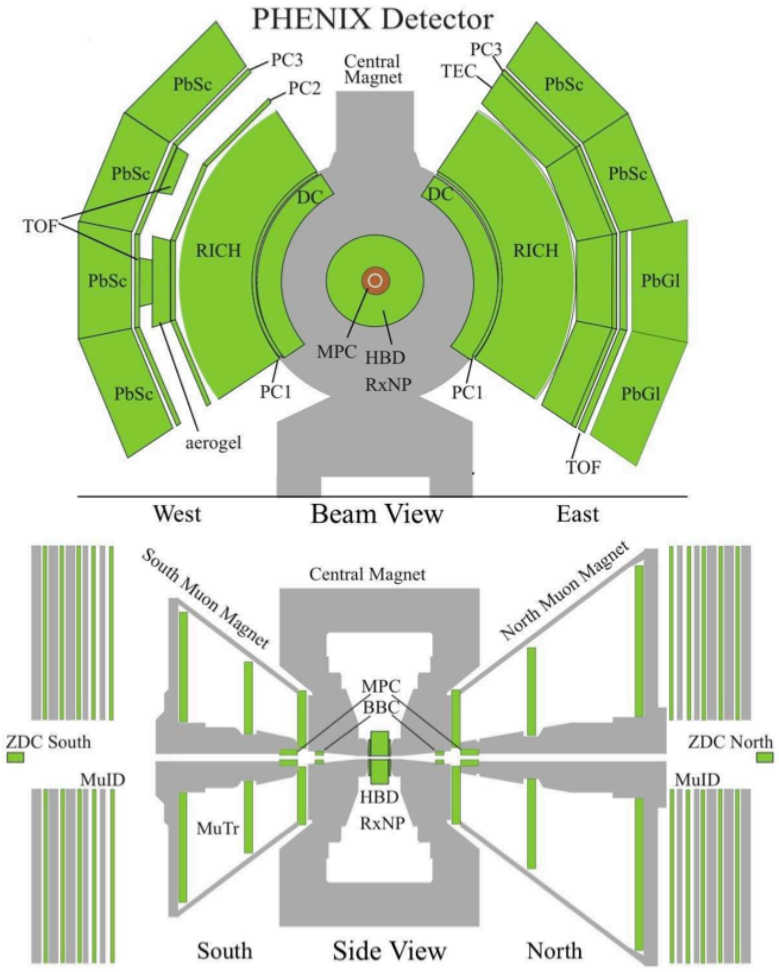

Figure 2.1: Beam view (top) and side view (bottom) of the PHENIX Detector setup in 2010.

The forward rapidity detectors, divided into North and South side, specialize in the detection of muons, featuring prominently in measurements related to heavy quark production, as well as measurements involving rapidity dependent variations in particle production.

The central arm, West and East arms, was designed for various measurements such as identification of electrons, tracking charged hadrons, and detecting photons. In this

thesis we focus on the neutral pion (π^0) and eta (η) reconstruction via the two photon decay channels and the direct photon measurements. These measurements are done with the Electromagnetic Calorimeter (EMCal) [160].

The geometry of the heavy ion collision is also studied via the forward detectors. The Beam-Beam Counter (BBC) [161] is used as trigger detector and also to identify the vertex of the collision. The reaction plane of the collision, see Sec. 1.2.3, is further studied by the BBC detector, the Muon Piston Calorimeter (MPC) [162] and Reaction Plane Detector (RXN) [163].

2.2.1 Trigger Determination

The two beams from each direction are crossing in the diamond shape interaction region. The longitudinal size of the bunch at RHIC for Au beam is designed to have RMS around 25 cm. Not every bunch crossing results in a collision, the trigger detectors identify the occurrence of the interaction. Every further study of the event needs a more precise determination of the interaction vertex. Furthermore, the time when the interaction occurs is necessary for the time-of-flight measurements which is used for the particle identification.

There are two detectors in PHENIX with the primary purpose of event determination, as well as measurement of the vertex of such events: the Beam-Beam Counters (BBC) [161] and the Zero Degree Calorimeters (ZDC) [164], see in Fig. 2.1. Both have a north and south portion, acting as multiplicity detectors, with high precision timing capabilities. In either case, an event is defined by a coincidence of signals - during a bunch crossing - in the North and South portions of the detector. The timing difference between the two signals can then be used to determine the vertex location along the beam axis. The BBC and ZDC therefore provide independent event determinations and event vertex measurements. However, the higher timing resolution of the BBC makes it the primary detector for both. The ZDC detector is not designed for the low-energy environment, where the transverse Fermi momentum ratio of the spectators are higher in comparison to those at 100 GeV beam energy. Therefore, due to the limited acceptance of the ZDC detector, it is not practical to use in the low-energy Au+Au collisions $\sqrt{s_{NN}} \leq 62.4$ GeV.

The BBC consists of two identical sets of 64 Čerenkov counters installed on both sides of the collision point along the beam axis. The BBC's are placed symmetrically 144 cm from the center of the interaction diamond which corresponds the pseudorapidity region of $3.0 < |\eta| < 3.9$. Each module of the BBC consists of 3 cm quartz radiator and a photomultiplier (PMT) for readout. The time of the interaction from the two separate counters define the time of the interaction, $(t_{\rm N} + t_{\rm S})/2$ where the $t_{\rm N}$ and $t_{\rm S}$ are the times measured in north and south side, respectively. The time of the collision provides the base-line for particle identification. The time resolution of the BBC's in the real environment of Au+Au collisions at $\sqrt{s_{NN}} = 200$ GeV is $\sigma = 52 \pm 4$ ps (RMS).

Name of the subdetector	rapidity	ϕ [rad]	Purpose
Beam Beam Counter (BBC)	$3.1 < \|\eta\| < 3.9$	2π	Minimum bias trigger; vertex, centrality and reaction plane determination; starts the timing
Zero-Degree Calorimeter (ZDC)	± 2 mrad ($\|\eta\| \geq 6$)	2π	Minimum bias trigger, centrality determination
Reaction Plane Detector (RXN)	$1.0 < \|\eta\| < 2.8$	2π	centrality, reaction plane determination
Muon Piston Calorimeter (MPC)	$3.1 < \|\eta\| < 3.8$	2π	forward π^0 measurement, reaction plane determination
Central Magnet	$\eta < 0.35$	2π	Up to 1.15 Tm
South Muon Magnet	$-2.2 < \eta < -1.1$	2π	
North Muon Magnet	$1.1 < \eta < 2.4$	2π	
Drift Chamber (DC)	$\|\eta\| < 0.35$	$2 \times \pi/2$	particle momentum measurement
Pad Chamber (PC)	$\|\eta\| < 0.35$	$2 \times \pi/2$	track matching
Time Expansion Chamber (TEC)	$\|\eta\| < 0.35$	$\pi/2$	track matching
Ring Imaging Čerenkov (RHIC)	$\|\eta\| < 0.35$	$2 \times \pi/2$	electron ID
Aerogel Detector (AGEL)	$0 < \eta < 0.35$	$\pi/4$	high-p_T hadron ID
Time of Flight (TOF)	$\|\eta\| < 0.35$	$\pi/4$	Hadron ID
Hadron Blind Detector (HBD)	$\|\eta\| \leq 0.45$	$3\pi/4$	electron ID
Lead-Scintillator (PbSc)	$\|\eta\| < 0.35$	$\pi/2 + \pi/4$	electromagnetic probes
Lead-Glass (PbGl)	$\|\eta\| < 0.35$	$\pi/4$	
Muon Tracker (MuTr)	$-2.25 < \eta < -1.1$	2π	momentum measurement
	$1.15 < \eta < 2.44$	2π	
Muon Identifier (MuID)	$-2.25 < \eta < -1.15$	2π	Muon ID
	$1.15 < \eta < 2.44$	2π	

Table 2.1: The summary of the PHENIX subdetectors.

The trigger requirements at $\sqrt{s_{NN}} = 200$ GeV are that at least one PMT in each BBC (North and South) have a hit and the collision vertex falls within the PHENIX central arm acceptance, i. e. $c(t_{\rm N} - t_{\rm S}) \sim |z| < 30$ cm. At lower collisions energies ($\sqrt{s_{NN}} =$ 39 and 62.4 GeV), the trigger requirements were at least two hits in each BBC. The trigger requirements will exclude some classes of events, the trigger selected events are referred as minimum bias events (MB events). Trigger efficiency w.r.t. inelastic Au+Au collisions is evaluated by a PHENIX detector simulation with the HIJING event generator [165]. The efficiency of the MB trigger was found $92 \pm 2\%$ at $\sqrt{s_{NN}} =$ 200 GeV, $85.7 \pm 2\%$ at $\sqrt{s_{NN}} = 62.4$ GeV and $85.9 \pm 2\%$ at $\sqrt{s_{NN}} = 39$ GeV. In p+p collisions, the efficiency of the trigger is around 50% at $\sqrt{s} = 200$ GeV [166].

2.2.2 Reaction Plane and Event Plane

The measurement of the geometry of a heavy ion collision (see in Sec. 1.2.3) is a difficult task. The reaction plane of the collision is defined by the beam axis and the vector connecting the two nuclei centers. However, the vector connecting the two nuclei cannot be measured directly. Instead the event plane (or participant plane) is inferred from the azimuthal density of the final hadrons detected in the forward rapidity detectors [167]. The detectors at forward rapidity that help to measure the event plane are the Beam-Beam Counter (BBC) [161], Muon Piston Calorimeter (MPC) [162] and Reaction Plane Detector (RXN) [163].

The event plane is determined for each harmonic of the Fourier expansion of the azimuthal distribution. The event flow vector $\vec{Q}_n = (Q_x, Q_y)$ and azimuth of the event plane ψ_n for n-th harmonic of the azimuthal anisotropy can be expressed as

$$Q_x = |\vec{Q_n}| \cos(n\psi_n) = \sum_i^M w_i \cos(n\phi_i), \tag{2.2}$$

$$Q_y = |\vec{Q_n}| \sin(n\psi_n) = \sum_i^M w_i \sin(n\phi_i) \tag{2.3}$$

or

$$\psi_n = \frac{1}{n} \tan^{-1}\left(\frac{Q_x}{Q_y}\right), \tag{2.4}$$

where M is the number of particles used to determine the event plane, ϕ_i is the azimuthal angle of each particle, w_i is a weight chosen to optimize the event plane resolution. The selected weights, w_i, can be for instance the transverse momentum (p_T), or selecting one type of particle (charge, particle identification). The optimization of the weights is discussed in [168], most often the w_i reflects the energy or multiplicity in the elements of the detector.

Electromagnetic Calorimeters	PbSc	PbGl
Type	Shashlik	Čerenkov
Radiation length (X_0) [mm]	21	29
Moliere radius [mm]	43	37
Cross section of a tower [mm^2]	52.5×52.5	40×40
Depth [mm] (X_0)	375 (18)	400 (14)
$\Delta\eta \times \Delta\phi$ of a tower	0.011×0.011	0.008×0.008
Number of sectors	6	2
Number of towers	15552	9216

Table 2.2: The summary of the parameters of the Electromagnetic Calorimeters at PHENIX. The calorimeter consists of two types of detectors: lead-scintillator (PbSc) and lead-glass (PbGl).

2.3 Electromagnetic Calorimeter

The Electromagnetic Calorimeter (EMCal) [160] is located in the central arm about 5 meters away from the interaction point. The purpose of the detector is to absorb the energy of electromagnetic showers, like those from impinging (primary) photons and electrons (unavoidably, the detector will be sensitive to the e.m. component of hadronic showers, too). The reconstruction of the invariant mass of photon pairs allows to identify light neutral mesons. The EMCal consists of two different types of detectors: first are the shashlik type lead-scintillator calorimeters (PbSc) of 6 sectors in total, and second are two sectors of lead-glass Čerenkov calorimeter (PbGl). The two different types of calorimeters have their advantages: the PbGl has finer granularity and better energy resolution, however, the PbSc has better linearity and better understood hadron response [169].

The basic properties of the EMCal are described in Tab. 2.2. Both of the sub-detectors, PbSc and PbGl, are required to have a wide dynamic range, from few hundred MeV up to 80 GeV. Energy scale uncertainty is the major contribution to the systematic error of a steeply falling cross section spectrum, thus the calorimeters are required to have less than 2% uncertainty in the absolute energy scale. The high multiplicity of the heavy ion collision demands very fine granularity about $\Delta\eta \times \Delta\phi \approx 0.01 \times 0.01$ to achieve less than 20% occupancy in a central Au+Au collision at $\sqrt{s_{NN}}$ = 200 GeV. In the following two sections, both sub-detectors are described in greater detail.

2.3.1 Lead-Scintillator Calorimeter

The PbSc electromagnetic calorimeter is a shashlik type [170, 171] sampling calorimeter made of alternating tiles of lead and scintillator, see in Fig. 2.2. Each tower contains

66 layers of lead and scintillator with a thickness of 1.5 mm and 4 mm, respectively. Four towers are mechanically combined which creates the basic building block of the PbSc module. The scintillator is made of Polystyrene (1.5 % PT/0.01 % POPOP). The edges of the tiles are plated with Al. The 66 layers in a tower are optically connected using the 36 longitudinally penetrating wavelength shifting fibers for light collection. The collected light is coupled in the backplane to 30 mmϕ FEU115M phototubes [172].

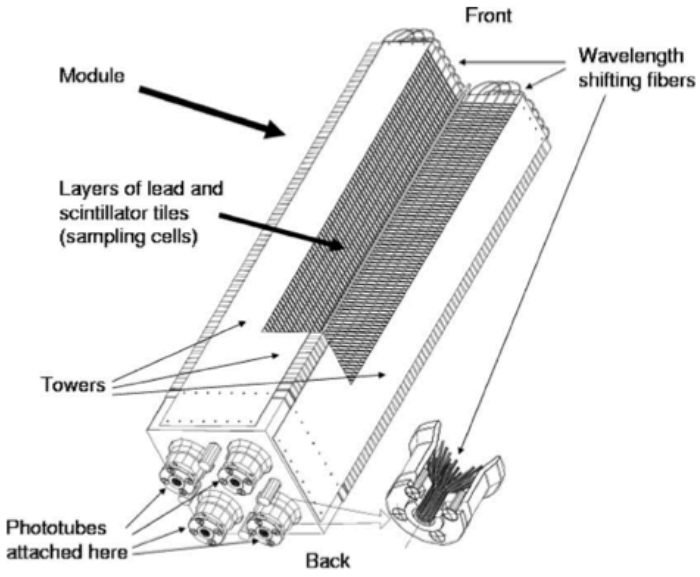

Figure 2.2: Interior view of the Lead-Scintillator Calorimeter (PbSc) module showing a stack of scintillator and lead plates, wavelength shifting fiber readout and leaky fiber inserted in the center hole.

The calibration and monitoring system [173] is based on a UV laser which supplies light to the calorimeter through a series of optical splitters and fibers. The YAG-laser light is split in 3 steps and delivered into 3888 modules in total. The laser amplitude is monitored by a phototube at emission and photodiodes in all the light splitters. The laser calibration system is established to normalize the initial energy calibration, which has been obtained by utilizing cosmic ray for all towers during construction. The gain of the amplifiers for the photodiodes is monitored by test pulses.

The calorimeter performance was tested at CERN and BNL beam facilities [174, 175] with a well calibrated electron-positron beam, see Fig. 2.3. The energy resolution could be fitted with a linear or quadratic functions. The obtained fits are:

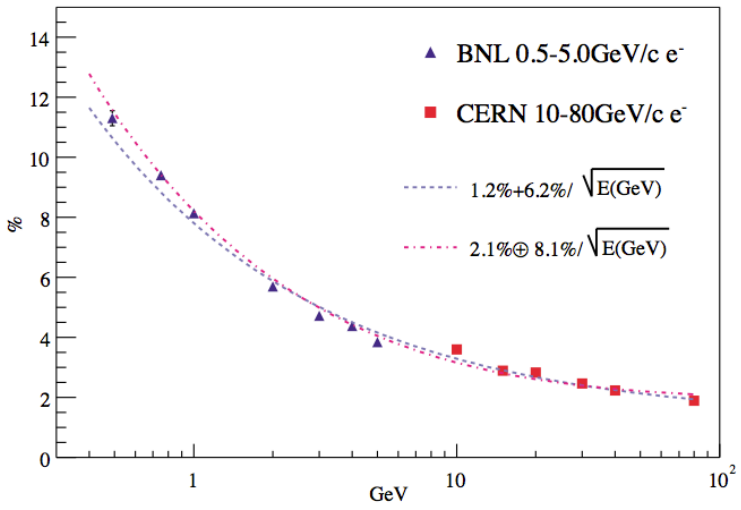

Figure 2.3: Lead-Scintillator (PbSc) energy resolution obtained by beam tests at CERN (red markers) and BNL (blue markers) [174]. The dashed line shows a linear formula $\sigma(E)/E = 1.2\% + 6.2\%/\sqrt{E[\text{GeV}]}$. The dashed-dotted line shows the quadratic formula $\sigma(E)/E = 2.1\% \oplus 8.1\%/\sqrt{E[\text{GeV}]}$.

- energy resolution

$$\frac{\sigma(E\ [\text{GeV}])}{E\ [\text{GeV}]} = 1.2\% + \frac{6.2\%}{\sqrt{E\ [\text{GeV}]}}(\text{linear}), \text{and} \tag{2.5}$$

$$= 2.1\% \oplus \frac{8.1\%}{\sqrt{E\ [GeV]}}(\text{quadratic}), \tag{2.6}$$

- position resolution

$$\left.\frac{\sigma_x(E\ [\text{GeV}])}{E\ [\text{GeV}]}\right|_{\theta=0} = 1.4\ \text{mm} + \frac{5.9\ \text{mm}}{\sqrt{E\ [\text{GeV}]}}, \tag{2.7}$$

$$\sigma_x(\theta) = (20.0 \cdot \sin\theta) \oplus \sigma_x(\theta = 0) \tag{2.8}$$

where the $\oplus$ is defined as a square root of the quadratic sum, i.e. $a \oplus b = \sqrt{a^2 + b^2}$ and θ is the angle of an incoming particle with respect to the perpendicular axis from the surface of the calorimeter.

2.3.2 Lead-Glass Calorimeter

The Lead-Glass Calorimeter was previously used in the WA98 experiment [176] at CERN for the neutral meson and direct photon measurement [177]. The 9216 elements

were dismantled and transported to the BNL laboratory where they were reassembled into two sectors of the PHENIX EMCal. The PbGl is a Čerenkov type detector, where each crystal is made from 55% PbO and 45% SiO_2 with a refraction index of n=1.648. The electron-positron pairs in the electromagnetic shower produce a constant number of Čerenkov photons per unit length, and the total length of all electron and positron tracks in the shower is linearly dependent on the total energy of the incoming particle, therefore, the total light produced is directly proportional to the energy.

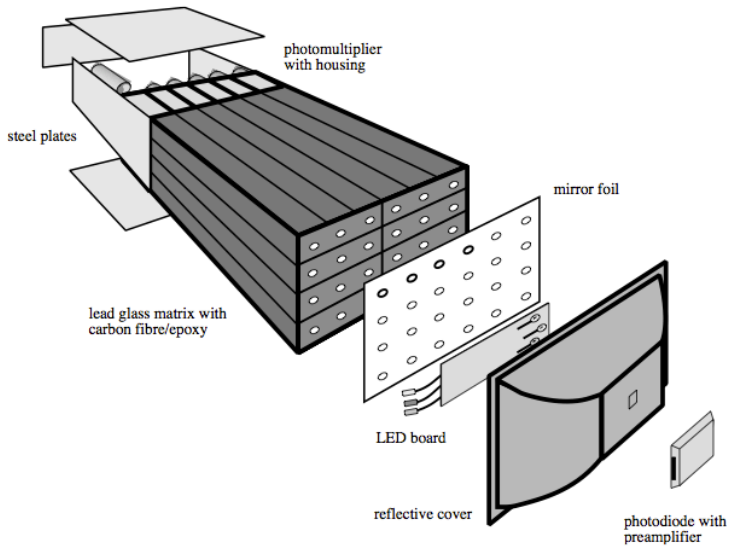

Figure 2.4: Interior view of the Lead-Glass Calorimeter (PbGl) module.

The PbGl element, in Fig. 2.4, with dimensions $4 \times 4 \times 40$ cm^3 are wrapped into a reflecting mylar foil and connected together into a full sector. A LED in front of each 24 towers creates a reference light measured by the PMTs in the back of the towers. The PbGl performance was measured in both CERN and BNL test beam facilities. The parametrization of the test beam results are summarized as

- energy resolution

$$\frac{\sigma(E\ [\text{GeV}])}{E\ [\text{GeV}]} = \frac{5.9\%}{\sqrt{E\ [\text{GeV}]}} \oplus 0.8\% \tag{2.9}$$

- position resolution

$$\frac{\sigma_x(E\ [\text{GeV}])}{E\ [\text{GeV}]} = \frac{5.9\ \text{mm}}{\sqrt{E\ [\text{GeV}]}} \oplus 0.2\ \text{mm} \tag{2.10}$$

2.4 Photon measurement with EMCal

The Moliere radius of the calorimeter (see Tab. 2.2) is the characteristic radius of the electromagnetic shower where 90% of the energy is contained. The tower sizes are comparable to the Moliere radius of the calorimeters. In the offline data reconstruction, individual towers are combined into clusters to reconstruct the full energy of the incoming particle. A noise threshold of 10 MeV is applied for every tower. The neighboring towers which share the same edges are combined into so-called isolated clusters. These isolated clusters contain hits for one or more particles thus further checks are required.

Identification of local maxima in an isolated cluster suggests multiple particles participating in the energy deposit. The requirements for the local maxima is that 1) it has to be the maximum energy in 3×3 tower area and 2) the energy in the center tower has to be more than 80 MeV. The cluster is splitted according to local maxima. The energy is shared according to the amplitude and the position of the local maxima using a simulated shower profile of an electromagnetic shower described in next section.

2.4.1 Cluster energy measurement

The study of the development of the electromagnetic shower in the EMCal was done in the beam tests. The beam consisted of precisely calibrated electrons and positrons. Using the electron and positron beam a parametrization of the energy deposits in towers was obtained with the empirical formula [178]:

$$\frac{E_i^{\rm pred}}{E_{\rm all}^{\rm meas}} = p_1\left(E_{\rm all}^{\rm meas},\theta\right)\cdot\exp\left(-\frac{(r_i/r_0)^3}{p_2(E_{\rm all}^{\rm meas},\theta)}\right) + p_3(E_{\rm all}^{\rm meas},\theta)\cdot\exp\left(-\frac{(r_i/r_0)}{p_4(E_{\rm all}^{\rm meas},\theta)}\right), \tag{2.11}$$

where the $E_i^{\rm pred}$ is the expected energy deposit in the tower caused by the incoming particle of measured energy $E_{\rm all}$ with impact angle of θ, the angle between the perpendicular axis from the surface of the detector and the incoming particle. The r_i is the distance of the ith tower center from the center of mass of the cluster (discussed in next section) and r_0 is the size of a single tower, see in Tab. 2.2. The parameters $p_i(E,\theta)$ are obtained from fits to the shower development using the test beam results as

$$\begin{aligned}
p_1(E,\theta) &= 0.59 - (1.45 + 0.13\ln E)\sin^2\theta, && (2.12)\\
p_2(E,\theta) &= 0.26 + (0.80 + 0.32\ln E)\sin^2\theta, && (2.13)\\
p_3(E,\theta) &= 0.25 + (1.45 - 0.36\ln E)\sin^2\theta, && (2.14)\\
p_4(E,\theta) &= 0.42. && (2.15)
\end{aligned}$$

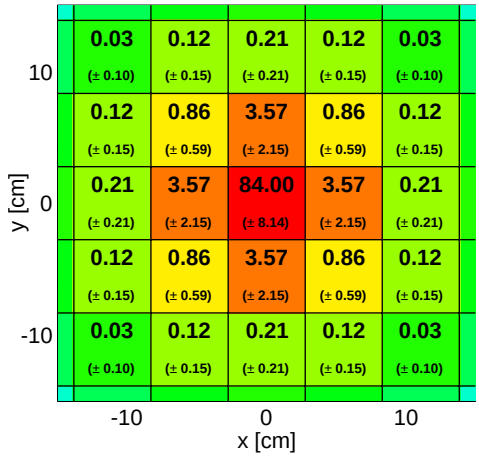

Figure 2.5: The fraction of deposited energy in each tower of the Lead-Scintillator by the electromagnetic shower with an impact point in $(0, 0)$cm and with no impact angle ($\theta = 0$). Each cell corresponds to one tower. The upper number in each cell represents the fraction (% from Eq. (2.11)) of the total deposited energy and the lower numbers represent the fluctuations (Eq. (2.16), with $E_{total} = 10$ GeV).

Fig. 2.5 shows an example of the energy deposits in towers with orthogonal impact at the center of a tower. Thus, the shower is developed symmetrically around the impact point. The first term of Eq. (2.11) describes a shower profile which is dominant at small distances from the impact point ($d \ll 5$ cm), while the second part describes an exponential behavior which becomes dominant over the large distances. However, the development of the shower is not unique, hence the fluctuations were studied in the beam test. The width and depth of the shower depends on the energy of the incoming particle. The non-zero impact angle of the particle results in the shift of the larger energy deposits from the impact point. The shape of the shower is distorted due to its energy and impact angle which is parametrized as $f(E, \theta) = (4./0.03)\sqrt{E}\sin^4\theta$. Due to threshold used in the clustering algorithm, the total energy of the cluster is biased as $q(E) = 0.005^2 + 0.0014^2 E^2$ [GeV^2]. In summary, the fluctuation of the energy deposits in the showers are described as

$$\sigma_i^2 = q(E_{\text{all}}^{\text{meas}}) + C E_i^{\text{pred}} \cdot \left(1 - \frac{E_i^{\text{pred}}}{E_{\text{all}}^{\text{meas}}} + f(E_{\text{all}}^{\text{meas}}, \theta)\left(1 - \frac{E_i^{\text{pred}}}{E_{\text{all}}^{\text{meas}}}\right)\right), \qquad (2.16)$$

where $C = 0.03$ GeV is the scale of energy fluctuation obtained during the test beam. The obtained parametrization of the electromagnetic showers are later used also in the identification process, too.

2.4.2 Cluster position measurement

The reconstruction of the correct position of the incoming particle is essential in the reconstruction of the neutral pions via the invariant mass at higher p_T from two photons decays (see Eq. (A.12)). The position measurement of the center of the cluster is also limited by the granularity, see Tab. 2.2. To take the center of the tower with the most deposited energy in the cluster is not sufficient for the analysis. One approach to get more the accurate position of the cluster is to calculate the center of gravity as

$$(x,y)_{\text{cent}} = \frac{\sum\limits_{\text{cluster}} (x_i, y_i) E_i}{\sum\limits_{\text{cluster}} E_i}, \tag{2.17}$$

where E_i and (x_i, y_i) is the deposited energy and coordinates of the tower center of the ith tower in the cluster, respectively. Eq. (2.17) gives the resolution of the position measurement about 50% of the tower sizes ($\sim$ 2.5 cm in PbSc, $\sim$ 2 cm in PbGl). More precise position determination demonstrated in Fig. 2.6 [179] is achieved by changing the linear energy weights in Eq. (2.17) as

$$(x,y)_{\text{cent}} = \frac{\sum\limits_{\text{cluster}} (x_i, y_i) w_i}{\sum\limits_{\text{cluster}} w_i}, \quad \text{where} \quad w_i = \max\left(0, w_0 + \ln\left(\frac{E_i}{\sum E_i}\right)\right), \tag{2.18}$$

where w_i represents the new weight, with the free parameter w_0. The w_0 sets a threshold for the fraction of the total shower energy deposited in the tower, so that channels close to the noise level will not contribute. In the new weights, w_i, the logarithm enhances the contribution of the shower periphery to the coordinate measurement. At larger distances from the center, the logarithmic energy deposit dependence is more linear as function of the distance. This linear behavior originates from the second term of the Eq. (2.11), which is dominant for larger distances. The optimal value of w_0 was found $\sim$ 3.0 to 4.0 for energies from $E = 0.5$ to 8.0 GeV. Fig. 2.6 shows how the logarithmic weight enhances the position resolution [179].

The acquired position is further corrected by the angle of the incoming particle, assuming it is a photon. Parametrization of the shower center-of-gravity in tower coordinates is [180]:

$$(x,y)_{\text{cent}} = \frac{1}{2} \frac{\sinh\left(\left[(x,y)_{\text{imp}} + \Delta - \delta\right]/b\right)}{\sinh\left(1/2b\right)} + \delta, \tag{2.19}$$

$$|(x,y)_{\text{imp}} + \Delta + \delta| \leq \frac{1}{2}, \tag{2.20}$$

where $(x,y)_{\text{imp}}$ is the impact point of the particle, b is the shower cross-sectional width, Δ is the mean displacement of the calculated shower center-of-gravity from the impact

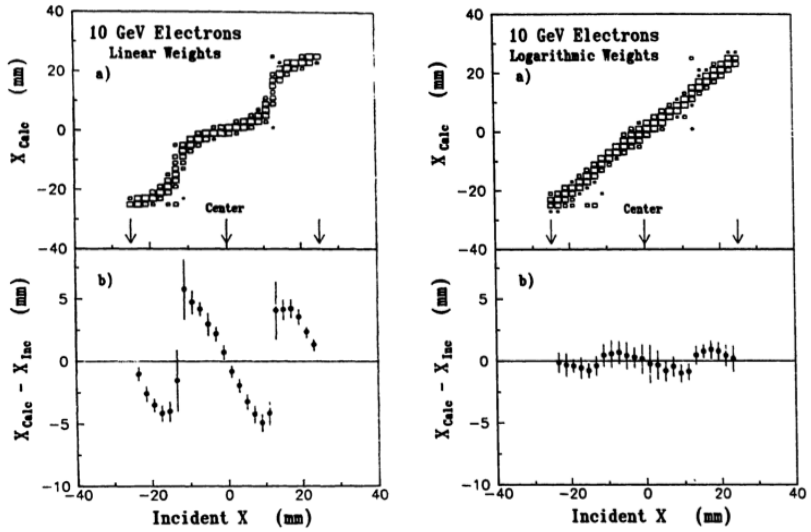

Figure 2.6: Position measurement [179] of electron in EMCal using the Eq. (2.17) in left panels and Eq. (2.18) in right panels. The upper panels are the calculated positions as a function of the impact (incident) on event by event basis. The lower panels show average of the difference of the calculated position from the incident position as a function of the incident position.

point $(x, y)_{\text{imp}}$ and δ is the phase shift related to the skewed shape of the shower projection. Using the parametrization of the electromagnetic shower in Eq. (2.11), the real impact parameter can be calculated by inverting the Eq. (2.19) and Eq. (2.20):

$$(x, y)_{\text{imp}} = b \cdot \sinh^{-1}\left[2((x, y)_{\text{cent}} - \delta)\sinh\left(1/2b\right)\right] - \Delta + \delta, \tag{2.21}$$

$$|(x, y)_{\text{cent}} - \delta| \leq \frac{1}{2}, \tag{2.22}$$

where the $\Delta = L_{\text{eff}} \sin(\theta)$, L_{eff} is the effective shower penetration in the calorimeter as determined by the position of the cascade-curve median in the longitudinal direction and θ the angle of the incoming particle. Furthermore, the b is given as $b = b_0 + b_1(E)\sin^2\theta$, where $b_0 \approx 7.3$ mm is the average width of a 1 GeV electromagnetic shower for $\theta = 0^\circ$ and $b_1 \propto \ln(E)$. Parameter δ is found to be essentially energy-independent and can be parameterized as a function of the impact angle only.

2.4.3 Photon identification

While neutral pion can be measured even without any particle identification (apart from the reconstructed invariant mass of the decay photons), photon identification of the clusters helps in the measurements to reduce the background caused by other

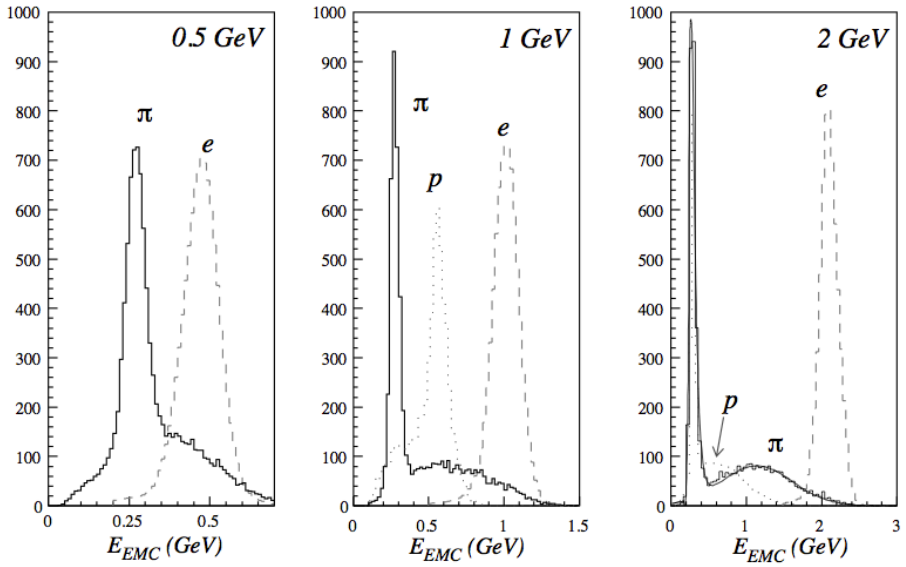

Figure 2.7: The energy spectra measured in the PHENIX EMCal with the test beam at BNL [175] when exposed to electrons, pions and protons of $p = 0.5,\ 1.0$ and 2.0 GeV/c.

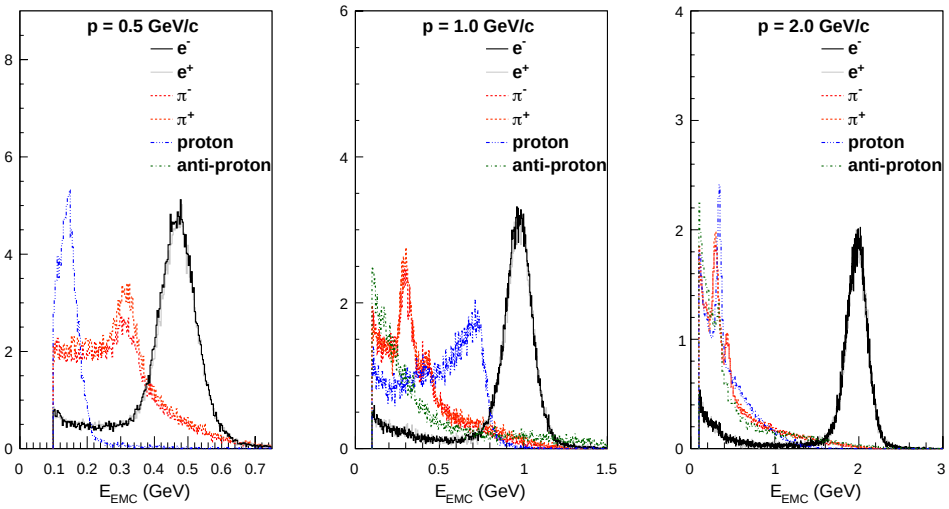

Figure 2.8: Simulated energy spectrum of electrons (positrons), pions and (anti)-protons of $p = 0.5,\ 1.0$ and 2.0 GeV/c in the PHENIX EMCal. Every primary and secondary cluster with the energy deposit larger than 0.1 GeV was used in the reconstruction.

particles, such as hadrons which leave part of their energy in the EMCal. In this section, we study the response of the EMCal when exposed to different particle spieces. We

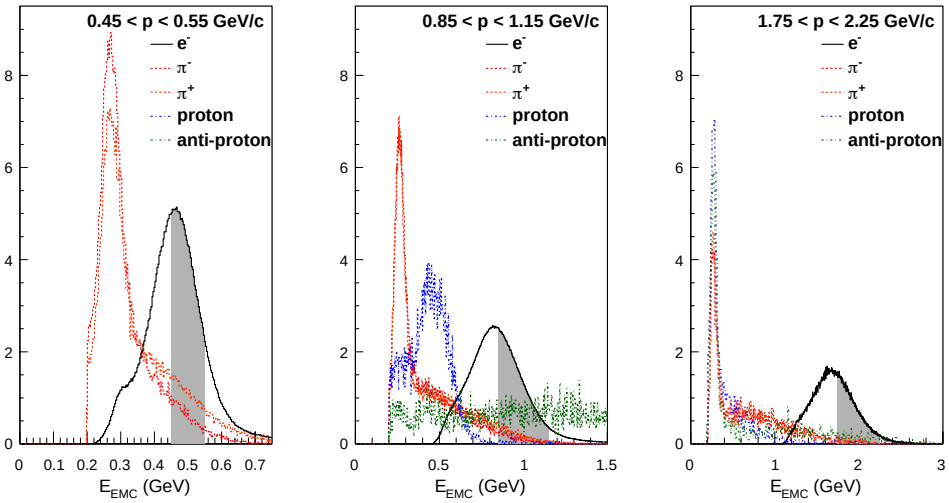

Figure 2.9: Particle response in PHENIX EMCal in real data, Au+Au collisions at $\sqrt{s_{NN}} = 200$ GeV. The identified particles are electrons, pions and (anti)-protons in three wider momentum bins illustrated by the grey shade and quantified in top of the panels: $0.45 < p < 0.55$; $0.85 < p < 1.15$ and $1.75 < p < 2.25$ GeV/c. Note that the real particle spectrum in heavy ion collisions is a steeply falling function, thus the lower edge of the selected bin contains more particles. Identification of the particles was done with different detectors, pions and protons with TOF and electrons with RICH. Only clusters with $E \geq 0.2$ GeV are considered.

divide the study into three major groups: 1) test-beam results, 2) simulated particles embedded into the real events and 3) real data taking period in Au+Au collisions. The details of the simulation procedure are discussed later in Sec. 3.3.

The first test of particle response functions were done with a precisely calibrated test beam of well defined particle composition. During the beam tests, EMCal used a different readout electronics with much lower noise level compared to those implemented in the real PHENIX experiment. In addition, the EMCal was exposed to a single particle species in the beam, and the energy was obtained by summing up the energies in 3x3 or 5x5 tower areas. Thus the test beam results describe the particle responses without the clusterization artifacts, the high multiplicity environment or the noise level in the readout electronics. The results are summarized in Fig. 2.7, where the electrons deposits their full energy smeared by the finite resolution of the calorimeter. The hadrons, protons and pions, behave usually like minimum ionizing particles (MIP), deposit a small amount of their energy, contribute mostly in the low-E_{EMC} part ($E_{EMC} < 0.2 - 0.4$ GeV) of the spectrum.

The second test was done with a single particle simulation at certain p_T with a realistic occupancy in the detector. The particles were simulated in the PHENIX de-

tector taking into account realistic material budget in front of the EMCal. All clusters with even a partial deposited energy from the simulated particles were considered in Fig. 2.8. The difference from the test beam results are due to the high multiplicity in the Au+Au collisions which results in the overlap of the individual clusters. The noise level of the electronics is included in the simulation. The clusterization algorithm is able to identify most of the energy from electromagnetic showers.

The final test was done during the data taking in Au+Au collisions in low multiplicity events, to minimize the accidental overlaps. The protons, antiprotons and charged pions ($\pi^{\pm}$) were identified in the TOF detector. The electrons were identified with help of the RICH detector. The particle tracks were identified in DC and PC detectors and projected onto the EMCal, and the matching cluster (with cut-off $E_{\text{cluster}} \geq 0.2$ GeV) was considered. Due to the limited statistics of the data taking period, the particles were chosen from a wider p_T bin shown in Fig. 2.9. The measured inclusive p_T spectrum of the individual particles is a steeply falling function which results in more particles in the lower edge of the p_T bin.

The response of different particles in EMCal shows a significant energy deposits by hadrons in the region where the electromagnetic shower (electrons) deposits its energy, see in Fig. 2.7, Fig. 2.8, Fig. 2.9. However, the shower developed by the hadrons is distinguishable from electromagnetic showers. The shower shape analysis (cuts) of the clusters reflects the probability the deposited energy was made by electromagnetic showers. The cuts are based on the assumption that the geometry of electromagnetic showers differs from hadronic showers. The χ^2 cut is defined as

$$\chi^2 = \sum_i \frac{\left(E_i^{\text{meas}} - E_i^{\text{pred}}\right)^2}{\sigma_i^2}, \tag{2.23}$$

where the E_i^{meas} and E_i^{pred} is the measured and predicted (from Eq. (2.11) of a total energy, $E_{\text{total}} = \sum_i E_i^{\text{meas}}$) deposits in ith tower and the σ_i is the predicted energy fluctuation of the electromagnetic shower. Fig. 2.10 shows the χ^2 distribution for electrons and pions at $p = 2$ GeV/c. The default $\chi^2 < 3$ cut is set to be 90% efficient for electrons as in Fig. 2.10, while at the same time it has about 20-30% efficiency for pions, protons and kaons (see also Fig. 2.11).

The more specific "stochastic" photon identification was developed in order to improve the threshold on identification of photon clusters. Instead of applying binary (yes/no type) shower shape descriptors, a mathematical expression is found from a combination of those descriptors, and the cut is applied on this mathematical formula. The advantage of the stochastic cut is that the shower can pass the combination of the different cuts (descriptors), even when one individual descriptor fails. The stochastic cut increases the probability that the cluster originates from photons or electrons and simultaneously rejects hadron clusters. The shower-shape analysis of the cluster includes the energy deposited in center tower compared to full energy of the cluster in

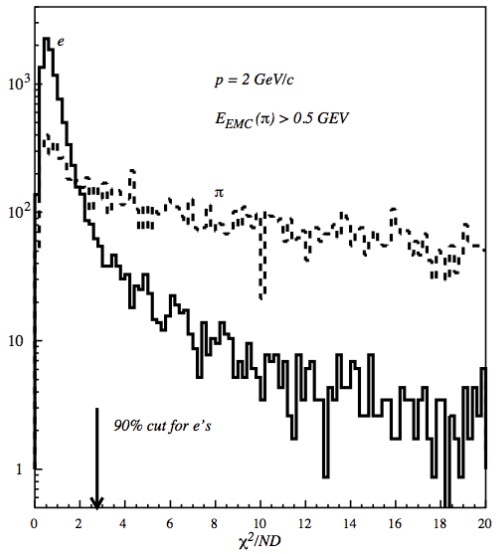

Figure 2.10: χ^2 distribution for showers induced by $p = 2$ GeV/c electrons and pions in the PbSc.

order to assure the deposited energy is by electromagnetic shower.

Development of the stochastic cut was done by using a GEANT simulation to study the responses of the detector. Four different "stochastic" cuts were developed as

$$\begin{aligned}
\text{stoch}_1 &= (0.3 + 4\exp(-E_{\text{all}}/E_{\text{cent}})) \cdot \left(1.9 - 0.67\chi^2\right) \\
&\quad \cdot (1.0 - \exp(-8\text{padisp}(1)/\text{padisp}(0))) > 1.4 \qquad (2.24) \\
\text{stoch}_2 &= (0.3 + 4\exp(-E_{\text{all}}/E_{\text{cent}})) \cdot \left(1.9 - 0.67\chi^2\right) > 1.4 \qquad (2.25) \\
\text{stoch}_3 &= (0.3 + 4\exp(-E_{\text{all}}/E_{\text{cent}})) \cdot \left(1.9 - 0.67\chi^2/\text{twrhit}\right) \\
&\quad \cdot (1.0 - \exp(-8\text{padisp}(1)/\text{padisp}(0))) > 1.4 \qquad (2.26) \\
\text{stoch}_4 &= (0.3 + 4\exp(-E_{\text{all}}/E_{\text{cent}})) \cdot \left(1.9 - 0.67\chi^2\right) > 1.4 \qquad (2.27)
\end{aligned}$$

where the E_{all} and E_{cent} are the total energy of the cluster and the energy deposit in the center tower, padisp() are the dispersions along the principal axis of the shower, twrhit is the number of towers in the cluster. The constants in the equations are obtained empirically to insure the highest likelihood to identify the electromagnetic cluster and simultaneously reject much background as possible.

Both the $\chi^2 < 3$ and stoch_2 cuts of the photon identifications are used in this thesis. The effect of the identification on cluster is studied with the simulations. Fig. 2.11 shows the cluster energy distribution caused by different particles distributed uniformly in momentum bin of $0 < p_T < 20$ GeV/c. Electromagnetic clusters are developed from e^+, e^- and γ and have similar energy as the original particle p_T. However, curves

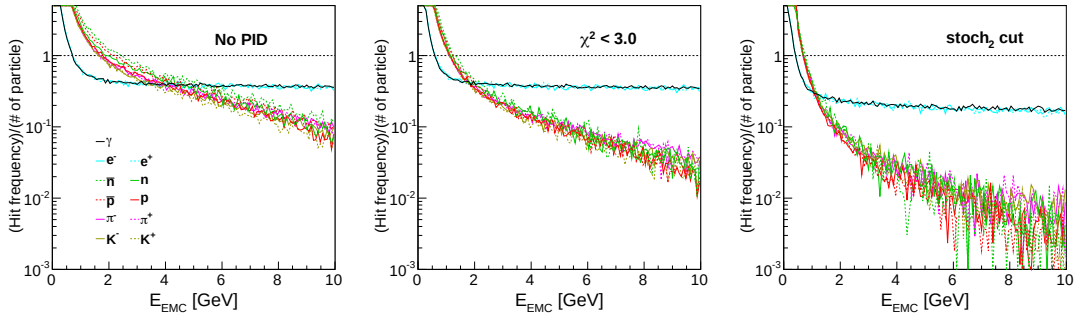

Figure 2.11: Cluster energy distribution from different particles passing different identification methods: without PID in left panel, $\chi^2 < 3$ in middle panel and stoch$_2$ in right panel. The cluster energy does not necessary reflect the total transverse momentum of the particles. The particles were generated uniformly in $|\eta| < 0.5$ and in 2π in azumuth in $0 < p_T < 20$ GeV/c, thus, not all particles are in the acceptance region.

corresponding to hadrons (protons $(p, \bar{p})$, neutrons $(n, \bar{n})$, π^+, π^-, K^+, K^-) show large amount of energy are deposited in low-energy clusters, since the hadrons are usually minimum ionizing particles or they do not deposit their full energy in the EMCal. Fig. 2.11 shows how the different PID cuts reduce the hadron contributions.

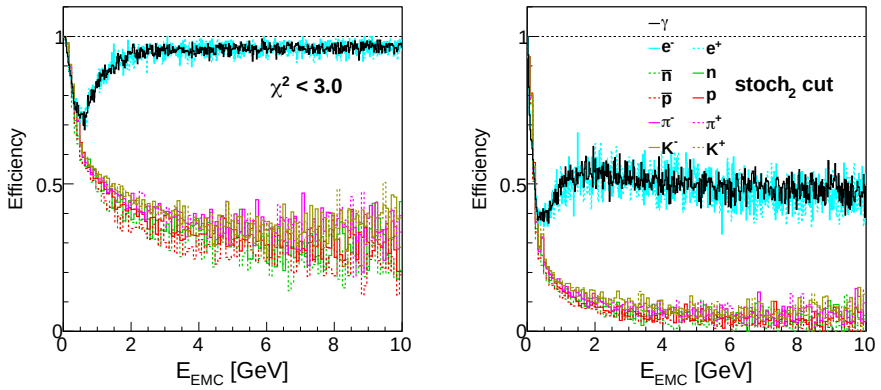

Figure 2.12: Cluster reconstruction efficiency as a function of deposited energy ($\varepsilon(E_{\rm EMC}) = N_{\rm PID}/N_{\rm noPID}$) for different particles using different PID cuts, $\chi^2 < 3.0$ in left panel and stoch$_2$ in right panel.

Fig. 2.12 shows efficiency of different identification cuts, defined as $\varepsilon(E_{\rm EMC}) = N_{PID}/N_{noPID}$, where N_{PID} is the number of cluster passing the identification cut, N_{noPID} is the number of all clusters. The χ^2 photons identification is over 90% efficient for the real electromagnetic clusters, the stoch$_2$ cuts are only 50% efficient for the same clusters. The neutral pion analysis is a correlation analysis (reconstruction of the

particles via 2γ decay channels), thus it can tolerate higher background from hadrons. However, the hadron contamination is much less when using the stoch_2 cuts, thus it is used for the direct photon analysis, for the reason that in this analysis is crucial to subtract as much background as possible.

Chapter 3

Run Conditions

3.1 General Information

In 2010, RHIC started the Au+Au low energy program and provided collisions from 19th March, 2010 to 8th April, 2010 at $\sqrt{s_{NN}} = 62.4$ GeV and between 9th April, 2010 - 22nd April, 2010 at $\sqrt{s_{NN}} = 39$ GeV. The trigger for these runs was set by the BBC detector, requiring at least one hit in both north and south side BBC (BBCNS ≥ 1) and the vertex to be within $|z_{\rm vtx}| < 38$ cm. Total number of events with the above trigger conditions are 700M at $\sqrt{s_{NN}} = 62.4$ GeV and 250M at $\sqrt{s_{NN}} = 39$ GeV. The integrated luminosity of the recorded events reached 0.11 nb^{-1} and 40 μb^{-1} for 62.4 and 39 GeV energies, respectively.

Fig. 3.1 left panel shows the event vertex distribution measured by the BBC detector. The data analysis is done only for events with a vertex cut $z_{\rm vtx} < 30$ cm. Particles from vertices further away can interfere with the central magnet (partially blocked, extra conversion,...) and generate a false signal for the data analysis. The offline requirement of trigger for the analysis was $BBC(N, S) \geq 2$, two or more hits in each side of the BBC, in order to reduce the background by $\sim 20\%$, which further reduces the trigger efficiency. The BBC efficiency was determined using the negative binomial fit method (NBD-fit method) [181]. The obtained minimum bias trigger efficiencies for the analysis are $85.9 \pm 2\%$ at $\sqrt{s_{NN}} = 39$ GeV and $85.7 \pm 2\%$ at $\sqrt{s_{NN}} = 62.4$ GeV with both statistical and systematical uncertainties.

The obtained multiplicity distribution of gamma clusters in the EMCal is shown in Fig. 3.1 right. The multiplicity is larger in higher energy collision at $\sqrt{s_{NN}} = 62.4$ GeV compared to $\sqrt{s_{NN}} = 39$ GeV and the highest multiplicities are achieved in central events when the impact parameter of the colliding nuclei is small.

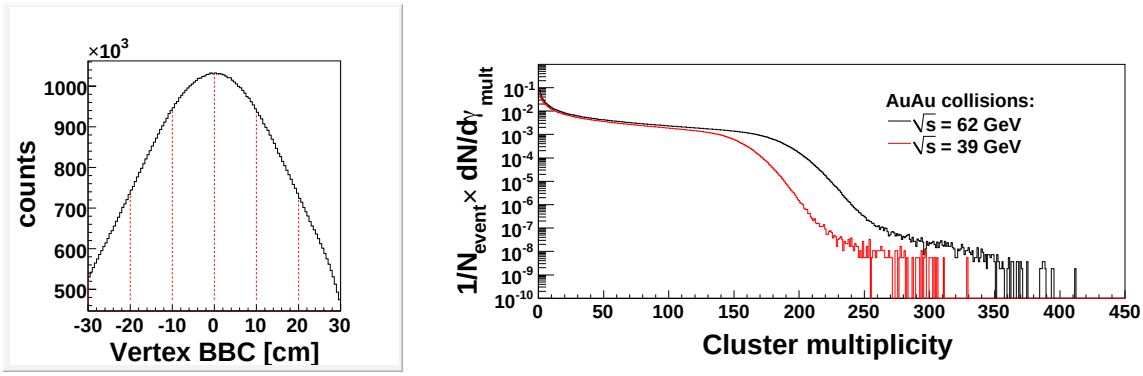

Figure 3.1: Left: vertex distribution in Au+Au collisions at $\sqrt{s_{NN}}$ = 39 GeV. Vertical lines separate vertex bins considered in event mixing. Right: EMCAL cluster multiplicity distribution in Au+Au collisions at $\sqrt{s_{NN}}$ = 62.4 and 39 GeV.

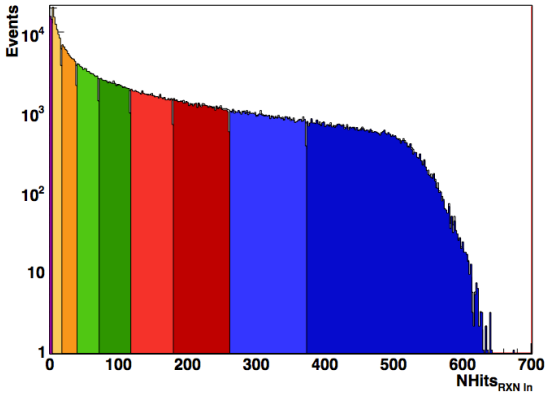

Figure 3.2: Hit distribution in Au+Au collisions at $\sqrt{s_{NN}}$ = 62.4 GeV in the inner Reaction Plane Detector (RXNin, $1.5 < |\eta| < 2.8$). The distribution is divided into 10% centrality bins between 0-86%.

3.1.1 Centrality classes

The events recorded by the minimum bias trigger are further assigned to centrality classes. The centrality is usually determined by the energy measured by ZDC and total charge multiplicity obtained by BBC detectors. As already described in Sec. 2.2.1, the same method cannot be used for the low energy collisions. Instead, the charge distribution of the inner part of the Reaction Plane Detector (RXNin, $1.5 < |\eta| < 2.8$) was used as shown in Fig. 3.2. The RXNin hit distribution is further divided into 5 separate centrality classes in both $\sqrt{s_{NN}}$ = 39 GeV and 62.4 GeV collision, as shown in Fig. 3.3.

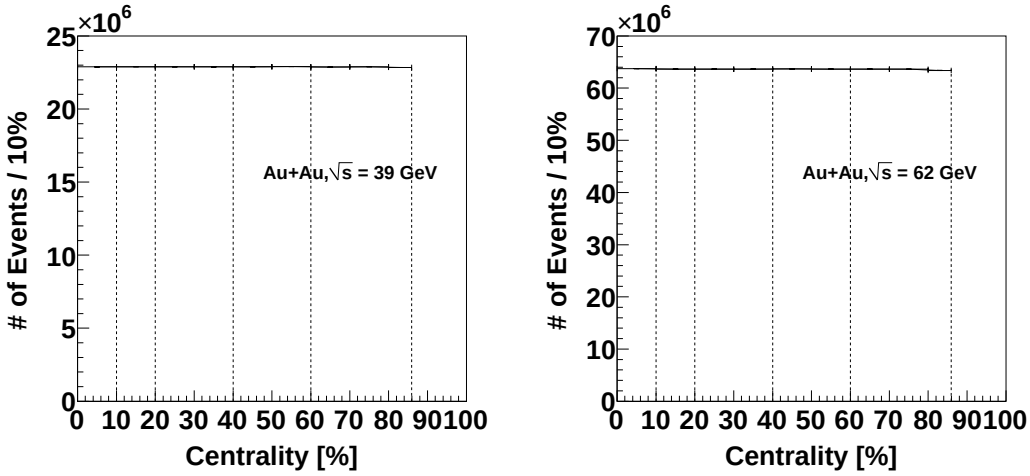

Figure 3.3: The event distribution corresponding to chosen centrality classes in Au+Au collisions at $\sqrt{s_{NN}} = 39$ GeV (left) and at $\sqrt{s_{NN}} = 62.4$ GeV (right). The distributions are divided into 5 different centrality classes, while the number of events are normalized by the centrality bin width (10%).

3.1.2 Glauber Model and Glauber Monte Carlo

The particle production at sufficiently high-p_T is dominated by the pQCD processes. In the heavy ion collisions, the probability of the hard scatterings is increased due to the large number of nucleons. The purpose of the Glauber Model [146] is to describe the geometrical properties of the heavy ion collision, see in Sec. 1.2.3. Glauber Model relates to quantities as the impact parameter b, $\langle N_{\rm part}\rangle$ and $\langle N_{\rm coll}\rangle$ the number of participants and number of binary collisions, respectively. There are two different approaches to calculate the geometry: (1) optical Glauber Model [182] and (2) Glauber Monte Carlo [92]. The overlapping functions of the nuclei are calculated analytically in the optical approach and by randomizing discrete nucleons in the Monte Carlo approach.

The Glauber Model provides simple way to describe a high-energy heavy ion collision. The model does not describe the dynamics of the collision, thus there are limitations of its use. The model calculates the thickness of nuclear matter in direct path of each incoming nucleon and uses the nucleon-nucleon inelastic cross section ($\sigma_{NN}^{\rm inel}$) to decide whether a nucleon-nucleon collision occurred.

The basic assumption of the Glauber Model is that the nucleons follow a realistic density distribution, using the Woods–Saxon density profile:

$$\rho(r) = 1/\left(1 + \exp\left((r - r_n)/d\right)\right),$$

where $r_n = 1.19A^{1/3} - 1.61A^{-1/3} = 6.55$ fm is the Woods–Saxon radius of the Au

nucleus ($A = 197$) and $d = 0.54$ is the diffuseness parameter. The Glauber Monte Carlo distributes the nucleons in both nuclei according to the density profile in every event. The individual nucleon-nucleon cross sections depend on the collision energies: $\sigma_{NN}(\sqrt{s_{NN}} = 200\,\text{GeV}) = 40$ mb, $\sigma_{NN}(\sqrt{s_{NN}} = 62.4\,\text{GeV}) = 37$ mb and $\sigma_{NN}(\sqrt{s_{NN}} = 39.0\,\text{GeV}) = 34$ mb.

In the Glauber Monte Carlo simulation 100k events were generated with a uniform impact parameter distribution, b from 0 to $2r_n$. The number of participants (N_{part}) and binary collisions are calculated from the geometrical distribution of the nucleons: the collision is considered when the transverse distance (d) between two nucleon centers is less than the square root of the nucleon-nucleon cross section ($d < \sqrt{\sigma_{NN}/\pi}$). In average over large amount of events, the charged hadron multiplicity has monotonic relation with the number of participants, in form as $dN_{\text{ch}}/d\eta = C_1 N_{\text{part}}^{\alpha}$ where C_1 and α are constant parameters. In this study we consider the charged hadron multiplicities measured in PC1, PC3 and RXN detectors.

The mean impact paramter $\langle b \rangle$, $\langle N_{\text{part}} \rangle$ and $\langle N_{\text{coll}} \rangle$ and $\langle T_{\text{AA}} \rangle$ is determined for each centrality class, see in Tab. 3.1. The systematic error of the average geometrical quantities is studied by:

- Variation of the inelastic scattering cross section: $\sigma_{NN}(\sqrt{s_{NN}} = 39\ \text{GeV}) = 31 - 37$ mb and $\sigma_{NN}(\sqrt{s_{NN}} = 62.4\ \text{GeV}) = 34 - 40$ mb.
- Variation of the Woods–Saxon Radius and diffusiveness: $(r_n, d) = (6.25\,\text{fm}, 0.53\,\text{fm})$ and $(6.65\,\text{fm}, 0.55\,\text{fm})$.
- Trigger efficiency uncertainty: varying the trigger efficiency within their statistical and systematic errors, $85.9 \pm 2\%$ at $\sqrt{s_{NN}} = 39$ GeV and $85.7 \pm 2\%$ at $\sqrt{s_{NN}} = 62.4$ GeV.

	$\sqrt{s_{NN}} = 39$ GeV			$\sqrt{s_{NN}} = 62.4$ GeV		
Centrality	$\langle N_{\text{coll}} \rangle$	$\langle N_{\text{part}} \rangle$	$\langle T_{AA} \rangle$	$\langle N_{\text{coll}} \rangle$	$\langle N_{\text{part}} \rangle$	$\langle T_{AA} \rangle$
0-10%	777.2	316.6	22.86	843.0	319.6	22.78
0-20%	496.7	227.2	14.61	535.8	229.7	14.48
0-40%	253.6	137.4	7.46	270.5	138.7	7.311
0-60%	81.81	59.33	2.40	85.71	59.74	2.316
60-85%	13.88	14.55	0.408	14.29	14.66	0.386

Table 3.1: The summary of the $\langle N_{\text{part}} \rangle$ and $\langle N_{\text{coll}} \rangle$ and $\langle T_{\text{AA}} \rangle$ parameters obtained from the Glauber Monte Carlo for Au+Au collisions at $\sqrt{s_{NN}} = 39$ and 62.4 GeV.

3.2 Dead, Hot and Warm Towers in EMcal

The channels which are not working properly in the EMCal distort the energy measurement when they are part of a cluster. Therefore, in the analysis is necessary to identify and remove those channels. The bad channels are divided into three categories: 1) Hot channels, where towers give unrealistically high hit rate, 2) Dead channels, when the channel give unrealistically low hit rate or do no count at all and finally 3) Warm channels, which usually produce high hit rate in certain energy bin only.

First, the hot and dead channels are identified as their rate deviate from the average value of the all channel hit rate distribution. Later, the warm channels are identified, which randomly produce ADC bit patterns which correspond to high energy deposit. Even if the average hit frequency of warm channels is not high, due to steeply falling spectrum of particles (e.g. photons) as a function of energy, the warm channels contribute un-physically high number of high-energy photon clusters. Furthermore, the certain bit pattern of the warm channel gives high contribution only in certain energy bin of the cluster, otherwise there is no visible deviation from other channels. The average hit distribution is plotted separately in bins of energy ($\Delta E \sim 1-2$ GeV) in order to identify all the remaining warm channels. Additional check of the remaining hot and warm channels was made by reconstructing the invariant mass of cluster-pair distribution: $M_{\text{clusterpair}} = \sqrt{2E_{\text{clus1}}E_{\text{clus2}}(1-\cos\theta)}$ (see also Eq. (A.12)). The warm channels create fake, unphysical, peaks in the invariant mass distribution. Due to their fixed position in the EMCal geometry, the fake peak moves to different position in each cluster-pair energy bin ($E_{\text{clus1}} + E_{\text{clus2}}$), while real particles peaks (π^0, η) have fixed peak position.

All the hot, dead and warm channels are marked for removal when analyzing the data from the EMCal, see in Fig. 3.4 and Fig. 3.5. In the reconstruction of the energy deposit in the clusters, it is required to have an additional tower between the center tower of the cluster and the removed tower (see Fig. 2.5), so called fiducial cut. Otherwise, the cluster is not considered for the analysis. Note that the removal of the towers also effects the acceptance ($\sim 5-10\%$, depending on the sector).

3.3 Simulation process

The framework of the PHENIX simulation is well developed to be able to study different responses of the detectors. In this work, a single particle generator is used, to generate single π^0, η or single γ. The particles are generated in the EXODUS Monte Carlo which is a "home-made" single particle event generator. EXODUS allows a flexible choice of different characteristic distributions: e.g. momentum (p or p_T), pseudo-rapidity window (η), azimuthal distribution (ϕ), total energy of particle (E_{total}). The EXODUS allows to modify or enhance decay channels of the particles (changing the true branching ratio), and it is also possible to generate multiple particles per event

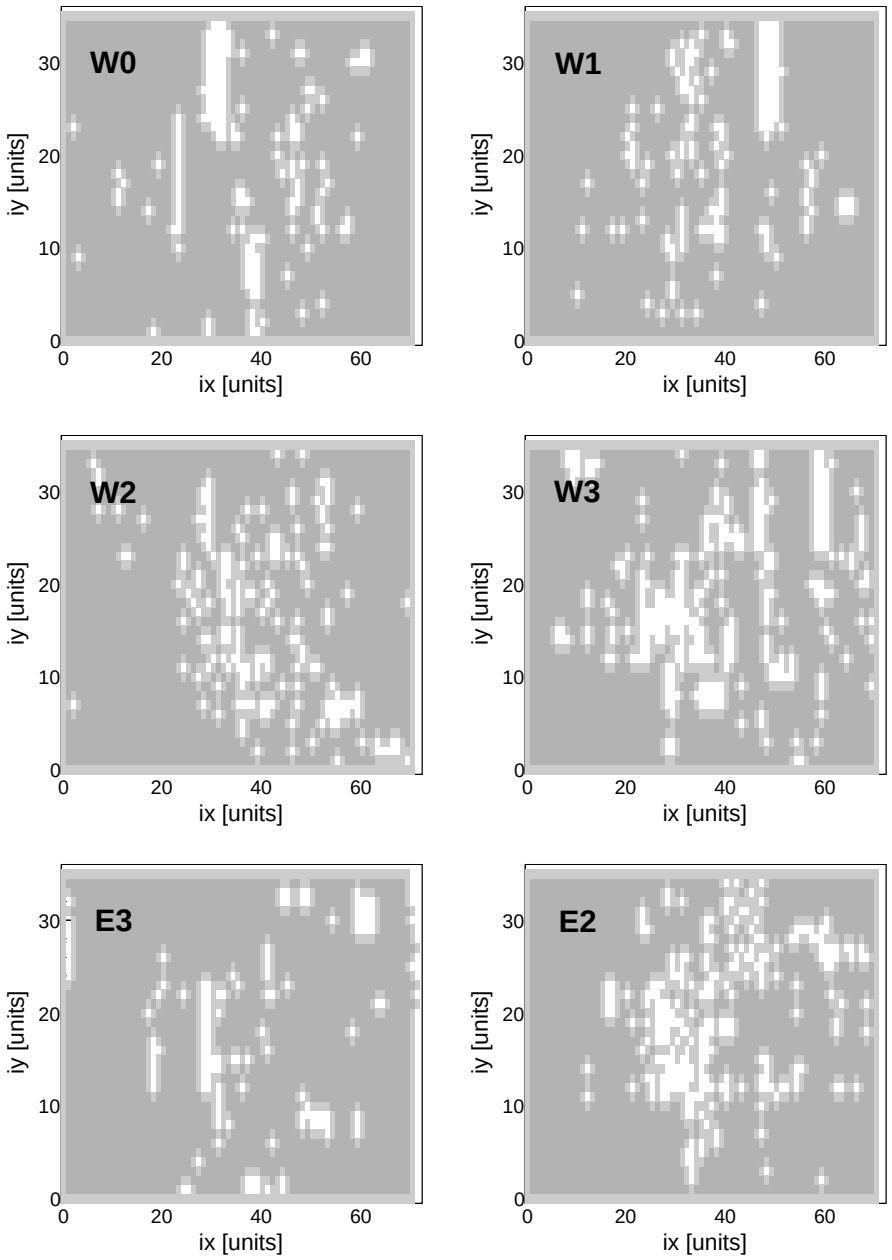

Figure 3.4: The tower map of the individual EMCal PbSc sectors. The white areas are the masked out channels, the dark areas are the healthy channels. The lighter areas between are the neighboring channels, which cannot contain the cluster center.

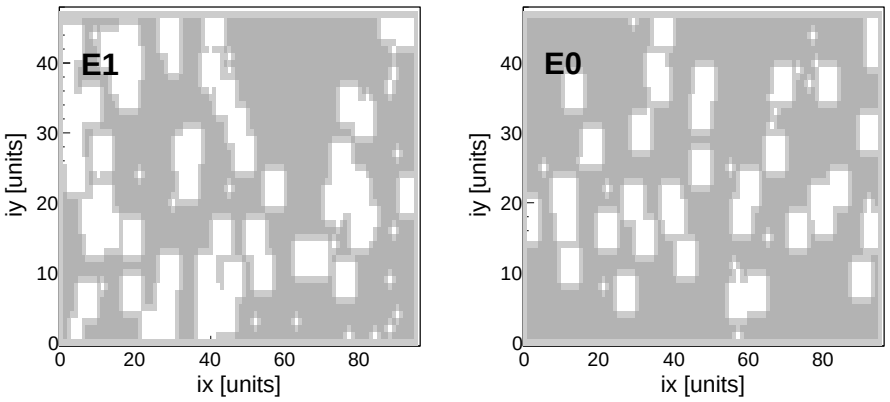

Figure 3.5: The tower map of the individual EMCal PbGl sectors. The white areas are the masked out channels, the dark areas are the healthy channels. The lighter areas between are the neighboring channels, which cannot contain the cluster center.

(particle cocktail).

The generated particles enter the PHENIX Integrated Simulation Application (PISA) framework [183] which generates realistic response of every detector available during the specific run. The geometry of every sub-detector, magnet and supporting material implemented in the GEANT3 [184] simulation to describe the real situation. The simulation results are stored in the same format as real data, Data Summary Tape (DST).

Output of the single particle (or particle cocktail) simulations are embedded into corresponding real Au+Au events at $\sqrt{s_{NN}}$ = 39 GeV or 62.4 GeV, requiring that the vertex in the simulation is not more than 5 cm away from the real event vertex. During the embedding procedure the simulated energy deposits are overlaid to real (underlying) event deposits. In each tower the deposited energies from simulated and real events are merged and the clusterization procedure is repeated on the merged deposits. This procedure allows us to study the reconstruction efficiency in real multiplicity environment.

In summary, the full procedure can divided into few simple steps:

- Generate single particles from EXODUS event generator. The four momentum of the particle with the particle ID is generated. The particle generator allows to change or enhance the decay modes of all particles.

- Insert single particles to the PHENIX Integrated Simulation Application (PISA) a full GEANT simulation of the PHENIX detector, and calculate the full detector response. Write out the simulation results in a normal (Data Summary Tape, DST) format, the same format is used for real data.

- Embed simulated DST into real DST. The energy deposits of towers are merged together. Rerun the clusterization algorithm on the new hit distribution.
- Write out every cluster which has a simulated energy deposit, again in the same form as the real data. In addition to the cluster information, the simulated particle properties are written out (such as original particle energy, production vertex, particle ID, ...).

The Monte Carlo method of the electromagnetic shower evolution are tuned to the real data. As first approximation, the test beam results were used. However, during the test beam the multiplicity of particles was lower than in the data taking period. The simulations were further tuned by using photon showers from data taking period, to be able to describe the real clusters as close as possible. The simulation results are also used to correct the raw data to detector efficiencies and acceptance.

Chapter 4

Measurement of π^0 at $\sqrt{s_{NN}} =$ 39 GeV and 62.4 GeV

In this section we describe the measurement of neutral pions (π^0) in the central arm of the PHENIX detector ($|y| < 0.35$) in Au+Au collisions at $\sqrt{s_{NN}} = 39$ GeV and 62.4 GeV in transverse-momentum p_T range $1 < p_T < 10$ GeV/c. The π^0 was reconstructed via the two photon decay channels (with the branching ratio of 98.82%). The inclusive production of π^0 was measured in different centrality bins and compared to corresponding p+p collision spectra.

4.1 Neutral Pion Reconstruction

The neutral pion decay kinematics is discussed in Sec. A.1.2. The neutral meson spectrum can be reconstructed from the invariant mass and momentum from the photon-pair:

$$M_{\gamma\gamma} = \sqrt{2E_1E_2 \times (1 - \cos\theta_L)}, \quad (4.1)$$

$$p_{\gamma\gamma} = E_1\mathbf{n}_1 + E_2\mathbf{n}_2, \quad (4.2)$$

where E_1 and E_2 are the photon energies, $\mathbf{n}_1$ and $\mathbf{n}_2$ are the unit vectors of the two clusters with respect to the interaction point and the θ_L is the opening angle ($\cos\theta_L = \angle\mathbf{n}_1\mathbf{n}_2$). In this analysis, we use the EMCal detector located at mid-rapidity ($|\eta| < 0.35$). Only the transverse momentum of the photon pair is considered, thus Eq. (4.2) is transformed to $p_T^{\gamma\gamma} = E_1\mathbf{n}_{T1} + E_2\mathbf{n}_{T2}$. In order to reduce the non-photonic clusters and the artifacts from the clusterization algorithm, only the clusters with higher than $E > 0.2$ GeV are considered. The minimum distance between the cluster centers has to be $d \geq 8$ cm, because of the finite tower size (PbSc, 5.25 cm). All the clusters are required to pass the $\chi^2 < 3.0$ cut, described by Eq. (2.23).

In order to reduce the background, further cuts are applied for the cluster pairs. For example, one high energy hit combined with lot of small energy clusters produces a

lot of combinatorial background. The asymmetry cut on the clusters, $\alpha < 0.8$ (see Eq. (A.11)), reduces the number of pairs with large energy differences. Both of the clusters of π^0 are required in the same sector to avoid the slightly different absolute calibrations in different sectors, and at the same time it reduces the combinatorial background. The cuts used in the analysis also reduce the systematic uncertainty of the measurement, as discussed later in Sec. 4.5.

All EMCal clusters passing the respective PID cut in a single event are used to reconstruct $M_{\gamma\gamma}$ in bins of the transverse momentum of the photon pair, $p_T^{\gamma\gamma}$. The π^0 mass peak is contaminated by uncorrelated background, which is significant especially at low-$p_T^{\gamma\gamma}$ bins. This uncorrelated, or "combinatorial" background comes from pairs that do not originate from the decay of the same π^0, and it is described and subtracted using "mixed event" technique. The method is based on reconstruction of uncorrelated photon clusters, where the two clusters are from two different events. It is important to note that the mixed events are chosen from similar centrality classes and vertex positions to reproduce similar shape of the combinatorial background as in real pairs. The signal to background ratio is increasing at higher p_T regions. The background is normalized and subtracted from the signal as

$$\frac{dN^{\pi^0}}{dM_{\gamma\gamma}} = \frac{dN^{Real}}{dM_{\gamma\gamma}} - \frac{dN^{Mixed}}{dM_{\gamma\gamma}} \times \frac{I_1^{Real} + I_2^{Real}}{I_1^{Mixed} + I_2^{Mixed}} \tag{4.3}$$

where I_1 and I_2 are the integrals of the invariant mass distribution between $80 - 100$ MeV/c^2 and $180 - 280$ MeV/c^2 respectively, i.e. outside the measured π^0 peak.

At lower p_T regions ($p_T < 2$ GeV/c) the mixed events do not perfectly reproduce the combinatorial background because of the contribution of clusters from (i) photon conversion and (ii) antineutron annihilation (see Fig. 4.1). Due to the particle production spectrum, a large number of low-p_T ($p_T \ll 1$ GeV/c) anti-neutrons are created in the collision, which would however make a significant contribution to the energy deposit in the annihilation process: $2m_n \sim 2$ GeV. The e^+e^- pair originating from the photon conversions has a typical $\theta = mc^2/E_\gamma$ opening angle, but if conversion happens in the strong magnetic field the opening angle is increasing because of the different charges of the pair. Thus, the e^+e^- pair creates two separate (correlated) and close clusters. Note, the increase of the opening angle of the pair in the magnetic field is momentum dependent (proportional to the energy of the photon), which increases the background in case of low-energy photon conversions. The remaining background (after mixed event subtraction) is estimated with a linear function. The systematic errors originating from the subtraction of the background are estimated in Sec. 4.5.

At higher p_T region ($p_T > 6$ GeV/c in 39 GeV runs and $p_T > 8$ GeV/c in 62.4 GeV runs), there are not enough counts in the background. Hence, in this region the background is estimated in a wider mass bin below and above the π^0 mass peak, $60 - 100$ MeV/c^2 and $180 - 300$ MeV/c^2, and the background average counts per bin is directly subtracted from the π^0 peak.

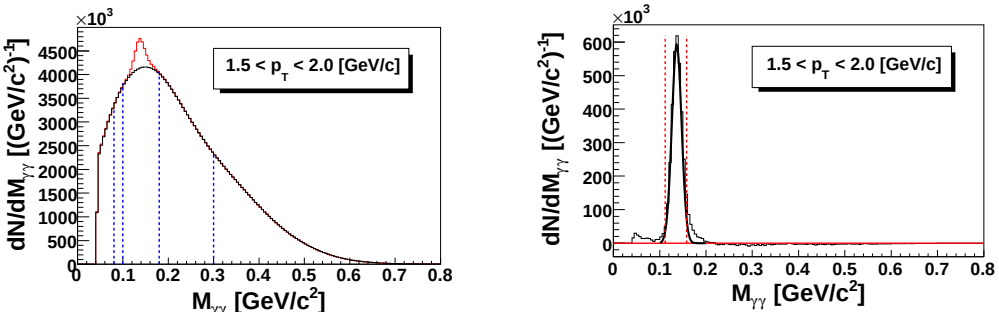

Figure 4.1: Left: the invariant masses of the real and mixed event $\gamma\gamma$ pairs reconstructed in PbSc in Au+Au collisions at $\sqrt{s_{NN}} = 39$ GeV. The red curve corresponds to the real events distribution and the black curve describes the combinatorial background. Blue lines display the two normalization regions below and above the π^0 peak. Right: $M_{\gamma\gamma}$ distribution after the normalization and subtraction of only the combinatorial background. The π^0 peak is fitted with a Gaussian function to extract the peak position and the width. The raw yield is extracted from the counts between the red lines (2 σ window).

4.1.1 Raw Yield of Neutral Pions

The π^0 peaks are fitted with a Gaussian function to estimate the peak position and width. The peak position and width are summarized in Fig. 4.4 for $\sqrt{s_{NN}} = 39$ GeV and Fig. 4.5 for $\sqrt{s_{NN}} = 62.4$ GeV. The peak position is calibrated to $M^{\pi^0}_{\gamma\gamma} = 140$ MeV/c^2 for $p_T > 3$ GeV/c. While the true width of the π^0 is about 8 eV, due to the finite energy and position resolution, the measured value is much higher. Using a nominal energy of two clusters $E_1 = E_2 = 2.5$ GeV (corresponds to $p_T^{\pi^0} \approx 5$ GeV/c), with the energy resolution of EMCal (as in Eq. (2.6)) the value is smeared $\sigma(E = 2.5 \text{ GeV}) = 0.13$ GeV. The position resolution for the same value according to Eq. (2.7) is $\sigma_x = 5$ mm. Implementing the smeared values into the Eq. (A.12), the 1σ limits will be smeared $M^{\pi^0}_{\gamma\gamma} \approx 131 - 148$ MeV/c^2. Thus, the calibrated data should show the peak width $\Delta M^{\pi^0}_{\gamma\gamma} \lesssim 10$ MeV/c^2. The raw yield of π^0's, in various centrality bins, are obtained by integrating the bin content in the mass window of $\left[M^{\pi^0}_{\gamma\gamma} - 2 * \Delta M^{\pi^0}_{\gamma\gamma}, M^{\pi^0}_{\gamma\gamma} + 2 * \Delta M^{\pi^0}_{\gamma\gamma}\right]$, see in Fig. 4.1.

Fig. 4.2 shows the obtained raw π^0 distribution as a function of p_T at both collision energies and in the two detectors separately. The obtained raw spectra in each sub-detector (PbSc and PbGl) are different in shape and magnitude. The acceptance difference of the sub-detectors causes the difference in the number of reconstructed π^0's. The change in the shape of the distribution originates from the different reconstruction efficiencies of the sub-detectors. In order to reconstruct the invariant yield of the neutral pions, we need to correct for the acceptance and efficiencies studied in the next

section. Due to the uncertainties in the simulation process for the PbGl we concentrate on the reconstruction of neutral pions only in the PbSc detector.

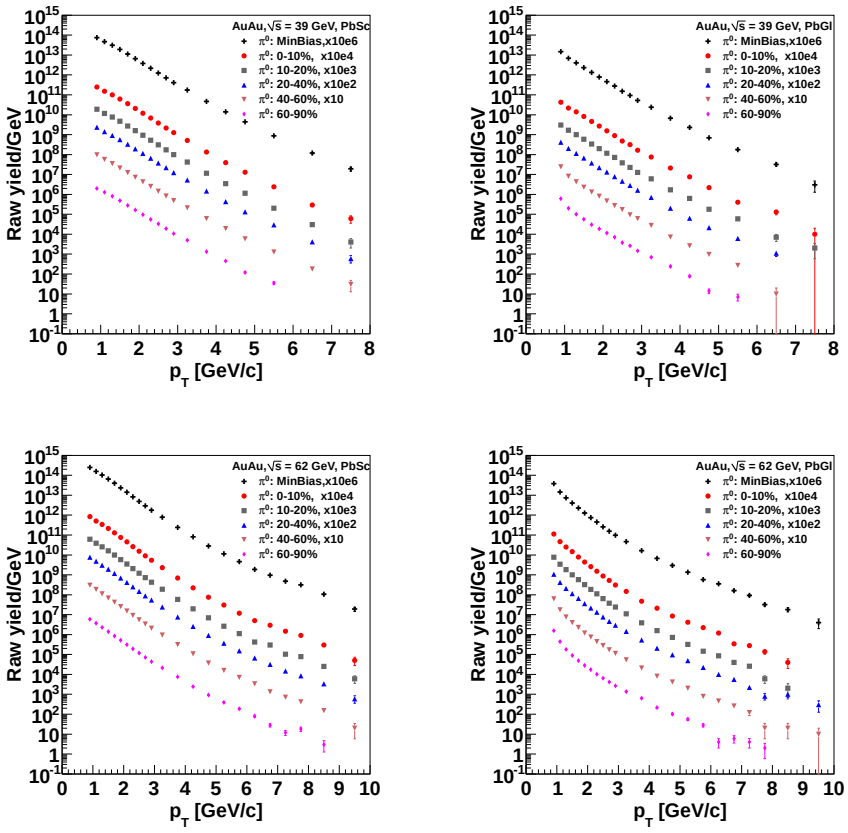

Figure 4.2: The raw π^0 yield in different centralities at $\sqrt{s} = 39$ GeV (upper panels) and $\sqrt{s} = 62$ GeV (lower panels) in PbSc (left) and PbGl (right).

4.2 Efficiency Studies

The obtained raw π^0 counts are influenced by the finite detector acceptance (Acc^{π^0}), the efficiency of reconstructing the two photons ($\varepsilon^{\pi^0}_{\text{efficiency}}$) and the finite energy and position resolution of the calorimeter (known as smearing, S^{π^0}). In order to reconstruct a π^0 both decay photons have to hit the detector which is constrained by the acceptance: the rapidity $|\eta| < 0.35$, azimuthal angle $2 \times \pi/2$ coverage and the dead and hot towers. For the π^0 reconstruction the energy of both photons has to be properly clusterized and the clusters need to pass the photon identification cut ($\chi^2 < 3.0$). As shown in Fig. 4.2, the π^0 spectrum is steeply falling as a function of the transverse momentum

(p_T), which is distorted by the finite energy resolution of the detector. This distortion changes the shape of the distribution, which has to be corrected to obtain the final result.

The detector effects are studied with the Monte Carlo method, described in details in Sec. 3.3. In total, 12M π^0's were generated uniformly in $|\eta| < 0.5$ rapidity and 2π azimuthal angle. The transverse momentum was generated uniformly in $0 < p_T^{\rm sim} < 15$ GeV/c interval in order to have enough statistics in every p_T region. The three detector effects mentioned above are estimated from the individual functions:

$$Acc^{\pi^0} = \frac{N_{\rm in}^{\pi^0}(p_T^{\rm sim})}{N_{\rm all}^{\pi^0}(p_T^{\rm sim})}, \tag{4.4}$$

$$\varepsilon_{\rm efficiency}^{\pi^0} = \frac{N_{\rm reco}^{\pi^0}(p_T^{\rm sim})}{N_{\rm in}^{\pi^0}(p_T^{\rm sim})}, \tag{4.5}$$

$$S^{\pi^0} = \frac{N_{\rm meas}^{\pi^0}(p_T^{\rm meas})}{N_{\rm reco}^{\pi^0}(p_T^{\rm sim})}, \tag{4.6}$$

where $p_T^{\rm sim}$ and $p_T^{\rm meas}$ are the true (simulated) and measured (reconstructed) transverse momentum of the π^0, $N_{\rm all}^{\pi^0}(p_T^{\rm sim})$ is the number of all generated π^0, $N_{\rm in}^{\pi^0}(p_T^{\rm sim})$ stands for the number of π^0 having both decay photons in acceptance, $N_{\rm reco}^{\pi^0}(p_T^{\rm sim})$ is the reconstructed spectrum filled with the simulated $p_T^{\rm sim}$ of the generated π^0 and $N_{\rm meas}^{\pi^0}(p_T^{\rm meas})$ is the measured p_T spectrum filled with the reconstructed p_T of the π^0. The number of reconstructed π^0 ($N_{\rm reco}^{\pi^0}$) has to include all the same cuts and requirements as in the real data analysis, see Sec. 4.1 and in Fig. 4.1. Thus, the combined efficiency can be factorized as

$$C^{\pi^0}(p_T^{\rm meas}) = S^{\pi^0}(p_T^{\rm sim}, p_T^{\rm meas}) \times \varepsilon_{\rm efficiency}^{\pi^0}(p_T^{\rm sim}) \times Acc^{\pi^0}(p_T^{\rm sim}) = \frac{N_{\rm meas}^{\pi^0}(p_T^{\rm meas})}{N_{\rm all}^{\pi^0}(p_T^{\rm sim})}\,. \tag{4.7}$$

Although one can factorize the correction factor into a pure acceptance factor and two effects due to reconstruction within the acceptance, the overall correction factor is determined by embedding one simulated π^0 decay gamma-pair into a real event. The π^0 reconstruction efficiency (often referred to $\varepsilon_{\rm eff}^{\pi^0}(p_T^{\rm sim})Acc^{\pi^0}(p_T^{\rm sim})$) was determined using the embedding method when one simulated π^0-decay γ-pair is embedded into a real event. The main purpose of embedding the simulated π^0's into the real events is to study the multiplicity effect on the photon clusters. When embedding the simulated π^0 to the real events, the vertex position is chosen to be less than 5 cm. Limiting the difference of the real and simulated event verteces assures very similar impact angle of the particles in the embedded event. After the simulated particle is embedded into the real event, i.e. energy deposits added at the tower level, the clusterization algorithm is repeated on the merged energy deposits. In efficiency studies only those clusters are

considered which contain any deposit from the simulated particle. In next two sections, we describe the procedure how the energy scale calibration was matched in real and simulated events and the iterative approach to unfold the smearing effect.

Energy scale

The largest systematic uncertainties originate from the different energy scale calibration in the Monte Carlo simulation and in real events. The steeply falling spectrum enhances the differences due to energy scale calibration. Fig. 4.3 shows the small difference in energy scale is generating a large uncertainty in the final spectrum. It is particularly important to obtain a good energy scale calibration at lower collision energies ($\sqrt{s_{NN}}$ = 62.4 and 39 GeV) as the spectrum is steeper than those at $\sqrt{s_{NN}}$ = 200 GeV (see in Tab. 6.1).

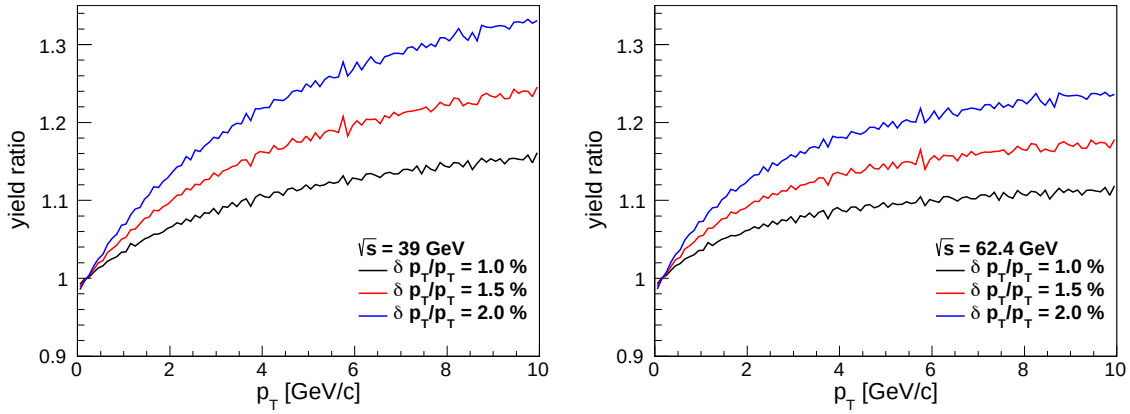

Figure 4.3: Illustration of the uncertainty in the final π^0 spectrum due to the uncertainty in energy scale (1, 1.5 and 2%). A small fractional energy scale shift generates much larger uncertainty in final spectrum. For the test, the fitted invariant yields were used, and the ratio of the distorted yield over the true yields are shown. The fits were done on the measured data in Au+Au collisions at $\sqrt{s_{NN}}$ = 39 and 62.4 GeV.

The Monte Carlo simulation of π^0 has to describe the same energy scale as in real data taking. The embedding method allows to tune the absolute normalization scale and the resolution. To obtain correct efficiency for the measured π^0, both the peak position and the peak width were tuned to the data, see in Fig. 4.4 and Fig. 4.5. The requirement of the difference in peak position has to be less than 1.5%, to accept the tuned absolute scale in Monte Carlo.

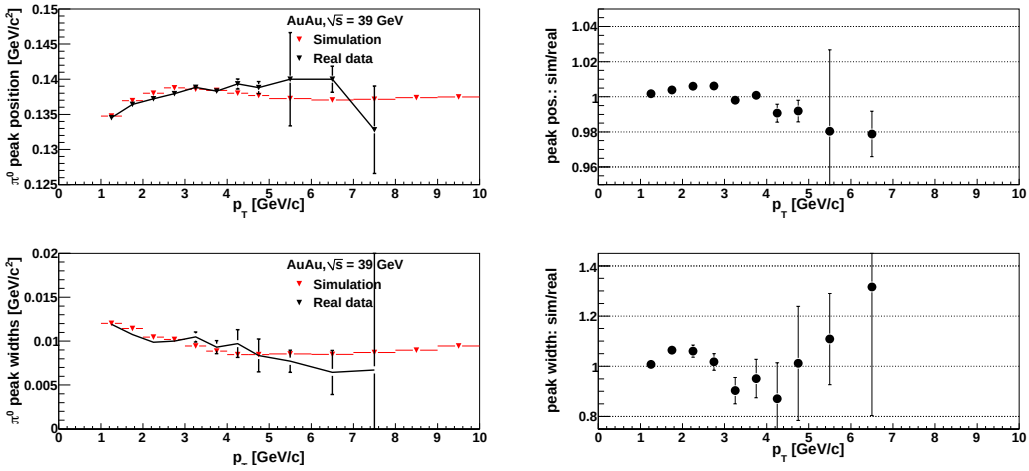

Figure 4.4: Left: The comparison of the mean π^0 peak position (upper panels) and width (lower panels) in real data and simulated events in Au+Au collisions in PbSc detector at $\sqrt{s_{NN}} = 39$ GeV. Right: Ratio between the peak positions and widths obtained from the simulation and real data from left panels.

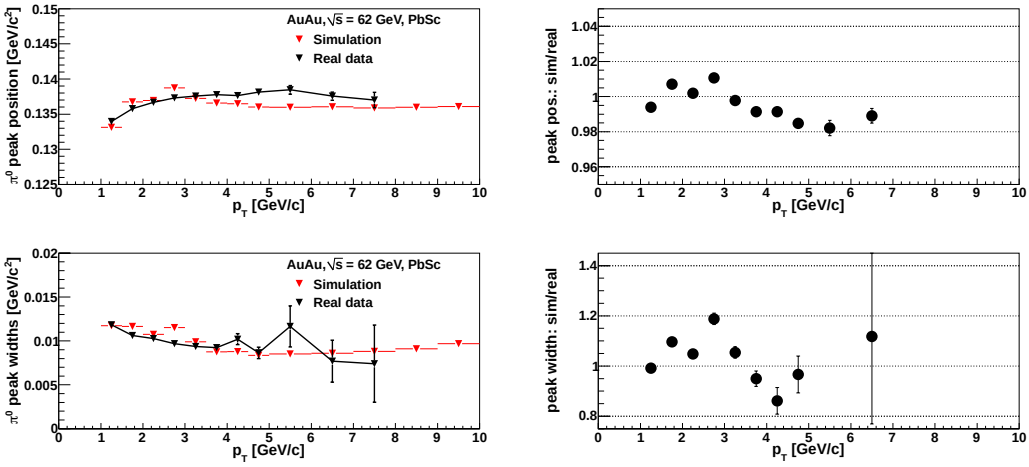

Figure 4.5: Left: The comparison of the mean π^0 peak position (upper panels) and width (lower panels) in real data and simulated events in Au+Au collisions in PbSc detector at $\sqrt{s_{NN}} = 62.4$ GeV. Right: Ratio between the peak positions and widths obtained from the simulation and real data from left panels.

Realistic Spectrum for Correction Function

The p_T distribution of π^0's generated in our simulation was uniform which is not affected by the finite momentum smearing caused by the detector. In order to correctly

account for the momentum smearing effect, we have to weight the generated π^0s with a p_T spectrum of realistic shape. The smearing correction depends on the final measured spectrum what is unknown in the beginning. This section describes the procedure how this uncertainty of the realistic spectrum is treated.

In addition to the smearing effect of the detector, the measured spectrum is shifted from the true distribution because of the effects of finite binning. The p_T spectrum is steeply falling function (exponential $f(p_T) \sim \exp(-6p_T)$ in the low-p_T region and power-law $f(p_T) \sim p_T^{-n}$ in high-p_T region) while the π^0 counts are measured in finite bin sizes. If Δ is the bin size, the counts measured in certain p_T bin are $\int_{p_T^{\rm mid}-\Delta/2}^{p_T^{\rm mid}+\Delta/2} f(p_T)dp_T/\Delta$, where $p_T^{\rm mid}$ is the center of the bin. The data point should be plotted at the center of the bin, in order to make comparisons to other measurements easier. But without bin-shift correction the measured spectrum would be higher than the true spectrum. Thus, a bin-shift correction has to be applied in every p_T bin center as

$$c_{\rm bin-shift} = \frac{\frac{1}{\Delta} \cdot \int_{p_T^{\rm mid}-\Delta/2}^{p_T^{\rm mid}+\Delta/2} f(p_T)dp_T}{f(p_T^{\rm mid})} \tag{4.8}$$

Both the smearing effect and the bin-shift correction depend on the final spectrum of the measured hadrons. Therefore, the process is done iteratively with a use of an initial spectrum.

The first approximation of the realistic spectrum for the $\sqrt{s_{NN}} = 39$ GeV was done with the Levy function (see Tab. 4.1) fit on the invariant cross section of measured π^0 at E706 experiment at Tevatron [185]. The obtained correction function $C^{\pi^0}(p_T)$ (including the smearing effect) was applied on the raw π^0 yield (shown in Fig. 4.2). The obtained corrected p_T spectrum was further corrected with the bin-shift correction. After both corrections, the p_T spectrum is refitted with the Levy function and the new correction function and bin-shift correction are determined. The iterative process is repeated until the corrected spectrum is not modified anymore as it reached the final spectrum.

In case of the measured π^0 spectrum in Au+Au collision at $\sqrt{s_{NN}} = 62.4$ GeV, similar process is applied. The initial spectrum for the corrections was taken from the earlier measured p+p spectrum of π^0's at same collision energy [186]. In both $\sqrt{s_{NN}} =$ 39 GeV and 62.4 GeV case, the spectrum did not change from 4th iteration, the further iterations were not changing the final result (3-4 iteration).

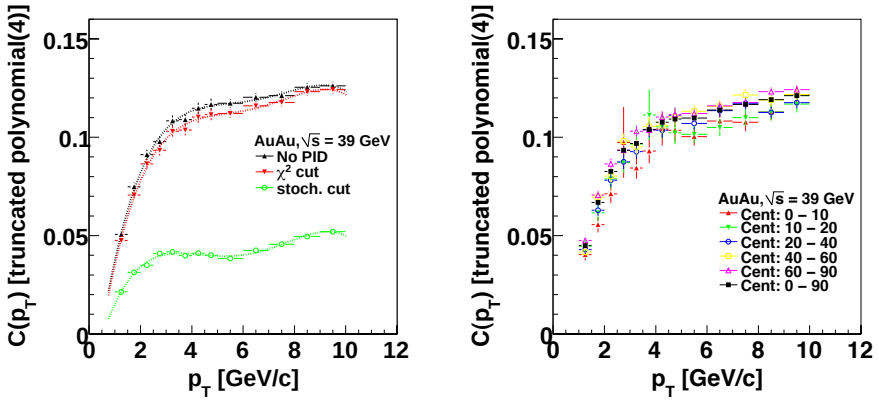

Figure 4.6: Combined efficiency and acceptance correction for π^0's measured at $\sqrt{s_{NN}}$ = 39 GeV in PbSc shown in Au+Au minimum bias data using different PID cut (left panel) and for every centrality class with a χ^2 PID cut (right panel).

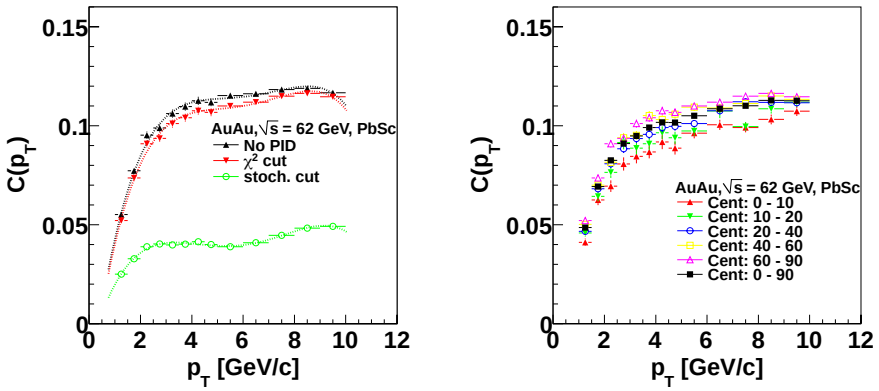

Figure 4.7: Combined efficiency and acceptance correction for π^0's measured at $\sqrt{s_{NN}}$ = 62 GeV in PbSc shown in Au+Au minimum bias data using different PID cut (left panel) and for every centrality class with a χ^2 PID cut (right panel).

4.3 Reconstruction of the Invariant Yield

The Lorentz invariant yield in heavy ion collisions is comparable with the invariant cross section in p+p collision. The total cross section is not measured in heavy ion collision, but it is calculable by using different models. The invariant yield is expressed as

$$E\frac{d^3\sigma}{dp^3} = \frac{d^3n}{p_T dp_T dy d\phi} \simeq \frac{d^2n}{2\pi p_T dp_T dy} \tag{4.9}$$

The rapidity is expressed as $y = \frac{1}{2}\ln\left((E+p_{\parallel})/(E-p_{\parallel})\right)$ and it is an Lorentz additive quantity. In the experiments the outgoing particle is measured tangent angle θ with respect to the beam axis, and the longitudinal component is expressed with the pseudorapidity, $\eta = \frac{1}{2}\ln\left((|p|+p_{\parallel})/(|p|-p_{\parallel})\right) = -\ln\left(\tan\left(\theta/2\right)\right)$. At the high energy limit or vanishing mass the rapidity and pseudorapidity are equal. The measured raw yield of π^0 (Fig. 4.2) is corrected for detector efficiencies and normalized by number of events to obtain the invariant yield

$$E\frac{d^3\sigma}{dp^3} = \frac{1}{N_{\text{event}}}\frac{1}{2\pi p_T}\frac{\Delta N^{\pi^0}}{\Delta p_T \Delta y}\frac{1}{C^{\pi^0}(p_T)c_{\text{bin-shift}}}, \tag{4.10}$$

where N_{event} is the number of events and $C^{\pi^0}(p_T)$ is the combined efficiency correction from Eq. (4.7) and shown in Fig. 4.6 and Fig. 4.7. The invariant yield is calculated for every centrality bin using the proper correction functions. The results of the final invariant yield in Au+Au collisions at $\sqrt{s_{NN}}$ = 39 GeV and 62.4 GeV are summarized in Fig. 4.8.

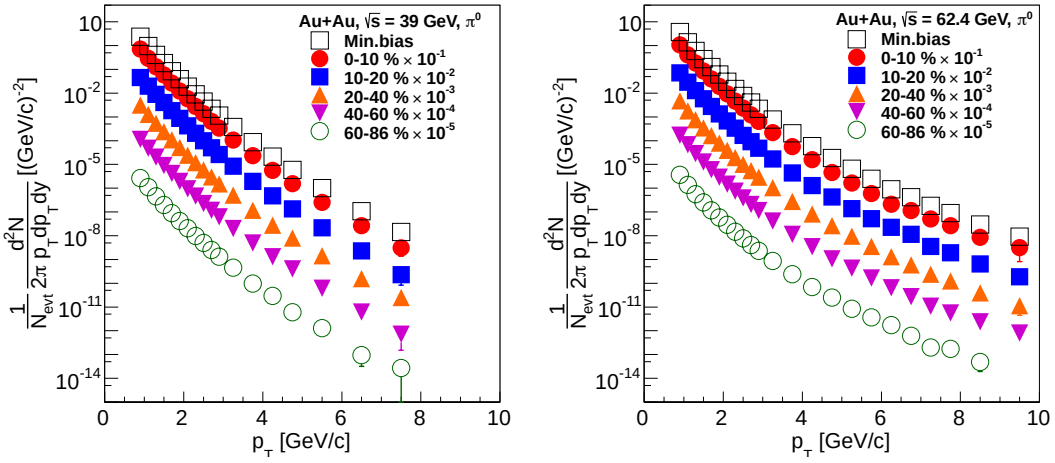

Figure 4.8: Invariant yields of π^0 in Au+Au at $\sqrt{s_{NN}}$ = 39 GeV (left) and 62.4 GeV (right) in all centralities and minimum bias. Only statistical uncertainties are shown.

4.4 p+p References at $\sqrt{s_{NN}}$ = 39 and 62.4 GeV

Evaluation of the nuclear modification factor (R_{AA}, see Eq. (1.41)) requires knowledge of a reference spectrum from p+p system taken at the same center-of-mass energy as the heavy-ion collision. In this section, we focus on obtaining the correct references. Note that the best option is using the measured A+A and p+p spectrum from the same

Function name	form	a	n	p_0	b1	b2
powerlaw	$a \cdot \frac{1}{p_T^n}$	3.46e+01	10.1	-	-	-
Hagedorn	$a \cdot \frac{p_T}{\sqrt{p_T^2+m_{\pi^0}^2}} \left(1+\frac{p_T}{p_0}\right)^{-n}$	2.52e+02	14.2	1.93	-	-
Tsallis	$a \cdot \left(1+p_T\frac{p_0}{n}\right)^{-n}$	2.45e+02	14.2	7.32	-	-
Lévy	$a \cdot e^{p_0/p_T}\frac{1}{p_T^n}$	6.48e+02	7.01	-10.9	-	-
ISR fit [187]	$a \cdot \left(e^{b_1 p_T^2 + b_2 p_T} + p_T/p_0\right)^{-n}$	4.14e+02	17.95	2.639	-0.0129	0.04975

Table 4.1: Different functions and parameters fitted over the measured π^0 spectrum at Run-6 p+p at $\sqrt{s} = 62.4$ GeV.

experiment as some systematic uncertainties may cancel (e.g. energy scale, same clusterization, acceptance, resolution and more), and the normalization of the spectrum is under control. Using a p_T spectrum from other experiments can result in larger uncertainties.

4.4.1 π^0 p+p references at $\sqrt{s} = 62.4$ GeV

For the p+p reference at $\sqrt{s} = 62.4$ GeV we use π^0 spectrum from earlier measurement in 2006 at PHENIX [186]. However, the p+p reference is measured only up to $p_T < 7$ GeV/c and the Au+Au p_T spectra are up to 10 GeV/c. For the missing interval from $p_T = 7 - 10$ GeV/c we need to extrapolate the existing p+p spectrum. We investigated different functional forms, summarized in Tab. 4.1, to extrapolate to higher p_T regions. The different fits and the deviation in every p_T bin are shown in Fig. 4.9. In addition an empirical formula was used on data from Intersecting Storage Rings (ISR) at CERN at $\sqrt{s} = 62.4$ GeV [187]. The slope parameters of the "ISR-fit" are fixed, only the normalization factor (a in the formula) is fitted to the PHENIX data.

For the extrapolation to the high-p_T we assume that the spectrum follows a single power law distribution. Where the assumption comes from the fact that the high-

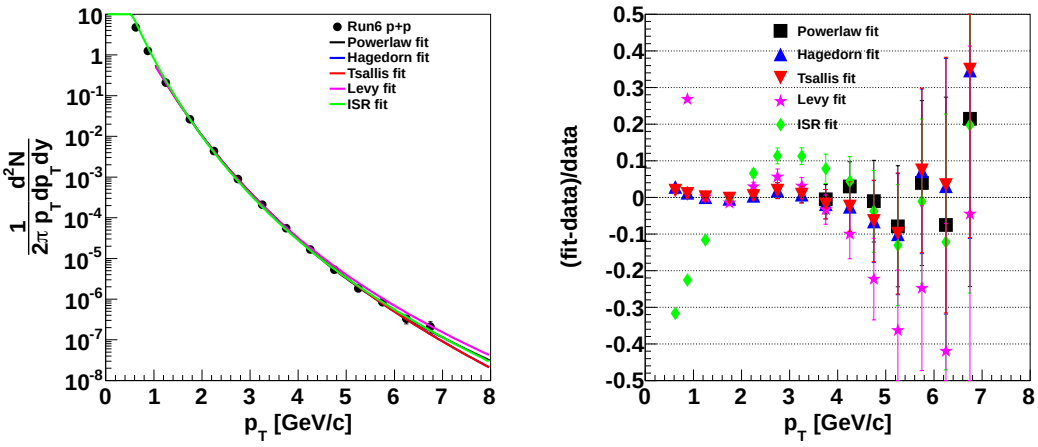

Figure 4.9: Left: π^0 at $\sqrt{s} = 62.4$ GeV in p+p system at PHENIX [186]. The data points are fitted with different function forms (see Tab. 4.1 and ISR function [187]). Right: The relative difference between data points and fit functions.

p_T processes are described by the pQCD. In practice, we fit the power-law function in $p_T > 4$ GeV/c and extrapolate to higher-p_T regions. During the fitting process, both systematic and statistical uncertainties were considered on each data point. It is natural that the fit over the data smoothens the point-by-point fluctuations of the data points. In addition, it is important to consider the limits of the extrapolation that originate from the fit uncertainties on the data points. We studied the uncertainties in two different ways:

- Fit function variation
  The power-law fit was fitted on the p+p data points at $\sqrt{s} = 62.4$ GeV, while some of the data points were randomly removed from the spectrum. In this procedure, we remove randomly some of the data points (from 1 up to 6 points), which will slightly change the fit parameters. The uncertainty of the fit function in higher p_T bins will be the systematic uncertainty of the extrapolation (Fig. 4.11).

- Data from ISR experiments
  Four data sets from ISR experiments were considered in the estimation of the systematic uncertainties in extrapolation to higher p_T bins: CCOR [45], CCRS [44], ABSC [188], R702 [189]. The different fit functions over the PHENIX data points were compared to each of the experimental points at ISR, see Fig. 4.10. Since, the ABSC data set needs to be normalized by a factor of two to match the Run-6 data, it was not used in further analysis. Due to the large nonuniform deviation of the CCRS and R702, we did not use them in further estimation of systematic errors (Fig. 4.11).

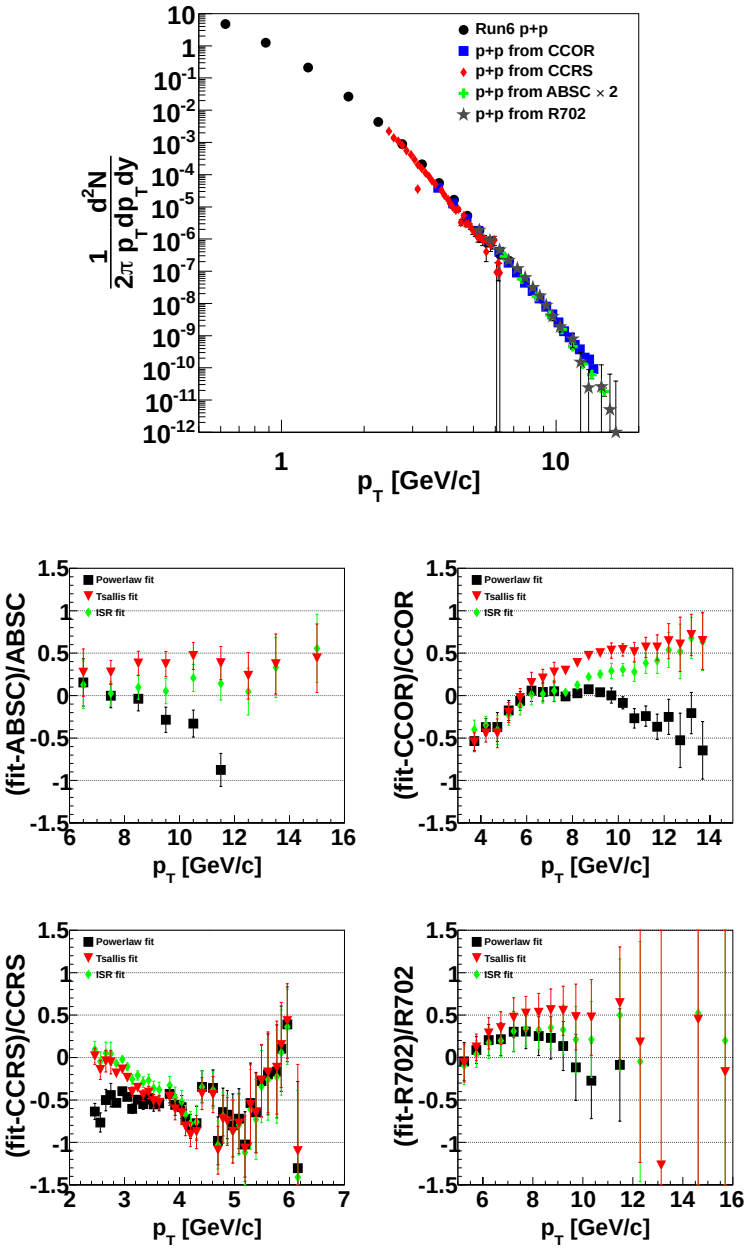

Figure 4.10: Upper panel shows the Run-6 p+p measured at $\sqrt{s} = 62$ GeV and the four ISR experiments [45] [44] [188] [189]. Lower panels show the comparison of the external experimental data with the three fit functions on PHENIX Run-6 p+p data (power law, Tsallis and ISR fit from Fig. 4.9). In the final extrapolation, the power law function is used.

The final estimation of extrapolation to higher p_T bins with the power-law fit function, $f(p_T) = 26.83 \cdot (p_T)^{-9.9}$ (see Tab. 6.1). Fig. 4.11 shows the estimated systematic error (yellow area) for the extrapolation from the first method. The estimated systematic error grows up to 18% at the highest $p_T \approx 10$ GeV/c. In addition, the CCOR data are within the estimated systematical uncertainties of the extrapolation in the p_T region from 7 to 10 GeV/c.

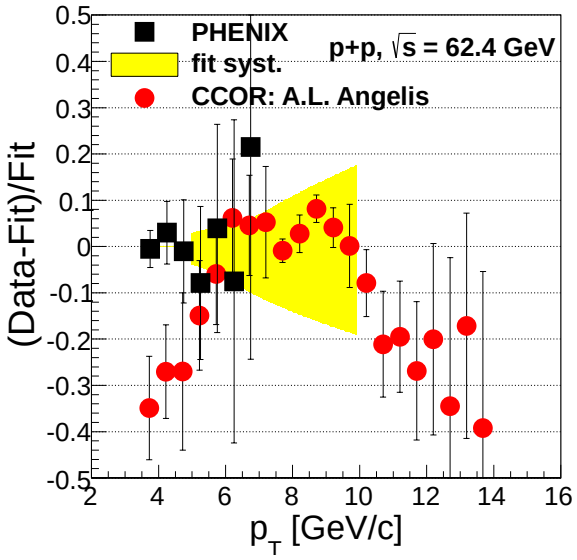

Figure 4.11: The final estimation of the systematic uncertainty on the extrapolation to higher p_T bins (from 7 to 10 GeV/c) using the power-law fit function at $\sqrt{s} =$ 62.4 GeV. The yellow error band is the result of the fit function variation when points are randomly removed (see text). The data points describe the ratio of the different data sets and the power-law fit.

4.4.2 π^0 p+p references at $\sqrt{s} = 39$ GeV

There are no data from p+p collisions at $\sqrt{s} = 39$ GeV provided by RHIC, thus measured in the PHENIX detector. As mentioned above, the measurements of the particle spectra in the same experiment result in very well controlled systematic uncertainties, which improves the calculated nuclear modification factor. In this section, we discuss various methods to estimate a p+p reference for 39 GeV Au+Au data using PHENIX p+p data measured at higher $\sqrt{s}$ energies, namely 62, 200 and 500 GeV. In addition, in the later part of the section we study the π^0 p+p measurement at $\sqrt{s} = 39$ GeV in the E706 fixed-target experiment at Tevatron.

The PHENIX experiment measured π^0 spectra in p+p collisions at three different energies, $\sqrt{s} = 500, 200$ and 62.4 GeV. We study two different extrapolation methods

to lower collision energy:

- "Linear" bin-to-bin extrapolation method
- x_T scaling method.

The region of interest is in the momentum interval $1 < p_T < 8$ GeV/c, where the Au+Au data were measured. The above mentioned methods were proposed in order to extrapolate for the missing measurement at p+p collision at $\sqrt{s} = 39$ GeV. The extrapolation methods were considered due to the previous experience, when the R_{AA} was calculated in Au+Au collisions at $\sqrt{s_{NN}} = 62.4$ GeV by using external and internal data as p+p reference. The resulting nuclear modification factor differed about $\sim 40\%$, see in Fig. 4.12. Due to this significant difference, we first considered the usage of extrapolation methods using only the data measured by PHENIX experiment. In following sections, we attempt to investigate the validity of these methods. In summary, we conclude that these methods are not reliable in our extrapolation, thus, for the final results we have to use the measured π^0 spectrum by E706 collaboration in p+p collisions.

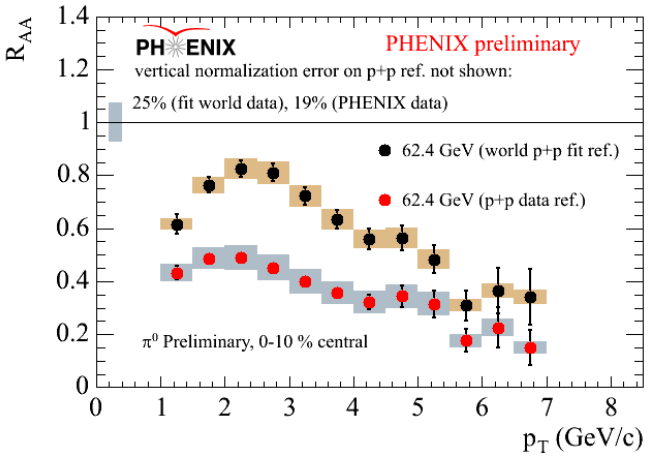

Figure 4.12: The nuclear modification factor (R_{AA}) in Au+Au collisions at $\sqrt{s_{NN}} = 62.4$ GeV calculated with two different p+p references: (i) using the world data and (ii) the p+p data from PHENIX.

4.4.3 "Linear" bin-to-bin extrapolation method

This scaling method assumes, that the data points of an invariant cross section at fixed p_T follows a $\sqrt{s}^m$ function, where for each p_T bin one slope (m) is defined. The p_T cross section is known to change at different $\sqrt{s}$, however, this method assumes

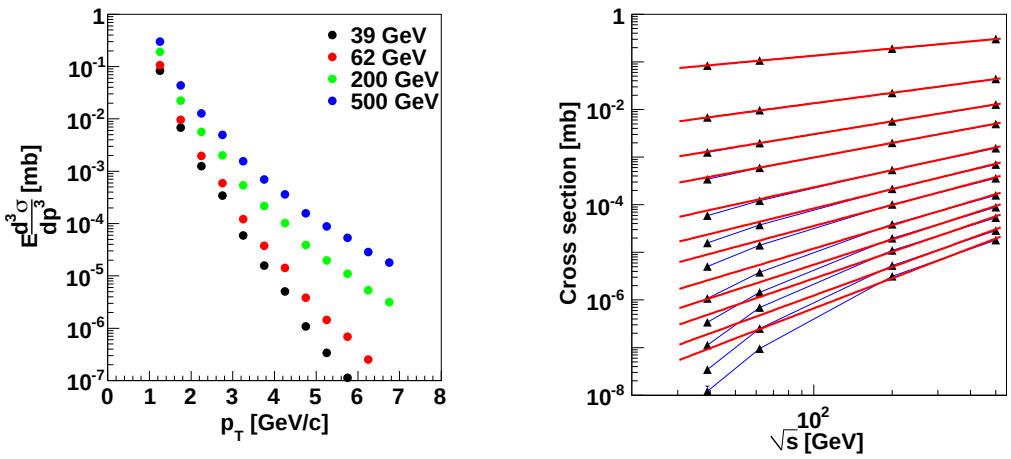

Figure 4.13: Left: the π^0 spectra generated using PYTHIA8 event generator. The spectra are shown in region $1 < p_T < 7$ GeV/c in a finite bins of$\Delta p_T = 0.5$ GeV/c Right: cross section of all p_T bins as a function of the $\sqrt{s}$. From top to bottom are the spectra points from low-p_T up to high-p_T. The red lines are power-law fits over all $\sqrt{s}$ energies, the blue lines connect the points which refer to same p_T bins.

that a single power-law can describe the $\sqrt{s}$ dependence in a fixed p_T bin. We focus on the study of the validity of the method in region $1 < p_T < 7$ GeV/c range in bins of $\Delta p_T = 0.5$ GeV/c. For each center-of-mass energy 10 M minimum bias events were generated with PYTHIA8 event generator (see Fig. 4.13 left). In right panel of Fig. 4.13 we plot invariant cross-section plot at fixed p_T bins as a function of the center-of-mass energy. Every set of points connected with the line are simulated in the same p_T bin.

The π^0 spectra are measured at three different energies ($\sqrt{s} = 62.4, 200, 500$ GeV). Therefore, we study the extrapolation method to lower $\sqrt{s} = 39$ GeV with "linear bin" extrapolation by using:

- 2 point method: using only the 62 and 200 GeV data point
- 3 point method: using all three data points: 62, 200 and 500 GeV.

In Fig. 4.14 we summarize the results of the fits on two and three points in each p_T bin. The higher p_T bins shows larger deviation from the fits when compared to simulated data points.

Both approaches (Fig. 4.14) can be used to extrapolate invariant cross-section down to 39 GeV. This extrapolated spectrum was then compared to the invariant cross-section generated by PYTHIA8. Fig. 4.15 shows that the method provides a consistent estimate of the invariant cross-section at low-p_T. However, in the higher p_T bins, the extrapolated points start to deviate significantly from the cross-section calculated by

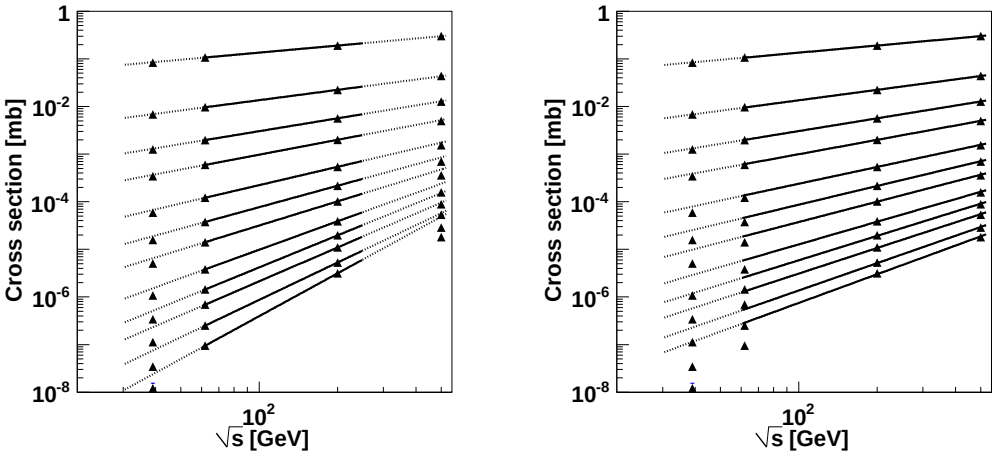

Figure 4.14: The two different powerlaw extrapolations that were used to get invariant p_T spectrum for 39 GeV data, same as in Fig. 4.13. The solid line represents the range of the fit on the data points and the dashed line shows the prolongation of the fit functions.

PYTHIA8. The same exercise was done to extrapolate up to 500 GeV data points (Fig. 4.15). In this case, obviously, we used 39, 62 and 200 GeV points in the 3 point method and the 62 and 200 GeV points in the 2 point method. The results show the same behavior and the deviation from the true spectrum depends on p_T (see Fig. 4.15).

We made an energy scan from $\sqrt{s} = 10$ GeV up to $\sqrt{s} = 550$ GeV (see Fig. 4.16) in order to study the $\sqrt{s}$ dependence in fixed p_T bins. The PYTHIA8 study suggests that the cross section cannot be described by a single power law as $\sqrt{s}^m$. The deviation from the power law behavior depends on the $\sqrt{s}$ and the choice of the fixed p_T bin. Thus, according to PYTHIA8 it seems the invariant cross-section obtained by the "linear" bin-to-bin method would overestimate the real spectrum. The discrepancy depends on the p_T bin.

4.4.4 x_T scaling method

This method is based on the observation that invariant cross-section spectra collapse to a universal curve, when plotted as a function of $x_T = 2p_T/\sqrt{s}$ (see in Sec. 1.1.2). Fig. 4.17 shows invariant cross-sections as a function of x_T generated by PYTHIA8. To calculate the 39 GeV spectra by the x_T scaling we use:

$$\sigma(39 \text{ GeV}, x_T) = \sigma(62.4 \text{ GeV}, x_T) \left(\frac{\sigma(200 \text{ GeV}, x_T)}{\sigma(62 \text{ GeV}, x_T)} \right)^{\alpha} \tag{4.11}$$

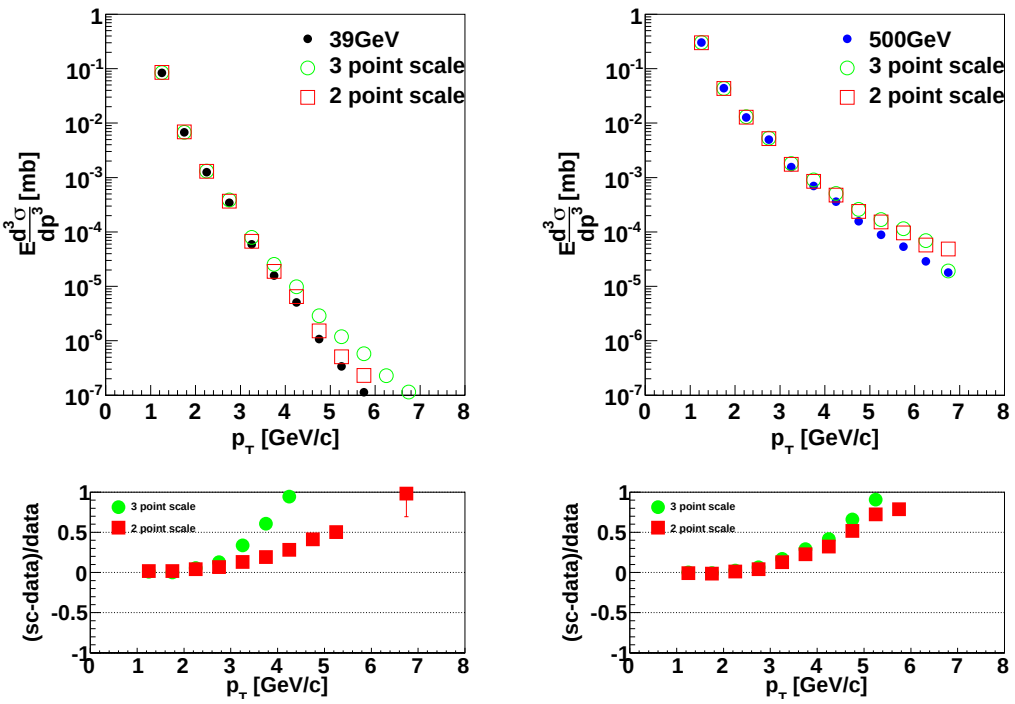

Figure 4.15: Top: The 39 GeV and 500 GeV invariant p_T spectra generated by PYTHIA8 compared with estimated spectra obtained by two and three point method described in text. Bottom: the ratio of the scaled versus the original spectra shows that the discrepancy between the extrapolation and generated cross-section rises with p_T.

where:

$$\alpha = \frac{\ln(39./62.)}{\ln(200./62.)} \tag{4.12}$$

Using the formula the 39 GeV spectrum was assessed and in Fig. 4.18 we compare it with the cross-section generated by PYTHIA8. However, it can be seen that the cross-section obtained by the x_T scaling method systematically underestimates the PYTHIA8 reference 39 GeV spectrum.

4.4.5 Comparison of measured data and extrapolation methods at $\sqrt{s} = 500$ GeV

In the previous sections (Sec. 4.4.3 and Sec. 4.4.4) we described two methods to extrapolate to lower $\sqrt{s} = 39$ GeV and higher $\sqrt{s} = 500$ GeV. The validity of the methods were tested with the PYTHIA8 Monte Carlo generator. For additional validity

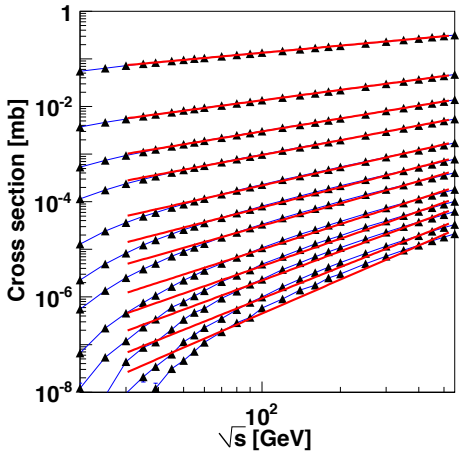

Figure 4.16: The results obtained by the PYTHIA8 energy scan from $\sqrt{s} = 10$ GeV up to $\sqrt{s} = 550$ GeV. The red line is a power law fit and the blue line connects the points which belong to same p_T bins. The discrepancy of the power-law fit from the generated cross-section grows as we move to higher p_T bins and smaller $\sqrt{s}$.

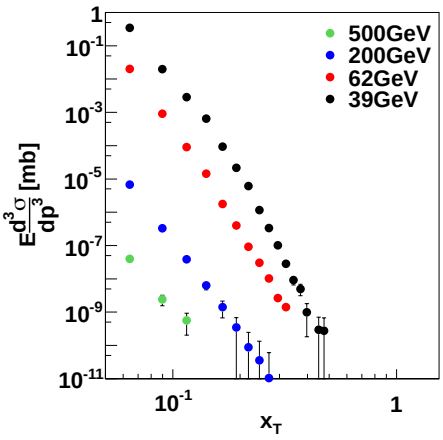

Figure 4.17: The invariant π^0 cross section according to PYTHIA8 as a function of x_T at different center of mass energies.

check, we perform the extrapolation methods by using the measured π^0 spectrum in p+p collisions at $\sqrt{s} = 62.4$ and 200 GeV to extrapolate to higher $\sqrt{s} = 500$ GeV which was also measured by PHENIX. Fig. 4.19 shows the π^0 spectrum in function of x_T for every energies and in function of $\sqrt{s}$ in every p_T bin as described in the extrapolation methods. The right panel in Fig. 4.19 shows the comparison between

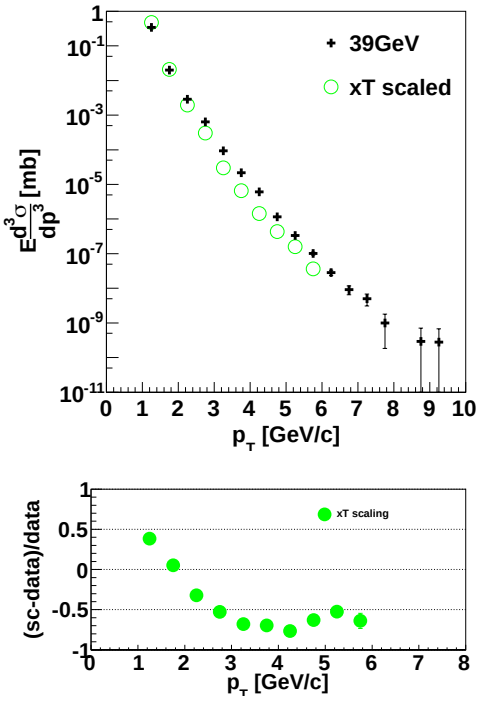

Figure 4.18: Up: the spectrum generated directly with PYTHIA8 compared to the one obtained with the x_T scaling method. Down: Ratio between cross-section assessed by x_T scaling method and direct calculation by PYTHIA8.

the extrapolated data and the measured data. The results of both methods using the measured data shows the same behavior as in previous Sec. 4.4.3 and Sec. 4.4.4 the results made with the PYTHIA8 event generator.

4.4.6 The E706 Measurement of π^0 at $\sqrt{s} = 39$ GeV

In the previous sections we described the scaling methods and we investigated its limits with the PYTHIA8 simulation and measured spectra. The extrapolation study suggests that scaling methods for downward (and upward) extrapolation of existing p+p data from PHENIX fail to describe the p_T spectrum at high p_T. This fact was also verified with the experimental data when using the 62.4 and 200 GeV we attempted to extrapolate to 500 GeV. Therefore, we will use as a reference the data from Tevatron E706 experiment (Fig. 4.21) [185]. However, the E706 data points below $p_T < 2$ GeV/c significantly deviate from any reasonable smooth curve. Therefore, in this region ($p_T <$ 2 GeV/c) we can use as a reference the "linear" bin-to-bin extrapolation method as reference to complete the E706 reference (see in Sec. 4.4.3).

A very important factor, when we use the measured data in other experiment, is

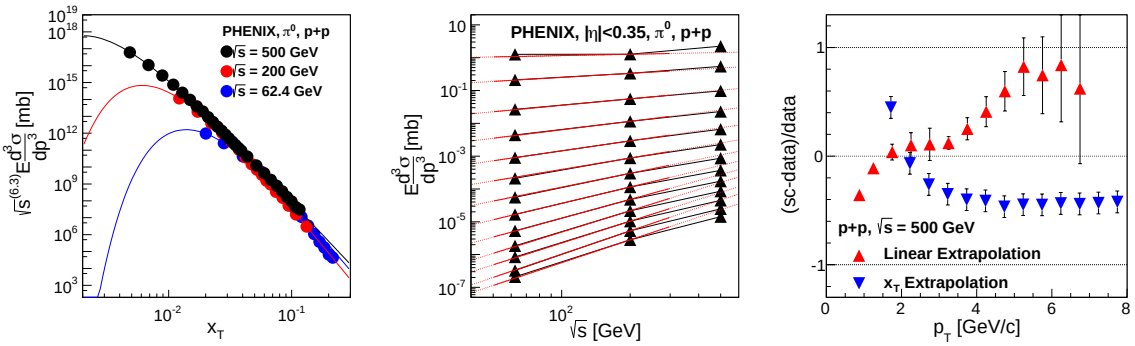

Figure 4.19: The linear and x_T scaling extrapolation method using the PHENIX data at $\sqrt{s} = 62.4, 200$ and 500 GeV. Left panel shows the π^0 cross section in function of x_T in p+p collisions, the lines are the individual Tsallis fit functions over the data points. The middle panel shows the cross sections in different p_T bins as a function of $\sqrt{s}$. The red lines are the fit results for 62.4 and 200 GeV points, the black lines are the connected data points. The right panel shows the final result from extrapolation compared to measured data at $\sqrt{s} = 500$ GeV.

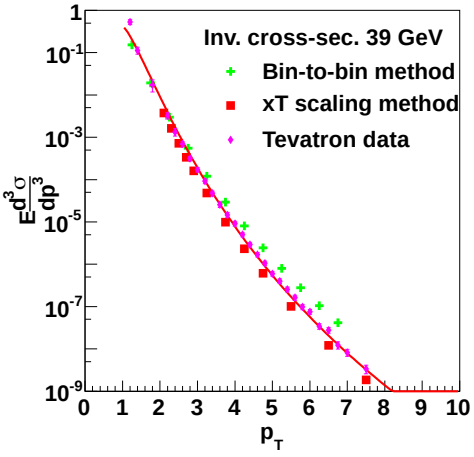

Figure 4.20: Invariant π^0 cross-section obtained from the PHENIX data by means of the bin-to-bin extrapolation and x_T scaling compared to the original Tevatron data [185]. The Tevatron data points are fitted with a Levy function, shown with a red line.

to consider the different setup of the experiment. The published data are normalized to one unit of rapidity ($|\eta| < 0.5$) as in the case of our measurement. However, the acceptance of the E706 experiment is $-1.5 < \eta < 0.5$, different from those of our measurement at PHENIX with the acceptance of $|\eta| < 0.35$. The $dN/d\eta$ distribution is known to be non-uniform. Thus, the measured data normalized in one unit of

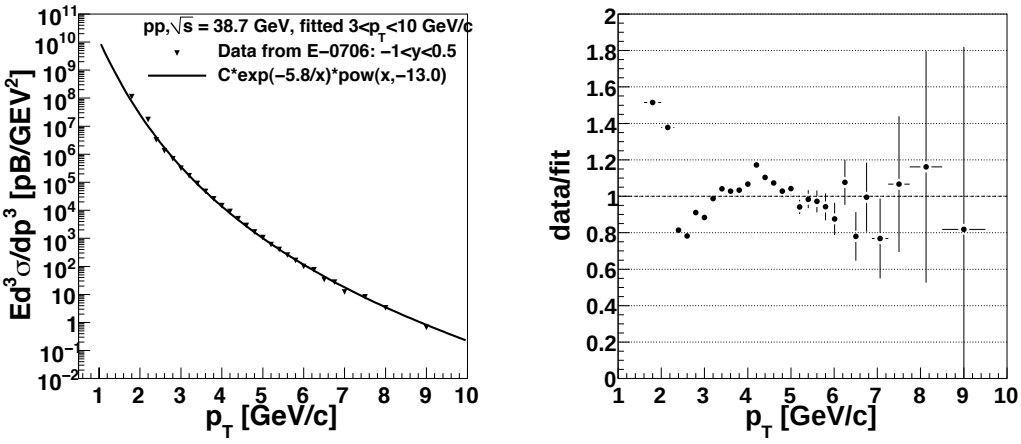

Figure 4.21: Left: π^0 invariant cross section measured in p+p at Tevatron at E_{Beam} = 800 GeV. The CM energy is $\sqrt{s} = 38.7$ GeV. Data are fitted with Levy function. Right: Ratio of Tevatron data to the Levy fit.

rapidity with two types of detectors in different rapidity acceptance leads to systematic deviation in the p_T spectrum. In addition, the $dN/d\eta$ distribution is narrower at higher p_T, where this difference is larger.

We study the effects of different acceptances of PHENIX and E706 experiment with the PYTHIA8 event generator. The π^0 spectra are generated in PYTHIA8 in E706 (-1.5 $< \eta <$ 0.5) and in PHENIX ($|\eta|$ <0.35) rapidity windows and they are later normalized to one unit of rapidity. The ratio of the two spectra gives us the correction factor which is used to transform the E706 data to PHENIX acceptance. Thus, we will obtain proper p+p reference for the 39 GeV Au+Au data, see in Fig. 4.22.

The systematic uncertainties of the correction function were investigated by comparing the rapidity distribution (dN/dy) of the π^0 measurement from E706 measurement [185] with the PYTHIA8 results (see Fig. 4.23). Both the E706 data and the PYTHIA8 generated distribution were fitted with a symmetrical Gaussian function around the zero rapidity. The σ parameters of the Gaussian fits to the rapidity distributions in various p_T bins describe the shape of both E709 and PYTHIA8 (see Fig. 4.24 left). The p_T distribution of the σ parameters ratios of E706 data and PYTHIA8 describes the uncertainty of the different shapes. Uncertainty in Gaussian widths can be deduced based on right hand side panel in Fig. 4.24, where we show a ratio of σ parameters from E706 data and PYTHIA8 as a function of p_T. The estimated uncertainty in magnitude of σ is shown as a yellow band. Range of the band was obtained from a weighted average of the points.

We estimate the systematic error as the fluctuation in the ratio of the integrals of the measured data and the simulated distribution around unity (see Fig. 4.24). We

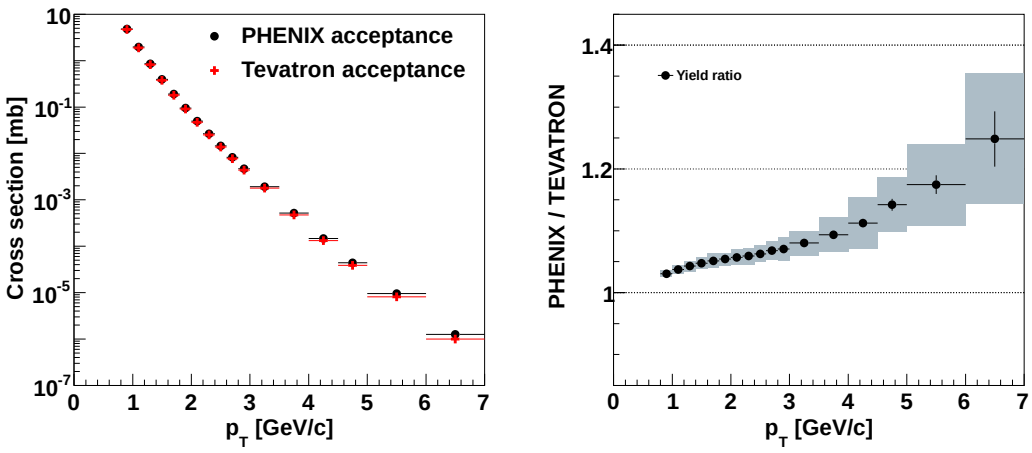

Figure 4.22: Left: the π^0 generated in PYTHIA8 event generator. The spectra are generated in different rapidity windows (PHENIX $|\eta|$ <0.35 and Tevatron -1.5< η <0.5). Right: the ratio of the simulated PHENIX and Tevatron spectra used as the correction function for the p+p reference. The error bands for each point represent the statistical uncertainty using limited statistic from the Monte Carlo. The boxes around the points are resulted from the systematic error study of the correction function (see in text and Fig. 4.24).

assume, that the systematic uncertainty of the Gaussian widths are p_T independent, while the widths themselves are different in each p_T bins. Right panel in Fig. 4.24 shows the uncertainty of the sigma distribution between the data and the PYTHIA8 simulation deviates by $\sim$ 13%. We observe large deviation in the low-p_T bins, resulting from the large systematic uncertainties of the data points. Note that in the low-p_T bins we use the linear bin-to-bin interpolation as the reference. While we change the width of Gaussian function by $\pm$13%, we compare the two integrals of rapidity distribution in PHENIX and E706 rapidity windows normalized to one unit of rapidity. This results, however, in a systematic uncertainty of the correction function which is p_T dependent.

4.5 Systematic Error Studies of Invariant Yields

In this section we estimate influence of various systematic uncertainties on extracted invariant yield from the invariant mass spectra. The systematic uncertainties are resulting from the uncertainties caused in each step of the analysis. We study the uncertainties in the invariant mass reconstruction and in the raw yield extraction. In the second part we study the uncertainties from the embedding and efficiency studies. The systematic errors are divided into three groups according to their behavior:

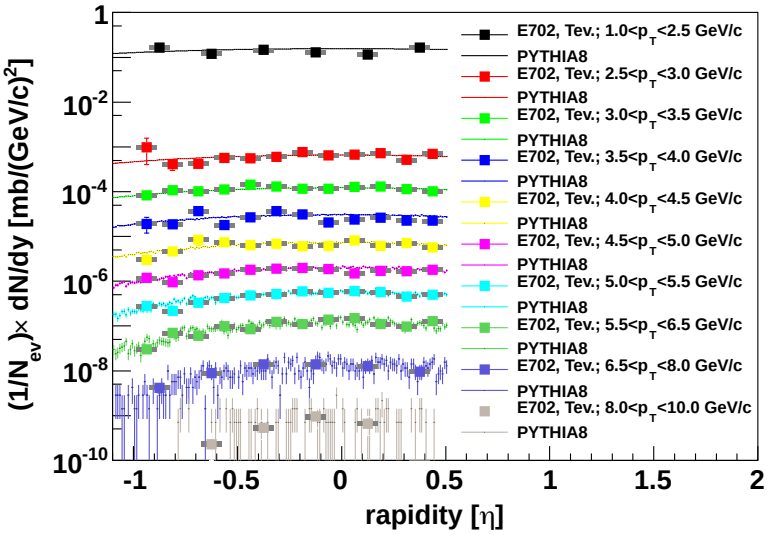

Figure 4.23: The rapidity distribution from E706 experiment [185] at Tevatron and the rapidity distribution of the PYTHIA8 simulation in different p_T bins.

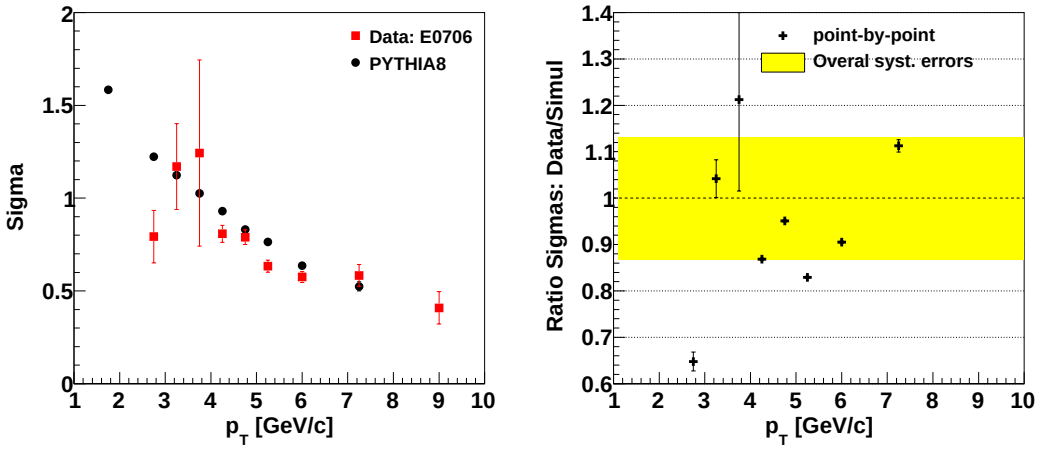

Figure 4.24: Left: The σ parameter from the Gaussian fits over the rapidity distribution in E706 data and PYTHIA8 simulation. Right: The comparison of the Gaussian σ parameter in data and simulation. The yellow band shows the p_T independent error-weighted sum of all the ratios.

- Type-A: p_T uncorrelated uncertainty. Point-by-point systematic uncertainty.
- Type-B: p_T correlated uncertainty. Every point moves up or down by the same

value.

- Type-C: p_T correlated uncertainty. Every point moves up or down by the same factor.

4.5.1 Extracting Raw π^0 from the Invariant Mass Distribution

When extracting the raw π^0 counts from the invariant mass distribution, we use certain approximations and cuts in the analysis, which introduce a systematic uncertainty. Here, we focus on the correlated and uncorrelated (or combinatorial) background subtraction from the invariant mass distributions.

The normalization intervals of the mixed event background

Mixed event background can be normalized to the measured invariant mass spectrum in different invariant mass regions around the π^0 peak. Uncertainty in normalization can be assessed by varying sizes and positions of normalization intervals and comparing extracted π^0 yield. Our study shows that the obtained π^0 yields depend on the normalization interval, and the yield ratios vary within 4% for $2 < p_T < 4$ GeV/c, 6% at $p_T \approx 1$ GeV/c. At higher p_T values, the systematic uncertainty of the normalization interval is within 2%. Fig. 4.25 shows the intervals where the mixed events were normalized and the difference of the extracted yields are summarized in the right panel.

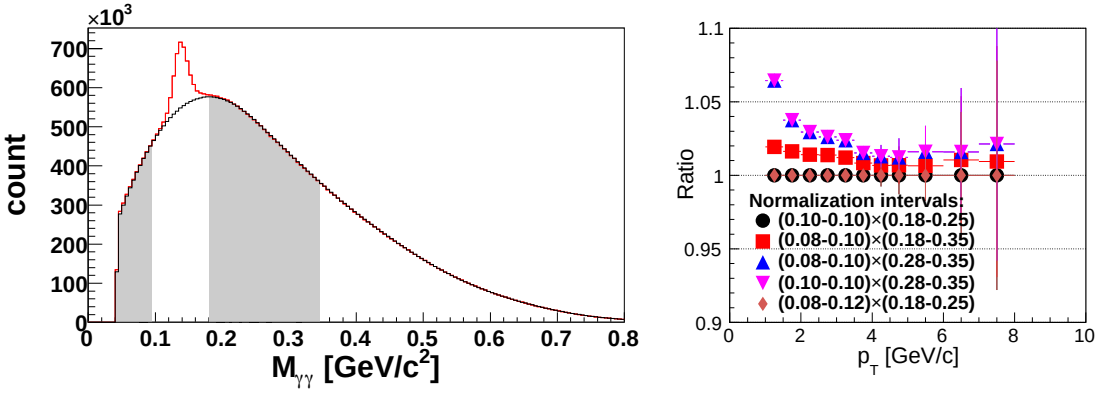

Figure 4.25: The yield extraction depending on the different intervals of the normalization of the combinatorial background. Left: the normalization intervals are chosen from the intervals indicated by the shaded vertical bands. The intervals in the analysis are [0.08-0.1] before the peak and [0.18-0.25] after the peak. Right: the variation of the normalization intervals changes the extracted yield about $\sim 4\%$ at low-p_T, while is negligible at higher p_T. The shown [0.1-0.1] interval represents that no normalization was used before the π^0 peak.

Systematic uncertainty following from subtraction of the correlated background

At low-p_T ($p_T < 2$ GeV/c) region, mixed event technique does not provide satisfactory description of the background shape (see in Sec. 4.1). The mixed event method cannot reproduce the additional correlated background. The remaining background is fitted by a linear function and subtracted from the raw π^0 counts. The fit region is a bit wider than the peak width in order to fit the background reliably. In Fig. 4.26 we show the systematic uncertainty that can emerge either from the choice of the fit region or functions which we use to describe the background (linear, parabolic and exponential.) We checked that extending fit region to lower or higher invariant mass regions did not change fitting parameters of the background fit.

On the other hand, using different functional forms to subtract the correlated background can change the extracted yield up to by 2-3% in the region $p_T < 2$ GeV/c, where the hadron contamination is more pronounced, see in Fig. 4.26. In higher p_T bins, the correlated background is negligible.

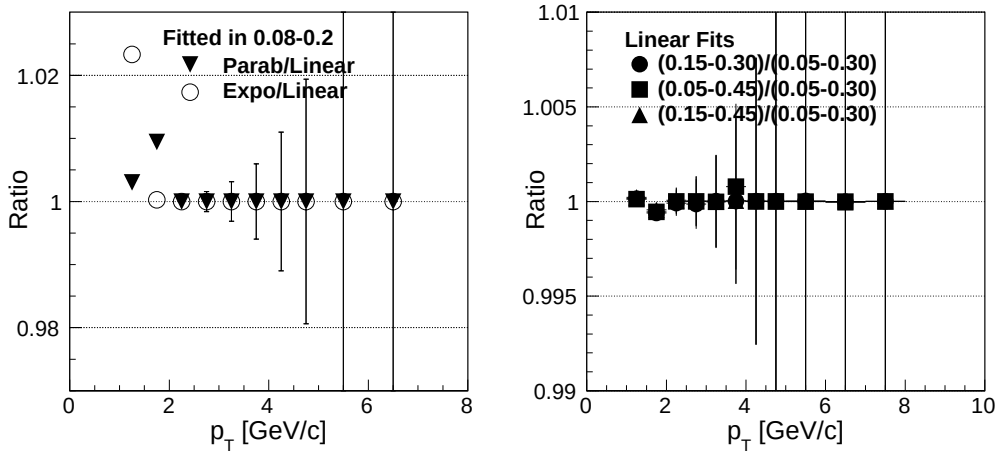

Figure 4.26: Left: The extracted yield ratio by using different functional forms to describe the conversion and hadron contamination background. Right: Sensitivity of extracted π^0 yield to the changes in the fit range of correlated background. The background was approximated by a linear function. Starting point of the fit varied from 0.02 GeV/c^2 to 0.08 GeV/c^2 and the end point was changed from 0.2 GeV/c^2 to 0.3 GeV/c^2. The plot shows the ratio of the π^0 yield extracted with a modified fit range of background to the yield which we get by the standard analysis (fit range 0.08 - 0.2 GeV/c^2).

Changing the interval in which the yield is extracted

The yield is extracted by integrating the bin content in 2σ regions around the peak. The Gaussian fit on the π^0 peak is used only to estimate the limits of the integral. However, the π^0 peak is not a perfect Gaussian and the binning of the invariant mass ($M_{\gamma\gamma}$) is finite, what introduce an uncertainty when extracting the raw counts of π^0's. The magnitude of the uncertainty is studied by varying the extraction interval. We extracted the yield from 3σ region and compared with our original yield. Estimated uncertainty following from the yield extraction is 2% in minimum bias and about 3% int the most central collisions, see Fig. 4.27 .

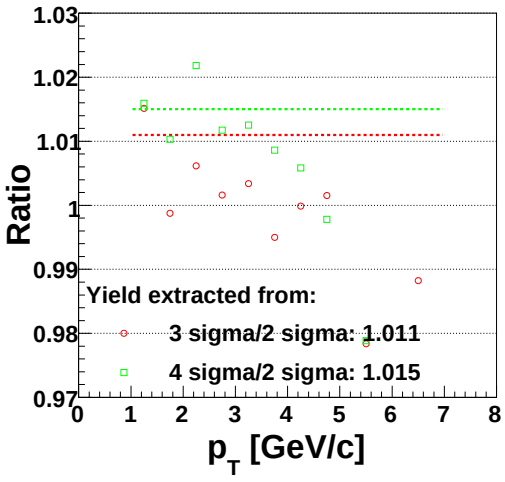

Figure 4.27: Ratio of π^0 yield obtained in 3 σ window around the mean of the π^0 peak to the yield obtained from 2 σ window which is used in this analysis.

4.5.2 Obtaining Systematic Errors from the Simulation

In this section, we focus on the systematic uncertainties from using the Monte Carlo to describe the correction function to the measured raw counts of π^0's. In addition, we study the photon cluster identification method. Additional systematic uncertainties are originating from the conversion on the material before the EMCal detector. The photon conversions produce an e^+e^- pair, which is strongly affected by the magnetic field. Additional systematic uncertainties are due to off-vertex π^0's, which originate from secondary decays of other particles (e.g. K^0_{short}). These systematical uncertainties are studied with the simulation procedures as described bellow.

Energy scale

The difference of energy scale between the simulation and the real data is 1-1.5% (see Fig. 4.4 and Fig. 4.5). During the embedding procedure it is possible to adjust the energy scale of the simulated π^0 by a certain factor. Due to the steeply falling p_T function of the measured spectrum, a small uncertainty in the energy scale can result in a large uncertainty in the spectrum, see Fig. 4.3. The uncertainty was studied using the embedding procedure with three shifted energy scales to mimic the uncertainty, $\delta p_T/p_T = 1.0, 1.5$ and 2.0%. In the embedding procedure, the simulated p_T distribution is uniform and it is weighted by the measured spectrum. The two p_T spectra at $\sqrt{s_{NN}} =$ 39 and 62.4 GeV have different slopes, which results in larger uncertainties at steeper slopes. The results of the energy scale studies were summarized in Fig. 4.3. We conclude that the energy scale uncertainty depends on the slope of the p_T spectrum and it is estimated to be around 17% and 14% at $\sqrt{s_{NN}} = 39$ and 62.4 GeV at fixed $p_T = 5$ GeV/c for the "input" energy scale uncertainty of $\sim 1.5\%$.

Systematic uncertainties obtained from the $\chi^2 < 3.0$ cut

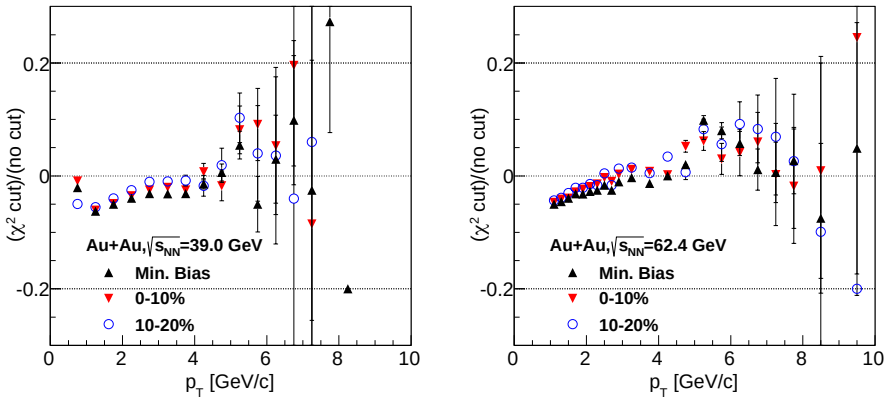

Figure 4.28: Ratio of the corrected spectrum using $\chi^2 < 3.0$ cut and no identification cut. The ratios are presented in Au+Au minimum bias collisions and two centrality classes at $\sqrt{s_{NN}} = 39$ GeV (left panel) and at $\sqrt{s_{NN}} = 62.4$ GeV (right panel).

The identification of the EMCal clusters is reducing the combinatorial background. We use in our analysis the $\chi^2 < 3.0$ cut on each cluster which can introduce a systematic uncertainty. The uncertainty was studied using the fully corrected spectrum with the χ^2 cut and without any PID requirements on the clusters. The π^0 yield can be reconstructed separately for both of the χ^2 and "no-cut" case. Fig. 4.28 shows the ratio of the fully corrected yields obtained using the two different PID requirements, which is no larger than 4-5%. The low-p_T part of the spectrum is more influenced

from the background fluctuations, which is suppressed when using a PID cut on the clusters. The estimation of the uncertainty resulted from the PID cut on the clusters is estimated to be around 3%.

Functional form of the correction factor

In our analysis we correct the raw yields with a parametrized correction factor $C^{\pi^0}(p_T)$ function for acceptance, efficiency and smearing effects as in Eq. (4.7). Different parametrization of the correction factor can produce some uncertainties in the final result. In order to estimate the uncertainty we compared the parametrized function form with the individual points obtained from the acceptance and efficiency studies.From the results we estimate the error to be 1-2 % for all p_T bins (see Fig. 4.29).

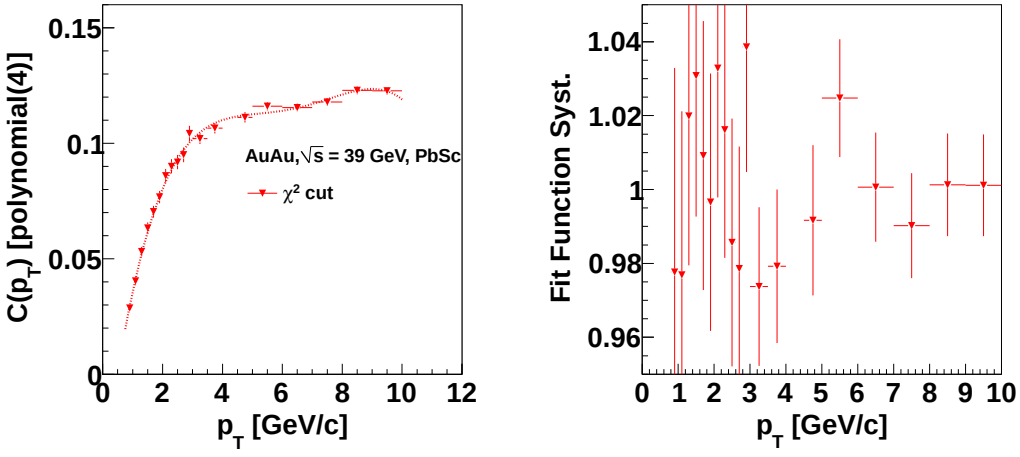

Figure 4.29: Left panel: Combined acceptance and efficiency correction for minimum bias in the form of a histogram and a smooth function (4th order polynomial). Right: Ratio of the histogram to the smooth function. The scatter of points around one gives an estimate of the systematic uncertainty in parametrization of $C^{\pi^0}(p_T)$.

Using different centrality-dependent p_T slopes for efficiency correction

During the embedding procedure, we assumed that the slope of the p_T spectrum in every centrality bin follows the slope of the minimum bias p_T spectrum. Different centrality bins can have, however, slightly different p_T slopes (see later in Tab. 6.1). This slightly affects the smearing term of the correction function which is used to correct invariant mass spectrum on reconstruction efficiency, acceptance and momentum smearing. Using proper slopes would, however, have only small effect of the order of 1% on the final results as can be judged from Fig. 4.30. There we show the ratio of a

correction function calculated with the correct slope to the correction function based on the minimum bias slope.

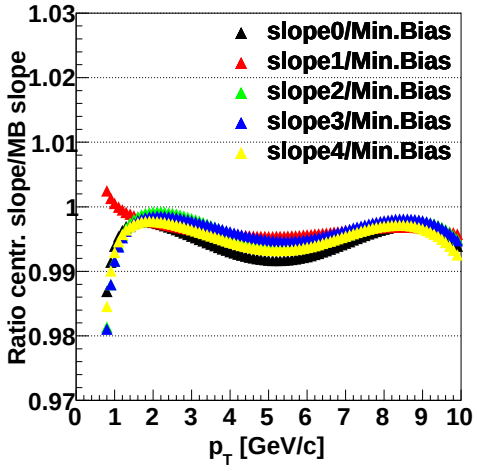

Figure 4.30: Ratio of a correction factor calculated with the proper slopes for a given centrality and the correction factor which we obtained based on slope of minimum bias sample. Systematic error which we introduce when we use the correction factor estimated from the minimum bias fit is in average below 1%.

Conversion systematic error

The estimation of the systematic errors from the conversion rely only on the simulation. From the previous analysis (in 2004) the "net loss" of π^0 due to the conversion was estimated to be 3%. The opening angle of the conversion pair, $\theta \sim 2m_e/p_T$, which is very small in the measured region of $p_T > 1$ GeV/c, thus resulting a single cluster in the EMCal. However, the magnetic field bends the conversion pairs and significantly enhances the opening angle. For this reason the most contribution of systematic uncertainties from conversion process are those which happens inside the magnetic field. In 2010, the HBD detector was installed inside the magnetic field, which increases the photon conversion in comparison to previous runs. The systematic uncertainty from the HBD is 4%. The total net loss in this analysis is 7%, which are included in the reconstruction efficiency of the π^0, see Eq. (4.5).

Off-vertex π^0

The largest source of off-vertex π^0s are the K^0_S. The K^0_S has a very short lifetime and its decay mode, $K^0_S \to \pi^0\pi^0$ (30%) generates the most of off-vertex π^0s. Because

of the K_S^0 short lifetime (0.89×10^{-10}s), the π^0s are still reconstructed in the EMCal and this effect has to be included in the systematic errors. The observation of the off-vertex π^0's is almost p_T independent due to the limited acceptance of the detector. The very low momentum K_S^0 decays close to the vertex, however the opening angle of the two π^0 is quite large. At higher momentum region the π^0's are more collimated, thus increasing the probability to observe them in the acceptance. The interpolation of these two effects results in the observed p_T independence of the off-vertex π^0's, and the systematic error is estimated at 1.5%.

4.5.3 Summary of systematic errors

Systematic Error Summary	$p_T < 2$ GeV/c	$2 < p_T < 5$ GeV/c	$p_T > 5$ GeV/c
Normalization of combinatorial bkg	4%	1%	1%
Hadron bkg	2%	<0.01%	<0.01%
2σ interval of extracting raw π^0	3%	3%	3%
Energy scale	9%(6%)	10% (9.%)	14.5% (10%)
Particle identification	3%	3%	3%
Correction function	2%	2%	2%
Smearing uncertainty	2%	1%	1%
Conversion	4%	4%	4%
Off-vertex	1.5%	1.5%	1.5%
Total	12.1% (10.0%)	11.9% (11.1%)	15.9% (11.9%)

Table 4.2: Summary of the systematic errors of the π^0 measurement at $\sqrt{s_{NN}} = 39$ GeV and 62.4 GeV (in brackets when the value is different).

4.6 Measurement of η at $\sqrt{s_{NN}} = 62.4$ GeV

In this section, we describe the analysis of η meson reconstruction in Au+Au minimum bias collisions at $\sqrt{s_{NN}} = 62.4$ GeV. The goal of the analysis is to obtain the η/π^0 production ratio which is important in further analysis. The η meson is reconstructed via the two photon decay channel which is very similar to the previous π^0 reconstruction. The major differences are the different mass (~ 550 MeV/c^2) and the branching ratio ($\sim 39.3\%$). In addition, in the η meson reconstruction is a significant increase in correlated background, which means also bigger systematic uncertainties due to the subtraction of this background.

4.6.1 Invariant Mass Reconstruction of η meson

The same cluster cuts are required for eta meson reconstruction as those applied in π^0 analysis. Due to the higher mass of the η meson, the typical opening angle is larger than that in π^0 case at same p_T, see Eq. (A.12). Thus, application of the same cluster pair cuts, namely requirement that both clusters are in the same sector, results in significant reduction of signal for $p_T < 5$ GeV/c. On other hand, the higher p_T reach is limited by the statistics. In this analysis we use two different analysis:

- 'Single' Reconstruction: Both cluster are in the same sector (same as in π^0 case)
- 'Double' Reconstruction: The cluster pairs are required to be in same or neighboring sectors, except that combination of PbSc and PbGl sectors are not allowed.

The invariant masses of η mesons are reconstructed in four p_T bins with the two cut methods, see in Fig. 4.31. The same event mixing technique was used to subtract the combinatorial background which was normalized in mass bins $397.5 < M_{\gamma\gamma} < 497.5$ MeV/c^2 and $597.5 < M_{\gamma\gamma} < 697.5$ MeV/c^2. The raw η counts are reconstructed in the two-σ window.

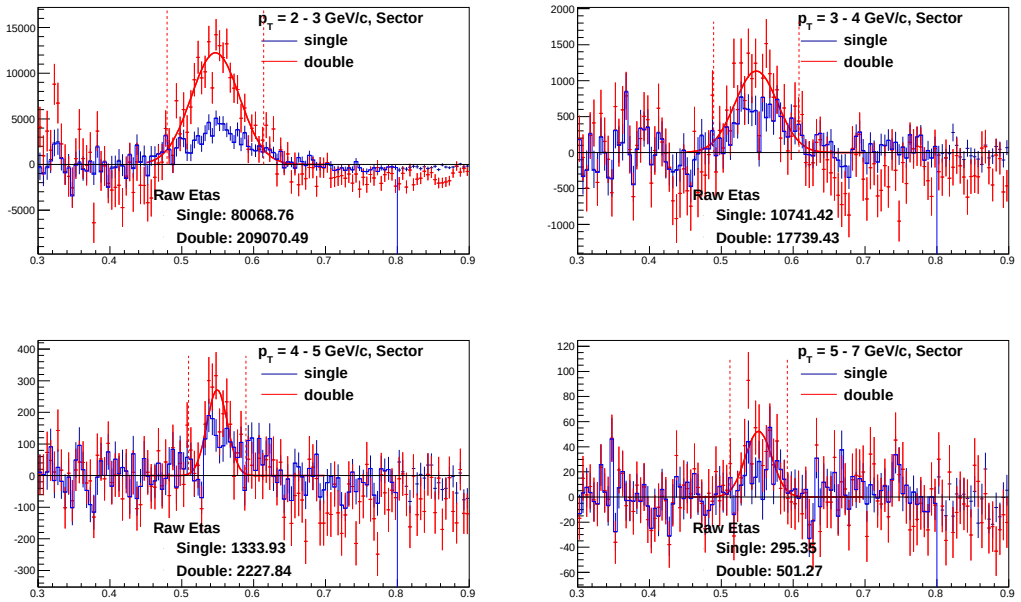

Figure 4.31: The subtracted (from combinatorial background) invariant masses of η meson in four p_T bins indicated on the figures in Au+Au minimum bias collisions at $\sqrt{s_{NN}} = 62.4$ GeV. The "single" cut (blue points) are the cluster pairs in same sector, the "double" cut (red points) are the cluster pairs in same or neighboring sectors.

4.6.2 Efficiency study for the η meson reconstruction

In order to estimate the acceptance, efficiency and smearing correction function (Eq. (4.7)), the same simulation procedure was used as in Sec. 4.2. For the simulation, 12M single η mesons were generated in pseudo-rapidity window of $[-0.5, 0.5]$, 2π angular distribution and with a flat p_T distribution between $0 < p_T < 10$ GeV/c. The simulated η meson events were embedded into real events to study the multiplicity effect on efficiency study.

The absolute energy scale calibration was inherited from the π^0 efficiency study. The smearing and bin-shift correction needs to have a realistic p_T spectrum as it was explained in the Sec. 4.2. The smearing and bin-shift correction is an iterative process and for the first iteration we used the π^0 p_T spectrum obtained in Au+Au at $\sqrt{s_{NN}}$ = 62.4 GeV.

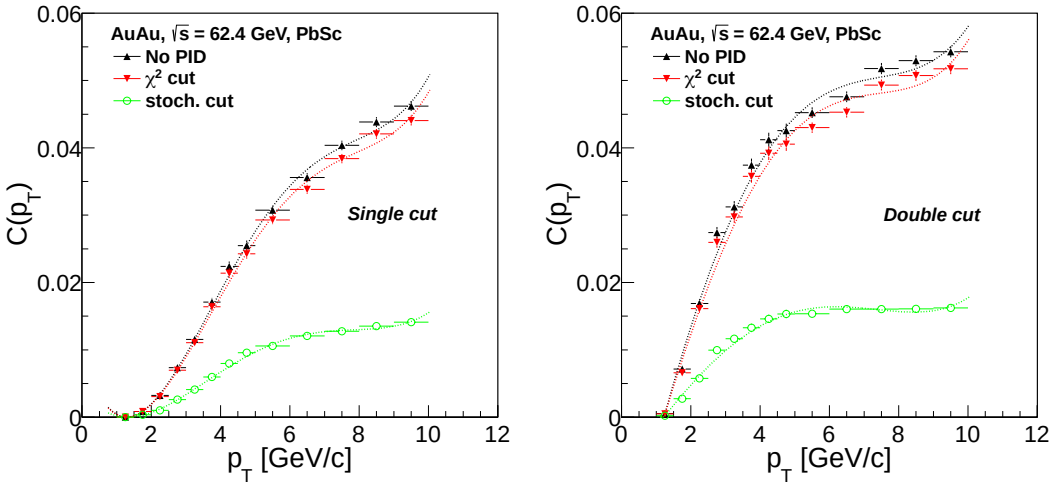

Figure 4.32: Acceptance, reconstruction efficiency and smearing correction function (see Eq. (4.7)) for η meson for "single" cut (left panel) and "double" cut (right panel) in Au+Au collisions at $\sqrt{s_{NN}}$ = 62.4 GeV.

Fig. 4.32 shows the correction function obtained from the embedding study of η mesons in Au+Au minimum bias collisions at $\sqrt{s_{NN}}$ = 62.4 GeV. The result is done for three different cluster identification methods, and they are showing the expected magnitude considering their identification efficiencies.

4.6.3 Measured η Invariant Yield and η/π^0 Ratio at $\sqrt{s_{NN}}$ = 62.4 GeV

The invariant yield of the η meson was reconstructed the same way as for the π^0's (see Eq. (5.2)). Fig. 4.33 left panel shows the reconstructed yield using only the 2γ decay

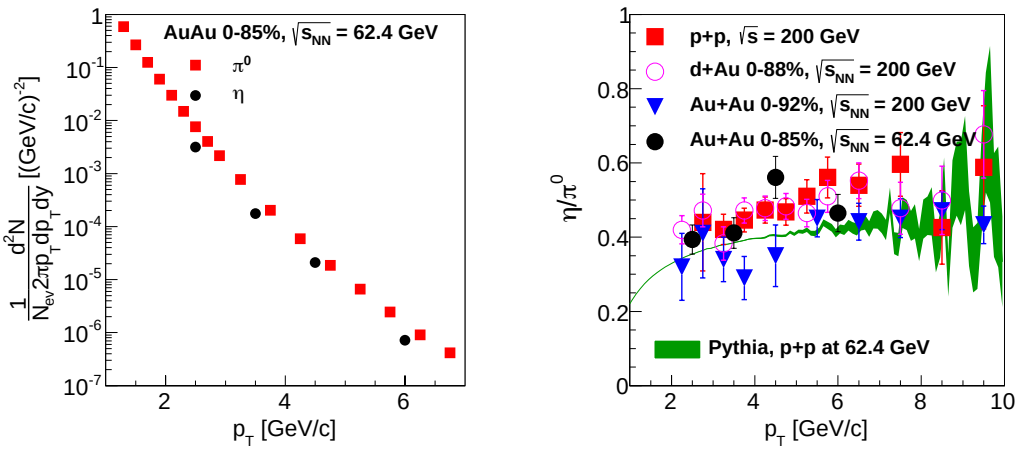

Figure 4.33: Left: Invariant yield of the η and π^0 mesons in Au+Au minimum bias collisions at $\sqrt{s_{NN}} = 62.4$ GeV. Particle production ratio of η and π^0 mesons in function of p_T in different collision systems (p+p, d+Au and Au+Au) at $\sqrt{s_{NN}} = 200$ GeV and 62.4 GeV. The dotted line corresponds to the generated particle ratio by PYTHIA8 event generator.

p_T [GeV/c]	η/π^0 ratio	stat+syst error
2.5	0.394	0.039
3.5	0.391	0.039
4.5	0.560	0.056
6	0.465	0.050

Table 4.3: The measured η/π^0 ratio at four different p_T values in Au+Au minimum bias collisions at $\sqrt{s_{NN}} = 62.4$ GeV.

channel. The invariant yield of η was compared with the corresponding π^0 invariant yield in Au+Au minimum bias collisions at $\sqrt{s_{NN}} = 62.4$ GeV. Fig. 4.33 shows the measured η/π^0 ratio in comparison with the previously measured particle ratios in p+p collisions at $\sqrt{s} = 200$ GeV, d+Au collisions at $\sqrt{s_{NN}} = 200$ GeV and Au+Au collisions at $\sqrt{s_{NN}} = 200$ GeV. The data are compared with the calculated ratio from the PYTHIA8 event generator. The final results are summarized in Tab. 4.3 and the data is in agreement within the uncertainties with the previous results at $\sqrt{s_{NN}} = 200$ GeV and the PYTHIA8.

Chapter 5

Measurement of direct-γ at $\sqrt{s_{NN}} = 62.4$ GeV

In this section, the analysis of the direct photons is described in Au+Au collision at $\sqrt{s_{NN}} = 62.4$ GeV. The analysis is done by the statistical subtraction method, which is based on the subtraction of decay photon contributions from the inclusive photon distribution. The main contribution to the decay photons are the neutral mesons, e.g. $\pi^0 \to 2\gamma$, $\eta \to 2\gamma$ and $\eta \to 3\pi^0$. The decay kinematics of the neutral mesons into photons is discussed in Sec. A.1.2, where we study the probability distributions of the decay photons from different channels of neutral meson. The procedure of the subtraction method can be described in the following steps:

- Generate the distribution of all photon-like clusters
- Correct for non-photonic clusters which pass the identification cuts
- Reconstruction of neutral meson photon decay clusters
  - Reconstruction of decay photon distribution from $\pi^0 \to 2\gamma$ decays
  - Additional decay photon contributions according to their cross section: η, ω, ...
- Subtraction of decay photon distribution: $\gamma_{\text{direct}} = \gamma_{\text{inclusive}} - \gamma_{\text{decay}}$
- Acceptance, efficiency and smearing correction of the raw direct-photon distribution

In the previous measurements [190], the raw distribution of inclusive photon were first corrected for the acceptance, efficiency and smearing. For this purposes, the single photon Monte Carlo simulation (as in Sec. 3.3) were used to estimate the correction factors. The corrected spectrum of decay photon was reconstructed from the neutral

meson decays. After that the decay photon contribution was subtracted from corrected inclusive photons. Thus, the obtained direct photon spectrum was already corrected for the detector effects.

However, in this work we follow a slightly different procedure. The change in the method was made after the consideration of the Monte Carlo simulation, where a large difference is observed comparing the correlated and uncorrelated photon efficiencies (see later in Fig. 5.6). The inclusive photons are a mixture of photons coming from hadron decays (correlated photon pairs) and direct photons (uncorrelated single photons). The acceptance and efficiency correction of correlated and uncorrelated photons are different. The mixture of the two types of photons is unknown at first, thus, the estimation of the corrections for inclusive photon distribution are unreliable. Therefore, the decay photon distribution is generated with the simulation at the raw data level. In this analysis, the subtraction of the raw decay photon distribution is done on the raw distribution of the inclusive photon distribution. After subtraction, only the raw distribution of direct photon remains, which are corrected according to a single photon Monte Carlo simulation.

5.1 Inclusive Photons Distribution

The inclusive photons are determined by the different photon identifications used on clusters, see in Sec. 2.4.3. In this study, the $\chi^2 < 3.0$ and stoch_2 identification cuts are considered on all clusters. The advantage of the stoch_2 cut is that it reduces the hadronic contamination in low-p_T region better than the χ^2 cut. The disadvantage of the stoch_2 cut is the $\sim 50\%$ efficiency (Fig. 2.12) on the real photon cluster which will greatly limit the high-p_T region due to the limited statistics. The raw photon yields with the different cuts are shown in Fig. 5.1.

5.1.1 Hadron contamination

The low-p_T part of the inclusive photon cluster distribution is contaminated by hadrons which leave part of their energy in the EMCal (see more in Sec. 2.4.3). However, at higher momenta hadrons often are minimum ionizing particles (MIP) particles. Few of the hadrons can start their hadronic shower already within the EMCal. The hadronic shower contains mainly pions: π^+, π^- and π^0. The electromagnetic part of hadron showers is an important factor in hadronic calorimeters (e.g. [191]). The π^0 part of the hadronic shower can leave a larger energy deposit in the EMCal, thus affecting the low-p_T part of the inclusive photon distribution.

The hadron contamination was studied in (1) GEANT simulations with a realistic (measured) hadron p_T spectrum and (2) the identified hadron tracks with matched clusters in EMCal from low-multiplicity events. The hadrons deposit typically less

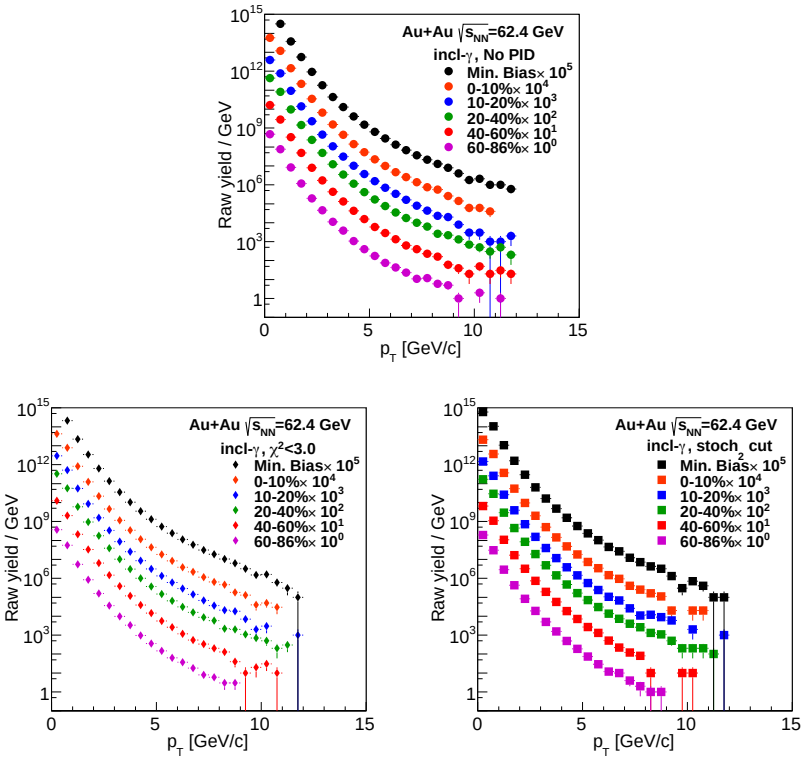

Figure 5.1: The raw inclusive photon yields measured in PbSc in Au+Au minimum bias collisions and different centrality bins at $\sqrt{s_{NN}} = 62.4$ GeV as a function of p_T. The top panel represents the yield without identification cuts on the photon-like clusters, the bottom two panels are with identification cuts: $\chi^2 < 3.0$ (left) and stoch$_2$ (right).

energy as their momentum ($E_{\rm cluster} \ll p_T^{h^\pm}$), while photons and electrons deposit almost all of their energy ($E_{\rm cluster} \approx p_T^{\gamma,e^\pm}$). The detector response for different particles were shown in Fig. 2.8 and in Fig. 2.9.

In order to estimate the hadron contamination in the photon measurement, we used the measured hadron spectra and simulated the distribution of the photon-like clusters with different PID cuts as a function of the cluster energy, $N_h(E_{\rm cluster})$. From these studies we derived the hadron contamination correction as $c(E_{\rm cluster}) = N_\gamma/(N_\gamma + N_h)$. In Fig. 5.2 we summarize the simulated result of hadron correction function with different PID cuts as a function of the deposited energy. The hadron contamination is significant at lower transverse momentum, and in addition, the rejection factor largely depends on the identification of the cluster.

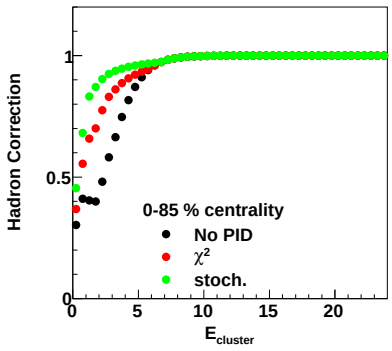

Figure 5.2: Hadron correction function to inclusive photons as function of the energy of the cluster. The different colors indicate the three identifications on the cluster, black without any identification, red with $\chi^2 < 3$ and green with the stoch$_2$ cut.

5.2 Determination of Decay Photon Spectrum

Decay photons can be divided into two groups. The main contribution to the decay photons ($\sim$ 80%) are the π^0 decays. The other neutral mesons decaying to π^0 or directly to γ. The decay photon contributions are reconstructed from the single particle simulation embedded into real events.

5.2.1 Decay photons from π^0

The description of the kinematics of the π^0 decay into two photons is explained in Sec. A.1.2. The analytical study of decay photon distribution (probability) as a function of the photon energy (E_T^γ) of a fixed π^0 momentum ($p_T^{\pi^0}$) shows a uniform photon energy distribution with the height of $2/p_T^{\pi^0}$ in the region of $0 < E_T^\gamma < p_T^{\pi^0}$. However, the analytical solution is not applicable in our data analysis, as the decay photon-like cluster distribution in the real detector is different from that of the non-correlated (single) photons, particularly at high p_T. The difference is due to the (necessarily) finite granularity and resolution of the EMCal as well as to the inherent limits of any clustering algorithm operating on real-life data. The PHENIX GEANT (see Sec. 3.3) simulation is used to reconstruct more realistic decay photon probabilities. The 15M π^0 were simulated in $0 < p_T < 15$ GeV/c in $\eta \in [-0.5, 0.5]$ and 2π in azimuth. Due to the limited acceptance of the detector, one or both photons can escape without being detected. The material in the front of the EMCal can cause photon conversion which is also part of the simulation. The conversion of the photons can cause multiple clusters in the EMCal detector. The simulated events are merged in the real events by the embedding procedure (see Sec. 3.3), which assures the realistic multiplicity environment as in the real data. The energy deposits made by the remnants of the original π^0 are

reconstructed into clusters using the same clusterization algorithm as for the inclusive photon-like clusters (see Sec. 5.1). All the clusters which carry a part of the energy of the original π^0's are considered in the reconstruction of the decay photon probabilities. In contrast to the analytical study of the decay photon probabilities in Sec. A.1.2, the realistic environment of the EMCal is considered: realistic material budget in the front of the detector, magnetic field, clusterization algorithm, photon identification of clusters (χ^2, stoch$_2$). Fig. 5.3 shows the obtained decay photon probabilities at three different π^0 p_T bins.

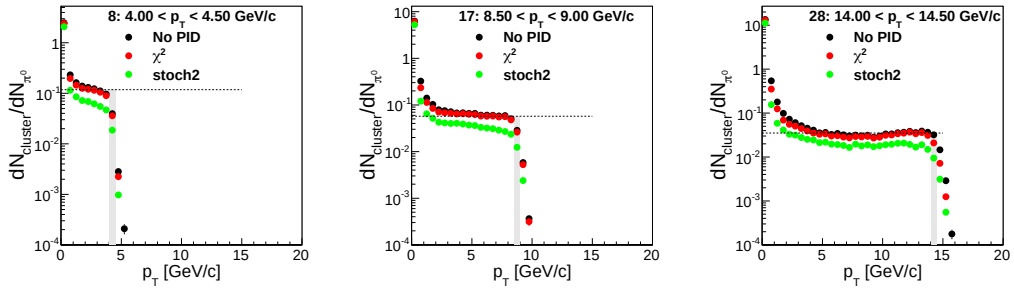

Figure 5.3: The decay photon-like cluster probability distribution as a function of photon cluster p_T^{cluster} for fixed π^0 transverse momentum bin: at low-momentum $4.0 < p_T < 4.5$ GeV/c (left), at mid-momentum $8.5 < p_T < 9.0$ GeV/c (middle) and at high-momentum $14.0 < p_T < 14.5$ GeV/c (right). The photon-like clusters are identified using three different cuts as no-PID, χ^2 and stoch$_2$ (see Sec. 2.4.3). The simulated π^0s are in three different p_T bins indicated on the panels and illustrated with the gray band. The dashed line illustrate the analytical $(2/p_T)$ decay probabilities.

The reconstructed "decay photon-like cluster probabilities" of π^0's already contain the acceptance and smearing effects of the detector as well as the clusterization artifacts. A large increase in the very low energy clusters is the results of the clusterization algorithm. Due to the the fluctuation in the energy deposited by the electromagnetic shower, the edges of the showers are detached from the main part and reconstructed as separate clusters. In the high multiplicity of the heavy ion collisions, clusters with larger energy than the initial π^0 appear when the photon deposit is combined with the energy deposited by an other particle. Reaching the $p_T > 10$ GeV/c π^0's (see in Fig. 5.3 right) the clusters from the symmetrical decays are starting to merge into one cluster. This effect appears in the realistic measurements, and will explain the decrease of the probability of clusters with $E_1 = E_2 \approx p_T/2$ and simultaneously the increase of the probability at around $(E_1 + E_2) \sim p_T$.

Decay photon distribution is reconstructed by folding the corrected π^0 spectrum (obtained from invariant yield in Fig. 4.8) with the probability functions of each p_T bin (see Fig. 5.3) for different PID cuts. In Fig. 5.4 summarize the decay photons

raw yield distribution using different PID cuts in minimum bias and in five centrality classes. The π^0 spectrum is fitted with a power law function from $p_T > 4$ GeV/c and used to extrapolate for $p_T > 10$ GeV/c. Note, that in this analysis we consider the decay photons only under $p_T < 10$ GeV/c. However, higher p_T π^0's can still contribute to the decay photon spectrum in this region, which is negligible due to the steeply falling p_T spectrum.

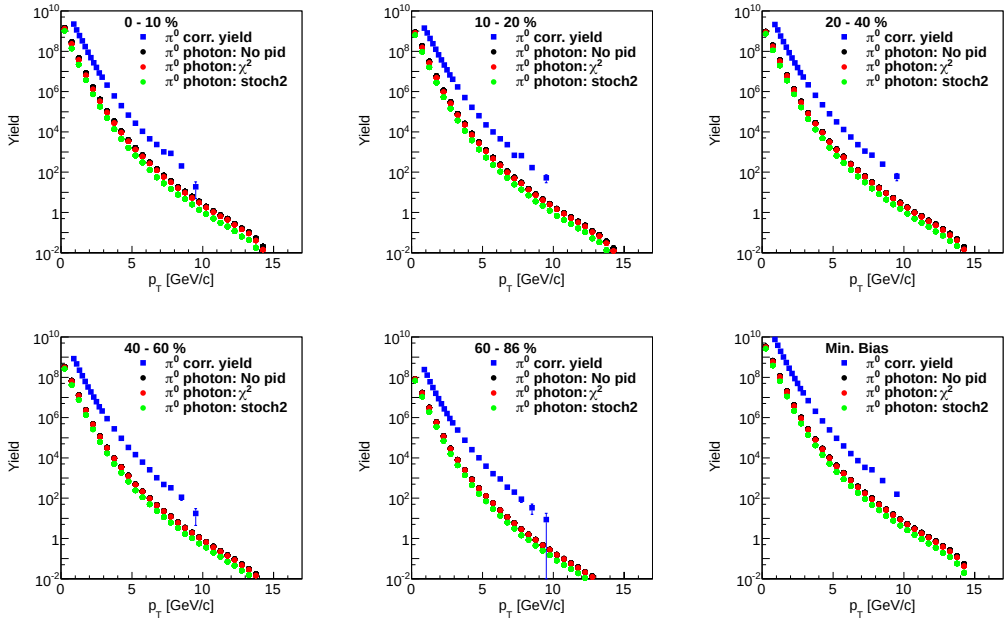

Figure 5.4: The π^0 decay photon raw cluster distribution using three different cuts on clusters: no-PID, χ^2 and stoch$_2$. Squares are the π^0 spectrum from Eq. (5.2) except the correction for N_{event} and $1/p_T$.

5.2.2 Remaining decay photon contributions

Other neutral mesons decaying via γ channels has to be added to the decay photon raw cluster distribution. One large contribution is coming from η mesons. The η probabilities are reconstructed with the same procedure as the π^0 probabilities. The neutral η decaying to two-photons with branching ratio of 39.31% has same kinematics as π^0 decay. The merging of two clusters into one single cluster occurs at higher p_T as mentioned in Sec. 4.6, due to the higher mass.

The other channels which decay to π^0 have further decays to γ which contribute to the decay photon distribution. However, the lifetime of η decay is $\tau_{1/2} \sim 5.0 \cdot 10^{-19}$s in what time the light would travel $c\tau_{1/2} = 1.499 \cdot 10^{-10}$ $m \sim 0.15$ nm. The short decay time of the η meson means that the three π^0's already contribute to the measured π^0

spectrum and therefore to the decay γ spectrum derived from it. The results of the different probability distributions are shown in Fig. 5.5. The kinematics of the η meson decays into photons are discussed in Sec. A.1.3. The decay photon distribution is not flat as a function of p_T^{cluster} due to the three-body decay channels (see in Fig. A.5).

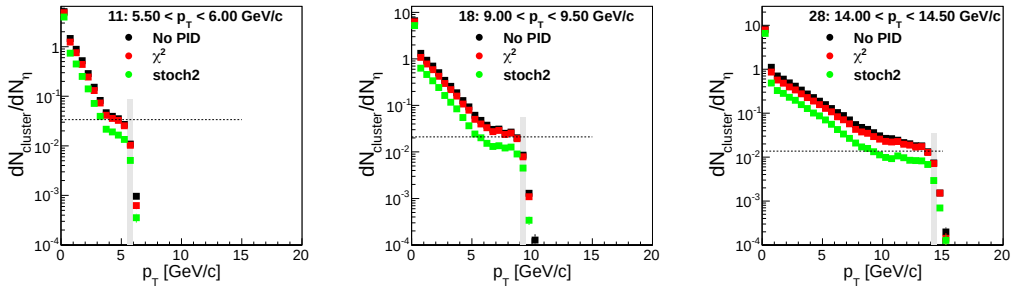

Figure 5.5: The η decay probability using three different cuts on clusters: no-PID, χ^2 and stoch$_2$. The simulated η are in three different p_T bins indicated on the panels and illustrated with the gray band. The dashed line represents the analytical solution for 2γ decay (as in π^0 case) normalized with the branching ratio ($\sim 39\%$).

The measurement of the η spectrum was discussed in Sec. 4.6.3. The decay photon distribution was reconstructed using the $\eta/\pi^0 \sim 0.45$ (see in Fig. 4.33) convoluted with the π^0 spectra. It is assumed that the ratio does not change in the different centrality bins. Due to the branching ratio of the 2γ channel ($\sim 39\%$), the obtained spectra are further normalized by the 0.39 factor to obtain the real decay photon distribution.

5.3 Direct Photon Raw Yield

Raw direct photons from the experimental point of view are defined as the $\gamma^{\text{raw}}_{\text{direct}} = \gamma^{\text{raw}}_{\text{incl}} - \gamma^{\text{raw}}_{\text{decay}}$, where all decay photon contributions are subtracted from the inclusive photons, see Fig. 5.7. As we described in the introduction, the subtraction of decay photon contribution from inclusive photons is done on the raw cluster level. We emphasize that this procedure is different from the previously done measurements. The difference of the acceptance and efficiency effects of correlated photons were examined using the photon distribution from the neutral pions, while single photons were used for the uncorrelated photon studies.

Fig. 5.6 shows the ratio of efficiencies of the uncorrelated and correlated photons. The correlated photons originated from high-p_T neutral pions are closer to each other, even merged into one cluster. The clusterization algorithm is not necessary able to distinguish and reconstruct the correct geometry and energy of the two clusters. The two photon energy deposits are merged into one cluster while the peripheral parts can be reconstructed as separate low energy clusters. This explains the excess of low-

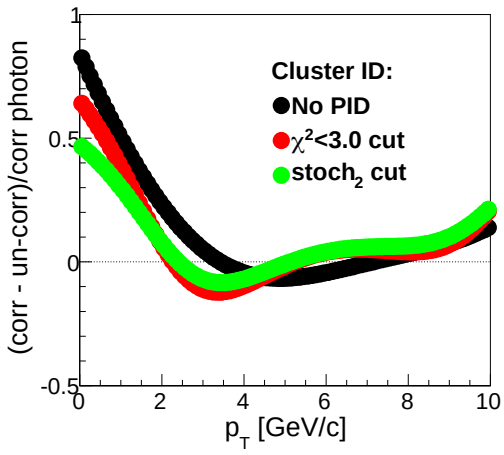

Figure 5.6: Different photon efficiency ratios obtained from correlated photon pair (neutral pion decays) and uncorrelated photons (single photons). The efficiencies were done using three different cluster identifications: No PID, $\chi^2 < 3.0$ cut and stoch$_2$.

and high-p_T part of the efficiency, shown in Fig. 5.6. The results show also strong p_T dependence in the efficiencies, up to $\sim 20\%$ difference in the high-p_T region.

Other decay photon contributions are estimated at few % which is added into the estimation of the decay photon contributions. The subtraction on the raw cluster level assures the remaining photon-like cluster distributions are only those of uncorrelated (direct) photon contributors.

5.4 Correction Function for Direct Photons

In this section, we reconstruct the acceptance, reconstruction efficiency and smearing correction, so called "correction function" similar to those for π^0 reconstruction in Sec. 4.2. After the subtraction of the decay photon background, only direct (or single uncorrelated) photons remain.

The correction function for direct photons were constructed in similar way as for the neutral pion corrections in the Sec. 4.2:

$$C^{\gamma}(p_T) = S^{\gamma}(p_T, p_T^{\rm meas}) \times \varepsilon^{\gamma}_{\rm efficiency}(p_T) \times Acc^{\gamma}(p_T) = \frac{N^{\gamma}_{\rm smeared}(p_T^{\rm meas})}{N^{\gamma}_{\rm all}(p_T)}\,, \qquad (5.1)$$

where the $S^{\gamma}(p_T, p_T^{\rm meas})$ refers to the smearing effect due to the finite energy resolution of the calorimeter, $\varepsilon^{\gamma}_{\rm efficiency}(p_T)$ is the efficiency of the reconstruction of photons and $Acc^{\gamma}(p_T)$ is the acceptance effect. In case of the photons, the transverse momentum is equal to the transverse energy, $p_T = E_T$.

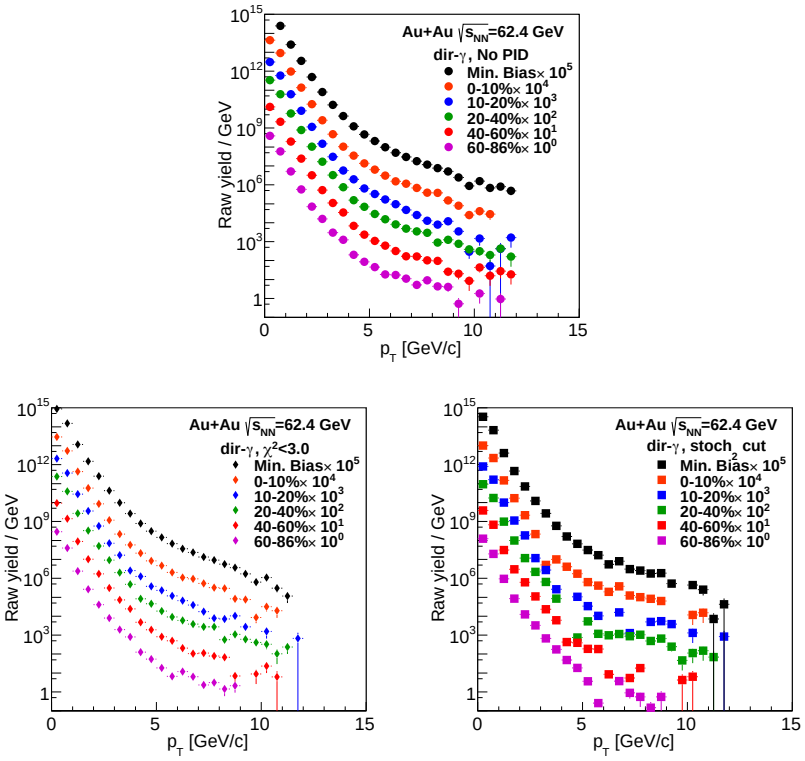

Figure 5.7: The raw direct photon yields ($\gamma_{\rm dir} = \gamma_{\rm incl} - \gamma_{\rm decay}$) measured in PbSc in Au+Au minimum bias collisions and different centrality bins at $\sqrt{s_{NN}} = 62.4$ GeV as a function of p_T. The panel in top is the yield without identification cuts on the photon-like clusters, the bottom two panels are with identification cuts: $\chi^2 < 3.0$ (left) and stoch$_2$ (right).

We simulate 15M single photons which were generated in $0 < p_T < 15$ GeV/c bin and in $\eta \in [-0.5, 0.5]$ and 2π azimuthal distribution. We note that the absolute calibration is already presented in the previous π^0 measurement. The simulated photons are embedded into real events and re-clusterized. Three different identification criteria for clusters were used on the MC, thus correction functions are evaluated in three versions. The identification criteria were the same as those used on the real data (see in Sec. 5.3). The correction functions are presented in Fig. 5.8.

5.5 Direct Photon Invariant Yield

In this section, the reconstruction of the direct photon invariant yield is discussed. At this stage, the raw inclusive photon yields are corrected for the hadron contamination. Furthermore, all the raw decay photon contributions are subtracted and only the raw

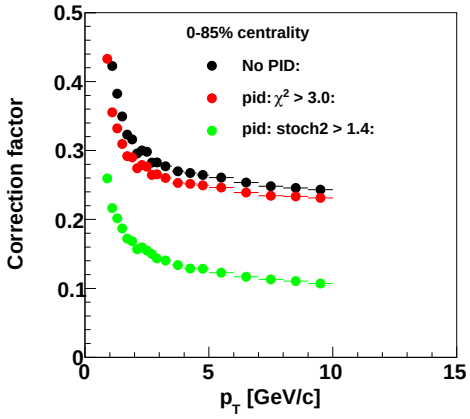

Figure 5.8: The correction function for direct photons in Au+Au minimum bias at $\sqrt{s_{NN}} = 62.4$ GeV reconstructed for different cluster identifications: no-PID, $\chi^2 < 3.0$ and stoch$_2$ cuts.

direct photon yield remains. These photons behave like uncorrelated photons, thus the correction function $C^{\gamma}(p_T)$ can be used (see in Fig. 5.8). Then the invariant yield of the direct photon is constructed as

$$E\frac{d^3\sigma}{dp^3} = \frac{1}{N_{\text{event}}}\frac{1}{2\pi p_T}\frac{\Delta N^{\gamma}}{\Delta p_T \Delta y}\frac{1}{C^{\gamma}(p_T)c_{\text{bin-shift}}}, \tag{5.2}$$

where N_{event} is the number of events. Similarly as in the π^0 analysis, we need to apply the bin shift correction because of the effects of finite binning (see Eq. (4.8)). The smearing and bin-shift correction is depending on the slope of the spectra as already discussed in the Sec. 4.2 for π^0 analysis. The process of obtaining the realistic spectrum and the correct smearing and bin-shift corrections is done iteratively. In the case of photons, we use as initial spectrum the power law slopes of the final π^0 spectra (Tab. 6.1).

Fig. 5.9 shows the obtained invariant yields of photons in Au+Au minimum bias collisions at $\sqrt{s_{NN}} = 62.4$ GeV, only the statistical uncertainties are shown. The invariant yields were reconstructed using all the three identification methods mentioned in previous chapters. The invariant yields in different centrality classes are not yet reconstructed.

5.5.1 Systematic Error Studies of Direct Photon Yields

We summarize the systematic errors resulting from the reconstruction of the direct photon yield, see Tab. 5.1. The choice of the cluster identification introduces a systematic uncertainty in the reconstruction of photon spectra. The energy scale uncertainty

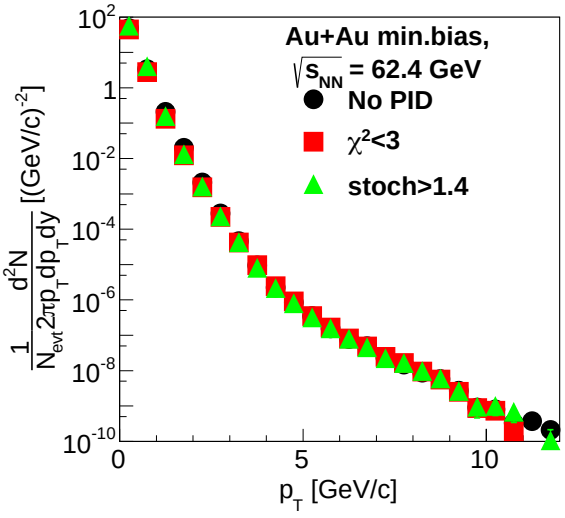

Figure 5.9: The invariant photon yield in Au+Au minimum bias collisions at $\sqrt{s_{NN}}$ = 62.4 GeV. Three different cluster identification methods were used to obtain the results: No-PID, $\chi^2 < 3.0$ cut and stoch$_2$ cut. Only the statistical uncertainties are shown. Please note that the analysis is still in progress, the results are not yet final.

(see Fig. 4.3) originates from the calibration of the photon-like clusters already discussed in neutral pion measurement, see in Sec. 4.2. Fig. 5.12 shows the ratio of invariant photon spectra with different cluster identifications.

Systematic Error Summary	$p_T < 4$ GeV/c	$p_T > 6$ GeV/c
Hadron bkg	10%	2%
Energy scale	8%	10%
Particle identification	10%	7%
Correction function	2%	2%
Smearing uncertainty	2%	1%
Conversion	5%	4%
Off-vertex	1.5%	1.5%
Total	18.4%	13.8%

Table 5.1: Summary of the systematic errors of the direct photon measurement in Au+Au collisions at $\sqrt{s_{NN}}$ = 62.4 GeV.

Conversion

Large number of photons are converted due to the material in front of the EMCal. The total conversion probability before the EMCal detector is about 15%. The resulting electron-positron pair propagates further and leaves an electromagnetic shower in the EMCal which is detected. However, the opening angle of the pair is very small, $\theta \sim m_e c^2/2$. The strong magnetic field can change the trajectories of the pair and enlarge the opening angle. Due to the magnetic field, the conversion pair leaves two separable clusters in the EMCal. If the conversion happens outside of the magnetic field, the electrons and positrons have very close impact positions ($d < 8$ cm) most of which will then end up in one single cluster, that also passes the photon PID cuts, i.e. will be counted, albeit with slightly different p_T (see below).

The magnetic field during the data taking was turned in the $+-$ setup, which means the inner and outer coils were opposed. The resulting strength of the magnetic field compared to different setups are shown in top panel in Fig. 5.10. The bottom panel in Fig. 5.10 shows the conversion probability due to the material in front of the EMCal. The magnetic field is negligible for distances larger than $r > 300$ cm.

In addition, the response of the calorimeter is known to be different for electrons and photons. Fig. 5.11 shows the mean energy deposited in the detector is less of the same momentum (p_T) electron-positron pair and a single photon. The mean of the smearing function for electron clusters is smaller than that for photon clusters by a factor of $\sim 3\%$. The total loss of the photons due to the conversions is estimated at $\sim 8\%$. The inclusive photon spectrum is corrected for the conversion loss of the photons. However, the uncertainty due to the correct estimation of the material budget is about 4-5%.

Off vertex Photons

Off-vertex photons are generated mainly by the long lived decays and photons from secondary interactions. The particles propagating through the material budget can emit a photon. The produced photons from the secondary interactions are dominant in the low-p_T region, $p_T < 2$ GeV/c. The high-p_T off-vertex photons originate from the decay photons of long lived particles (e.g. $K^0_S \to 2\pi^0$) and those are not included in the estimation of decay photon spectrum. The estimated uncertainty is about $\sim 1.5\%$ for $p_T > 2$ GeV/c from the background to the real photon measurement. Note that the decay photon contribution from K^S_0 in the region $p_T < 2$ GeV/c is increasing. However, the due to the large hadron contamination explained in next section, we do not consider the direct photon spectrum in the very low-p_T region.

Hadron Contamination

The hadron contamination was estimated using the Monte Carlo simulation, which includes both the hadron shower development and the detector response. The correc-

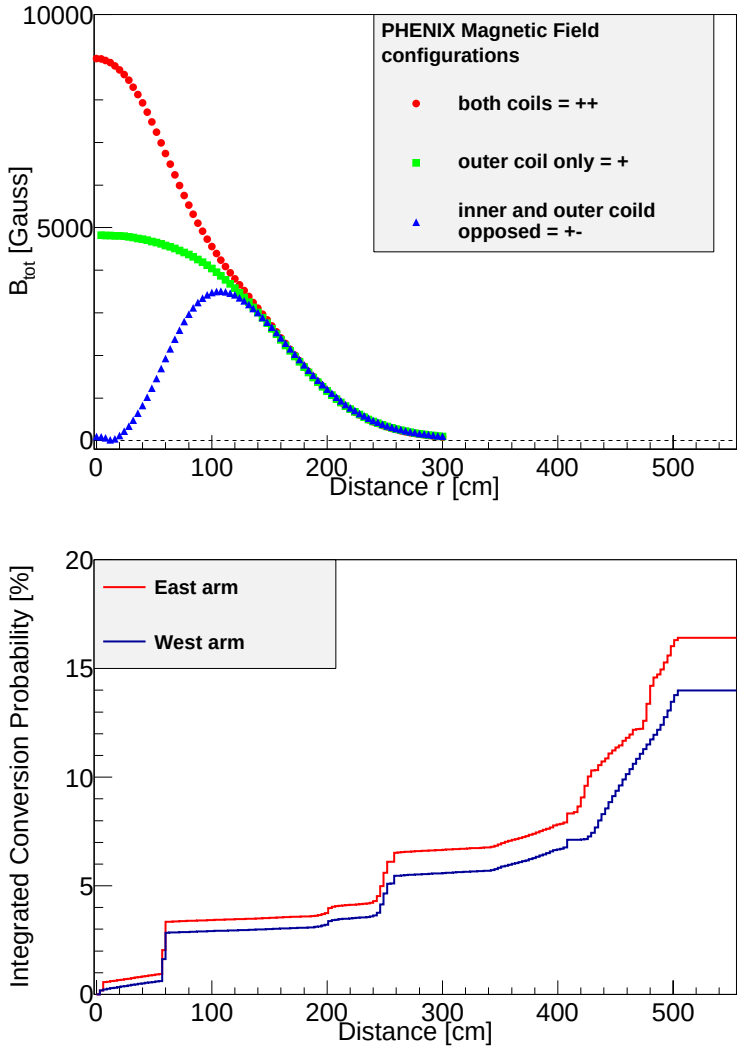

Figure 5.10: The different magnetic field strength (upper panel) and the integrated conversion probability (bottom panel) on the materials in West and East arms as a function of the distance from the interaction point.

tion on inclusive photon-like clusters, which we use to reduce the hadron contamination, largely depends on how well the simulation describes the real data. Two important factors need to be considered for the systematic uncertainties: the deposited energy by hadrons and the shower shape. The deposited energy is sufficiently described by the simulation as seen in Fig. 2.8 and in Fig. 2.9.

The different cluster identifications attempt to remove the hadron contamination by applying different shower shape cuts. Fig. 5.2 shows that large contamination of

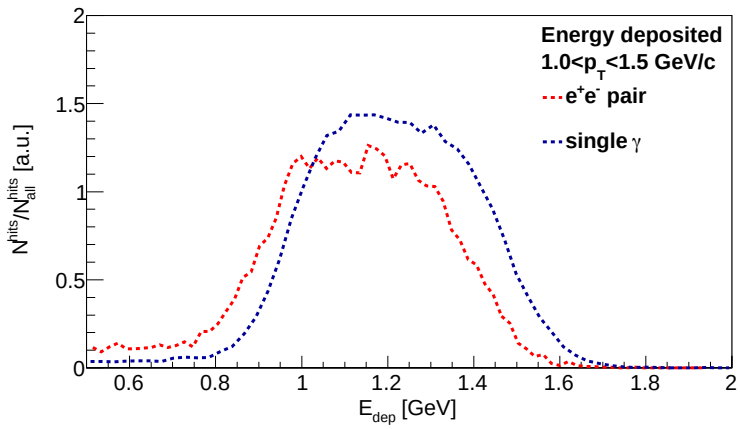

Figure 5.11: The simulated energy deposit in the EMCal detector of an electron-positron pair and a single photon in $1.0 < p_T < 1.5$ GeV/c. The distributions are normalized to number of hits in the detector. Note: the mean deposited energy by electron-position pairs is less as from the single-γ.

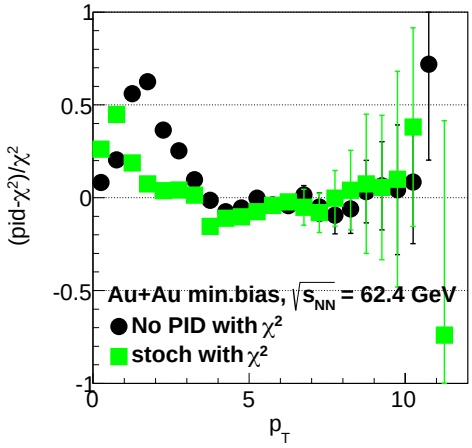

Figure 5.12: The ratio of the invariant yields reconstructed via different cluster identification to those yields reconstructed with the $\chi^2 < 3.0$ cut. The invariant yields are reconstructed in Au+Au minimum bias collisions at $\sqrt{s_{NN}} = 62.4$ GeV.

hadrons appears only at low-p_T region. The hadron rejection in the direct photon measurement largely depends on the PID cut applied on the clusters. The clusters without the PID cuts are not considered for direct photon reconstruction in the low-p_T due their low efficiency for hadron contamination rejection (shown previously in Fig. 2.11). The results of the invariant yield ratios using the different PID reconstruction are shown in

Fig. 5.12. In the same figure it is shown the systematic differences of the yields when using the χ^2 and stoch$_2$ cuts in the region $p_T = 2 - 5$ GeV/c, and it is estimated to be around 10%. At larger p_T values, the hadron contamination decreases (as shown in Fig. 2.11 and Fig. 2.12) and also the uncertainty originated from it.

Correction function uncertainties

In this section, we summarize the systematic uncertainties resulting from the parametrization of the correction factor $C^{\gamma}(p_T)$ (see Eq. (5.1)). Similarly as in the π^0case, we studied several polynomial parametrization of the correction function in order to estimate the systematic uncertainty introduced by the choice of the parametrization. For the final data analysis, we used a 4th order polynomial function to describe the correction function as shown in Fig. 5.8. For the systematic error estimation, we compared the 4th order polynomial with 5th and 3rd order polynomials. The difference of the correction function between a 4th and 5th order polynomial fit is estimated to be less than $< 2\%$, see in Fig. 5.13.

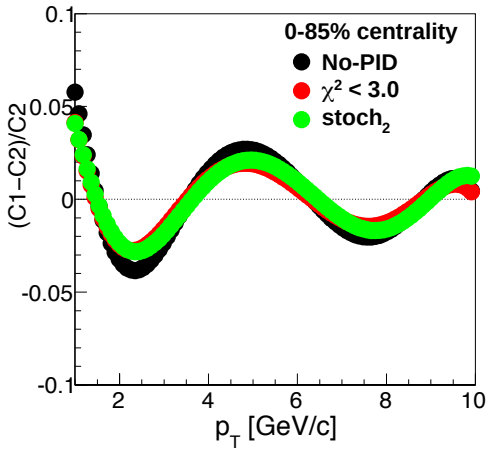

Figure 5.13: The ratio of two different parametrization of the correction functions for the direct photons in Au+Au minimum bias collisions at $\sqrt{s_{NN}} = 62.4$ GeV. The different colors represent the three PID cuts used for the reconstruction of the direct photon spectrum.

5.6 Summary

In summary, note that the analysis is still ongoing, this is not an approved PHENIX result yet. However, the thesis presents the detailed description of a new method for

the direct photon reconstruction. In comparison with previous analyses (e.g. [190]) it has the advantage to handle the correlated and uncorrelated photons separately. Similar analysis was done in Au+Au collisions at $\sqrt{s_{NN}} = 200$ GeV [156]. However, the published results do not include the study of the stoch_2 identification of the clusters, presented in this thesis.

Chapter 6

Results

6.1 π^0 Invariant Yield Results in Au+Au collisions at $\sqrt{s_{NN}}$ = 39 and 62.4 GeV

The invariant yields (see Eq. (5.2)) of π^0's in Au+Au minimum bias collision and different centrality bins at $\sqrt{s_{NN}}$ = 39 and 62.4 GeV are shown in Fig. 6.1. The invariant yield is reconstructed via $\pi^0 \to 2\gamma$ channel in rapidity window $|\eta| < 0.35$ and normalized to one unit of rapidity. Generally, the invariant yields can be divided into two parts: (i) low-p_T part, governed by hydrodynamics which exhibits an exponential shape, and (ii) high-p_T part that is dominated by the hard scattering, and can be approximated by a power law function (see Sec. 1.1.2). The power law exponent, n, of the high-p_T distribution carries interesting information about the $\sqrt{s}$ evolution of the soft-QCD radiation e.g. [192].

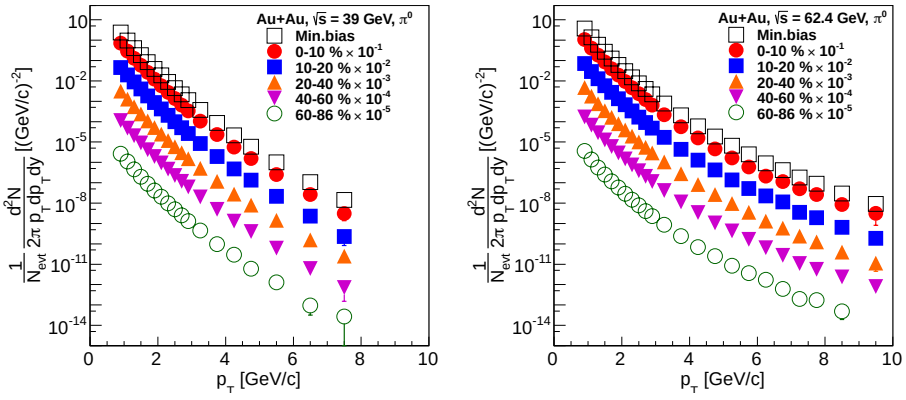

Figure 6.1: Invariant yields of π^0 in Au+Au at $\sqrt{s_{NN}}$ = 39 GeV (left) and 62.4 GeV (right) in all centralities and minimum bias. Only statistical uncertainties are shown.

In order the extract the n values for different $\sqrt{s}$, the invariant yields are fitted by a power-law function for $p_T > 4$ GeV/c and the results are summarized in Tab. 6.1 (note that values at $\sqrt{s_{NN}} = 200$ GeV are slightly different compared to [193] because of the different limits in fitting procedure). As discussed in Sec. 1.1.2 in the scale–less pQCD theory, the slope of the p_T distribution is expected to follow a power law distribution p_T^{-4} characteristic for a vector–boson exchange process between the two point–like particles. However, the distribution at finite collision energy is steeper due to the running coupling, evolution of the parton distribution function, k_T smearing and higher-twist phenomena. These effects are expected to play less important role with increasing c.m. system energy and thus $\lim_{\sqrt{s}\to\infty} n \to 4$.

Left panel of Fig. 6.2 (also in Tab. 6.1) shows the values of the power law exponents extracted from the π^0 spectra in Au+Au and p+p collisions at different energies in the range $\sqrt{s} = 39 - 200$ GeV. For the completeness of our study, the n values from the charged hadron spectra in Pb+Pb and p+p collisions at $\sqrt{s_{\rm NN}} = 2760$ GeV measured by the ALICE collaboration [9] are also shown.

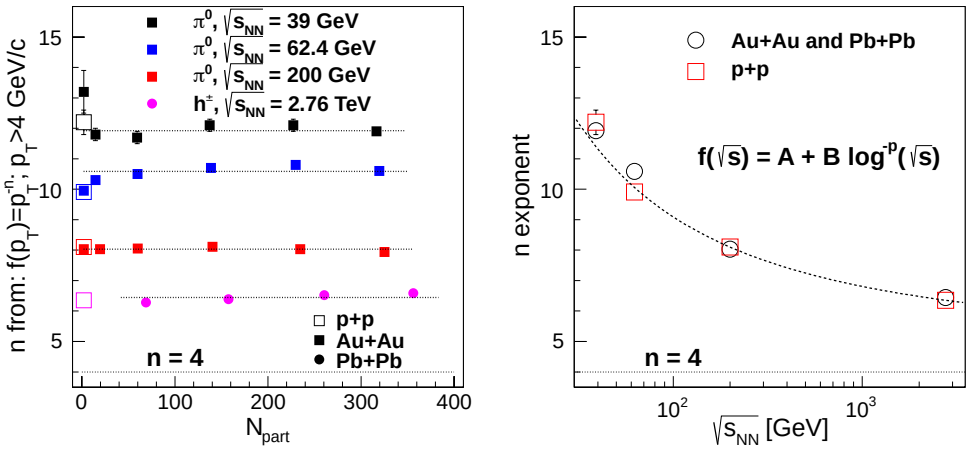

Figure 6.2: Left: The n values from the power law function fit ($f(x) = p_T^{-n}$) at the region $p_T > 4$ GeV/c at various collision systems and energies. Data from heavy ion collisions are plotted with full symbols, p+p collisions with open symbols and dashed lines represent the average overall centralities. Right: Extracted n values for all centralities in Au+Au and Pb+Pb collisions compared to those in p+p collisions as a function of energy. The dotted line over the point represents an empirical function fit. In both panels we indicate the expected slope of $n = 4$ for a vector–boson exchange.

There is no significant dependency of n values on the centrality (Fig. 6.2 left), however, the slope parameters show ordering $n_{\sqrt{s}=39} > n_{\sqrt{s}=62.4} > n_{\sqrt{s}=200} > n_{\sqrt{s}=2.76}$ (right panel of Fig. 6.2). The c.m. energy dependency of extracted n values was fitted by an empirical function $f(\sqrt{s}) = A + B\log^{-p}\sqrt{s}$, where $A = 76.2 \pm 15$, $B = 4.81 \pm 0.3$ and $p = -1.89 \pm 0.2$. It is interesting to note that n values are converging to the

expected p_T^{-4} dependency rather slowly. However, one has to take into account that we are extracting the n exponent from π^0 spectrum at RHIC energies and from charged hadrons at LHC. Obviously, to compare the n exponents from π^0 spectra would be more appropriate.

Collision type	Power law ($f(x) = (1/p_T)^n$) slope, n, value (error)		
	$\sqrt{s_{NN}} = 39$ GeV	$\sqrt{s_{NN}} = 62.4$ GeV	$\sqrt{s_{NN}} = 200$ GeV
Au+Au, Min. Bias	11.9 ± 0.1	10.6 ± 0.03	7.94 ± 0.02
Au+Au, 0-10%	12.1 ± 0.2	10.8 ± 0.06	8.03 ± 0.02
Au+Au, 10-20%	12.1 ± 0.2	10.7 ± 0.05	8.11 ± 0.02
Au+Au, 20-40%	11.7 ± 0.2	10.5 ± 0.05	8.05 ± 0.02
Au+Au, 40-60%	11.8 ± 0.2	10.3 ± 0.07	8.03 ± 0.02
Au+Au, 60-86%	13.2 ± 0.7	9.95 ± 0.14	8.03 ± 0.03
p+p	12.2 ± 0.4	9.91 ± 0.12	8.10 ± 0.01

Table 6.1: The fit results of the power law on neutral pion spectrum measured in Au+Au minimum bias collisions, different centralities and p+p collisions at $\sqrt{s_{NN}} = 39$, 62.4 GeV and compared with the previously published data at $\sqrt{s_{NN}} = 200$ GeV [193, 194]. The functions are fitted for $p_T > 4$ GeV/c.

6.1.1 x_T scaling

Fig. 6.3 shows the scaled invariant yields and $n_{\text{eff}}(x_T)$ (see Eq. (1.10)) extracted from the π^0 spectrum in Au+Au minimum bias and p+p collisions. The x_T dependency of the $n_{\text{eff}}(x_T)$ coefficient can be divided into two parts: (i) the low-x_T part shows a monotonic rise (ii) high-x_T shows a constant behavior. The Fig. 6.3 left panel shows the x_T scaled invariant cross section according to Eq. (1.9) in p+p and in Au+Au minimum bias collisions. A common trend is observed at high-x_T region, i.e. the scaled spectra overlap over wide x_T region which corresponds to n_{eff}=const. The deviation at lower x_T from the common trend can be attributed to transition between soft and hard processes which depends on the $\sqrt{s}$. Right panel of Fig. 6.3 shows the $n_{\text{eff}}(x_T)$ as a function of x_T. The shape and the magnitude are very similar between p+p and Au+Au for the $\sqrt{s_{NN}}$ ratio of 62.4/200. Similar behavior is observed also for the $\sqrt{s}$ ratio of 39/200 evaluated in p+p collisions, however, the low-x_T region in 39/200 deviates significantly from 62.4/200 pair. The 39/200 ratio measured in Au+Au exhibits a very different behavior in the full range of x_T values compared to other ratios.

The rise of the $n_{\text{eff}}(x_T)$ at lower x_T can be attributed to the dominance of soft processes [195]. The $n_{\text{eff}}(x_T)$ at high-x_T region are dominated by the pQCD processes [52], in which case one would expect $n_{\text{eff}} \approx$ const, although not necessary equal to 4 due to the higher order processes. While the scaling factor in Au+Au collisions at 39/200 GeV combination shows similar rise as in p+p collision, it may not even reach the plateau

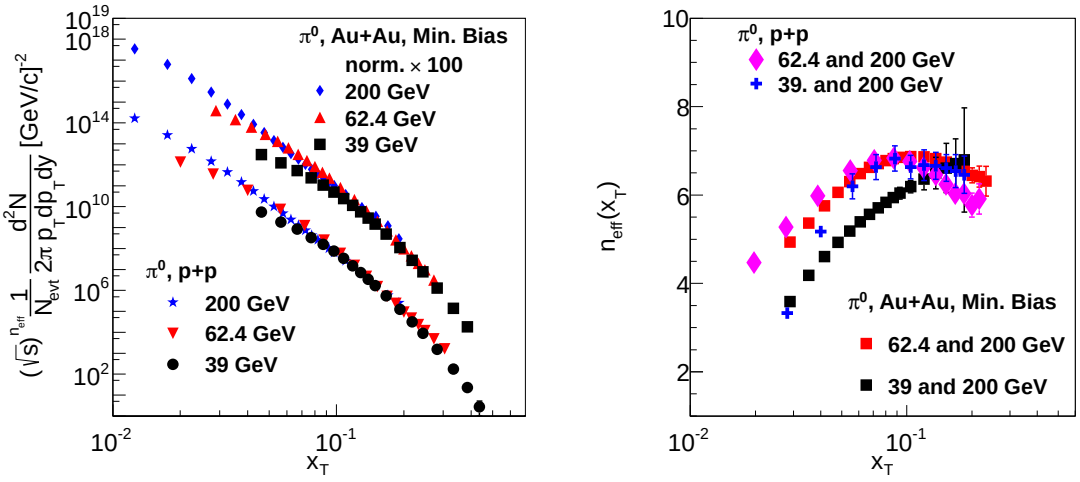

Figure 6.3: Left: The comparison of the scaled invariant cross section and invariant yields in p+p and in Au+Au minimum bias collisions at three collision energies as a function of $x_T = 2p_T/\sqrt{s_{NN}}$. Right: The scaling factor $n_{\rm eff}(x_T)$ of the x_T scaling of π^0's in p+p and in Au+Au minimum bias collisions at various energies indicated in the panel.

within observed x_T region. One possible explanation could be that the hard scattering does not dominate the p_T range up to ~ 4 GeV/c in $\sqrt{s_{NN}} = 39$ GeV Au+Au collisions.

6.2 Nuclear Modification Factor of π^0 in Au+Au collisions at $\sqrt{s_{NN}} = 39$ and 62.4 GeV

Determination of the p+p reference for the R_{AA} calculation was discussed in Sec. 4.4. In summary, the p+p reference for $\sqrt{s_{NN}} = 62.4$ GeV was obtained from the previously measured π^0 spectrum at PHENIX and extrapolated to the $7 < p_T < 10$ GeV/c region by a power law function. The systematic errors originating from the extrapolation are shown in Fig. 4.11. Because there is no p+p measurement at $\sqrt{s_{NN}} = 39$ GeV at RHIC we used the data measured by the E706 collaboration at Tevatron. Since the E706 experiment has different rapidity coverage as compare to PHENIX, we have corrected the p+p spectrum by the PYTHIA8 simulation. The acceptance correction function and its systematic error was calculated in Sec. 4.4.2.

Extracted nuclear modification factor, R_{AA}, as defined in Eq. (1.41), from $\sqrt{s_{NN}} =$ 39 and 62.4 GeV data is shown in Fig. 6.4. The $R_{\rm AA}$ values were determined for five centrality bins in Au+Au collisions. The data are compared to previously measured R_{AA} in Au+Au collisions at $\sqrt{s_{NN}} = 200$ GeV [8]. As explained in the Sec. 1.5.1,

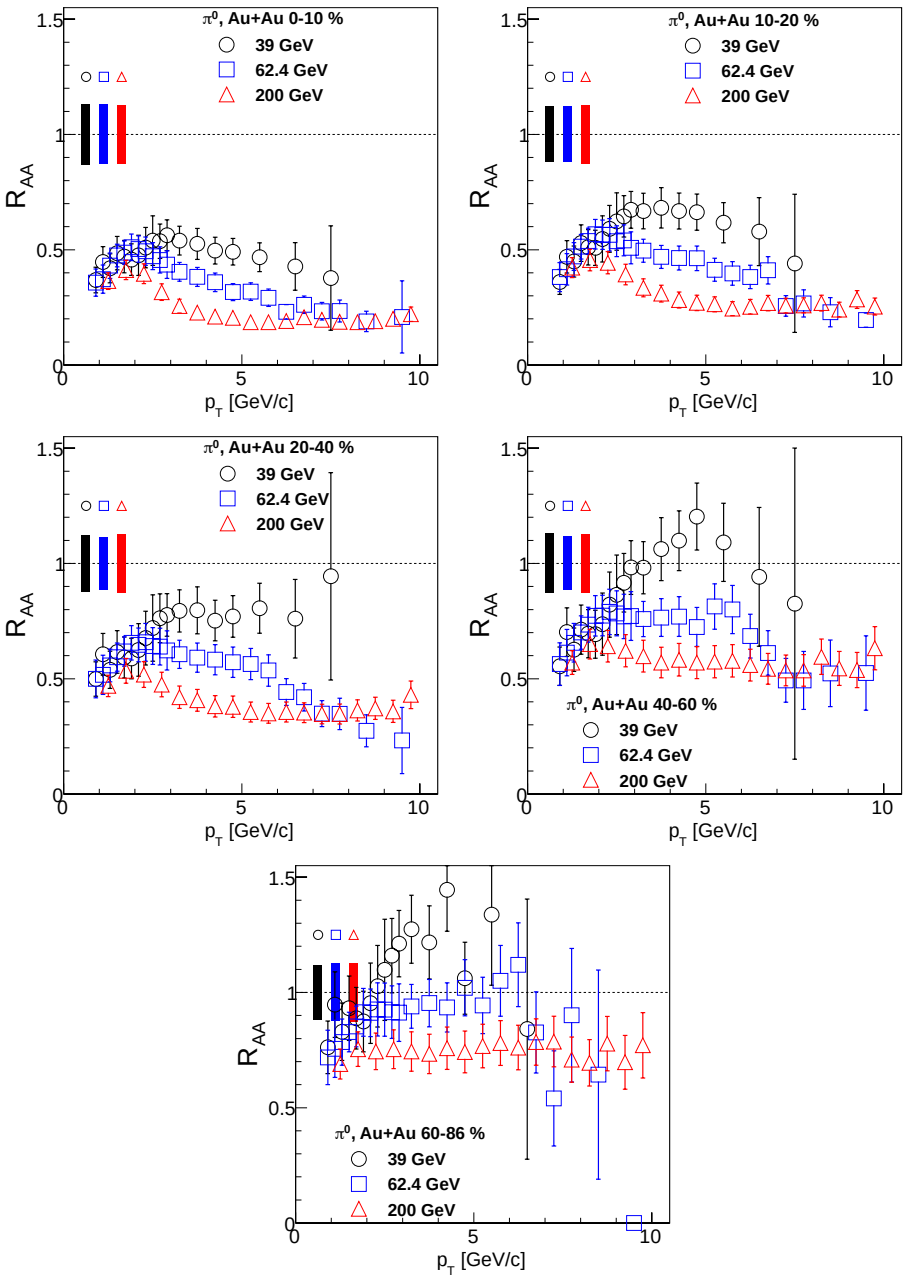

Figure 6.4: Neutral pion nuclear modification factor (R_{AA}) as a function of p_T in Au+Au collision in different centrality bins at $\sqrt{s_{NN}}$ = 39 GeV, 62.4 GeV and 200 GeV. The error bars give the quadratic sum of the statistical uncertainties and the p_T dependent systematic uncertainties. The boxes around unity combine the $\langle N_{\mathrm{coll}} \rangle$ and the absolute normalization uncertainties.

an analysis of the suppression at different collision energy provides an opportunity to study the transition from enhancement ($R_{AA} > 1$) to the suppression ($R_{AA} < 1$) of particle production. The final results are shown with the quadratic sum of statistical and systematical uncertainties. The boxes around unity show the p_T independent uncertainties combined with the $\langle N_{\rm coll} \rangle$ uncertainties.

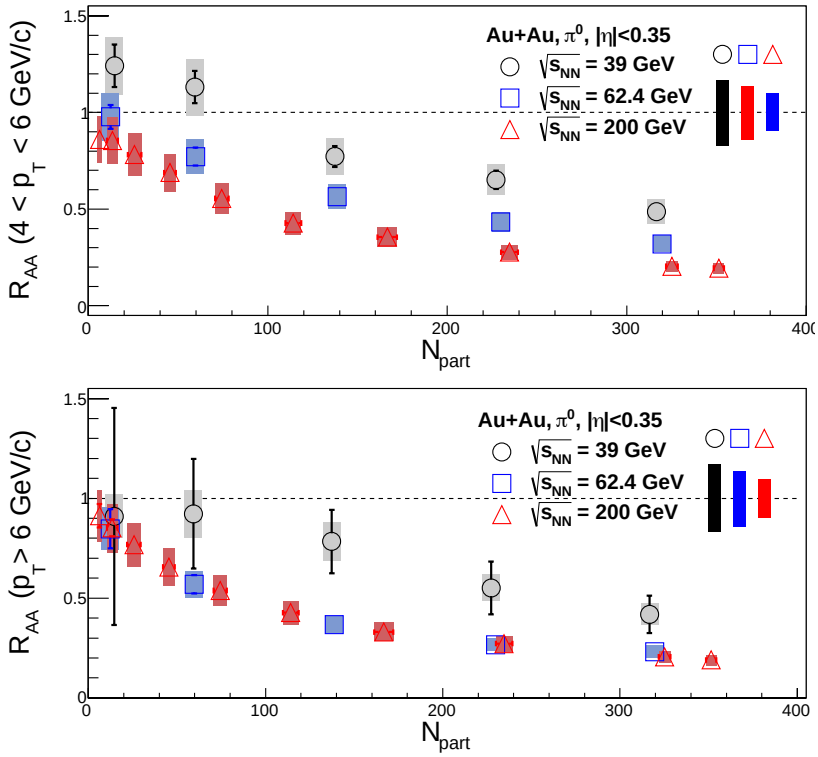

Figure 6.5: Neutral pion nuclear nuclear modification factor ($R_{\rm AA}$) as a function of $N_{\rm part}$ averaged in $4 < p_T < 6$ GeV/c bin (upper panel) and $p_T > 6$ GeV/c bin (lower panel) in Au+Au collision at $\sqrt{s_{NN}}$ = 39 GeV, 62.4 GeV and 200 GeV. The error bars are calculated as the quadratic sum of the statistical uncertainties and centrality dependent systematic errors and the $\langle N_{\rm coll} \rangle$ uncertainties. The boxes around unity correspond to the systematic uncertainties of the p+p reference and centrality independent systematic uncertainty of Au+Au collisions.

The $R_{\rm AA}$ values in Fig. 6.4 show similar behavior in the low-p_T range ($p_T < 2$ GeV/c) at the three different c.m. energies. This can be explained by the fact that the low-p_T particle production is dominated by the soft processes (see Sec. 6.1), which vary relatively slowly as a function of collision energies. For example, the average charged particle multiplicity density (dN_{ch}/dy) or transverse energy density (dE_T/dy) [96] do not change by more then factor of 2 within the $\sqrt{s_{NN}} = 39 - 200$ GeV c.m. energy range. Furthermore, the elliptic flow (v_2) varies by less than 5% in the same collision energy

range (see Fig. 1.23) [134]. In some models [196], the Cronin effect may further enhance the low-p_T particle production around $p_T \sim 3-4$ GeV/c. In the measured p_T region, the data are in agreement with little or no presence of the Cronin enhancement [141].

The hard scattering processes, and thus the suppression effect, dominate at higher p_T values. The data in Fig. 6.4 suggest that the suppression is dominant in the most central collisions (0-10%) at all three collision energies. In the mid-peripheral (40-60%) collisions the data exhibit substantial suppression at $\sqrt{s_{NN}} = 62.4$ and 200 GeV for $p_T > 4$ GeV/c, while the data at $\sqrt{s_{NN}} = 39$ GeV are consistent with no suppression at $p_T > 4$ GeV/c. The R_{AA} at $\sqrt{s_{NN}} = 62.4$ GeV is consistent for all centralities with the measurements at $\sqrt{s_{NN}} = 200$ GeV for the higher momentum region $p_T > 6$ GeV/c. Note that the same value of the nuclear modification factor does not mean the same magnitude of energy loss. Due to the steeper slopes at lower c.m. energy ($n_{62} - n_{200} \approx 2$, in Tab. 6.1), the fractional energy loss should be smaller in the case of $\sqrt{s_{NN}} = 62.4$ GeV.

The average value of $R_{\rm AA}$ was calculated in the two p_T bins: in the lower bin $4 < p_T < 6$ GeV/c and in higher bin $p_T > 6$ GeV/c, see in Fig. 6.5. The error bars are calculated as the quadratic sum of the statistical uncertainties and centrality dependent systematic errors and the $\langle N_{\rm coll} \rangle$ uncertainties. The boxes around unity correspond to the systematic uncertainties of the p+p reference and centrality independent systematic uncertainty of Au+Au collisions. We observe that the suppression of π^0 at $\sqrt{s_{NN}} = 39$ GeV only starts to dominate in the region of $N_{\rm part} > 100$, while it is pronounced already at lower centrality classes at $\sqrt{s_{NN}} = 62.4$ and 200 GeV.

6.2.1 Phenomenological Energy Loss

The alternative quantity to $R_{\rm AA}(p_T)$ suggested in [197] is the $S_{\rm loss}$ variable, defined as $S_{\rm loss}(p_T) \equiv \delta p_T / p_T$. The momentum difference δp_T corresponds to difference between the two p_T values, where the invariant yields of the T_{AA}-scaled p+p and Au+Au collisions are the same ($T_{AA} d^2N^{pp}/dp_T dy = d^2N^{AA}/dp_T dy \equiv f(p_T)$):

$$\delta p_T(f(p_T)) = \left(p_T^{pp} - p_T^{AA}\right). \tag{6.1}$$

Since the shape of the p+p and Au+Au spectra are power law of the same or very similar n exponent(Tab. 6.1), the $S_{\rm loss}$ would be independent of p_T at each collision energy and centrality. The $S_{\rm loss}$ quantity reflects, although in a simplified way, the trends of the average fractional energy loss of the initial parton.

Fig. 6.7 shows the calculated fractional energy loss of neutral pions, $S_{\rm loss}^{\pi^0}(p_T)$, as a function of the p_T^{pp}. The values are shown in Au+Au collisions for different centrality bins at three different energies ($\sqrt{s_{NN}} = 39$, 62.4 and 200 GeV). The point-by-point statistical uncertainties are coming from the vertical uncertainties of the invariant yields in both Au+Au and p+p collisions as in Fig. 6.1. These vertical uncertainties are then converted into the horizontal uncertainties in calculating the δp_T. Each of the type B

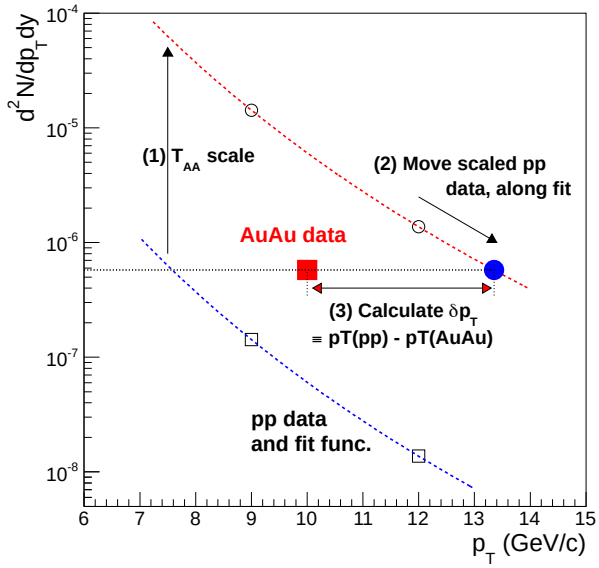

Figure 6.6: The illustration of phenomenological energy loss ($S_{\rm loss} = \delta p_T/p_T$) calculation method: (1) The measured spectrum in p+p collision (open squares) is scaled up by T_{AA} to corresponding Au+Au centrality (open circles). (2) the T_{AA}-scaled spectrum is fitted with a power law function and the data are interpolated to p_T^{pp} (blue circle), where $d^2N^{AA}/dp_Tdy = T_{AA}d^2N^{pp}/dp_Tdy$. (3) The momentum difference is calculated according to Eq. (6.1).

systematic uncertainties (see in Sec. 4.5) are individually calculated in the same way. Then, the p_T dependence of systematic uncertainties are propagated to the $S_{\rm loss}^{\pi^0}$ values.

The increase of $S_{\rm loss}^{\pi^0}$ in the low-p_T region ($p_T < 2$ GeV/c) has the same collective flow origin as the low-p_T bump in $R_{\rm AA}$ (see Fig. 6.4). In the high transverse momentum region the $S_{\rm loss}^{\pi^0}$ for all c.m. energies is, to a large extent, p_T independent similarly to the $R_{AA}(p_T)$. The $S_{\rm loss}^{\pi^0}$ has comparable values in Au+Au collisions at $\sqrt{s_{NN}} = 39$ and 62.4 GeV, while at $\sqrt{s_{NN}} = 200$ GeV they are systematically larger in every centrality. At peripheral collisions (60-86%) the fractional energy loss vanish at $\sqrt{s_{NN}} = 39$ and 62.4 GeV, whereas, at $\sqrt{s_{NN}} = 200$ GeV it is still above zero.

Due to the universality of the fragmentation function, the π^0 p_T distribution and the underlying jet spectrum have the same shape (the parent-child relationship introduced by Bjorken [198]). One can assume the fragmentation function of the parton is unchanged from the presumption the fragmentation process occurs outside of the medium. Thus, the fractional momentum loss can be interpreted as the average fractional energy loss $\langle\varepsilon\rangle = \langle\Delta E/E\rangle$ of the parent parton. Similar conclusion was reached using a theoretical energy loss model [199].

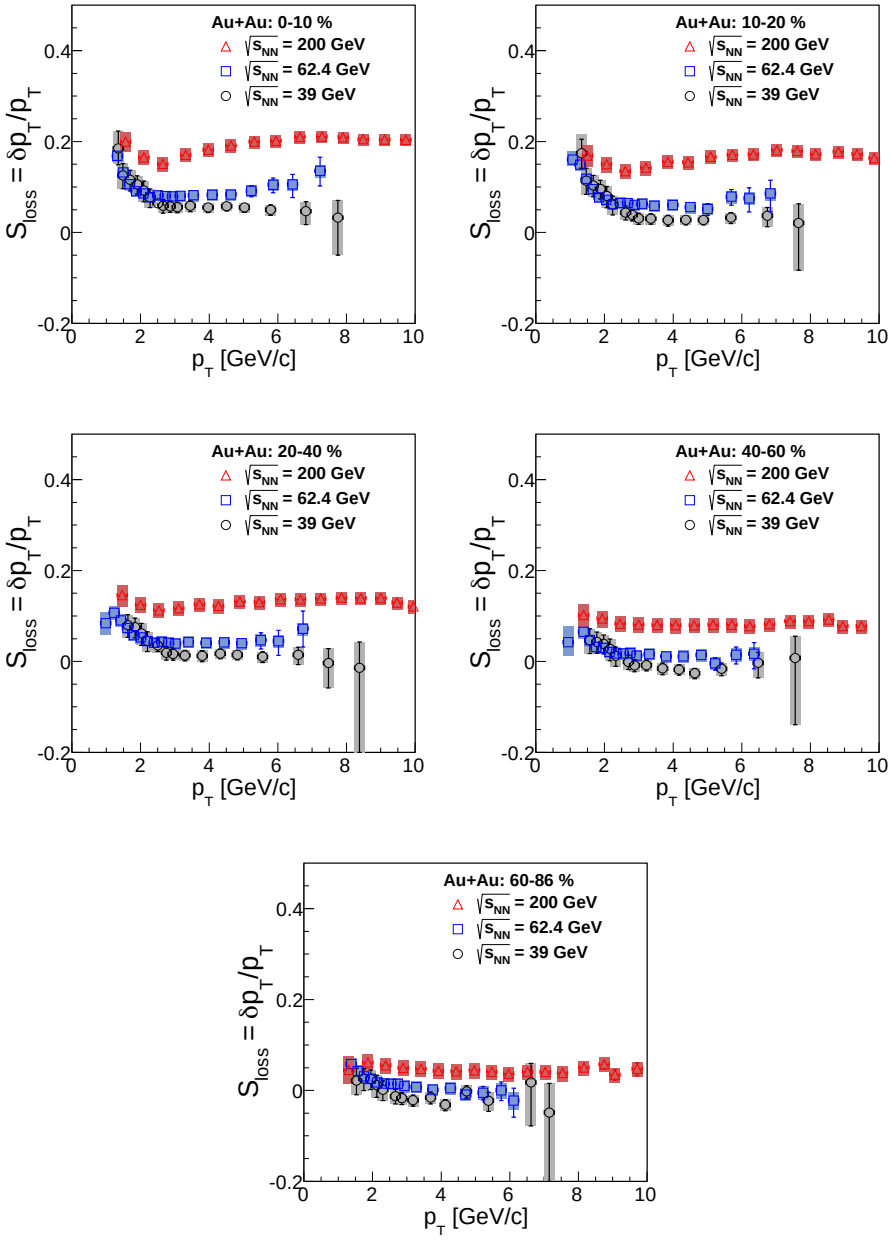

Figure 6.7: The fractional energy loss $S_{\rm loss} = \delta p_T/p_T$ (see text) of π^0's in Au+Au collisions at different collision energies, namely $\sqrt{s_{NN}} = 39$, 62.4 and 200 GeV. Each panel indicates different centralities.

Chapter 7

Discussion

7.1 Invariant Yields

The analyses of neutral mesons and direct photons were presented in Au+Au collisions at energies $\sqrt{s_{NN}} = 39$ and 62.4 GeV. The results were compared to the previously measured data in Au+Au collisions at $\sqrt{s_{NN}} = 200$ GeV. The measured η/π^0 ratio (see Fig. 4.33) from Au+Au minimum bias collisions at $\sqrt{s_{NN}} = 62.4$ GeV is consistent with the ratio from PYTHIA p+p calculation. The η/π^0 ratio is comparable, within quoted uncertainties, to the previously measured ratio in Au+Au, d+Au and p+p collisions at $\sqrt{s_{NN}} = 200$ GeV.

The shape of transverse momentum distributions of the neutral pions (see Fig. 6.1) at different energies were studied. The spectra were fitted by a power law functional form in the $p_T > 4$ GeV/c range and the power low exponent n has been extracted. We observed no significant dependency of exponent n on the centrality in Au+Au collisions and the the n values are comparable to those in p+p collisions at same collision energies (see Fig. 6.2). For completeness, we compared the slopes obtained from charged hadron spectra in Pb+Pb and p+p collisions at $\sqrt{s_{NN}} = 2760$ GeV [9]. The n exponents of power law fits are converging to the expected $n = 4$ value rather slowly.

In order to find the transition between the soft and hard particle production, we conducted the x_T-scaling studies in p+p and Au+Au collisions (see Fig. 6.3). The x_T-scaling shows similar soft to hard transition in Au+Au and p+p collisions at $\sqrt{s_{NN}}$ = 200 and 62.4 GeV. However, at $\sqrt{s_{NN}} = 39$ GeV collision energy the transition from soft to hard production occurs at higher p_T values in Au+Au collisions as in p+p collisions. The soft processes change slowly in heavy ion collisions, while the hard processes become steeper at lower collision energies $\sqrt{s}$, which results the hard scattering processes are dominant at higher p_T's.

7.2 Nuclear Modifications of Particle Production

The suppression of π^0's was observed at high-p_T in the most central Au+Au collisions at all three collision energies, $\sqrt{s_{NN}}$ = 39, 62.4 and 200 GeV (see Fig. 6.4). Centrality dependence of $R_{\rm AA}$ shows still significant suppression in mid-peripheral collisions at $\sqrt{s_{NN}}$ = 62.4 and 200 GeV, while the suppression is not as evident at $\sqrt{s_{NN}}$ = 39 GeV. The R_{AA} measured at $\sqrt{s_{NN}}$ = 39 GeV shows no dependency on centrality for $N_{\rm part} < 100$ (see Fig. 6.5), similarly as the R_{AA} in Cu+Cu collisions at $\sqrt{s_{NN}}$ = 22.4 GeV (in Sec. 1.5.1). The nuclear modification of particle production was also tested with a phenomenological fractional ($\Delta E/E$) energy loss model (see Fig. 6.7). In the momentum $4 < p_T < 10$ GeV/c region, the fractional energy loss is p_T independent in the collision range of $\sqrt{s_{NN}}$ = 39–200 GeV.

7.2.1 Theoretical Model Comparisons

There are several theoretical models attempting to describe the energy loss mechanism as introduced in Sec. 1.3. The systematic study of the transport coefficient ($\hat{q}$ in short, the virtuality transfer per unit length) of the different energy loss models was done in e.g. [8] in Au+Au collisions at $\sqrt{s_{NN}}$ = 200 GeV. However, the systematic study of theoretical model parameters [200] shows a large uncertainty (factor of ~ 2) of the gluon density, related to the transport coefficient, used in the opacity expansion (see in Sec. 1.3.2). The leading hadron suppression was also observed at LHC [9, 10] in Pb+Pb collisions at $\sqrt{s_{NN}}$ = 2760 GeV in a wide p_T region. The R_{AA} shows a steep rise as a function of p_T, which was predicted by several energy loss models [201].

Furthermore, the path-length dependence of the energy loss is studied via the high-p_T v_2 or $R_{AA}(\phi, p_T)$ (see Sec. 1.3.1) measurements. A first attempt to study the path-length dependence of the energy loss calculations showed a large deviation in all theoretical model approaches [202]. The energy loss mechanisms are also studied by use of the fully reconstructed jets in heavy ion collision, and compared to those in p+p collisions: at RHIC by STAR [203] and PHENIX [204] and at the LHC mainly by ATLAS [205] and CMS [206] collaborations.

Further studies of energy loss models are necessary in order to understand the suppression of leading hadrons (or jets) in terms of initial geometry (or path-length [207, 193]), centrality and collision energy (i. e. $\sqrt{s_{NN}}$ = 17.3–2760 GeV). In following sections, we compare three theoretical approaches to describe the $R_{AA}(p_T)$ measured at $\sqrt{s_{NN}}$ = 39 and 62.4 GeV.

Analytical approach - Vitev et al.

One of the theoretical approaches to describe the energy loss mechanism is the GLV framework [16]. As it was discussed in Sec. 1.3, the first step is the description of the thermodynamical medium. In this approximation, the medium is described by the

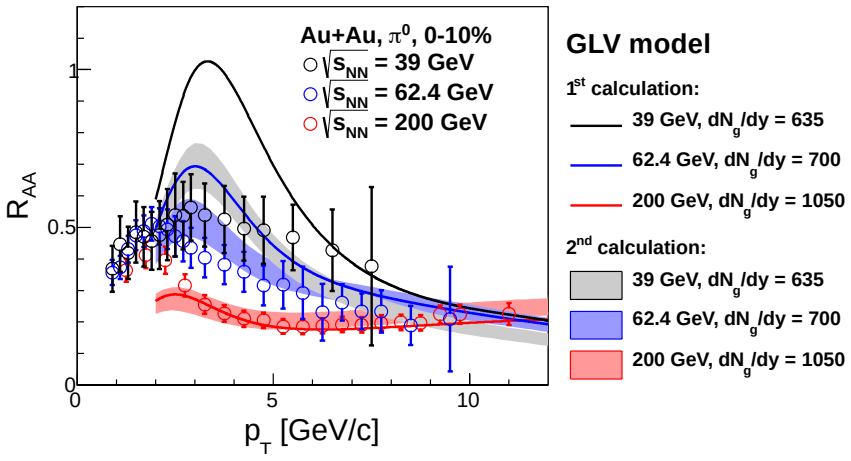

Figure 7.1: The nuclear modification factor (R_{AA}) in Au+Au most central collisions (0-10%) at three different energies, $\sqrt{s_{NN}}$ = 39, 62.4 and 200 GeV. The data points are shown with the quadratic sum of statistical and systematical uncertainties. The two versions of pQCD calculation (see in text) in the GLV framework are presented with solid curves (obtained with a parametrization of initial-state multiple scattering [208]) and bands (calculated within the same framework but with 30% larger initial-state parton mean free paths [209]) the energy loss varied by ±10%.

Bjorken expansion model [93]. In this model, the system is described by the relativistic hydrodynamics of ideal fluid [210]. The energy-momentum tensor of the relativistic ideal fluid can be written as

$$T_{\mu\nu} = (\epsilon + p)u_\mu u_\nu - g_{\mu\nu}p, \tag{7.1}$$

where $\epsilon(x)$ and $p(x)$ are the local energy density and the pressure, $u_\mu(x)$ is the four velocity of the fluid. In the thermodynamical system the energy and momentum is conserved, $\partial_\mu T^{\mu\nu} = 0$. The initial transverse energy density profile in this calculation is obtained from the framework of Glauber Model. The fluid expands only in the longitudinal direction, the velocity is defined as $v_z = z/t$. Previous study showed that the transverse velocity $v_T = (v_x, v_y)$ is not affecting the energy loss up to $v_T \lesssim 0.6c$ [211], thus it is neglected in this model. After the description of the medium is established, next step is the definition of the energy loss mechanism. The radiation intensity is inversely proportional to the mean free path of the gluon ($\lambda_g = (n\sigma)^{-1}$, where n the order of the opacity expansion and σ is the cross section of the radiation process). The opacity factor scales by the sum of N distinct targets: $L/\lambda_g = N\sigma/A_\perp$, where $A_\perp$ is the overlap region. The fractional energy loss in the GLV formalism [196] is derived as

$$\epsilon = \frac{\Delta E}{E} \approx \frac{9C_R\pi\alpha_s^3}{4}\frac{1}{A_\perp}\frac{dN^g}{dy}\frac{L}{E}\ln\frac{2E}{\mu^2 L} + \ldots, \tag{7.2}$$

where C_R is the color-factor ("Casimir") associated with gluon emission from a parton (for gluon $C_{\rm gluon} = 3$, or quark $C_{\rm quark} = 4/3$), α_s is the QCD coupling, μ is the Debye screening mass of the medium, dN^g/dy is the gluon density and L is the path-length of the parton propagating through the medium. The gluon density can be estimated from the charged hadron rapidity density as $dN^g/dy \approx (3/2)dN^{ch}/dy$ (assuming the initial state is purely gluonic). For this calculation, the densities are derived for $\sqrt{s_{NN}}$ = 39 and 62.4 GeV from the scaling behavior of the charged hadron multiplicity [212].

In Fig. 7.1 we compare the nuclear modification factor of the π^0's in the most central Au+Au collisions at three different energies $\sqrt{s_{NN}}$ = 39, 62.4 and 200 GeV. Two calculations are presented, where the first is obtained with a parametrization of initial-state multiple scattering [208]; the second is calculated within the same framework but with 30% larger initial-state parton mean free paths [209], reducing the Cronin effect. At high-p_T, the theoretical result is compatible with the $\sqrt{s_{NN}}$ = 200 GeV Au+Au data. However, the calculations at lower energies are not consistent with the data, the only qualitative agreement is that the turnover point of the R_{AA} curves moves to higher p_T with lower collision energy, as observed in the data. In this model calculation, large uncertainties originate from the unknown cold nuclear effects (Cronin effect, cold nuclear energy loss) as they are interfering with the final state parton energy loss. Further data, mainly from p+Au or d+Au collisions would further constrain the parameters of the model.

Monte Carlo approach - Renk et al.

Generally, in the Monte Carlo shower approach of the energy loss, one studies the development of the parton shower in the medium, while the fragmenting parton decreases its virtuality via gluon radiation. The parton shower evolution can be continued also in vacuum (i.e. as in p+p collisions) once the parton exits the medium. Later the modified shower hadronizes just like in vacuum, i.e. hadronization is assumed to take place outside the medium. One possibility is to use Lund fragmentation model as implemented in PYTHIA.

In this calculation the initial profile of the collision is described by the Glauber Monte Carlo model, and the created medium evaluated using viscous event-by-event three dimensional hydrodynamical evolution [213, 214]. The initial profile includes the event-by-event fluctuations.

The in-medium parton shower was evaluated by using the Monte Carlo code of YaJEM [17]. The model calculates the in-medium modification of the parton shower, similarly as PYTHIA calculates it in the vacuum. The model assumes that partons traversing the medium pick up additional virtuality which opens phase space for additional branchings in the shower, thus softening the parton spectrum. The key ingredient of this model is the increase of the virtuality of the shower parton due to medium

interaction

$$\Delta Q_a^2 = \int_{\tau_a^0}^{\tau_a^0+\tau_a} \hat{q}(\zeta) d\zeta,$$

where τ_0^a is the production time of the parton a and τ_a its lifetime and $\hat{q}(\zeta)$ is the transport coefficient along the ζ parton trajectory. The hard parton propagating in the medium also loses energy via elastic scattering, characterized by transport coefficient $\hat{e}$. The elastic energy loss in this calculation is fixed at about $\sim 10\%$ from the I_{AA} measurement in Au+Au collision at $\sqrt{s_{NN}} = 200$ GeV.

The parton shower is then converted to hadrons by the Lund string model [215]. In this model, the effective formation of hadrons ("hadronization") depends on the mass m_h and the energy E_h of the hadron:

$$\tau \sim E_h/m_h^2,$$

i.e. the formation time for π^0 for example at $p_T = 5$ GeV/c is $\gtrsim$50 fm. The diameter of the created medium ($d_{\text{med}} \sim 10 - 15$ fm) depends on the diameter of the nucleus, but it is safe to assume the π^0 is formed outside of the medium. Thus, the relevant energy loss is assumed to happen during the parton shower and the hadronization is not affected by the medium.

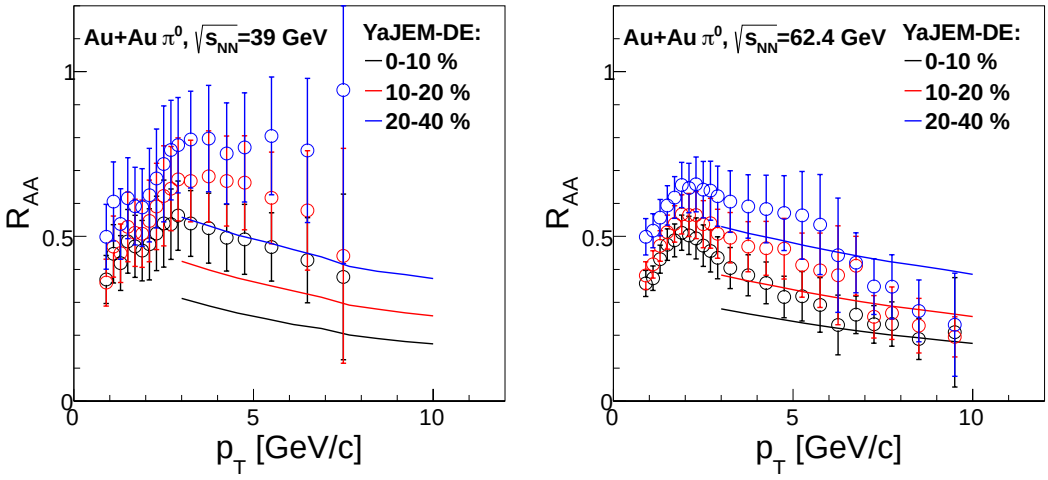

Figure 7.2: The nuclear modification factor in Au+Au collisions at three different energies at $\sqrt{s_{NN}} = 39$ GeV (left), 62.4 GeV (right) in three different centralities. The solid lines represent the nuclear modification calculated by the YaJEM-DE model [17].

Fig. 7.2 shows the recent calculation of pion suppression using the YaJEM-DE model at $\sqrt{s_{NN}} = 39$ and 62.4 GeV. The model has a very good description of different

observables at $\sqrt{s_{NN}} = 200$ and 2760 GeV [216, 217] and describes the data fairly well at higher collision energies $\sqrt{s_{NN}} = 62.4$ GeV. However, the model underestimates the data at lower energy $\sqrt{s_{NN}} = 39$ GeV. The disagreement at lower $\sqrt{s_{NN}}$ is probably due to the interplay of different particle production processes. In this calculation only the pQCD processes are included to calculate the nuclear modification factor. However, from our earlier studies (see in Fig. 6.3) we concluded that the region where pQCD processes are dominant is shifted to higher p_T values at lower $\sqrt{s_{NN}}$. This would mean that the pQCD processes calculated by this model are not yet dominant in the measured range, thus additional processes have to be included to describe the data.

Dipole approach - Kopeliovich et al.

A different approach to describe the suppression of high-p_T hadrons was proposed by Kopeliovich et al [18]. The model relies on the assumption that the virtuality of the created parton is equal to its energy, $E \simeq Q$. The model describes the energy loss in different time frames: (i) the parton propagates in the medium (for time t_p [218]) after which (ii) the pre-hadron ($q\bar{q}$) is created and transverse the medium (for time t_f) when survives the propagation through the matter and (iii) the final hadron is created. The hard scattered partons follow a steeply falling $\hat{p}_T$ spectrum, such the final state high-p_T hadrons are created more frequently when carrying a large fraction of the original momentum, $z_h = E_h/E_{q/g} \to 1$. The interval in which the leading hadron is created shrinks down

$$t_p \leq \frac{E}{\kappa}(1 - z_h), \tag{7.3}$$

where E is the total energy of the parton and $\kappa \approx 1$ GeV/fm is the typical tension of the string between outgoing quarks. Furthermore, the pre-hadron life time is expressed by the formation time of hadron wave function [219]

$$t_f = \frac{2z_h E}{m_{h^*}^2 - m_h^2}, \tag{7.4}$$

where m_h and m_{h^*} are the masses of the hadron and the first radial excitation h^*. According to the uncertainty principle, it takes proper time t_f to create the final state hadron from the pre-hadron dipole, $q\bar{q}$. The size of the initial dipole is small and the evolution of the dipole size in the medium is characterized by the transport coefficient $\hat{q}$. The survival probability of the dipole is characterized by the medium density and total propagation length [18]. For example, in case of a pion with $p_T = 5$ GeV/c and carrying the fraction $z_h = 0.7$, $t_p \approx 3.5$ fm/c and $t_f \approx 24$ fm/c (using $h^* = \rho(770)$).

In this approach, the medium is considered as a static homogenous cylinder with a transverse profile calculated from the optical Glauber Model. The transport coefficient was estimated from the fit of the most central (0-10%) data at each collision energy. The fitted transport coefficients are later used to calculate the energy loss for the different transverse profiles, the centrality and the path-length dependence.

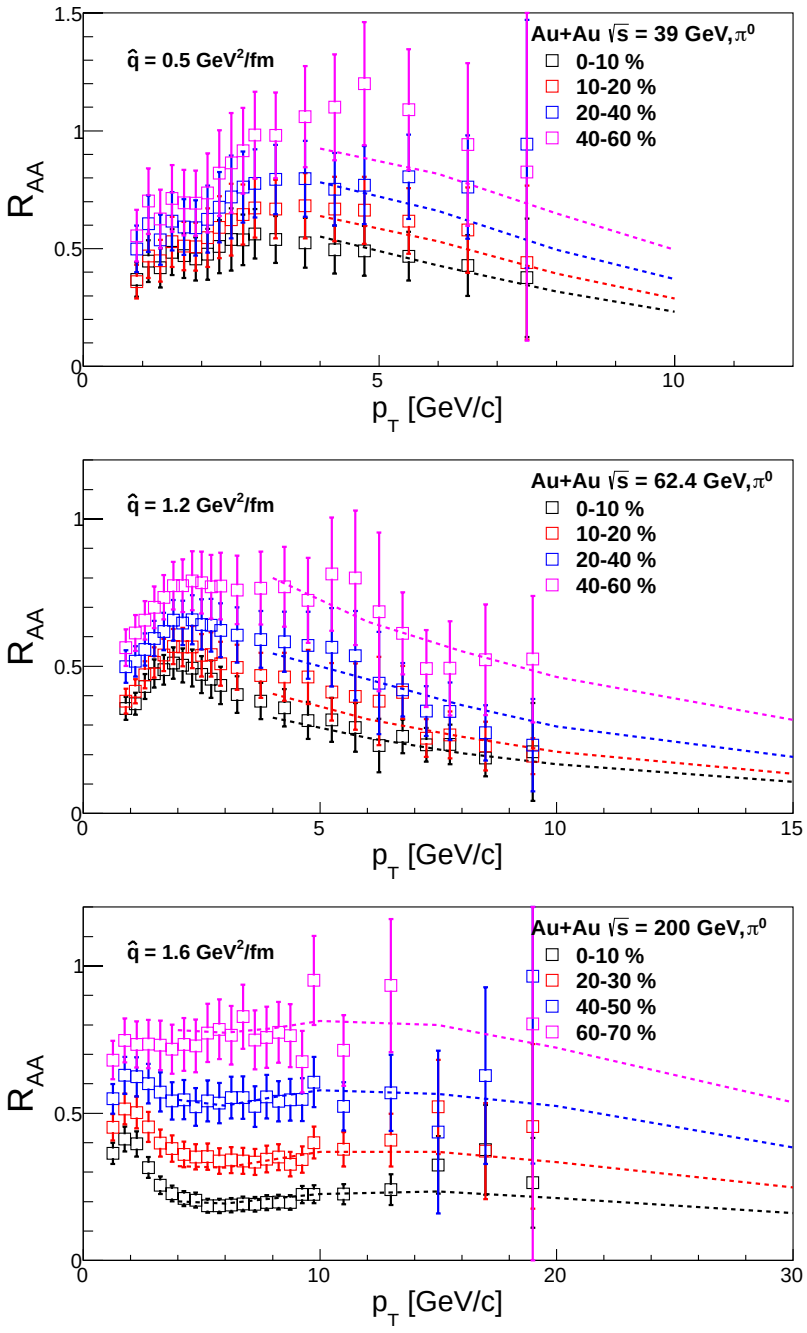

Figure 7.3: The nuclear modification factor in Au+Au collisions at different centralities and three different energies, $\sqrt{s_{NN}}$ = 39, 62.4 and 200 GeV. The data points are shown with the quadratic sum of statistical and systematical uncertainties. The model comparison as in [220] is shown with dashed lines in each centrality bins, the fitted transport coefficient $\hat{q}$ is presented for every energy.

In Fig. 7.3 we summarize the model calculation in Au+Au collisions in each centrality bin and at three different collision energies, $\sqrt{s_{NN}} = 39$, 62.4 and 200 GeV [220]. Due to the initial state interaction [221], the large $x_T = (2p_T/\sqrt{s})$ region of particle production is suppressed, where the model predicts suppression of high-x_T particle production. The suppression of the high-x_T particles depends strongly on the input parameter of the initial state interaction (ISI) model. The ISI model parameters are constrained from the d+Au (or p+A) collisions. The measured R_{AA} at $\sqrt{s_{NN}} = 200$ GeV in the momentum region $5 < p_T < 20$ GeV/c is consistent with the model. The model is also successful in the description of the nuclear modification factor at LHC energies [220], $\sqrt{s_{NN}} = 2.76$ TeV. At lower energy the suppression due to the ISI is reached earlier at $\sqrt{s_{NN}} = 39$ and 62.4 GeV is showing decreasing behavior for $p_T > 4$ GeV/c. The observation is consistent with the data within the uncertainties, see in Fig. 7.3 [220].

Model comparison

Three theoretical models were tested on the measured data. The basic assumptions of each model are summarized in Tab. 7.2.1. The analytical calculation (see Fig. 7.1) by Vitev et al. (GLV) [16] shows similar p_T dependency of the nuclear modification factor as the data. The energy loss calculation is comparable with the data in $\sqrt{s_{NN}} = 62.4$–2760 GeV region, however, at $\sqrt{s_{NN}} = 39$ GeV it underestimates the data at highest measured p_T values. The main uncertainty comes from the cold nuclear effects, which are not under control in the lower energy collisions. The model is not sensitive to the transverse expansion of the medium, as opposed to a jet-quenching Monte Carlo model (YaJEM-DE) by Thorsten Renk [17] (see Fig. 7.2). Here, the main uncertainties of the suppression come from the dynamical description of the medium. The transverse flow of the medium greatly influences the jet development inside the medium. The medium is modeled by a realistic 3D hydrodynamical calculations including viscosity. The model successfully describes the data at higher collision energies, $\sqrt{s_{NN}} = 62.4$–2760 GeV. However, at lower c.m. energies the model systematically underestimates the data, because in this model only the pQCD processes are included. The last model discussed here is based on the dipole approach by Kopeliovich et al. (Dipole) [18] (see Fig. 7.3). In contrast to the previously discussed models, it predicts a very short parton propagation in the medium after which a $q\bar{q}$ dipole is created. The model successfully describes the $R_{AA}(p_T)$ dependency at $\sqrt{s_{NN}} = 39$–2760 GeV energies, while the transport coefficient is much smaller than in previous models. The dipole evolution model has not yet implemented a dynamical medium evolution in the calculation. Note that the most realistic medium was used in the YaJEM-DE framework.

In the most central (0-10%) Au+Au collisions all three theoretical model calculations show similar R_{AA} value around $p_T \sim 10$ GeV/c at $\sqrt{s_{NN}} = 39$–200 GeV range, which is consistent with our data. The two pQCD based models (GLV and YaJEM-DE) derive the energy loss from assumed local energy density (or gluon density) (see

	GLV	YaJEM-DE	Dipole
	Medium		
Medium description	Bjorken expansion	3D hydro model	Static medium
Longitudinal evolution	yes	yes	no
Transverse evolution	no	yes	no
Tuned	multiplicity	multiplicity, $h^{\pm}$ spectra, v_n	-
'Soft' hadron production	yes	no	no
	Energy Loss		
Shower profile	leading parton	full shower	leading parton and dipole
transport coefficient $\langle\hat{q}\rangle$	calculated local gluon density	calculated local energy density	fitted on data
Centrality description	-	moderate	good
L dependency	-	good	good

Table 7.1: Summary of the basic assumptions in three theoretical model calculations to describe the measured R_{AA} in Au+Au collisions at $\sqrt{s_{NN}} = 39$ and 62.4 GeV.

Tab. 7.2.1). The gluon density in the GLV formalism is primarily estimated from the charged hadron multiplicity, in the YaJEM-DE formalism, it is estimated from the viscous hydrodynamical model. In contrast to the dipole model, the transport coefficient ($\hat{q}$) is estimated from the fits on the most central (0-10%) collisions at each collision energy. This fact deprives the model of the ability to predict the energy loss at different collisions energies.

The hadron production at very low-p_T region ($p_T < 2$ GeV/c) is governed by the hydrodynamical medium, while at the very high-p_T region ($p_T > 10$ GeV/c) it is dominated by the pQCD processes. However, the intermediate region is not yet fully understood, especially in the lower collision energies $\sqrt{s_{NN}} = 39$–62.4 GeV. As our studies show (see Fig. 6.3), the 'soft' particle production is dominant up to larger p_T region at the lower collision energies. The soft hadron production is partially included in the GLV model, however, the YaJEM-DE and the dipole model has not implemented them. The missing part of the particle production in the GLV and YaJEM-DE models could be the cause of the underestimation of the data. The data are used to fit the dipole model parameter, therefore, per definition shows no such difference.

Chapter 8

Summary

This work presents the measurements of the neutral mesons and direct photons in Au+Au collisions at $\sqrt{s_{NN}} = 39$ and 62.4 GeV. The main results on the evolution of π^0 suppression in Au+Au collisions from $\sqrt{s_{NN}} = 39$ GeV up to 200 GeV were published in [12], where the author of this thesis was the principal author.

The main contribution of the author of this thesis consists in the data analysis of the neutral pion, η and direct photon reconstruction in Au+Au collisions at $\sqrt{s_{NN}} = 39$ and 62.4 GeV. The correct energy calibration and the reconstruction of the dead-hot map of the detector (see Sec. 3.2) is necessary before the data analysis. The details of the data analyses of neutral mesons and direct photons are summarized in the Chapter IV and V. The neutral pions are measured up to $p_T < 8$ and 10 GeV/c at $\sqrt{s_{NN}} =$ 39 and 62.4 GeV, respectively. In order to evaluate the nuclear modification occurring in the Au+Au collisions, the p+p references are needed. The summary of obtaining the p+p references are presented in Sec. 4.4. The η/π^0 ratio was reconstructed in Au+Au minimum bias collisions at $\sqrt{s_{NN}} = 62.4$ GeV up to $p_T < 7$ GeV/c. The direct photons were reconstructed via the subtraction method using two different PID cuts up to $p_T < 10$ GeV/c in Au+Au minimum bias collisions at $\sqrt{s_{NN}} = 62.4$ GeV.

The invariant yields of neutral pions and x_T scaling results suggest the transition from the soft processes to hard processes occurs at higher p_T values in the lower collision energies. The nuclear modification factor in the most central Au+Au collision in the collision energy range $\sqrt{s_{NN}} = 39$–200 GeV shows the suppression of the neutral pion production. The π^0 production shows no suppression in the mid-peripheral region, while at higher collision energies it is still suppressed.

The further study of the nuclear modification of particle production could provide an interesting information about properties of the QCD medium. There is an ongoing program at RHIC which aims to study even lower c.m. range $\sqrt{s_{NN}} = 19$–27 GeV. Note that in the light of the presented results, the region where the pQCD processes dominate could be reached only at even higher p_T values. In addition to the 19–27 GeV program it would be also very beneficial to measure the p+p references at $\sqrt{s_{NN}} = 39$

and 62.4 GeV to improve the systematic errors on published R_{AA}. Furthermore, for the better understanding of the cold nuclear effects, the measurement in d+Au (or p+Au) collision are needed. With this data it will be certainly easier to constrain further the theoretical models to improve out knowledge of QCD phase transition.

The main contributions of the author of this thesis:

- Sector-by-sector energy recalibration of the low energy data (not disused in this thesis). Identification of the dead, hot and warm towers (Sec. 3.2).
- Analysis of the neutral meson production in Au+Au collisions at $\sqrt{s_{NN}} = 39$ and 62.4 GeV:
  - Reconstruction of invariant mass of neutral pions (Sec. 4.1) and eta mesons (Sec. 4.6.1).
  - Raw yield reconstruction for neutral pion (Sec. 4.1.1) and eta mesons (Sec. 4.6.1).
  - Monte Carlo simulation for the efficiency studies (Sec. 4.2, Sec. 4.6.2).
  - Study of the systematic errors (Sec. 4.5).
- Study of the neutral pion p+p references:
  - Extrapolation of the inclusive π^0 yield to higher p_T region at $\sqrt{s_{NN}} =$ 62.4 GeV and the related systematic error studies (Sec. 4.4.1).
  - Study of extrapolation methods at $\sqrt{s_{NN}} = 39$ GeV (Sec. 4.4.3, Sec. 4.4.4, Sec. 4.4.5).
  - Reconstruction of acceptance correction function for E706 data and the systematic error studies (Sec. 4.4.6).
- Evaluation of the neutral pion R_{AA} from $\sqrt{s_{NN}} = 39$ and 62.4 GeV data and systematic error studies.
- Analysis of the direct photons:
  - Inclusive photon reconstruction (Sec. 5.1).
  - Cluster identification studies (Sec. 2.4.3).
  - Reconstruction of decay photon contributions (Sec. 5.2).
  - Hadron contamination studies (Sec. 5.1.1).
  - Systematic error studies (Sec. 5.5.1).
- Principal author of the paper: "Evolution of π^0 suppression in Au+Au collisions from $\sqrt{s_{NN}} = 39$ to 200 GeV" [12].

Appendix A

Neutral Mesons

A.1 Neutral Mesons

In this section we discuss few basic features of the neutral mesons and their decays. Two neutral mesons are studied in detail, π^0 and η. In Tab. A.1 we summarize the basic properties of the particles, such as the mass, decay width and the dominant decay modes. These two neutral mesons (π^0 and η) are usually reconstructed via their dominant 2γ decay modes. In addition, they are the dominant source of the decay photon background in the direct photon reconstruction, discussed in Sec. 1.4. For the both the neutral mesons and direct photon analysis it is crucial to understand the kinematics of the decay of the neutral mesons.

neutral meson	π^0	η
mass [MeV/c^2]	134.9766 ± 0.0006	547.853 ± 0.024
width Γ [eV/c^2]	7.73 ± 0.16	1300 ± 70
selected decay modes	2γ (98.82%) $e^+e^-\gamma$ (1.174%)	2γ (39.31%) $3\pi^0$ (32.57%) $\pi^+\pi^-\pi^0$ (32.57%) $\pi^+\pi^-\gamma$ (4.60%)

Table A.1: Basic properties of neutral mesons [222]: π^0 and η.

A.1.1 Breit-Wigner Formula

In this section we follow the convention of $\hbar = c = 1$. The lifetime distribution of the particle is described by the decay rate Γ which corresponds to probability per unit time that a given particle decays. This can be written as:

$$dN = -\Gamma N dt \quad \rightarrow \quad N(t) = N(0)e^{-\Gamma t}, \tag{A.1}$$

where $N(t)$ is the number of particles surviving at the time t. The relation between decay width and mean lifetime of the decaying particle state follows from the uncertainty principle ($\Delta E \Delta t \sim 1 (= \hbar)$):

$$\tau = \frac{1}{\Gamma}. \tag{A.2}$$

Most particles have many possible decay modes with different branching ratios B_i, the fraction of all particles of the given type that decay into the specific mode i. The total decay rate ($\Gamma_{\rm tot}$) is the sum of all the decay widths of individual decay modes. The relations between the total decay rate, mean lifetime and branching ratio are:

$$\Gamma_{\rm tot} = \sum_i \Gamma_i, \quad \tau = \frac{1}{\Gamma_{\rm tot}} \quad \text{and} \quad B_i = \frac{\Gamma_i}{\Gamma_{\rm tot}}. \tag{A.3}$$

The decay form and shape is determined from the exponential time dependence as in Eq. (A.1). The energy dependence of the cross section of the particle decay is the Fourier transform of the time pulse, $\psi(t)$. The wave function of the decaying state with resonance energy E_R and width Γ, as well as its Fourier transform can be written as

$$\psi(t) = \psi(0) e^{-iE_R t - \Gamma t/2}, \tag{A.4}$$

$$\chi(E) = \int_0^\infty dt e^{iEt} \psi(t) = \psi(0) \cdot \frac{K}{(E - E_R) + i\Gamma/2}, \tag{A.5}$$

where K is constant. The cross section $\sigma(E)$ measuring the probability a particle decaying into two particles is proportional to $\chi^*(E)\chi(E)$:

$$\sigma(E) = \sigma_{\rm max} \cdot \frac{\Gamma^2/4}{(E - E_R)^2 + \Gamma^2/4}, \tag{A.6}$$

is called the Breit-Wigner formula. The cross section falls to half of its peak value $E - E_R = \pm\Gamma/2$ and Γ is referred as FWHM (Full-Width at Half-Maximum).

A.1.2 2-Body Decay Kinematics

In this section we study the decay kinematics of $\pi^0 \to 2\gamma$ decay. In the rest frame (RF) of the π^0 the two photons are created with opposite momenta with energy $m_\pi/2$ (see in Tab. A.1). The photons are generated with the random angular distribution with respect to the π^0 momentum. Then the photons are Lorentz boosted to the laboratory frame (LAB). The energy and momentum components of the two photons can be decomposed into two components:

$$E^{\rm LAB}_{\pm,||} = \gamma\left(E^{\rm RF} \pm \beta E^{\rm RF}_{||}\right) = \gamma\frac{m_\pi}{2}(\cos\theta^* \pm \beta), \quad \text{(A.7)}$$

$$E^{\rm LAB}_{\perp} = E^{\rm RF}_{\perp} = \frac{m_\pi}{2}\sin\theta^*, \quad \text{(A.8)}$$

$$p^{\rm LAB}_{\pm,||} = \gamma\left(\beta E^{\rm RF} \pm p^{\rm RF}_{||}\right) = \gamma\frac{m_\pi}{2}(1 \pm \beta\cos\theta^*), \quad \text{(A.9)}$$

$$p^{\rm LAB}_{\perp} = E^{\rm RF}_{\perp} = \frac{m_\pi}{2}\sin\theta^*, \quad \text{(A.10)}$$

where $E_{||}$ and $E_\perp$ refer to a longitudinal and perpendicular component of the photon energy with respect to the π^0 momentum and θ^* is the emission angle in RS w.r.t. π^0 momentum (see in Fig. A.1). It is useful to define the two photon asymmetry parameter

$$\alpha = \left|\frac{E_+ - E_-}{E_+ + E_-}\right| \quad \text{(A.11)}$$

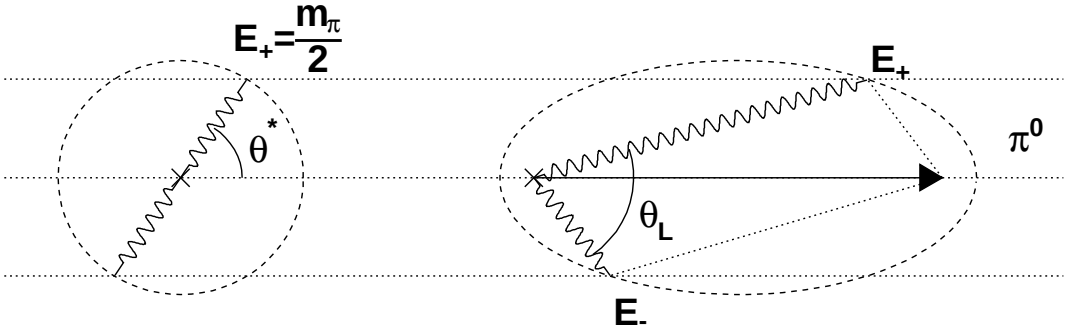

Figure A.1: Decay kinematics of the $\pi^0 \to \gamma\gamma$. The left one is in the rest frame (RF) and the right one in laboratory frame.

The asymmetry parameter is used later in the analysis in Chapter V. The invariant mass of the π^0 is reconstructed from the energy and opening angle in LAB frame (θ_L) of the decay products. Using the Eq. (A.10) and the usual four-momentum algebra, we can derive to:

$$M^2_\pi = (G_+ + G_-)^2 = 2E_+E_- - 2E_+E_-\cos\theta_L, \quad \text{(A.12)}$$

where the θ_L is the opening angle between the two photons. The θ^* decay angle in the RF of the π^0 is randomly distributed. The decay photons and the π^0 momentum form a plane, thus the geometry does not depend on the azimuthal angle ϕ. Thus, the number of photons per θ^* is given by the Jacobian

$$dN_\gamma = \sin\theta^* d\theta^* \quad \text{(A.13)}$$

The angular distribution of the photons using the Eq. (A.7-A.10)

$$\frac{dE_\gamma}{d\theta^*} = \mp\frac{1}{2}E_\pi\beta\sin\theta^* \tag{A.14}$$

Using the chain rule we see that

$$\left.\frac{dN_\gamma}{dE_\gamma}\right|_{y=0} = \frac{dN_\gamma}{d\theta^*}\frac{d\theta^*}{dE_\gamma} = \frac{2}{p_{T_\pi}}, \tag{A.15}$$

where p_{T_π} is the transverse momentum of the pion. Fig. A.2 shows decay photon distribution when a neutral pion is generated by a power law distribution ($\propto p_{T_\pi}^{-7}$) in $10 < p_{T_\pi} < 15$ GeV/c momentum bin.

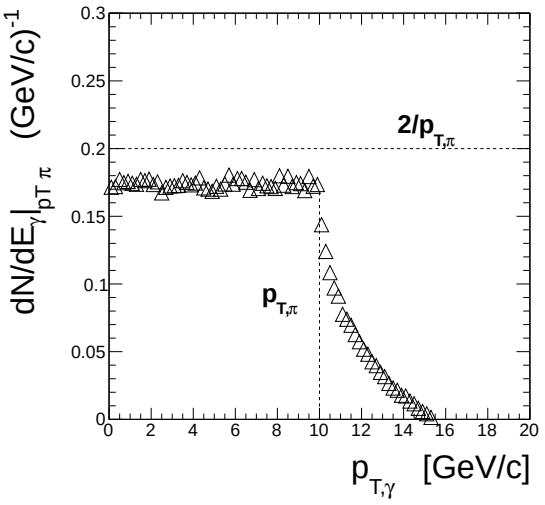

Figure A.2: The decay photon spectrum as a function of photon $p_{T,\gamma}$ of $\pi^0 \to 2\gamma$ decays where π^0's are generated by a power-law distribution ($f(p_T) = p_T^{-7}$) in the region of $10 < p_{T,\pi} < 15$ GeV/c. The dotted line represents the uniform distribution limit of decay photons with a fixed $p_{T,\pi} = 10$ GeV/c, thus $2/p_{T,\pi} = 0.2$ (GeV/c)$^{-1}$.

According Eq. (A.15) the decay photon distribution is flat. Since asymmetry $\alpha = \beta\cos\theta^*$ it is quite easy to see that $dN_\gamma/d\alpha$ is also flat (constant with α). We consider the pions to be measured in mid-rapidity ($\eta \approx 0$) where our detectors are located. Knowing Eq. (A.15) one can evaluate the decay photon distribution provided the π^0 p_T distribution has power law form $dN_\pi/dp_T \approx p_T^{-n}$ ($n = 7$ in case of $\sqrt{s} = 200$ GeV)

$$\left.\frac{dN_\gamma}{dE_\gamma}\right|_{\pi^0} = \int_{p_T=E_\gamma}^{\sqrt{s}/2}\frac{2}{p_{T_\pi}}\frac{1}{p_{T_\pi}^n}dp_{T_\pi} = \frac{2}{n}E_\gamma^{-n}, \tag{A.16}$$

and thus the double ratio of π^0 decay photon to π^0 distribution

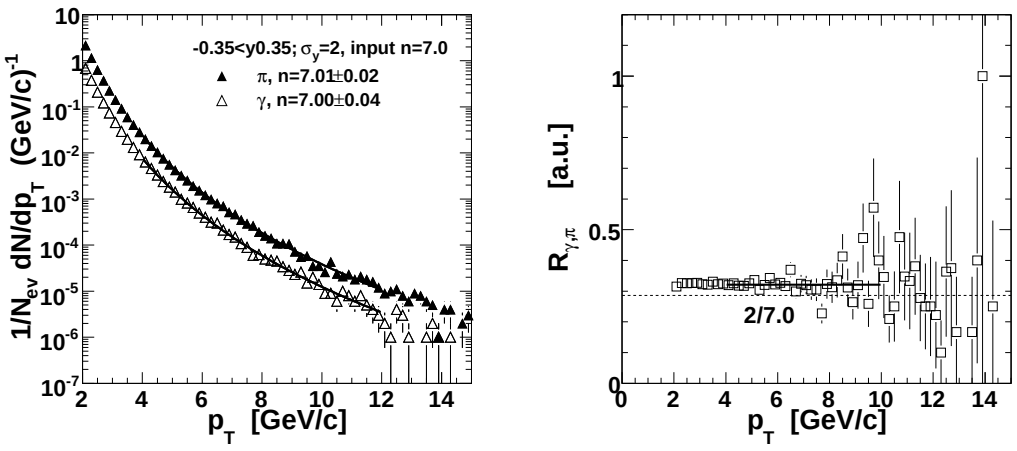

Figure A.3: The π^0 distribution generated according p_T^{-7} and Gaussian rapidity of the width $\sigma_y = 2$ together with the decay photon distribution (left panel). The particles are included only if they are in the rapidity region $|\eta| < 0.35$. The ratio of decay photon to the mother π^0 distribution, $R_{\gamma,\pi}$ (right panel). The solid line is the $0th$-order polynomial fit, the dashed line represents an expectation value according Eq. (A.17).

$$R_{\gamma,\pi} = \frac{dN_\gamma/dE_\gamma}{dN_\pi/dp_{T_\pi}} = \frac{2}{n}. \tag{A.17}$$

It is important to notice that this is valid only for mid-rapidity where the pion has no longitudinal component $E_\pi \approx p_{T_\pi}$. For the more general case where π^0 is not emitted perpendicular to the beam axis the simple scaling Eq. (A.17) does not hold. Fig. A.3 shows the results of the decay photon distribution using a realistic power-law distribution of p_{T_π}.

A.1.3 3-Body Decay Kinematics

The two main contributions for the decay-γ spectrum from the η mesons are the neutral decays. The $\eta \to 2\gamma$ decay channel is very similar to π^0 decay described in the previous section. In this section we focus on the three-body decay $\eta \to 3\pi^0$ which further produces 6 photons.

The decay rate of the $\eta \to 3\pi^0$ in the rest frame can be written as [223]:

$$\Gamma = \frac{1}{\tau} = \frac{1}{m_\eta} \frac{1}{(2\pi)^{3n-4}} \prod_{i=1}^{n} \frac{d^3\vec{p_i}}{2E_i} \delta^4 \left(\sum_{i=1}^{n} \vec{p_i} \right) \sum_{\text{spins}} |\langle f|T|i\rangle|^2, \tag{A.18}$$

where $n = 3$ is the number of decaying particles, $m_\eta = 547.85$ MeV/c^2 mass of the η mesons and $p_i = (E_i, \vec{p_i})$ is the four-vector of the ith daugther particles. Here we

construct a Monte-Carlo simulation for the three-body decay kinematics. The three-body decay can be treated as two time two-body decay. First, the η decays into π^0 and a unphysical W particle which is combination of two π^0's. The schematic view of the η decay is in Fig. A.4.

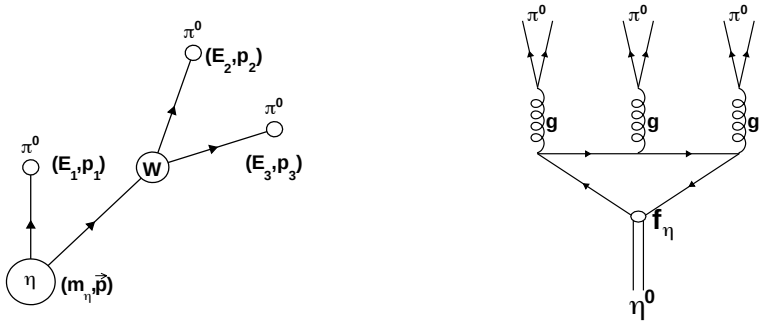

Figure A.4: The schematic view (left) and Feynman diagram (right) of the three-body η meson decay. The decay is treated as two-body decay into one π^0 and intermediate W particle. The W decays further into two π^0s.

The two π^0 combined into one W particle with the invariant mass of

$$W^2 = \left(\sum_{i=2}^{n} p_i\right)^2 = (p_2 + p_3)^2, \tag{A.19}$$

where the kinetic range is

$$4m_{\pi^0}^2 \leq W^2 \leq (m_\eta - m_{\pi^0})^2 . \tag{A.20}$$

In the rest frame of the η, the momentum and energy of the first decaying π^0 is given by

$$\vec{p_1} = \frac{1}{m_\eta}\sqrt{[(m_\eta + m_{\pi^0})^2 - W^2]\,[(m_\eta - m_{\pi^0})^2 - W^2]}, \tag{A.21}$$

$$E_1 = \sqrt{m_{\pi^0}^2 + \vec{p_1}^{\,2}} = \frac{1}{m_\eta}(m_\eta^2 + m_{\pi^0}^2 - W^2). \tag{A.22}$$

The four-vector of the intermediate particle state is $(E_{23}, \vec{p_{23}}) = (W, -\vec{p_1})$. The decay of intermediate particle is treated as a two-body decay. The first step is moving into the rest frame, $\vec{p_{23}} = \vec{0}$. In this frame, the two decaying π^0 decay back-to-back, with the momentum of $|\vec{p}| = \left(\sqrt{W^2 - \vec{p_1}^{\,2}}\right)/2$ (half of the invariant mass of the intermediate W particle). Then the two decaying π^0s $p_\pm = \left(\sqrt{\vec{p}^2 + m_{\pi^0}^2}, \pm\vec{p}\right)$ are boosted into the

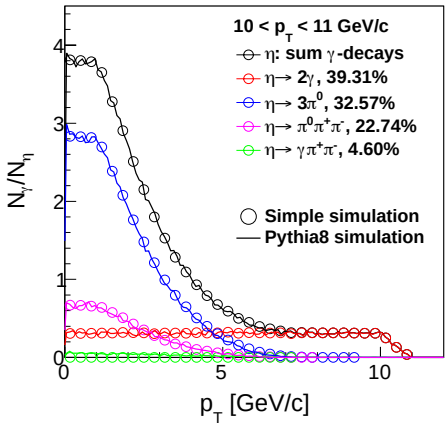

Figure A.5: Decay photon distribution from different η decay channels: $\eta \to 2\gamma$ (39.31%) and $\eta \to 3\pi^0 \to 6\gamma$ (32.57%), $\eta \to \pi^0\pi^+\pi^- \to 2\gamma\pi^+\pi^-$ (22.74%), $\eta \to \gamma\pi^+\pi^-$ (4.60%). The study was made in $10.0 < p_T < 11.0$ GeV/c with a simple simulation described in text and the PYTHIA8 event generator [126].

η rest frame. For the last step all the three decaying particles are boosted into the laboratory frame.

After three-body decay of the η to 3 π^0s, each π^0's decays to two photons as described in previous chapter. The two additional decay channels of η meson are similar three-body decay, with the slightly different mass $m_{\pi^\pm} = 139.57$ MeV/c^2 in $\eta \to \pi^0\pi^+\pi^-$ and with zero mass for γ in $\eta \to \gamma\pi^+\pi^-$. Fig. A.5 shows distributions the decay photons from η mesons generated momentum bin $10 < p_T < 11$ GeV/c. The decay photons are combination from four channels weighted by their branching ratios.

Bibliography

[1] E. V. Shuryak, Phys.Rept. **61**, 71 (1980).

[2] M. Gyulassy and M. Plumer, Phys.Lett. **B243**, 432 (1990).

[3] R. Baier, Y. L. Dokshitzer, A. H. Mueller, S. Peigne, and D. Schiff, Nucl.Phys. **B483**, 291 (1997), hep-ph/9607355.

[4] U. A. Wiedemann, Nucl.Phys. **B582**, 409 (2000), hep-ph/0003021.

[5] X.-N. Wang and X.-f. Guo, Nucl.Phys. **A696**, 788 (2001), hep-ph/0102230.

[6] PHENIX Collaboration, K. Adcox *et al.*, Phys.Rev.Lett. **88**, 022301 (2002), nucl-ex/0109003.

[7] STAR Collaboration, C. Adler *et al.*, Phys.Rev.Lett. **89**, 202301 (2002), nucl-ex/0206011.

[8] PHENIX Collaboration, A. Adare *et al.*, Phys.Rev.Lett. **101**, 232301 (2008), 0801.4020.

[9] ALICE Collaboration, K. Aamodt *et al.*, Phys.Lett. **B696**, 30 (2011), 1012.1004.

[10] CMS Collaboration, S. Chatrchyan *et al.*, Eur.Phys.J. **C72**, 1945 (2012), 1202.2554.

[11] WA98 Collaboration, M. Aggarwal *et al.*, Phys.Rev.Lett. **100**, 242301 (2008), 0708.2630.

[12] PHENIX Collaboration, A. Adare *et al.*, Phys.Rev.Lett. **109**, 152301 (2012), 1204.1526.

[13] S. Turbide, C. Gale, E. Frodermann, and U. Heinz, Phys.Rev. **C77**, 024909 (2008), 0712.0732.

[14] I. Vitev and B.-W. Zhang, Phys.Lett. **B669**, 337 (2008), 0804.3805.

[15] F. Arleo, K. J. Eskola, H. Paukkunen, and C. A. Salgado, JHEP **1104**, 055 (2011), 1103.1471.

[16] M. Gyulassy, P. Levai, and I. Vitev, Nucl.Phys. **B594**, 371 (2001), nucl-th/0006010.

[17] T. Renk, Phys.Rev. **C78**, 034908 (2008), 0806.0305.

[18] B. Kopeliovich, I. Potashnikova, and I. Schmidt, Phys.Rev. **C83**, 021901 (2011), 1012.2854.

[19] P. A. Dirac, Proc.Roy.Soc.Lond. **A117**, 610 (1928).

[20] E. Fermi, Z.Phys. **88**, 161 (1934).

[21] H. Yukawa, Proc.Phys.Math.Soc.Jap. **17**, 48 (1935).

[22] M. Gell-Mann, Phys.Rev. **125**, 1067 (1962).

[23] Y. Ne'eman, Nucl.Phys. **26**, 222 (1961).

[24] M. Gell-Mann, Phys.Lett. **8**, 214 (1964).

[25] G. Zweig, PRINT-64-170 (1964).

[26] R. Blankenbecler, S. J. Brodsky, and J. Gunion, Phys.Lett. **B42**, 461 (1972).

[27] G. 't Hooft, Nucl.Phys. **B35**, 167 (1971).

[28] E. Rutherford, Phil.Mag. **11**, 166 (1906).

[29] E. Rutherford, Phil.Mag. **12**, 134 (1906).

[30] E. Rutherford, Phil.Mag. **21**, 669 (1911).

[31] R. Hofstadter, Rev.Mod.Phys. **28**, 214 (1956).

[32] M. Rosenbluth, Phys.Rev. **79**, 615 (1950).

[33] D. Coward *et al.*, Phys.Rev.Lett. **20**, 292 (1968).

[34] W. Bartel *et al.*, Phys.Lett. **B28**, 148 (1968).

[35] M. Breidenbach *et al.*, Phys.Rev.Lett. **23**, 935 (1969).

[36] J. Bjorken, Phys.Rev. **179**, 1547 (1969).

[37] J. Martin *et al.*, Phys.Rev. **D20**, 5 (1979).

[38] W. Panofsky, SLAC-PUB-0502 (1968).

[39] R. Feynman, In Brown, L.M. (ed.): Selected papers of Richard Feynman 497-518 (1989).

[40] J. Callan, Curtis G. and D. J. Gross, Phys.Rev.Lett. **22**, 156 (1969).

[41] HERA Combined Structure Functions Working Group, C. Gwenlan, Nucl.Phys.Proc.Suppl. **191**, 5 (2009), 0902.1807.

[42] G. Cocconi, Nucl.Phys. **B28**, 341 (1971).

[43] J. Allaby *et al.*, Phys.Lett. **B28**, 67 (1968).

[44] F. Busser *et al.*, Nucl.Phys. **B106**, 1 (1976).

[45] CERN-Columbia-Oxford-Rockefeller Collaboration, CCOR Collaboration, A. Angelis *et al.*, Phys.Lett. (1978).

[46] S. Berman, J. Bjorken, and J. B. Kogut, Phys.Rev. **D4**, 3388 (1971).

[47] R. Blankenbecler, S. J. Brodsky, and J. Gunion, Phys.Rev. **D12**, 3469 (1975).

[48] R. Cahalan, K. Geer, J. B. Kogut, and L. Susskind, Phys.Rev. **D11**, 1199 (1975).

[49] D. Antreasyan *et al.*, Phys.Rev.Lett. **38**, 112 (1977).

[50] H. J. Frisch *et al.*, Phys.Rev.Lett. **44**, 511 (1980).

[51] D. L. Jones and J. Gunion, Phys.Rev. **D19**, 867 (1979).

[52] F. Arleo, S. J. Brodsky, D. S. Hwang, and A. M. Sickles, Phys.Rev.Lett. **105**, 062002 (2010), 0911.4604.

[53] K. A. Brueckner, Phys.Rev. **86**, 106 (1952).

[54] M. Han and Y. Nambu, Phys.Rev. **139**, B1006 (1965).

[55] O. Greenberg, Phys.Rev.Lett. **13**, 598 (1964).

[56] Particle Data Group, W. Yao *et al.*, J.Phys. **G33**, 1 (2006).

[57] Crystal Ball Collaboration, D. Williams *et al.*, (1988).

[58] PLUTO Collaboration, C. Berger *et al.*, Phys.Lett. **B82**, 449 (1979).

[59] TASSO Collaboration, R. Brandelik *et al.*, Phys.Lett. **B86**, 243 (1979).

[60] D. Barber *et al.*, Phys.Rev.Lett. **43**, 830 (1979).

[61] PLUTO Collaboration, C. Berger *et al.*, Phys.Lett. **B86**, 418 (1979).

[62] JADE Collaboration, W. Bartel *et al.*, Phys.Lett. **B91**, 142 (1980).

[63] J. R. Ellis, M. K. Gaillard, and G. G. Ross, Nucl.Phys. **B111**, 253 (1976).

[64] D. Duke and R. Roberts, Phys.Lett. **B85**, 289 (1979).

[65] D. Gross and F. Wilczek, Phys.Rev. **D8**, 3633 (1973).

[66] H. D. Politzer, Phys.Rept. **14**, 129 (1974).

[67] S. Bethke, Prog.Part.Nucl.Phys. **58**, 351 (2007), hep-ex/0606035.

[68] N. Nielsen, Am.J.Phys. **49**, 1171 (1981).

[69] R. Field and R. Feynman, Nucl.Phys. **B136**, 1 (1978).

[70] M. Jacob, CERN-TH-2700 (1979).

[71] J. Owens, Rev.Mod.Phys. **59**, 465 (1987).

[72] G. Bunce, N. Saito, J. Soffer, and W. Vogelsang, Ann.Rev.Nucl.Part.Sci. **50**, 525 (2000), hep-ph/0007218.

[73] R. K. Ellis, W. J. Stirling, and B. Webber, Camb. Monogr. Part.Phys.Nucl. Phys.Cosmol. **8**, 1 (1996).

[74] Y. L. Dokshitzer, Sov.Phys.JETP **46**, 641 (1977).

[75] V. Gribov and L. Lipatov, Sov.J.Nucl.Phys. **15**, 438 (1972).

[76] G. Altarelli and G. Parisi, Nucl.Phys. **B126**, 298 (1977).

[77] J. Pumplin *et al.*, JHEP **0207**, 012 (2002), hep-ph/0201195.

[78] H.-L. Lai *et al.*, Phys.Rev. **D82**, 054021 (2010), 1004.4624.

[79] R. Thorne, A. Martin, W. Stirling, and G. Watt, p. 305 (2007), 0706.0456.

[80] R. D. Ball *et al.*, Nucl.Phys. **B838**, 136 (2010), 1002.4407.

[81] L. Cormell and J. Owens, Phys.Rev. **D22**, 1609 (1980).

[82] H. Fritzsch and P. Minkowski, Phys.Lett. **B69**, 316 (1977).

[83] J. C. Collins and M. Perry, Phys.Rev.Lett. **34**, 1353 (1975).

[84] K. G. Wilson, Rev.Mod.Phys. **47**, 773 (1975).

[85] Z. Fodor and S. Katz, JHEP **0404**, 050 (2004), hep-lat/0402006.

[86] F. Karsch, E. Laermann, A. Peikert, C. Schmidt, and S. Stickan, p. 180 (2000), hep-lat/0010027.

[87] Y. Aoki, G. Endrodi, Z. Fodor, S. Katz, and K. Szabo, Nature **443**, 675 (2006), hep-lat/0611014.

[88] F. Karsch, K. Redlich, and A. Tawfik, Phys.Lett. **B571**, 67 (2003), hep-ph/0306208.

[89] G. Endrodi, Z. Fodor, S. Katz, and K. Szabo, JHEP **1104**, 001 (2011), 1102.1356.

[90] T. Ludlam, Nucl.Phys. **A750**, 9 (2005).

[91] PHENIX Collaboration, K. Adcox *et al.*, Nucl.Phys. **A757**, 184 (2005), nucl-ex/0410003.

[92] B. Alver, M. Baker, C. Loizides, and P. Steinberg, (2008), 0805.4411.

[93] J. Bjorken, Phys.Rev. **D27**, 140 (1983).

[94] E-802 Collaboration, L. Ahle *et al.*, Phys.Lett. **B332**, 258 (1994).

[95] NA49 Collaboration, T. Alber *et al.*, Phys.Rev.Lett. **75**, 3814 (1995).

[96] PHENIX Collaboration, S. Adler *et al.*, Phys.Rev. **C71**, 034908 (2005), nucl-ex/0409015.

[97] E. Iancu, (2012), 1205.0579.

[98] T. Renk, H. Holopainen, U. Heinz, and C. Shen, Phys.Rev. **C83**, 014910 (2011), 1010.1635.

[99] T. Renk, H. Holopainen, J. Auvinen, and K. J. Eskola, Phys.Rev. **C85**, 044915 (2012), 1105.2647.

[100] R. Baier, Y. L. Dokshitzer, A. H. Mueller, S. Peigne, and D. Schiff, Nucl.Phys. **B484**, 265 (1997), hep-ph/9608322.

[101] S. A. Bass *et al.*, Phys.Rev. **C79**, 024901 (2009), 0808.0908.

[102] R. Baier, A. Mueller, and D. Schiff, Phys.Lett. **B649**, 147 (2007), nucl-th/0612068.

[103] H. Liu, K. Rajagopal, and U. A. Wiedemann, JHEP **0703**, 066 (2007), hep-ph/0612168.

[104] SLAC-E-146 Collaboration, R. Becker-Szendy *et al.*, (1993).

[105] H. Bethe and W. Heitler, Proc.Roy.Soc.Lond. **A146**, 83 (1934).

[106] L. Landau and I. Pomeranchuk, Dokl.Akad.Nauk Ser.Fiz. **92**, 535 (1953).

[107] A. B. Migdal, Phys.Rev. **103**, 1811 (1956).

[108] SLAC-E-146 Collaboration, P. Anthony *et al.*, Phys.Rev. **D56**, 1373 (1997), hep-ex/9703016.

[109] A. Majumder and M. Van Leeuwen, Prog.Part.Nucl.Phys. **A66**, 41 (2011), 1002.2206.

[110] U. A. Wiedemann, CERN-PH-TH-2009-026 (2009), arXiv:0908.2306.

[111] F. Dominguez, C. Marquet, A. Mueller, B. Wu, and B.-W. Xiao, Nucl.Phys. **A811**, 197 (2008), 0803.3234.

[112] U. W. Heinz, arXiv:0901.4355 (2009).

[113] S. A. Voloshin, A. M. Poskanzer, and R. Snellings, (2008), arXiv:0809.2949.

[114] ALICE Collaboration, K. Aamodt *et al.*, Phys.Rev.Lett. **108**, 092301 (2012), 1110.0121.

[115] N. Armesto, C. A. Salgado, and U. A. Wiedemann, Phys.Rev. **D69**, 114003 (2004), hep-ph/0312106.

[116] P. B. Arnold, G. D. Moore, and L. G. Yaffe, JHEP **0206**, 030 (2002), hep-ph/0204343.

[117] N. Armesto, L. Cunqueiro, and C. A. Salgado, Nucl.Phys. **A830**, 271C (2009), 0907.4706.

[118] K. Zapp, G. Ingelman, J. Rathsman, J. Stachel, and U. A. Wiedemann, Eur.Phys.J. **C60**, 617 (2009), arXiv:0804.3568.

[119] I. Lokhtin and A. Snigirev, Eur.Phys.J. **C45**, 211 (2006), hep-ph/0506189.

[120] B. Schenke, C. Gale, and S. Jeon, Phys.Rev. **C80**, 054913 (2009), arXiv:0909.2037.

[121] M. Djordjevic and M. Gyulassy, Phys.Lett. **B560**, 37 (2003), nucl-th/0302069.

[122] S. Wicks, W. Horowitz, M. Djordjevic, and M. Gyulassy, Nucl.Phys. **A784**, 426 (2007), nucl-th/0512076.

[123] M. G. Mustafa and M. H. Thoma, Acta Phys.Hung. **A22**, 93 (2005), hep-ph/0311168.

[124] PHENIX Collaboration, S. Adler *et al.*, Phys.Rev.Lett. **96**, 032301 (2006), nucl-ex/0510047.

[125] STAR Collaboration, B. Abelev *et al.*, Phys.Rev.Lett. **98**, 192301 (2007), nucl-ex/0607012.

[126] T. Sjostrand, S. Mrenna, and P. Z. Skands, Comput.Phys.Commun. **178**, 852 (2008), arXiv:0710.3820.

[127] R. Baier, Y. L. Dokshitzer, A. H. Mueller, and D. Schiff, Phys.Rev. **C64**, 057902 (2001), hep-ph/0105062.

[128] T. Renk, Phys.Rev. **C79**, 054906 (2009), 0901.2818.

[129] A. Drees, Nucl.Phys. **A630**, 449C (1998).

[130] R. J. Fries, B. Muller, and D. K. Srivastava, Phys.Rev.Lett. **90**, 132301 (2003), nucl-th/0208001.

[131] S. Turbide, R. Rapp, and C. Gale, Phys.Rev. **C69**, 014903 (2004), hep-ph/0308085.

[132] E. Feinberg, Nuovo Cim. **A34**, 391 (1976).

[133] V. Begun, M. I. Gorenstein, A. Kostyuk, and O. Zozulya, Phys.Rev. **C71**, 054904 (2005), nucl-th/0410044.

[134] STAR Collaboration, L. Adamczyk *et al.*, (2013), 1301.2348.

[135] P. Costa, AIP Conf.Proc. **89dok2**, 255 (2007), hep-ph/0702232.

[136] P. Romatschke and U. Romatschke, Phys.Rev.Lett. **99**, 172301 (2007), 0706.1522.

[137] H. Song and U. W. Heinz, J.Phys. **G36**, 064033 (2009), 0812.4274.

[138] P. Kovtun, D. Son, and A. Starinets, Phys.Rev.Lett. **94**, 111601 (2005), hep-th/0405231.

[139] B. Schenke, S. Jeon, and C. Gale, Phys.Rev. **C85**, 024901 (2012), 1109.6289.

[140] C. Gale, S. Jeon, B. Schenke, P. Tribedy, and R. Venugopalan, (2012), 1210.5144.

[141] PHENIX Collaboration, S. Adler *et al.*, Phys.Rev.Lett. **98**, 172302 (2007), nucl-ex/0610036.

[142] J. Cronin *et al.*, Phys.Rev. **D11**, 3105 (1975).

[143] PHENIX Collaboration, A. Adare *et al.*, Phys.Rev.Lett. **101**, 162301 (2008), 0801.4555.

[144] WA98 Collaboration, M. Aggarwal *et al.*, Phys.Rev.Lett. **85**, 3595 (2000), nucl-ex/0006008.

[145] PHENIX Collaboration, A. Adare *et al.*, Phys.Lett. **B670**, 313 (2009), 0802.0050.

[146] M. L. Miller, K. Reygers, S. J. Sanders, and P. Steinberg, Ann.Rev.Nucl.Part.Sci. **57**, 205 (2007), nucl-ex/0701025.

[147] D. G. d'Enterria and D. Peressounko, Eur.Phys.J. **C46**, 451 (2006), nucl-th/0503054.

[148] R. Chatterjee and D. K. Srivastava, Phys.Rev. **C79**, 021901 (2009), 0809.0548.

[149] S. Rasanen, Nucl.Phys. **A715**, 717 (2003), nucl-th/0210007.

[150] R. Chatterjee, E. S. Frodermann, U. W. Heinz, and D. K. Srivastava, Phys.Rev.Lett. **96**, 202302 (2006), nucl-th/0511079.

[151] H. Holopainen, S. Rasanen, and K. J. Eskola, Phys.Rev. **C84**, 064903 (2011), 1104.5371.

[152] PHENIX Collaboration, A. Adare *et al.*, Phys.Rev.Lett. **109**, 122302 (2012), 1105.4126.

[153] R. Petti, J.Phys.Conf.Ser. **316**, 012026 (2011), 1107.5379.

[154] H. van Hees, C. Gale, and R. Rapp, Phys.Rev. **C84**, 054906 (2011), 1108.2131.

[155] PHENIX Collaboration, A. Adare *et al.*, Phys.Rev. **D86**, 072008 (2012), 1205.5533.

[156] PHENIX Collaboration, S. Afanasiev *et al.*, arXiv:1205.5759 (2012), 1205.5759.

[157] M. Harrison, T. Ludlam, and S. Ozaki, Nucl.Instrum.Meth. **A499**, 235 (2003).

[158] Phenix Collaboration, J. Gregory *et al.*, (1992).

[159] PHENIX Collaboration, D. Morrison *et al.*, Nucl.Phys. **A638**, 565 (1998), hep-ex/9804004.

[160] PHENIX Collaboration, L. Aphecetche *et al.*, Nucl.Instrum.Meth. **A499**, 521 (2003).

[161] PHENIX Collaboration, M. Allen *et al.*, Nucl.Instrum.Meth. **A499**, 549 (2003).

[162] PHENIX Collaboration, S. Campbell *et al.*, (2013), 1301.1096.

[163] PHENIX Collaboration, E. Richardson *et al.*, Nucl.Instrum.Meth. **A636**, 99 (2011), 1012.0873.

[164] C. Adler *et al.*, Nucl.Instrum.Meth. **A499**, 433 (2003).

[165] X.-N. Wang and M. Gyulassy, Phys.Rev. **D44**, 3501 (1991).

[166] PHENIX Collaboration, S. Belikov, J. Hill, J. Lajoie, H. Skank, and G. Sleege, Nucl.Instrum.Meth. **A494**, 541 (2002).

[167] A. M. Poskanzer and S. Voloshin, Phys.Rev. **C58**, 1671 (1998), nucl-ex/9805001.

[168] P. Danielewicz, Phys.Rev. **C51**, 716 (1995), nucl-th/9408018.

[169] G. David *et al.*, IEEE Trans.Nucl.Sci. **43**, 1491 (1996).

[170] J. Badier *et al.*, Nucl.Instrum.Meth. **A348**, 74 (1994).

[171] E. Tarkovsky, Nucl.Instrum.Meth. **A379**, 515 (1996).

[172] G. David, E. Kistenev, S. Stoll, S. N. White, and C. Woody, IEEE Trans.Nucl.Sci. **42**, 306 (1995).

[173] G. David *et al.*, IEEE Trans.Nucl.Sci. **45**, 705 (1998).

[174] T. Awes *et al.*, Nucl.Instrum.Meth.A (2002), nucl-ex/0202009.

[175] G. David *et al.*, IEEE Trans.Nucl.Sci. **45**, 692 (1998).

[176] S. Neumaier and J. Urbahn, (1995).

[177] M. Aggarwal *et al.*, Nucl.Phys. **A698**, 135 (2002).

[178] A. Bazilevsky, V. Kochetkov, V. Semenov, S. White, and E. Kistenev, Instrum.Exp.Tech. **42**, 167 (1999).

[179] T. Awes *et al.*, Nucl.Instrum.Meth. **A311**, 130 (1992).

[180] PHENIX Collaboration, J. Mitchell *et al.*, Nucl.Instrum.Meth. **A482**, 491 (2002), nucl-ex/0201013.

[181] M. Tannenbaum, Phys.Lett. **B498**, 29 (2001).

[182] J. Chauvin, D. Lebrun, A. Lounis, and M. Buenerd, Phys.Rev. **C28**, 1970 (1983).

[183] A. Trivedi *et al.*, (1997).

[184] R. Brun, F. Bruyant, M. Maire, A. McPherson, and P. Zanarini, (1987).

[185] Fermilab E706 Collaboration, L. Apanasevich *et al.*, Phys.Rev. **D68**, 052001 (2003), hep-ex/0204031.

[186] PHENIX Collaboration, A. Adare *et al.*, Phys.Rev. **D79**, 012003 (2009), 0810.0701.

[187] D. G. d'Enterria, J. Phys. **G31**, S491 (2005), nucl-ex/0411049.

[188] C. Kourkoumelis *et al.*, Phys. Lett. **B84**, 271 (1979).

[189] A. G. Clark *et al.*, Phys. Lett. **B74**, 267 (1978).

[190] PHENIX Collaboration, S. Adler *et al.*, Phys.Rev.Lett. **94**, 232301 (2005), nucl-ex/0503003.

[191] B. Bleichert, C. Grupen, and D. Mattern, Nucl.Instrum.Meth. **199**, 461 (1982).

[192] L. Apanasevich *et al.*, Phys.Rev. **D59**, 074007 (1999), hep-ph/9808467.

[193] PHENIX Collaboration, A. Adare *et al.*, (2012), 1208.2254.

[194] PHENIX Collaboration, A. Adare *et al.*, Phys.Rev. **D83**, 032001 (2011), 1009.6224.

[195] S. Berman, J. Bjorken, and J. B. Kogut, Phys.Rev. **D4**, 3388 (1971).

[196] R. Neufeld and I. Vitev, Phys.Rev. **C86**, 024905 (2012), 1105.2067.

[197] PHENIX Collaboration, S. Adler *et al.*, Phys.Rev. **C76**, 034904 (2007), nucl-ex/0611007.

[198] J. Bjorken, Phys.Rev. **D8**, 4098 (1973).

[199] W. Horowitz and M. Gyulassy, Nucl.Phys. **A872**, 265 (2011), 1104.4958.

[200] W. Horowitz and B. Cole, Phys.Rev. **C81**, 024909 (2010), 0910.1823.

[201] N. Armesto *et al.*, J.Phys. **G35**, 054001 (2008), 0711.0974.

[202] PHENIX Collaboration, S. Afanasiev *et al.*, Phys.Rev. **C80**, 054907 (2009), 0903.4886.

[203] J. Putschke, Nucl.Phys. **A855**, 83 (2011).

[204] PHENIX Collaboration, D. Perepelitsa, J.Phys.Conf.Ser. **389**, 012006 (2012).

[205] Atlas Collaboration, G. Aad *et al.*, Phys.Rev.Lett. **105**, 252303 (2010), 1011.6182.

[206] CMS Collaboration, S. Chatrchyan *et al.*, Phys.Rev. **C84**, 024906 (2011), 1102.1957.

[207] PHENIX Collaboration, A. Adare *et al.*, Phys.Rev.Lett. **105**, 142301 (2010), 1006.3740.

[208] R. Sharma, I. Vitev, and B.-W. Zhang, Phys.Rev. **C80**, 054902 (2009), 0904.0032.

[209] I. Vitev, Phys.Lett. **B606**, 303 (2005), nucl-th/0404052.

[210] L. Landau, Izv.Akad.Nauk Ser.Fiz. **17**, 51 (1953).

[211] M. Gyulassy, I. Vitev, X.-N. Wang, and P. Huovinen, Phys.Lett. **B526**, 301 (2002), nucl-th/0109063.

[212] R. Neufeld, I. Vitev, and B.-W. Zhang, Phys.Rev. **C83**, 034902 (2011), 1006.2389.

[213] H. Niemi, G. Denicol, P. Huovinen, E. Molnar, and D. Rischke, Phys.Rev. **C86**, 014909 (2012), 1203.2452.

[214] H. Niemi, G. Denicol, H. Holopainen, and P. Huovinen, (2012), 1212.1008.

[215] B. Andersson, G. Gustafson, G. Ingelman, and T. Sjostrand, Phys.Rept. **97**, 31 (1983).

[216] T. Renk, (2011), 1106.0581.

[217] T. Renk and K. J. Eskola, Phys.Rev. **C84**, 054913 (2011), 1106.1740.

[218] B. Kopeliovich and F. Niedermayer, Sov.J.Nucl.Phys. **42**, 504 (1985).

[219] B. Kopeliovich, H.-J. Pirner, I. Potashnikova, I. Schmidt, and A. Tarasov, Phys.Rev. **D77**, 054004 (2008), 0801.0251.

[220] B. Kopeliovich, J. Nemchik, I. Potashnikova, and I. Schmidt, Phys.Rev. **C86**, 054904 (2012), 1208.4951.

[221] B. Kopeliovich, J. Nemchik, I. Potashnikova, M. Johnson, and I. Schmidt, Phys.Rev. **C72**, 054606 (2005), hep-ph/0501260.

[222] Particle Data Group, C. Amsler *et al.*, Phys.Lett. **B667**, 1 (2008).

[223] J. Sollfrank, P. Koch, and U. W. Heinz, Z.Phys. **C52**, 593 (1991).